INSTITUT D'AERONOMIE SPATIALE DE BELGIQUE

3 - Avenue Circulaire
B - 1180 BRUXELLES

AERONOMICA ACTA

A - N° 298 - 1985

Frontiers of the plasmasphere
(Theoretical aspects)

by

J. LEMAIRE

BELGISCH INSTITUUT VOOR RUIMTE-AERONOMIE

3 - Ringlaan
B - 1180 BRUSSEL

FOREWORD

This work constitutes a review of the theoretical work published by the author on the subject of the formation theory of the plasmapause. Chapters 2 and 3 also contain results and original contributions which have not yet been presented elsewhere.

The ideas developed in chapters 4 and 5 concerning the formation and deformation mechanisms of the plasmapause have been illustrated in a montage produced at the Centre Audio-Visuel of Louvain-la-Neuve. Videotapes of this film are available at the Belgian Institute for Space Aeronomy.

This report has been presented at the Université Catholique de Louvain-la-Neuve and serves as dissertation in order to obtain the degree of "Agrégé de l'Enseignement Supérieur".

AVANT-PROPOS

Ce mémoire constitue le recueil de l'ensemble des travaux théoriques que l'auteur a publié sur le sujet de la théorie de la formation de la plasmapause. Il contient également aux chapitres 2 et 3 des résultats et des contributions originales qui n'ont pas encore été présentées ailleurs.

Les idées développées dans les chapitres 4 et 5 concernant les mécanismes de formation et de déformation de la plasmapause ont été illustrées dans un montage filmé réalisé au Centre Audio-Visuel de Louvain-la-Neuve. Des video-cassettes de cette animation sont disponibles à l'Institut d'Aéronomie Spatiale de Belgique.

Ce mémoire a été présenté à l'Université Catholique de Louvain et représente la dissertation présentée par l'auteur en vue de l'obtention du grade d'Agrégé de l'Enseignement Supérieur.

VOORWOORD

Dit verslag omvat het geheel der theoretische werken door de auteur gepubliceerd op het vlak van de theorie van de vorming der plasmapauze. In de hoofdstukken 2 en 3 bevinden zich ook resultaten en originele bijdragen die nog nergens anders voorgesteld werden.

De ideeën ontwikkeld in de hoofdstukken 4 en 5 betreffende de vormings- en vervormingsmechanismen van de plasmapauze werden geïllustreerd in een montage gerealiseerd in het Centre Audio-Visuel van Louvain-la-Neuve. Videocassettes van deze film zijn in het Belgisch Instituut voor Ruimte-Aeronomie beschikbaar.

Dit verslag werd voorgesteld aan de Université Catholique de Louvain-la-Neuve en dient als verhandeling om de graad van "Agrégé de l'Enseignement Supérieur" te bekomen.

VORWORT

Dieser Bericht enthaltet die theoretischen Arbeiten publiziert vom Autor über der Theorie der Bildung der Plasmapause. In den Kapiteln 2 and 3 befinden sich auch Resultaten und Originalbeiträge die nimmer irgendwo anders präsentiert worden sind.

Die Ideen entwickelt in den Kapiteln 4 und 5 hinsichtlich der Bildung- und Verbildungsmechanismen der Plasmapause wurden illustriert in einer montage realisiert in den Centre Audio-Visuel von Louvain-la-Neuve. Videokassetten dieses Films sind verfügbar in Belgischen Institut für Raum-Aeronomie.

Dieser Bericht wurde präsentiert am Université Catholique de Louvain-la-Neuve und dient als Abhandlung um dem Grad von "Agrégé de l'Enseignement Supérieur" zu bekommen.

Abstract

In Chapter 2, the formation of the "Light Ion Trough" (i.e. the depression of the ion densities H^+ and He^+), observed in the mid-latitude ionosphere, is explained by two different mechanisms; 1) along the magnetic force lines located beyond a critical latitude (dependent on the angular velocity of the exospheric plasma), the lightest ions escape from the ionosphere to fill the equatorial potential well resulting from the centrifugal force whose component parallel to the magnetic field, exceeds at a larger distances, that of the gravitational force; 2) the light ions also escape from the ionosphere like in the polar wind, in order to restore diffusive equilibrium in the magnetic flux tubes which have been emptied during a recent magnetic storm.

In chapter 3 the variations of the equatorial density (n_{eq}), of the total content (N_T), and of the temperatures ($T_\parallel$, $T_\perp$) inside a plasma element moving with the velocity $\underline{E} \times \underline{B}/B^2$, have been derived; $\underline{B}(r,\varphi)$ is the intensity of the equatorial magnetic field (see appendix A) and $\underline{E}(r,\varphi)$ is the intensity of the equatorial electric field (see appendix B) given by empirical models deduced from observations.

When it is assumed that the ionosphere is a perfect conductor ($\Sigma_p = \infty$; i.e. in the framework of the magnetohydrodynamic approximation) these plasma elements move along the equipotential surfaces of the stationary electric field $\underline{E}$.

At large distances these drift paths have a pronounced e asymmetry in the direction from dawn (0600 LT) to dusk (1800 LT). This asymmetry has different physical consequences, described in the sections 3.1 to 3.4. :

1) A daily variation of the equatorial density (n_{eq}) with a minimum at 1800 LT and a maximum at 0100 - 0200 LT where the radial distance (L) and the equatorial cross section (S) of the magnetic flux tubes both go through a minimum.

2) A daily variation of the total content (N_T) of the flux tube containing the plasma element.

3) A daily variation of the temperature ($T_\parallel$ and $T_\perp$), with a maximum in the midnight sector, resulting from the quasi-adiabatic compression of the magnetic flux tubes between 1800 LT and 0200 LT.

4) The heating of the thermal plasma in the outer regions of the plasmasphere resulting from the fast (quasi-adiabatic) compression in the night-side, followed by a much slower (quasi-isothermal) decompression of the day-side.

In section 3.5 one describes a numerical simulation of the equatorial density variation of plasma elements drifting along their closed paths. The effects of the gradual refilling of the magnetic flux tubes by evaporation and upward diffusion of the ionospheric plasma are illustrated in section 3.6.

In chapter 4, one describes the historical context within which our experimental and theorical understanding of the plasmasphere and of its equatorial limit (: the plasmapause) has developed since 1963. Appendix G is a review of the older theory for the formation of this plasmapause. In the sections 4.2 - 4.5 it is shown that a plasma element dielectric constant (κ) is large with respect to that of vacuum, (as it is the case for all ionospheric and magnetospheric plasmas) can undergo a drift in the direction of the gravitation force (or centrifugal force) when this element is electromagnetically coupled with the ionosphere the transverse Pedersen conductivity is not infinitely large (i.e., as in the MHD approach). When the value of the integrated Pedersen electric conductivity (Σ_p) is of the order of 0.1 - 10 Siemens, a plasma element denser than the background falls into the gravitational potential well with a velocity (i.e., the interchange velocity, $\underline{u}$) whose maximum value is proportional to Δnm, the excess of mass density, to $\underline{g}$, the gravitational acceleration (or centrifugal acceleration); u is also inversely proportional to Σ_p.

When $\Sigma_p = \infty$, the velocity $\underline{u}$ is equal to zero, and, the plasma elements are forced to move along the closed equipotentials of the E- field (as described in chapter 3, and, as assumed in the MHD theory). On the other hand when, nowhere along the field lines, the value of the transverse conductibility becomes infinitely large all plasma density depressions (plasma holes) tend to accumulate along an asymptotic drift path that we identify as the outer edge of the plasmapause region. This asymptotic drift path is determined by the balance of the gravitational and centrifugal forces. Beyond this asymptotic trajectory any perturbance of a distribution of density which diminishes with the radial distance is unstable. The plasma located beyond the ZRF surface (Zero Radial Force surface) tends to escape and to detach from the central mass of the plasma (the plasmasphere), retained in the gravitational potential well. At each enhancement in the angular convection velocity, the centrifugal force peels of the plasmasphere at a smaller radial distance and leads to the formation of a "knee" in the radial distribution of the plasma density at the ZRF surface. When afterwards, the convection velocity decreases, this detachment of plasma blocks occurs by interchange instability at larger radial distances. The intermediate region between the old and the new plasmapause fills then up again by evaporation and upward diffusion of ionospheric plasma until the saturation level is reached, or more often, until a new disturbance of the geo-electric and geomagnetic field occurs. This leads then to the formation of multiple plasmapauses (in steps) (see section 4.9).

The drift of plasma elements in the gravitation field with maximum interchange velocity $\underline{u}$ also permits to explain the gradual disappearance of the density gradients inside the plasmasphere (section 4.10).

The positions of the plasmapause (i.e. the asymptotic path of the "plasma holes") are calculated in chapter 5 for a time dependent electric field $\underline{E}$ model. This simulates the deformations of the plasmapause surface during a sudden increase of the geomagnetic activity (sections 5.1). The deformations of the plasmapause during a period of 5 days in which a succession of important magnetic storms happened has also been simulated.

These numerical results are compared to series of observations in the sections (2.8), (4.8) and (5.3)

Résumé

Dans le chapitre 2, la formation du "Light Ion Trough" (c.à.d. la dépression de la densité des ions H^+ et He^+) observée dans l'ionosphère de latitude moyenne est expliquée par deux mécanismes complémentaires; 1) le long des lignes de forces magnétiques situées au-delà d'une certaine latitude (qui dépend de la vitesse angulaire du plasma exosphérique) les ions les plus légers s'échappent de l'ionosphère pour combler le puits de potentiel équatorial résultant de la force centrifuge dont la composante parallèle au champ magnétique dépasse, à grande distance, celle de la force gravifique; 2) dans les tubes de forces magnétiques vidés de leur contenu en plasma froid au cours d'un récent orage magnétique, les ions légers s'échappent également de l'ionosphère comme dans le vent polaire, afin de rétablir l'équilibre de diffusion au sein de ceux-ci.

Dans le chapitre 3 on déduit les variations de la densité équatoriale (n_{eq}) du contenu total (N_T) et des températures ($T_\parallel$, $T_\perp$) au sein d'un élément de plasma en suivant sa dérive avec la vitesse $\underline{E} \times \underline{B}/B^2$. $\underline{B}(r, \varphi)$ est l'intensité du champ magnétique équatorial (voir appendice A) et $\underline{E}(r, \varphi)$ est l'intensité du champ électrique équatorial (voir appendice B). Ces deux distributions sont données par des modèles empiriques déduits d'observations (et dont il n'est pas le propos dans cette thèse d'analyser les origines pas plus qu'il n'est nécessaire de justifier ici de l'existence du champ de force gravifique g qui est également une donnée du problème). Dans l'hypothèse où l'ionosphère est un parfait conducteur ($\Sigma_p = \infty$; c.à.d. dans le cadre de l'approximation magnétohydrodynamique) ces éléments de plasma se déplacent le long des surfaces équipotentielles du champ électrique stationnaire $\underline{E}$.

A grande distance ces trajectoires fermées sur elles-mêmes (à condition que les champs $\underline{E}$ et $\underline{B}$ soient stationnaires) ont une asymétrie prononcée dans la direction aube (0600 TL) - crépuscule (1800 TL). Cette asymétrie entraîne plusieurs conséquences physiques décrites dans les sections 3.1 à 3.4.

1) Une variation diurne de la densité équatoriale (n_{eq}) avec un minimum à 1800 TL et un maximum à 0100-0200 TL où la distance radiale (L) et la section équatoriale (S) du tube de force magnétique passent tous deux par un minimum;

2) Une variation diurne du contenu total (N_T) du tube de force contenant l'élement de plasma;

3) Une variation diurne des températures ($T_{\parallel}$ et $T_{\perp}$), avec un maximum dans la région de minuit, résultant de la compression quasi-adiabatique des tubes de force magnétique entre 1800 TL et 0200 TL;

4) Un chauffage du plasma thermique dans les régions extérieures de la plasmasphère résultant de cette compression rapide (quasi-adiabatique) du côté nuit, suivie d'une décompression beaucoup plus lente (quasi-isotherme) du côté jour.

Dans la section 3.5 on décrit une simulation de la dérive des éléments de plasma et de leur densité équatoriale lorsqu'ils se déplacent le long de leurs trajectoires fermées. Celle-ci est obtenue à partir d'un programme d'ordinateur. Les effets du remplissage progressif des tubes de forces magnétiques par évaporation et diffusion du plasma ionosphérique est également illustrée dans la section 3.6.

Dans le chapitre 4 on décrit en premier lieu le contexte historique dans lequel ont évolué depuis 1963 nos connaissances expérimentales et théoriques sur la plasmasphère et sur sa frontière équatoriale : la plasmapause. Dans l'appendice G se trouve un résumé et une critique de l'ancienne théorie de formation de cette plasmapause. Dans les sections 4.2-4.5 on montre qu'un élément dont la constante diélectrique (κ) est grande par rapport à celle du vide (comme c'est le cas pour les plasmas ionosphériques et magnétosphériques) peut subir une dérive dans la direction de la force gravifique (ou centrifuge) lorsque celui-ci est couplé électromagnétiquement avec une ionosphère dont la conductibilité électrique (transversale) de Pedersen n'est pas infiniment grande comme dans l'approximation MHD. Lorsque la valeur de la conductibilité électrique intégrée de Pedersen (Σ_p) est de l'ordre 0.1-10 Siemens, un élément de plasma plus dense que le milieu ambiant tombe dans le champ de potentiel gravifique avec une vitesse ("interchange velocity", $\underline{u}$) dont la valeur maximale est proportionnelle à Σ_p, à Δnm, l'excès de densité, à $\underline{g}$, l'accélération gravifique (ou centrifuge); u est aussi inversément proportionnelle à Σ_p.

Lorsque $\Sigma_p = \infty$, la vitesse $\underline{u}$ devient nulle et les éléments de plasma sont forcés de se déplacer le long des équipotentielles fermées du champ $\underline{E}$ (comme décrit dans le chapitre 3 et comme généralement supposé dans la théorie MHD). Par contre lorsque la valeur de la conductibilité transversale n'est infiniment grande nulle part le long des lignes de force, toutes les dépressions de plasma (plasma holes) ont tendance à s'accumuler le long d'une trajectoire asymptotique que nous identifions avec la plasmapause. Cette trajectoire asymptotique est déterminée par la balance des forces gravifiques et centrifuges. Dans la région au-delà de celle-ci toute perturbation d'une distribution de densité décroissant avec la distance radiale est instable. Le plasma situé au-delà de la surface ZRF (Zero Radial Force surface) tend à se détacher et à s'éloigner de la masse centrale de plasma (la plasmasphère) qui elle est maintenue dans le puits de potentiel gravifique. Lors de chaque augmentation de la vitesse angulaire de convection dans le secteur après minuit, la force centrifuge "épluche" la plasmasphère à une distance radiale plus faible et donne lieu à la formation d'une décroissance abrupte dans la distribution radiale de densité de plasma à l'endroit de la ZRF surface.

Lorsqu'ensuite, la vitesse de convection rediminue, ce détachement de blocs de plasma se fait par instabilité d'échange à des distances radiales plus grandes. La région intermédiaire entre l'ancienne et la nouvelle plasmapause se remplit alors par évaporation et par diffusion du plasma ionosphérique, jusqu'à atteindre un niveau de saturation, ou plus fréquemment, jusqu'à l'apparition d'une nouvelle perturbation du champ géoélectrique et géomagnétique. Ceci donne alors lieu à la formation de plasmapauses multiples (en gradins) (voir section 4.9). La dérive d'élément de plasma dans la champ gravifique avec la vitesse maximale $\underline{u}$ permet également d'expliquer la disparition graduelle des gradients de densité au sein de la plasmasphère (section 4.10).

Dans le chapitre 5 on calcule les positions de la plasmapause (c.à.d. la trajectoire asymptotique de "plasma holes") avec un modèle de champ électrique $\underline{E}$ dépendant du temps pour simuler les déformations de cette surface de discontinuité au cours d'une augmentation brusque de l'activité géomagnétique (section 5.1), ainsi que lors d'une suite de variations de Kp au cours d'une période de 5 jours durant laquelle a eu lieu une succession d'orages magnétiques importants.

Ces résultats sont comparés avec diverses observations dans les sections (2.8), (4.8) et (5.3).

Samenvatting

In hoofdstuk 2, wordt de vorming van de "Light Ion Trough" (d.w.z. de depressie van de dichtheid der ionen H^+ en He^+), waargenomen in de ionosfeer van gemiddelde breedte, uitgelegd door twee bijkomende mechanismen; 1) langs de magnetische krachtlijnen verder gelegen dan een bepaalde breedte (die afhankelijk is van de hoeksnelheid van het exosferische plasma) ontsnappen de lichtste ionen uit de ionosfeer om de equatoriale potentiaalkuil te vullen die volgt uit de middelpuntleidende kracht waarvan de samenstellende kracht, parallel met het magnetisch veld, op grote afstand die van de zwaartekracht overtreft; 2) in de magnetische krachttubes die van hun inhoud in koude plasma geledigd werden tijdens een recente magnetische storm, ontsnappen de lichte ionen eveneens uit de ionosfeer zoals in de poolwind, teneinde het diffusie-evenwicht te herstellen.

In hoofdstuk 3 worden de variaties van de equatoriale dichtheid (n_{eq}) van de totale inhoud, (N_T) en de temperaturen ($T_{\parallel}$, $T_{\perp}$) afgeleid binnen een plasma-element door zijn afdrijving met de snelheid $\underline{E}\ \underline{B}/B^2$ te volgen. $\underline{B}(r, \varphi)$ is de intensiteit van het equatoriaal magnetisch veld (zie appendix A) en $\underline{E}(r, \varphi)$ is de intensiteit van het equatoriaal elektrisch veld (zie appendix B) gegeven door empirische modellen afgeleid uit waarnemingen (het gaat er in deze thesis niet om de oorsprong te onderzoeken, zoals het ook niet nodig is hier het bestaan van het zwaartekrachtsveld g te rechtvaardigen dat eveneens een gegeven van het probleem uitmaakt) aan te tonen. In het geval waar wij veronderstellen dat de ionosfeer een uitstekende geleider is ($\Sigma_p = \infty$; d.w.z. in het kader van de magnetohydrodynamische benadering) verplaatsen deze plasma-elementen zich langs de equipotentiale oppervlakken van het stationair elektrisch veld $\underline{E}$.

Op grote afstanden zijn deze trajecten op zichzelf gesloten (op voorwaarde dat de velden $\underline{E}$ en $\underline{B}$ stationair zijn) en hebben een uitgesproken asymmetrie in de richting dageraad (0600 TL) - avondschemering (1800 TL). Deze asymmetrie brengt meerdere fysische gevolgen met zich mee, beschreven in de afdelingen 3.1 tot 3.4.

1) Een dagelijkse variatie van de equatoriale dichtheid (n_{eq}) met een minimum bij 1800 LT en een maximum bij 0100-0200 TL waar de radiale afstand (L) en het equatoriale deel (S) van de magnetische krachttube allebei door een minimum gaan.

2) Een dagelijkse variatie van de totale inhoud (N_T) van de krachttube die het plasma-element bevat.

3) Een dagelijkse van de temperaturen ($T_\parallel$ en $T_\perp$), met een maximum in het middernachtgebied, dat volgt uit de quasi-adiabatische samendrukking van de magnetische krachttubes tussen 1800 TL en 0200 TL.

4) Een verwarming van het thermische plasma in de buitenste gebieden van de plasmasfeer die volgt uit deze snelle (quasi-adiabatische) samendrukking van de nachtzijde, gevolgd door een veel tragere (quasi-isothermische) drukvermindering van de dagzijde.

In de afdeling 3.5 wordt een simulatie van de afdrijving der plasma-elementen en hun equatoriale dichtheid beschreven wanneer ze zich verplaatsen langs hun gesloten trajecten. Deze simulatie wordt met een computerprogramma bekomen. De effecten van het progressief vullen van de magnetische krachttubes door evaporatie en diffusie van het ionosferische plasma wordt eveneens in afdeling 3.6 geïllustreerd.

In hoofdstuk 4 wordt in de eerste plaats de historische context beschreven waarin sedert 1963 onze experimentele en theoretische kennis van de plasmasfeer en haar equatoriale grens : de plasmapauze, zich ontwikkelde. In appendix G bevindt zich een samenvatting en een kritiek van de oude vormingstheorie van deze plasmapauze. In de afdelingen 4.2-4.5 toont men aan dat een plasma-element, waarvan de diëlektrische constante (κ) groot is t.o.v. die van het vacuüm, (zoals dat het geval is voor alle ionosferische en magnetosferische plasma's) een afdrijving kan ondergaan in de richting van de zwaartekracht (of middelpuntvliedende kracht) wanneer dit element elektromagnetisch gekoppeld wordt met een ionosfeer waarvan de transversale elektrische geleidbaarheid van Pedersen niet oneindig groot is zoals bij de MHD benadering. Wanneer de waarde van de geïntegreerde elektrische geleidbaarbeid van Pedersen (Σ_p) van de orde van 0.1-10 Siemens is, valt een plasma-element dat dichter is dan het omgevend milieu in het gravitatiepotentiaalgebied $\underline{g}$ met een snelheid ("interchange velocity", $\underline{u}$) waarvan de maximale waarde evenredig is aan Σ_p, aan Δ_{nm}, de overmaat aan dichtheid, aan g, de gravitatieversnelling (of centrifugale); ze is omgekeerd evenredig aan Σ_p.

Wanneer $\Sigma_p = \infty$, wordt de snelheid $\underline{u}$ gelijk aan nul en de plasma-elementen worden gedwongen zich te verplaatsen langs de gesloten equipotentialen van het veld $\underline{E}$ (zoals beschreven in hoofdstuk 3 en zoals algemeen verondersteld in de MHD theorie). Anderzijds wanneer de waarde van de transversale geleidbaarheid nergens langs de krachtlijnen oneindig groot is, hebben alle plasmadepressies (plasma holes) de neiging zich opeen te stappelen langs een asymptotisch traject dat wij identificeren met de plasmapauze. Dit asymptotisch traject wordt bepaald door het evenwicht van de zwaarte- en middelpuntvliedende kracht. In het gebied hierboven is elke storing van een dichtheidsverdeling die afneemt met de radiale afstand onstabiel. De plasma die zich boven het oppervlak ZRF bevindt (Zero Radial Force surface) probeert zich los te maken en zich te verwijderen van de centrale massa van de plasma (de plasmasfeer) die zelf vastgehouden wordt in de gravitatiepotentiaalkuil. Bij elke verhoging van de convectiehoeksnelheid in het gebied na middernacht, "schilt" de middelpuntvliedende kracht op zo'n manier de plasmasfeer op een zwakkere radiale afstand en geeft aanleiding tot de vorming van een "knie" in de radiale verdeling van de plasmadichtheid op de plaats van het ZRF oppervlak.

Wanneer daarna, de magnetische activiteit (K_p) opnieuw vermindert, gebeurt deze onthechting van plasmablokken door wisselonstabiliteit op grotere radiale afstanden. Het tussengebied tussen de oude en de nieuwe plasmapauze vult zich dan door evaporatie en diffusie van ionosferische plasma tot een verzadigingsniveau bereikt wordt of vaker tot een nieuwe storing van het geo-elektrisch en geomagnetisch veld optreedt. Dit geeft dan aanleiding tot de vorming van veelvuldige plasmapauzen (in trappen) (zie afdeling 4.9). De afdrijving van plasma-elementen in het zwaartekrachtsveld met de maximale snelheid $\underline{u}$ laat eveneens toe de graduele verdwijning (diffusie) van de dichtheidsgradiënten binnen de plasmasfeer te verklaren (afdeling 4.10).

In hoofdstuk 5 wordt een computerprogramma gebruikt, dat ontwikkeld werd om de posities van de plasmapauze te berekenen (d.w.z. het asymptotisch traject van de "plasma holes" met een model van elektrisch veld $\underline{E}$ afhankelijk van de tijd om de vervormingen van dit discontinuïteitsoppervlak na te bootsen tijdens een plotse stijging van de geomagnetische activiteit (afdeling 5.1), alsook tijdens een opeenvolging van variaties van K_p tijdens een periode van 5 dagen waarin er zich een opeenvolging van belangrijke magnetische stormen voordeed.

Deze resultaten worden vergeleken met verschillende waarnemingen in de afdelingen (2.8), (4.8) en (5.3).

Zusammenfassung

In Kapitel 2, die Formung der "Light Ion Trough" (d.h. die Depression der Dichtigkeit der Ionen H^+ und He^+), beobachtet in der Ionosphäre von mittlere Breite, ist erklärt durch zwei Nebenmechanismen; 1) längs der magnetischen Kraftlinien weiter gelegen wie eine bestimmte Breite (abhängig von der Winkelgeschwindigkeit des exosphärischen Plasmas) entwischen die leichtste Ionen aus der Ionosphäre um das Potential minimum zu füllen resultierend aus der Zentrifugalkraft wovon die zusammensetzende Kraft, parallel mit dem magnetischen Feld, in grösser Entfernung die der Schwerkraft übertrift; 2) in den magnetischen Krafttuben die geleert wurden von Inhalt in kattern Plasma während eines rezenten magnetischen sturmes, entwischen die leichte Ionen auch der Ionosphäre wie im Polarwind, um das Diffusionsgleichgewicht wieder zu herstellen.

In Kapitel 3 werden die Variationen der äquatorialen Dichtigkeit (n_{eq}) des Gesamtinhaltes, (N_T) und die Temperaturen ($T_\parallel$, $T_\perp$) abgeleitet innerhalb einem Plasmaelement durch sein Abtreibung mit der Schwindigkeit $\underline{E} \times \underline{B}/B^2$ zu folgen. $\underline{B}(r, \varphi)$ ist die Intensität des äquatorialen magnetischen Feldes (bitten wenden Anhang A) und $\underline{E}(r, \varphi)$ ist die Intensität des äquatorialen elektrischen Feldes (bitte wenden Anhang B) gegeben durch empirische Modellen abgeleitet von Beobachtungen (es handelt in dieser These nicht um der Ursprung zu untersuchen, wie es auch nicht nötig ist hier die Existenz des Schwerkraftfeldes g zu rechtfertigen das ebenfalls ein der Daten des Problemes ist. Falls wo wir annehmen das die Ionosphäre ein vortrefflicher Leiter ist ($\Sigma_p = \infty$, d.h. im Rahmen der magnetohydrodynamischen Annäherung) bewegen diese Plasmaelementen sich längs der äquipotentialen Oberflächen des stationären elektrischen Feldes $\underline{E}$.

In grösser Entfernungen besitzen diese Trajekten eine deutliche Asymmetrie in der Richtung von 0600 LZ 1800 LZ. Diese Asymmetrie hat mehrere physische Folgen, die in Abteilung 3.1 bis zu 3.4 beschrieben worden sind.

1) Eine tägliche Variation der äquatorialen Dichtigkeit (n_{eq}) mit einem Minimum an 1800 LZ und einem Maximum an 0100-0200 LZ wo die radiale Entfernung (L) und der äquatoriale Durchschnit (S) der magnetischen Krafttube beide durch ein Minimum geben.

2) Eine tägliche Variation des totalen Inhaltes (N_T) der Krafttube der das Plasmaelement enthaltet.

3) Eine tägliche Variation der Temperaturen ($T_\parallel$ und $T_\perp$), mit einem Maximum im Mitternachtsgebiet, resultierend aus der quasi-adiabatischen Verdichtung der magnetischen Krafttubes zwischen 1800 LZ und 0200 LZ.

4) Die Erwärmung des thermischen Plasmas in den äusserste Gebieten der Plasmasphäre resultierend aus dieser schnelle (quasi-adiabatischen) Verdichtung der Nachtseite, gefolgt durch eine viel lagere (quasi-isothermische) Verdichtungsminderung der Tagseite.

In Abteilung 3.5 wird eine Simulation der Abtreibung der Plasmaelementen und ihrer äquatorialen Dichtigkeit beschrieben wenn Sie sich bewegen längs ihren geschlossen Trajekten. Diese Simulation wird mit einem Komputerprogramm bekommen. Die Effekten der progressiven Fülling der magnetischen Krafttubes durch Verdampfung und Diffusion des ionosphärischen Plasmas wird auch in Abteilung 3.6 illustriert.

In Kapitel 4 wird an erster Stelle der historische Kontext beschrieben worin seit 1963 unsere experimentelle und theoretische Kenntnis der Plasmasphäre und ihrer äquatoriale Grenze : die Plasmapause, sich entwickelte. In Anhang G befindet sich eine Zusammenfassung und einer Kritik über der alten Formungstheorie dieser Plasmapause. In den Abteilungen 4.2-4.5 zeigt man das ein Plasmaelement, wovon die Dielektrizitätskonstante (κ) gross ist hinsichtlich die von Vakuum, (wie für alle ionosphärische und magnetosphärische Plasmas) kann abtreiben in der Richtung von der Schwerkraft (oder Zentrifugalkraft) wenn dieses Element elektromagnetisch gekoppelt wird mit einer Ionosphäre wovon die transversale elektrische heitfähigkeit von Pedersen (Σ_p) zwischen 0.1-10 Siemens ist, fällt ein Plasmaelement das dichter ist dan das ungebende milieu in Potential Minimum mit einer Geschwindigkeit ("interchange velocity", $\underline{u}$) wonvon der maximale Wert proportional ist zu Δnm, das Zuviel aan Dichtigkeit, zu $\underline{g}$, die Schwerkraftbeschleunigung (oder zu $\underline{g}$, die Schwerkraftbeschleunigung (oder Zentrifugal beschleunigung); Sie ist umgekehrt proportional zu Σ_p.

Wenn $\Sigma_p = \infty$, wird die Geschwindigkeit $\underline{u}$ gleich am 0 und die Plasmaelementen sind gezwungen sich längs die geschlossen Feldlinien zu bewegen (wie beschrieben in Kapitel 3 und wie allgemein angenommen in der MHD Theorie). Anderseits wenn der Wert der transversalen Leitfähigkeit irgendwo längs der Kraftlinien unendlich gross ist, sind alle Plasmadepressionen geneigt sich zufeinander zu türmen längs einem asymptotischen Trajekt das wir identifizieren mit der Plasmapause. Dieser asymptotische Trajekt wird bestimmt durch das Gleichgewicht der Schwer- und Zentrifugalkraft. Im Gebiet hier oben ist jede Störung von einer Dichtigkeitsverteilung der abnehmt mit der radialen Entfernung unstabil. Der Plasma der sich über der ZRF (Zero Radial Force Oberfläche) Oberfläche befindet, versucht sich los zu machen und sich zu entfernen von der zentralen Massa des Plasmas (die Plasmasphäre) selbst festgehaltet in Gravitation Feld. Bei jeder Erhöhung der Winkelgeschwindigkeit im Gebiet nach Mitternacht, "schält" die Zentrifugalkraft so die Plasmasphäre in einer schwachen radialen Entfernung und gibt Anlass zu der Formung eines Knies in der Radialen Verteilung der Plasmadichtigkeit auf dem Platz der ZRF Oberfläche.

Wenn danach, die magnetische Aktivität (K_p) wieder vermindert, geschieht diese Loslassung von Plasmablocks durch Wechselunstabiliteit in grossen radialen Entfernungen. Das Zwischengebiet zwischen der alten und der neuen Plasmapause füllt sich dan durch Verdampfung und Diffusion von ionosphärischen Plasmas bis ein Sättigungsniveau erreicht wird, oder öfters, bis eine neue Störung des geo-elektrischen und geomagnetischen Feldes auftritt. Es gibt den Anlass zu der Formung von mehreren Plasmapausen (in Stufen) (Abteilung 4.9). Die Abtreibung von Plasmaelementen im Schwerkraftsfeld mit der maximalen Geschwindigkeit $\underline{u}$ leidt auch zu des graduelle Verschwinden der Dichtigkeitsgradienten binnen der Plasmasphäre zu erklären (Abteilung 4.10).

In Kapitel 5 wird ein Komputerprogramm gebraucht, das entwickelt wurde um die Positionen der Plasmapause zu berechnen (d.h. der asymptotische Trajekt der "Plasma holes") mit einem modell von elektrischen Feldes $\underline{E}$ abhängig von der Zeit um die Verbildungen dieser Umstätigkeitsoberfläche zu simulieren während einer plötzen Steigung der geomagnetischen Aktivität (Abteilung 5.1), und auch während einer Reihenfolge von Variationen von K_p während einer Periode von 5 Tagen worin eine Reihenfolge von wichtige magnetische Sturmen auftrat.

Diese Resultaten werden vergleicht mit verschiedenen Beobachtungen in den Abteilungen (2.8), (4.8) und (5.3).

TABLE OF CONTENT

Page

Illustration of the Magnetosphere in the Solar Wind

The central shaded volume surounding the Earth is the Plasmasphere

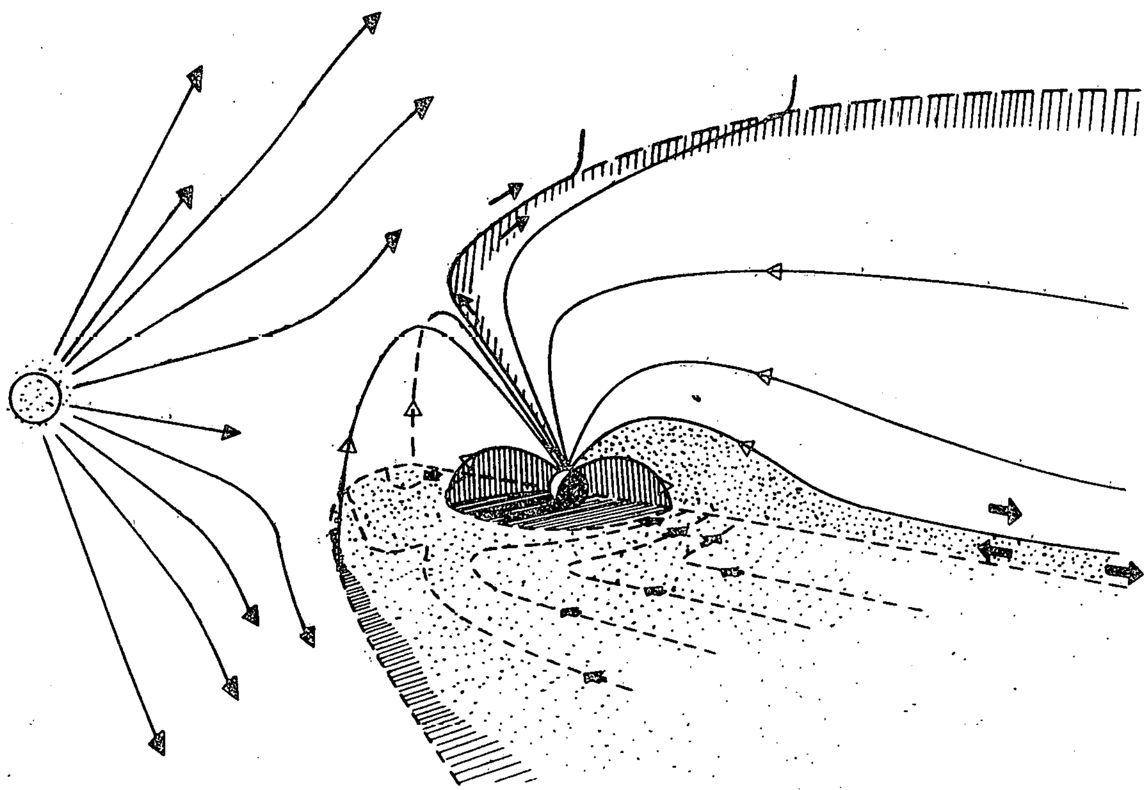

PREFACE

The fact that the Earth has a magnetic field similar to that of a simple bar magnet was first recognized by Gilbert, physician to Queen Elizabeth I, in a book on terrestrial magnetism, which appeared in 1600. Despite extensive ground-based observations and extensive theoretical work, notably by Birkeland, Størmer, Bartels, Chapman, Ferraro and Alfvèn, progress in understanding the problems of geomagnetic activity and of the outer space Earth environment was relatively slow until the International Geophysical Year is 1957 and the launching of the first artificial satellite. For many years, ionospheric physicicists were concerned mainly with problems of ionospheric effects on radio propagation as observed from ground. There was almost no mean to investigate questions associated with the extension of the ionosphere and geomagnetic field into space, in the regions above 300 km altitude which were not directly observable from the ground.

In the early 1950's, however, Storey caused a significant change in this attitude with his discovery that the behaviour of very low frequency radio signals called whistlers, which are associated with lightning flashes, can only be interpreted if the radiowave propagates along geomagnetic field lines out to large distances (25,000 km or four Earth radii) and if a relatively dense plasma exists in these outer regions to permit these waves to propagate. In fact, this plasma is now known to exist and constitutes the upper extension of the ionosphere into the magnetosphere.

The word magnetosphere was coined by Gold in 1959. It refers to the region of space surrounding the Earth in which the geomagnetic field has a controlling influence on the plasma which it contains. The intimate connection between the ionosphere and the outer parts of the magnetosphere, and, in particular, the fact that similar phenomena occur in magnetically conjugate regions in both hemispheres of the Earth, was the essence of Gold's concept of the magnetosphere, and is the basis of modern magnetospheric physics.

The first major discovery of the space era was made in 1958 by Van Allen and his colleagues, using Geiger-tube observations from the satellite Explorer I. They found that the Earth's magnetic field contained trapped charged particles of energies ranging up to hundreds of MeV. These energetic particles are trapped in the geomagnetic field for very long periods of time. They bounce back and forth between magnetically conjugate mirror points, and, drift parallel to constant magnetic L-shells forming a Ring Current which is the source of the largest geomagnetic disturbances observed at low latitudes.

In addition to the energetic Van Allen's protons and electrons, plasma of much lower energy is trapped along the geomagnetic field lines. The plasma of lowest temperature observed in the magnetosphere is of ionospheric origin and forms a wide doughnut-shaped region which extends to four or five Earth radii in the equatorial plane of the magnetosphere. This high density region is illustrated in the figure on the first page by heavy shadings encircling the Earth; this region filled with cold corotating plasma has been called : the plasmasphere. It is the formation and the dynamics of this region which is studied in this monograph.

In 1960, Gringauz and his colleagues, who flew ion traps on LUNIK 1 and 2, noted drastic decreases in the thermal ion fluxes at several Earth radii. This rather sharp "knee" in the equatorial thermal plasma density was rediscovered in 1963 by Carpenter using whistler wave observations. This sharp density gradient determines the position of the equatorial plasmapause (PP) region, i.e. the outer edge of the plasmasphere. The position of this surface of discontinuity is found to vary with the local time angle (see fig. 1c) and is formed closer to the Earth when geomagnetic activity increases.

In 1965 Muldrew discovered a well defined trough in the mid-latitude ionospheric electron density distribution. In 1969 Taylor et al. identified at mid-latitudes a similar knee in the light ions (H^+ and

He^+) density of the upper ionosphere, above an altitude of 800-900 km (see fig. 1d).

For several years, this Light Ion Trough (LIT) has been identified as the low altitude field aligned projection of the equatorial plasmapause. But after 1974 it became clear that the LIT is a different boundary located along magnetic field lines at slightly lower invariant latitudes than the equatorial plasmapause. This indicates that LIT has another origin and that its formation is based on a different mechanism than the equatorial plasmapause.

Furthermore, the temperature of the corotating thermal plasma trapped in the plasmasphere increases with radial distance. A separate suprathermal ion population with anisotropic pitch angle distributions has even been observed with the most recent spacecraft. A theory for the heating of plasma confined in the outer part of the plasmasphere is advanced in this monograph. Physical mechanisms for the formation of the Light Ion Trough and of the equatorial Plasmapause are also presented.

1. INTRODUCTION

The plasmasphere is a broad plasma ring in the magnetosphere encircling the Earth like a doughnut. A meridional section of this ring is shown by the shaded area in fig. 1a. This vast region is filled up with cold thermal plasma of ionospheric origin. The plasmasphere constitutes the magnetospheric extension of the topside ionosphere at low and mid-latitudes.

At the outer frontier of the plasmasphere the plasma density decreases sometimes by two orders of magnitudes (from 300 cm^{-3} to 3 cm^{-3}) in a distance of less then 1300 km (i.e. less than 0.2 R_E; R_E is the Earth radius : 6371 km). This sharp "knee" in the equatorial density distribution forms the Plasmapause region (PP) and is illustrated in fig. 1b. The plasmapause surface is nearly parallel to the geomagnetic field lines as shown in fig. 1a.

The plasmapause extends in the equatorial plane up to geocentric distances of 4-5 R_E in the post-midnight, and even to larger radial distances in the dusk local time sector (1800 LT) (see fig. 1c). But the equatorial distance of the plasmapause depends not only on the local time angle (φ), it is also a sensitive function of the geomagnetic activity conditions. For instance, during prolonged periods of very quiet geomagnetic conditions (i.e. when the geomagnetic index K_p is smaller than 1 for more than one day) the radius of the equatorial plasmapause can extend beyond geostationary orbit (i.e. beyond 6.6 R_E). On the contrary, during very disturbed periods of time, when $K_p > 7$, the sharp "knee" in the equatorial plasma density can be observed at equatorial distances smaller than 3 R_E. An empirical relationship between L_{pp}, the post-midnight equatorial distance of the plasmapause, and K_p, has been deduced by Carpenter and Park (1973), from a large number of whistler observations :

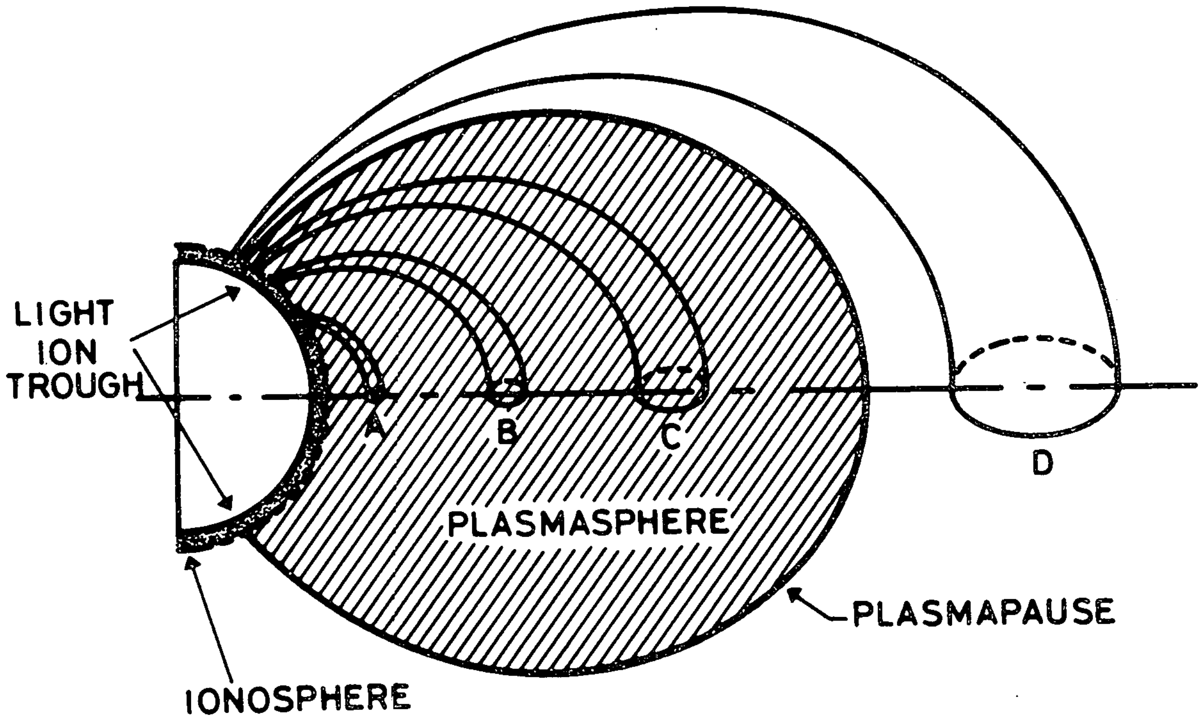

Fig. 1a.- Meridional cross section of the plasmasphere (light shaded area) and of the ionosphere (heavy shaded area). The outer edge of the plasmasphere is called the plasmapause. The plasmapause surface or region is nearly field aligned and forms a toroïdal surface around the Earth. In the plasmapause region the plasma density decreases abruptly by two orders of magnitude. Light ion troughs are also observed at altitudes above 1000 km in the mid-latitude ionosphere. Four magnetic flux tubes have also been represented. Their equatorial cross section S_{eq} and volume V increase with the equatorial radial distance L, when the magnetic flux $S_{eq}.B_{eq}$ is conserved (from, Carpenter and Park, 1973).

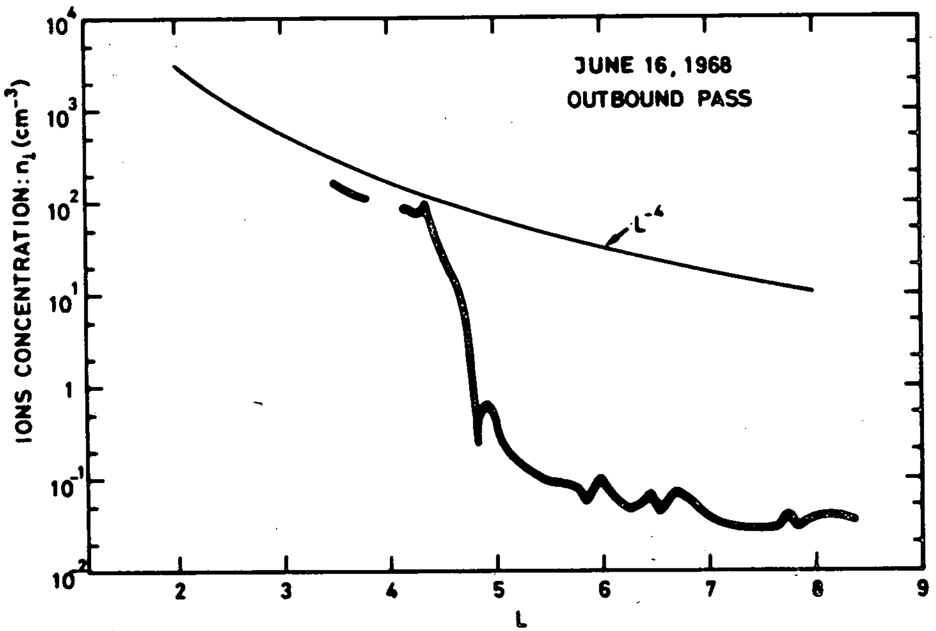

Fig. 1b.- Equatorial ion density as a function of radial distance in Earth's radii measured along the outbound pass of the OGO 5 satellite, on June 16, 1968. This profile shows a plasma density decrease from 100 cm^{-3} to less than 1 cm^{-3} over a distance of 0.3 R_E. This measurement was made in the 2100 LT region. The solid line represents an L^{-4} density variation (from, NSSDC, Greenbelt, Md, 1978).

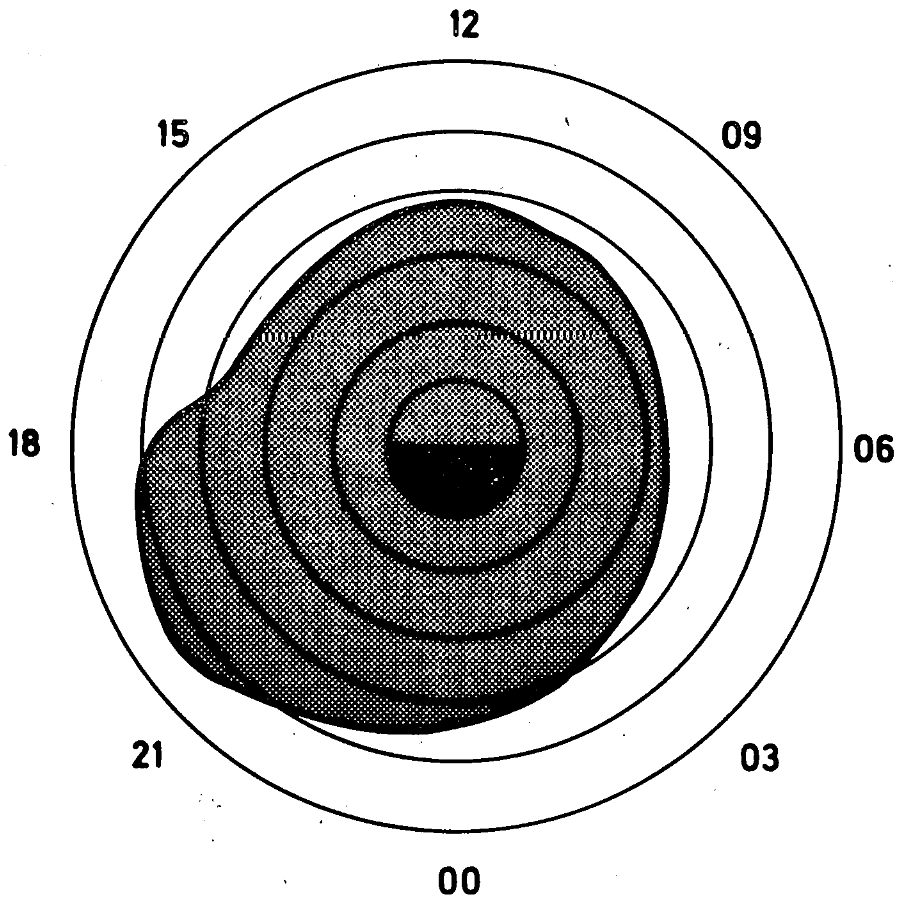

Fig. 1c.- Equatorial radius of the plasmapause versus local time. The solid line represents the average behavior during periods of moderate, steady geomagnetic agitation (K_p = 2-4) (after Carpenter, 1966).

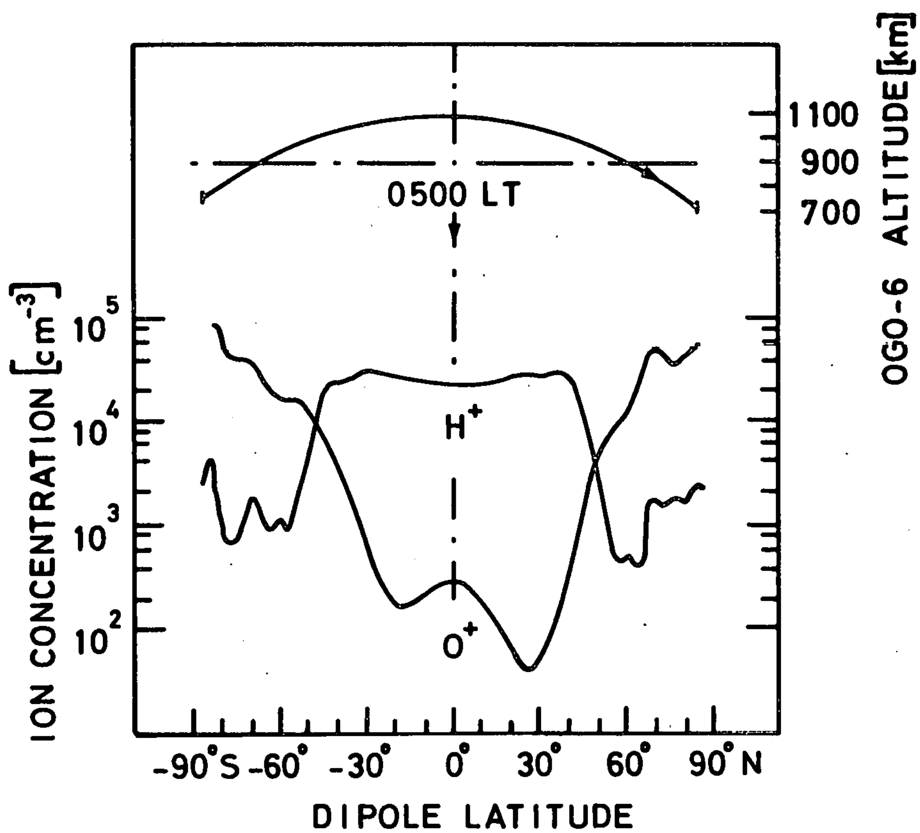

<u>Fig. 1d.</u>- Latitudinal variation of H^+ and O^+ ion concentrations in the topside ionosphere. These data are obtained from OGO 6 ion mass spectrometer measurements made on September 23, 1969 during very quiet geomagnetic conditions. The large H^+ density gradients at mid-latitudes correspond to the Light Ion Trough region (after Taylor <u>et al</u>. 1971).

$$L_{pp} = 5.7 - 0.47\ K_p \tag{1.1}$$

This important relationship will be a corner-stone in this study.

A large amount of observations concur now to indicate that the characteristic plasmapause density gradient is formed by peeling off the relatively dense plasmasphere in the post-midnight local time sector. It is this peeling off mechanism which will be described and discussed in the present monograph and especially in chapter 4.

The Light Ion Trough (LIT) is another frontier of the plasmasphere observed in the topside ionosphere at mid-latitude along magnetic field lines which are slightly closer to the Earth than those corresponding to the equatorial plasmapause. Across this low altitude boundary the concentration of the light ions (H^+, He^+) decreases rapidly as the latitude increases. The topside ionosphere at latitudes beyond the LIT is significantly depleted from its light ion contents (see fig. 1d). The origin of this depletion and the formation of this LIT are suggested and discussed in chapter 2.

Chapter 3 is devoted to a study of different aspects of plasma transport in the equatorial region of the plasmasphere. The diurnal variation of the equatorial density is discussed in section 3.1 and simulated with a computer program in section 3.6. The diurnal variation of the total content of particles in the magnetic flux tube associated with a drifting plasma element is studied in sections 3.2 and 3.3. The effects of flux tube refilling and depletion by field aligned ionization flows has also been considered in sections 3.3 and 3.6. The variations of the equatorial plasma temperature as a result of the diurnal cycle of quasi-adiabatic compressions followed by quasi-isothermal flux tube expansions is envisaged in section 3.4.

In section 4.1 we review the historical background in which the ideas concerning the plasmapause have evolve since the early 1960's when Carpenter and Gringauz discovered this characteristic boundary.

The mechanism of plasma interchange motion which has been ignored in the earlier MHD theory for the formation of the plasmapause, has been described in sections 4.3 and 4.4. The effect of plasma interchange motion on the drift path of cold plasma density irregularities are illustrated in section 4.6. The role played by plasma interchange motion and the effect of the centrifugal force in the mechanism of formation of an equatorial density "knee" are emphasized in section 4.7. Comparisons with observations can be found in section 4.8. The reason for the formation of "multiple plasmapauses" is explained in section 4.9. In section 4.10 we discussed the role played by plasma interchange motion on the smoothing out of plasmapause density gradients.

The deformations of the plasmasphere and of its outer boundary when the magnetospheric convection electric field is time-dependent are described in Chapter 5. The results of different numerical model simulations have been presented and discussed there. The case of an ideal short duration geoelectric field enhancement has first been considered in section 5.1. The deformations of the plasmasphere during the large substorm events of 29, 30 and 31 July 1977 have also been simulated. The results of this simulation and a comparison with observations are given in section 5.2. Further observational support for the physical mechanisms presented in this monograph are given in the final section before the general conclusions.

A series of Appendices describing magnetic field models, electric field models and the distribution of the integrated Pedersen conductivity which are used in the computer model simulations, can be found at the end of this monograph. Finally an updated list of References, a list of Symbols and a list of the pages of the figures have been added at the end.

2. THE LIGHT ION TROUGH (LIT)

2.1. Preliminary remarks

Although the existence of a characteristic trough in light ions density has been observed by Taylor et al. (1969) in the mid-latitudes ionosphere, after the "knee" in the equatorial plasma density, we will first discuss the formation of this mid-latitude feature which, originally, has been considered as the low altitude signature of the plasmapause. We start this study with the LIT since the ionosphere is the source of all the cold plasma stored up and trapped in the magnetic flux tubes forming the plasmasphere. Furthermore, the LIT is formed at the feet of magnetic field lines which are located inside the plasmasphere at nearly one L value from the equatorial plasmapause (see fig. 1a). It is therefore preferable to examine first the physical reason for the existence of the LIT before we examine those for the formation of the equatorial plasmapause. The theory for the formation of the mid-latitude light ion trough will be developed in this chapter 2 while that for the equatorial plasmapause will be introduced in chapter 4.

Further in this chapter we discuss the field aligned distribution of the gravitational plus centrifugal potential (section 2.2), the different classes of particle trajectories (section 2.4), the particle velocity distributions (section 2.5), and the plasma density (section 2.6) in rotating ion-exospheres; the upward flow of ions resulting from the existence of an equatorial potential well is introduced in section 2.7; the location of the LIT for the corotation electric field as well as for other magnetospheric electric field distributions, are calculated in section 2.3. In the final section 2.8 the theoretical results are compared to LIT observations.

2.2. Potential distribution in rotating ion-exospheres

Above the F-region ionization peak the plasma density and pressure decrease steadily with altitude. The collision mean-free-path is much larger than the gyroradius of the charged particles. Diffusion perpendicular to the magnetic field direction is largely inhibited, while the diffusion coefficient along magnetic field lines increases rapidly with altitude. Plasma inhomogeneities tend to become field aligned in the upper ionosphere and in the magnetosphere. Indeed, density gradients get smeared much faster in the direction parallel than perpendicular to the magnetic field. A plasma irregularity produced in the F-region extends rapidly in the whole volume of a magnetic flux tube.

Under steady state conditions, the field aligned plasma distribution in a flux tube is determined by the gravitational and centrifugal potential distribution :

$$\phi_g \ (r, \lambda) = - \left[\frac{GM_E}{r} + \frac{1}{2} \Omega^2 r^2 \cos^2 \lambda \right] + c^{te} \qquad (2.1)$$

where G is the gravitational constant; M_E is the mass of the Earth; r and λ are the radial distance and latitude, respectively; Ω is the angular velocity of the planetary exosphere.

The gravitational and centrifugal forces induce a small charge separation electric field in the plasma, as a consequence of the difference in ion and electron masses. When the bulk velocity of the plasma has a non-vanishing and non-uniform field aligned component the inertial force ($m d\underline{v}/dt$), which is larger for ions than for the electrons, induces an additional charge separation electric field.

The existence of a charge separation electric field in an ionized atmosphere has been demonstrated by Pannekoek (1922) and Rosseland (1924) in the case of hydrostatic equilibrium. The origin and consequence of the charge separation electric field in a plasma in hydrodynamic equilibrium has been reviewed by Lemaire and Scherer (1973; 1974) with applications to the solar and polar wind.

For the sake of simplicity let us first consider that there is no net plasma bulk velocity along low and mid-latitude geomagnetic field lines. The plasma is then in hydrostatic equilibrium. This implies that the boundary conditions (density, temperature, and velocity distributions) are symmetrical at magnetically conjugate points in the northern and southern ionosphere. The field aligned plasma velocity is then equal to zero and the ion and electron pitch angle distributions are symmetrical with respect to the 90° pitch angle direction. In such an ideally symmetrical plasmasphere the field aligned distribution of the charge separation electrostatic potential $\phi_E(r, \lambda)$ precisely coïncides with that of the Pannekoek-Rosseland electric field :

$$\phi_E(r, \lambda) = - \frac{m_i T_e - m_e T_i}{e(T_i + T_e)} \phi_g(r, \lambda) \tag{2.2}$$

where m_i and m_e are the ion and electron masses respectively; T_i and T_e are the ion and electron temperatures. Eq. (2.2) is deduced from the plasma quasi-neutrality condition

$$n_i [\phi_g(r, \lambda), \phi_E] \cong n_e [\phi_g, \phi_E] \tag{2.3}$$

It is worthwhile to mention that the commonly used magnetohydrodynamic (MHD) approximation, assuming that magnetic field lines are equipotential (i.e. that $\underline{E} \cdot \underline{B} = 0$), is not strictly applicable to planetary ion-exosphere, indeed the gradient of $\phi_E(r, \lambda)$, although small, has always a non vanishing field aligned component.

For the Pannekoek-Rosseland electric potential (2.2) distribution the ratio of the total potential energy

$$\psi_\alpha = m_\alpha\, \phi_g + Z_\alpha\, e\, \phi_E \tag{2.4}$$

and thermal energy, $k\,T_\alpha$, is the same for the electrons ($\alpha \equiv e$) and the much heavier ions ($\alpha \equiv i$)

$$\frac{\psi_\alpha}{kT_\alpha} = \frac{\psi_i}{kT_i} = \frac{\psi_e}{kT_e} = \frac{m_i + m_e}{k(T_i + T_e)}\, \phi_g\, (r,\, \lambda) \tag{2.5}$$

As a consequence, scale heights of the electron and ions densities are then identical as they must be to satisfy the quasi-neutrality condition at all altitudes along a given geomagnetic field line.

The application of the Pannekoek-Rosseland electric potential distribution (2.2) to multi-ionic plasma or to expanding ion-exospheres (like the solar corona, or the polar wind) has led in the past to misleading results (see reviews by Lemaire and Scherer, 1973, 1974). Note however, that the Pannekoek-Rosseland polarization field (2.2) is a valid approximation for any single ionic constituent plasma as long as there is not net charged particle flux along the magnetic field lines. This is for instance the case in the rotating ion exosphere models which have been studied by Lemaire (1976b) and which will be discussed in following paragraphs. Pure hydrogen plasma will be considered, also for the sake of simplicity; as a consequence of symmetric boundary conditions in both hemispheres there is no net interhemispheric mass nor heat flow; the pitch angle distribution of the electrons and ions is symmetric with respect to 90° pitch angle but it is not necessarily isotropic. The extension to multi-ion plasma and to field aligned mass flow has been discussed by Lemaire and Scherer (1970, 1971a, 1971b, 1972, 1978) and by Lemaire (1972) for different types of ion exospheres and for a variety of different boundary conditions. In the more general cases of multi-ionic plasmas with or without interhemispheric flows there is unfortunately no such simple expression as eq. (2.2) for the field aligned potential distribution ϕ_E. The values of $\phi_E(r, \lambda)$ can then be determined to a good approximation by solving the quasi-neutrality equation

$$\Sigma_\alpha Z_\alpha n_\alpha [\phi_g, \phi_E] = 0 \qquad (2.6)$$

by an iteratative numerical procedure as described by Lemaire and Scherer (1969). In eq. (2.6) Z_α e is the electric charge of the particles α. But for the object in this work we can limit our study to the simplest cases of single ionic exospheres in hydrostatic equilibrium, and where eqs. (2.2) and (2.5) are applicable. This is usually a satisfactory approximation in the plasmasphere. It should be noted, however, that beyond the LIT, where the light ions are flowing out of the mid-latitude ionosphere, the parallel electric field becomes larger than the Pannekoek-Rosseland field.

The total potential energy (ψ) of an electron or a hydrogen ion is then given by eqs (2.5) and (2.1). The distribution of ψ_e or ψ_{H^+} along different dipole magnetic field lines (L = 2, 3, 5.78, 10 and 15) are illustrated in fig. 2 as a function of latitude λ, for the case of an ion-exosphere rotating with the angular velocity of the Earth's ionosphere (i.e. for $\Omega = \Omega_E = 7.29 \times 10^{-5}$ rad s^{-1}). It has also been assumed that the ion temperature is equal to the electron temperature.

Taking into account that the equation of the dipole field line L is given by

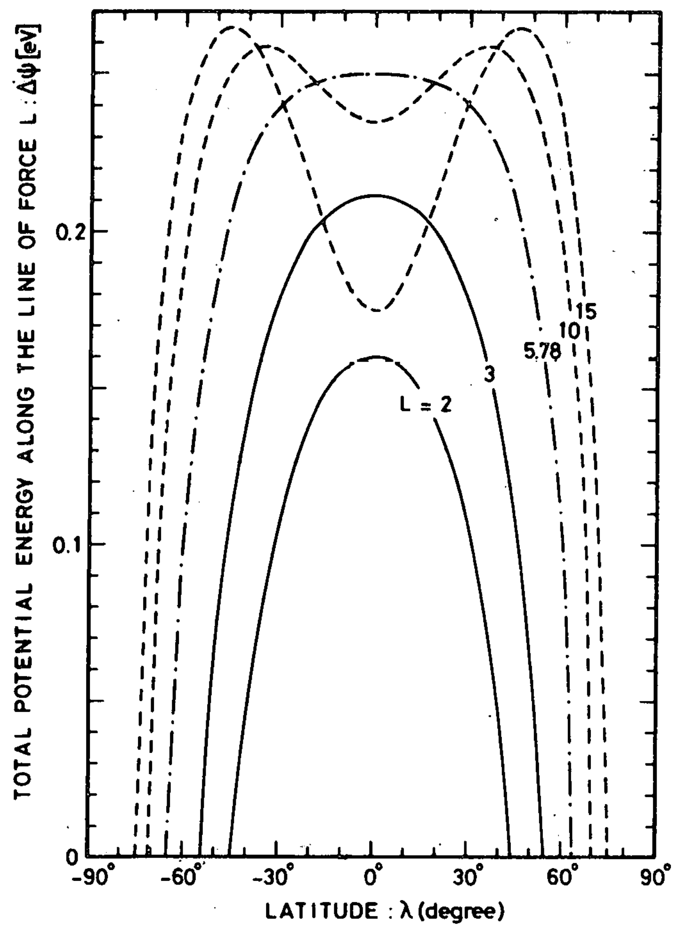

Fig. 2.- Gravitational plus rotation potential energy of H^+ ions along different magnetic field lines corotating with the Earth. For $L \leqq 5.78$, the total potential ψ, has a maximum value in the equatorial plane at $\lambda = 0$; for $L > 5.78$, ψ has a minimum at the equator and two symmetrical maxima out of the equatorial plane at $\lambda = \lambda_m$ (from Lemaire, 1974).

$$r/R_E = L \cos^2 \lambda, \tag{2.7}$$

the difference of potential energy (in eV) between two points at different latitudes λ and λ_o on the same field line (L) is given by

$$[\psi\ (L, \lambda)]_{\lambda_o}^{\lambda} = - \frac{0.324}{L} \left[\frac{1}{\cos^2\lambda} - \frac{1}{\cos^2\lambda_o}\right.$$

$$\left. + \frac{1}{3} \left(\frac{\Omega}{\Omega_E}\right)^2 \left(\frac{L}{L_c}\right)^3 (\cos^6 \lambda - \cos^6 \lambda_o)\right] \tag{2.8}$$

where the critical L_c value is defined by

$$L_c = \left(\frac{2GM_E}{3\Omega^2 R_E^3}\right)^{1/3} \tag{2.9}$$

It can be verified that when $\Omega = \Omega_E$ and with M_E and R_E respectively equal to the Earth's mass (5.977×10^{24} kg) and radius (6371 km), L_c = 5.78 (Lemaire, 1974).

Along a dipole magnetic field line with L larger than L_c the total potential energy of charged particles increases with altitude to a maximum value at the radial distance

$$r_m = L\ R_E \left(\frac{L_c}{L} \right)^{3/4} \tag{2.10}$$

and at the latitude

$$\lambda_m = \arccos \left(\frac{L_c}{L} \right)^{3/8} \qquad (2.11)$$

It can be seen from the dashed lines in fig. 2 that at larger radial distances along the field line L (i.e. for $r \in [r_m, LR_E]$ and $\lambda \in [\lambda_m, o])$, the potential energy ψ_{H^+} is a decreasing function of altitude; it has a minimum value in the equatorial plane given by

$$\Psi_{eq} = [\psi]_{\lambda_o}^{o} = - \frac{m_i + m_e}{2} \frac{GM_E}{LR_E} \left[1 + \frac{L^3}{3L_c^3} - \frac{LR_E}{r_o} - \frac{1}{3} \left(\frac{r_o}{L_c R_E} \right)^3 \right] \qquad (2.12)$$

where $r_o = R_E + h_o$ is the radial distance corresponding to the altitude (h_o) of a reference level. We have chosen the reference level at the exobase altitude of 1000 km where the Coulomb collision mean free path of thermal ionospheric electrons and proton becomes equal to the plasma density scale height (Lemaire, 1976b).

2.3. Zero-Parallel-Force surface (ZPF)

At the latitudes λ_m and $-\lambda_m$ the field aligned components of the gravitational and centrifugal forces balance each other. These points correspond to maxima in the field aligned potential distribution. The maximum of the potential barrier is given by

$$\Psi_m = [\Psi]_{\lambda_o}^{\lambda_m} = - \frac{m_i + m_e}{2} \frac{GM_E}{LR_E} \left[\frac{4}{3} \left(\frac{L}{L_c} \right)^{3/4} - \frac{LR_E}{r_o} - \frac{1}{3} \left(\frac{r_o}{L_c R_E} \right)^3 \right] \qquad (2.13)$$

(Lemaire, 1976b). These maxima are also located at a surface which we will call the Zero-Parallel-Force (ZPF) surface.

A meridional cross section of the ZPF surface for a corotating ion-exosphere is shown by a dashed line in fig. 3. This surface is the locus of all the points separating two potential wells : the low altitude gravitational potential well and the equatorial potential well resulting from the rotation of exospheric plasma around the Earth. The field line L = 8.5 penetrates the ZPF surface at the latitude $\lambda_m = \pm 30°$ and at the radial distance $r_m = 6.37\ R_E$.

The equatorial cross-section of the ZPF surface is a circle whose radius is equal to 5.78 R_E for a uniformly corotating exosphere : i.e. when the magnetospheric electric field coïncides with the corotational electric field described in Appendix B. Although corotation is a satisfactory approximation in the inner magnetosphere, at larger radial distances magnetotail convection electric fields perturb considerably the uniform corotation flow. This is the case especially in the night side local time sector and during periods of high geomagnetic activity when the convection velocity has an azimuthal component which exceeds the corotation velocity in the post-midnight local time sector for L > 4. As a consequence of the asymmetries in the magnetospheric convection flow pattern, the actual ZPF surface has not an ideal cylindrical symmetry. When magnetospheric convection is determined by McIlwain's E3H electric field and M2 magnetic field distributions (see Appendix A and B), the ZPF surface has a minimum minimorum equatorial distance $(r_{ZPF})_{min} = 4.56\ R_E$ at φ = 0140 LT in the post-midnight local time sector (see fig. 4). It will be shown later in this section how the geomagnetic field lines corresponding to the minimum equatorial distances of the ZPF surface are related to the Light Ion Through (LIT).

In the next sections we will however first discuss the different classes of orbits for particles spiraling along dipole magnetic field lines, different types of velocity distribution and their corresponding density distributions along magnetic field lines. It will be shown that along field lines which traverse the ZPF surface there is a new class of orbits corresponding to particles trapped in the equatorial

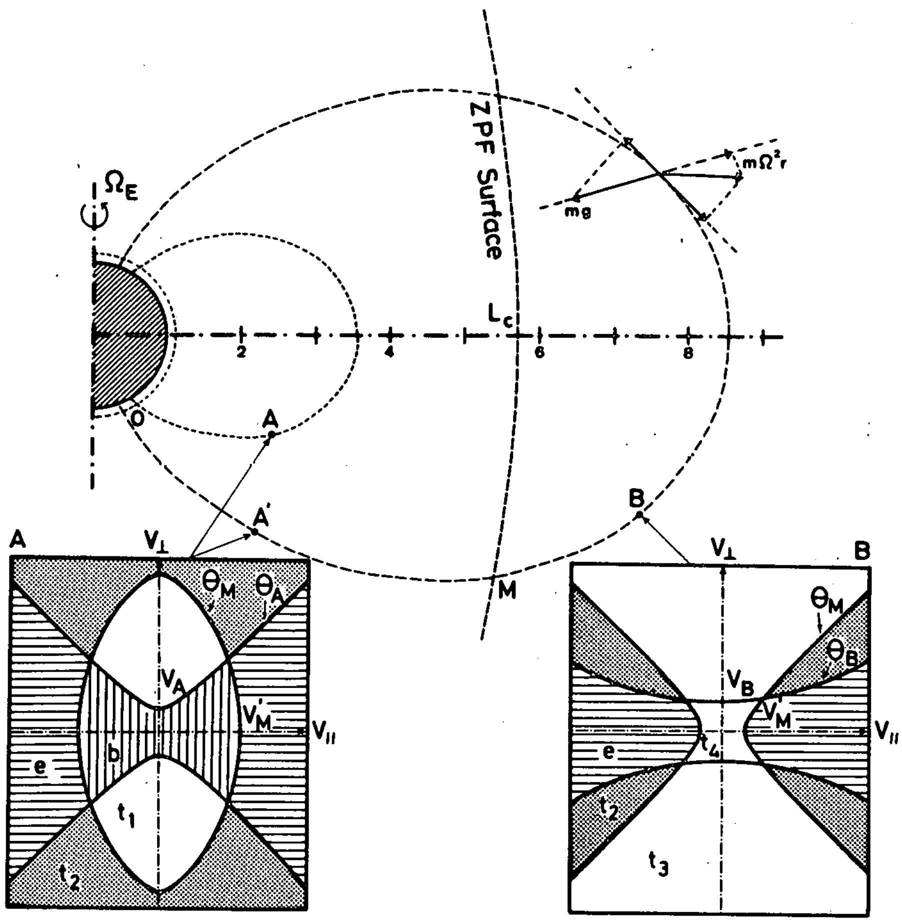

Fig. 3.- Two dipole magnetic field lines: L = 3.5 and L = 8.5. The meridional cross-sections of the Zero-Parallel-Force (ZPF) surface where the field aligned component of the gravitational and centrifugal force are equal. L_c is the equatorial distance of the ZPF surface. L_c = 5.78 for an ion-exosphere corotating with the Earth angular velocity (Ω_E). The two panels show the different region in the velocity space corresponding to the different classes of orbits of charged particles below (at A, and A') and above the ZPF surface (at B) (after, Lemaire 1976b).

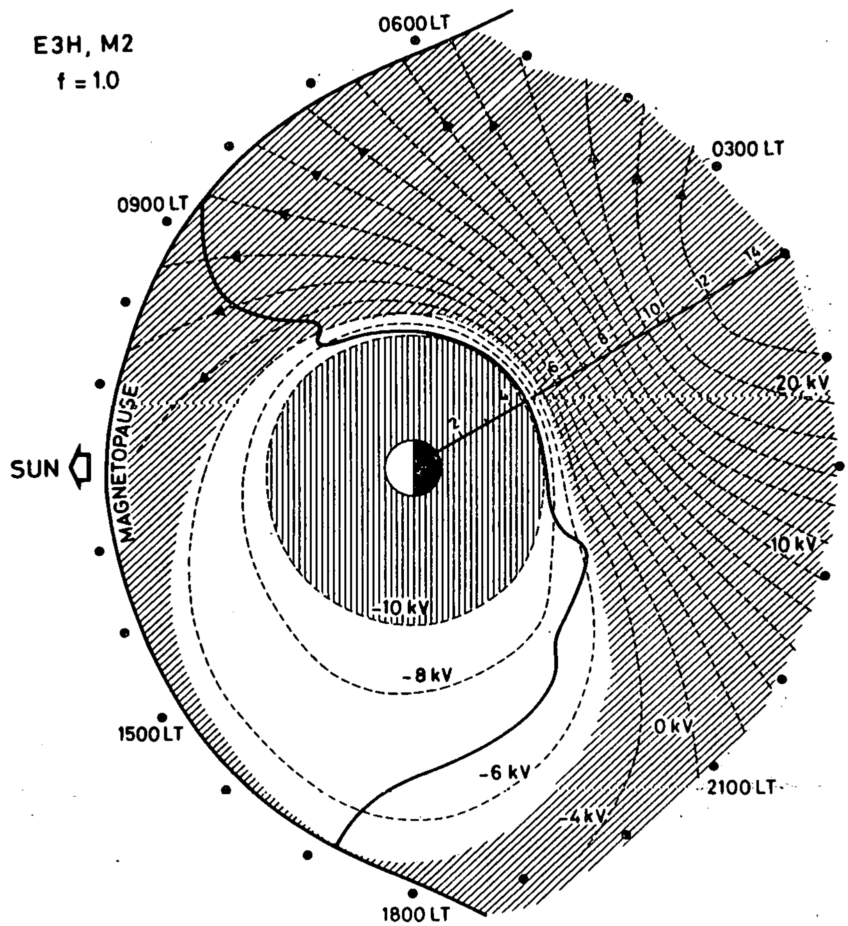

Fig. 4.- Equatorial cross section of the magnetosphere showing the electric equipotential lines corresponding to the E3H electric field distributions described in Appendix B (dashed lines). The streamlines of background plasma elements are parallel to the equipotential curves. The outer shaded area corresponds to the region outside the last closed equipotential. The solid line running across the nightside corresponds to the equatorial section of the Zero Parallel Force (ZPF) surface. The innermost shaded area tangent to the ZPF surface corresponds to the region of the plasmasphere where plasma streamlines never traverse the ZPF surface.

potential well. But this potential well exists only for field lines with L larger than L_c.

2.4. The classes of orbits for charged particle in rotating ion exospheres

Depending on their kinetic energy and pitch angle the orbits of particles spiraling along a magnetic field line can be organized in different classes illustrated in the two lower panels of fig. 3 (e) " escaping" particles, (b) ballistic particles and various types of trapped particles (t_1, t_2, t_3, t_4) (see Lemaire, 1976b).

Considering that the total energy and magnetic moment of charged particles are conserved when they spiral along magnetic field lines, one can define at any point A a loss cone angle θ_A by

$$\sin^2 \theta_A = \frac{B_A}{B_o} \frac{\frac{1}{2} mv^2 + [\psi]_{\lambda_o}^{\lambda}}{\frac{1}{2} mv^2} \qquad (2.14)$$

where $B_A/B_o = \eta_A$ is the ratio of the magnetic field intensity at the point A (r_A, λ_A) and at a reference level (r_o, λ_o). Any particle whose pitch angle, θ, is smaller than θ_A or larger than $\pi - \theta_A$ has its magnetic mirror points in the collision dominated region below the reference level (i.e. below h_o = 1000 km). The particles with these small pitch angles are in the loss cones or source cones; these particles belong either to the escaping class (e) or to the ballistic class (b) illustrated by the shaded areas (e) and (b) in panel A of fig. 3.

"Escaping" particles have enough kinetic energy to overcome the gravitational potential barrier. The escaping particles from one hemisphere penetrate in the opposite hemisphere and precipitate in the conjugate ionosphere below the reference altitude h_o, where they experience elastic or inelastic pitch angle deflections by collisions.

The central shaded area (b) of the panel A represents the region of velocity space ($v_\parallel$, $v_\perp$) corresponding to all particles emerging from the ionosphere but which have a kinetic energy smaller than the equatorial potential barrier illustrated in fig. 2. These ballistic particles never traverse the equatorial plane, they are reflected by the gravitational potential barrier and fall back into the collision-dominated ionospheric region.

The particles with pitch angles outside the source or loss cones (i.e. for $\theta_A < \theta < \pi - \theta_A$) have at least one magnetic mirror point above the altitude h_o. The trapped orbits are represented by the areas (t_1, t_2, t_3 and t_4) in the two lower panels of fig. 3. The trapped particles (t_1) with the lowest energy have two reflection points in the hemisphere below the ZPF surface. This is why they are not found in panel B referring to a point, B located above the ZPF surface. The higher energy particles (t_2) have magnetically conjugate mirror points in both hemispheres below the ZPF surface. The trapped particles of the classes t_3 and t_4 are only found beyond the ZPF surface. The panel B of fig. 3 shows the region in velocity space ($v_\parallel$, $v_\perp$) corresponding to these trapped particles. The particles of lowest energy (t_4) are unable to escape out of the equatorial potential well. The particles (t_3) have higher energies and their magnetic mirror points are located above the ZPF surface; their pitch angle is larger than θ_M and smaller than $\pi - \theta_M$, where θ_M is given by

$$\sin^2 \theta_M = \eta_M \frac{V^2 + \psi_M^*}{V^2} \tag{2.15}$$

(Lemaire, 1976b); V stands for the normalized particle velocity ($V^2 = m\, v^2/2kT_o$); ψ_M^* is the maximum value of the field aligned potential energy expressed in kT_o units ($: \psi_M^* = \psi_M/kT_o$) where ψ_M is given by eq. (2.13); the asterisk corresponding to dimensionless physical quantities will be omitted below.

2.5 Particle velocity distributions

Once all possible orbits or particle classes have been identified the question is to determine the population density for each of these different classes of orbits : i.e. the velocity distribution in all regions of the velocity space ($V_\parallel$, $V_\perp$). For the ballistic (b) and escaping (e) particles emerging from the ionosphere it is quite natural to assume that their distribution is the same maxwellian distribution as in the collision dominated ionosphere below the reference level h_o :

$$f\ (v \in \{b \cup e\}) = \frac{N_o}{(\pi mkT_o)^{3/2}} \exp\ (-V^2 - \psi) \tag{2.16}$$

where T_o is ionospheric temperature : $T_e = T_{H^+} = 3000$ K.

When the effect of Coulomb collisions can be neglected in the ion-exosphere, the velocity distribution of the trapped particles is independent of that of the ballistic particles emerging from the ionosphere. In the exospheric models the usual assumption made by Eviatar et al. (1964), Hartle (1969), Bauer (1973) or Lemaire and Scherer (1970) is that

$$f(v \in \{t_1 \cup t_2 \cup t_3 \cup t_4\}) = 0 \tag{2.17}$$

i.e. that there are no trapped particles at all. These exospheric models describe ideal conditions where the trapped particles would be removed immediately from the flux tube as soon as they are deflected into trapped orbits by rare collisions in the ion-exosphere.

Such ideal conditions are more or less satisfied in the polar wind not only because the polar cap flux tubes are considered to be "open", but also because of the very low collision frequency resulting from the low polar wind densities. However, along mid- and low latitude field lines the densities are higher, the collision frequency larger, and, E x B convection along closed streamline cannot remove the trapped plasma from the inner magnetosphere. These flux tubes at L < 4-5 eventually become saturated with trapped thermal particles. The velocity distribution is than an isotopic maxwellian function. But in the meantime any intermediate velocity distribution can be found in the outer part of the plasmasphere where magnetic flux tubes depleted from time to time are often in a dynamical state of refilling. Immediately after a substorm associated depletion of magnetic flux tubes, the velocity distribution of the ions and electrons is likely to be highly anisotropic with maximum particle flux at small pitch angles i.e. in the source cones which are soon refilled with escaping (e) and ballistic (b) particles. The trapped orbits corresponding to large pitch angles in the panels A and B of fig. 3, however, are missing or at least underrepresented in what we call an Exospheric Equilibrium (EE) velocity distribution.

On the contrary when, after a few days, all trapped orbits have become populated by the rare collisions and when the trapped particles are eventually in thermal equilibrium with the escaping and ballistic ones, the velocity distribution is isotropic and maxwellian. This final isotropic velocity distribution corresponds to Diffusive Equilibrium (DE).

In between these two extreme models (EE and DE) there is a wide spectrum of intermediate kinetic models with more or less trapped particles of the different classes t_1, t_2, t_3 and t_4. The density and higher order moments of the velocity distribution are then intermediate between the Exospheric Equilibrium ones and the Diffusive Equilibrium ones. All these kinetic models are in hydrostatic equilibrium, indeed up to this stage we have restricted our study to the cases of symmetric pitch angle distributions for which there is no net interhemispheric mass flow. The bulk speed or average velocity of the particles is then equal to zero and the pressure distribution is then that corresponding to a stratified atmosphere in hydrostatic equilibrium.

However, interhemispheric plasma flows exist in the LIT and in the outer plasmasphere. These flows can be described either by an appropriate kinetic theory as in the case of the polar wind (see Lemaire and Scherer, 1970, 1973, 1974; Lemaire, 1972) or by integrating the non-linear hydrodynamic equations (Banks and Holzer, 1968; Bailey et al., 1973, 1978; Singh and Schunk, 1982; Sojka et al. 1981; Raitt et al. 1978; Schunk and Watkins, 1979; Li et al. 1983). But for the purpose of the present study it is not necessary to enter in this much more complicated modelling technics.

Furthermore, as emphasized in a recent review by Fähr and Shizgal (1983), present collisionless models, although indispensable to understand the basic kinetic processes are idealized mathematical representations. Indeed, because of the faster escape of particles with highest energies, it is expected that the velocity distribution of the exospheric ions departs from a maxwellian function, at energies larger than the critical escape velocity. Departures from an isotropic maxwellian velocity distribution are also expected as a result of the dependence of the Coulomb collision cross section on the kinetic energy of the particles. But these first order corrections to the collisionless kinetic model calculations donot change the main physical conclusions of the zero-order kinetic theory originally proposed by Eviatar et al (1964) for non-rotating and symmetrical ion-exospheres, by Lemaire (1976b, and in this study) for rotating and symmetrical ion-exospheres, or by Lemaire and Scherer (1970, 1973, 1974) for asymmetrical ion-exosphere with field-aligned plasma flows.

In the following subsection we determine and discuss the field-aligned density distribution for kinetic models with different velocity distributions for the trapped particles.

2.6. Field aligned density distribution in rotating ion-exospheres

The integration of the maxwellian velocity distribution (2.16) over the region (b) and (e) of the velocity space shown in panel A of fig. 3 gives the density contributed by the ballistic and escaping particles at the points A or A' below the ZPF surface

$$n_A^{(b,e)} = N_o e^{-\psi_A} \left[1 - (1 - \eta_A)^{1/2} e^{-\eta_A \psi_A / (1 - \eta_A)} \right] \qquad (2.18)$$

This density distribution corresponds to the Exospheric Equilibrium (EE) and is illustrated by the lower solid line in fig. 5 for L = 4. The plasma density (N_o) and temperature (T_o) at the reference level (h_o = 1000 km) are respectively 10^3 cm^{-3} and 3000 K. Furthermore, the ion-exosphere is assumed to rotate with the Earth's angular velocity (Ω_E). Note that Eviatar et al. (1964) have derived an analogous expression for non-rotating ion-exospheres.

The upper solid line corresponds to the Diffusive Equilibrium (DE) density distribution sometimes also called barometric distribution :

$$n_A^{(e,b,t_1,t_2)} = N_o\ e^{-\psi_A} \qquad (2.19)$$

The magnetic field line L = 4 does not traverse the ZPF surface whose minimum minimorum equatorial distance is equal to 5.78 R_E for a corotating ion-exosphere. Along this field line the potential $\psi_A = \psi(L, \lambda_A)$ has a maximum value in the equatorial plane for $\lambda_A = 0$, and as a consequence of eq. (2.19), the field aligned DE density distribution has a minimum value at equatorial latitudes.

Note that the vertically hatched area in fig. 5 corresponds to the density contributed by the trapped particles t_1 and t_2 is in thermal equilibrium with those escaping out of the Earth's ionosphere. Their contribution to the density is much larger than that of ballistic (b) and escaping (e) particles. Therefore, when after a large substorm event

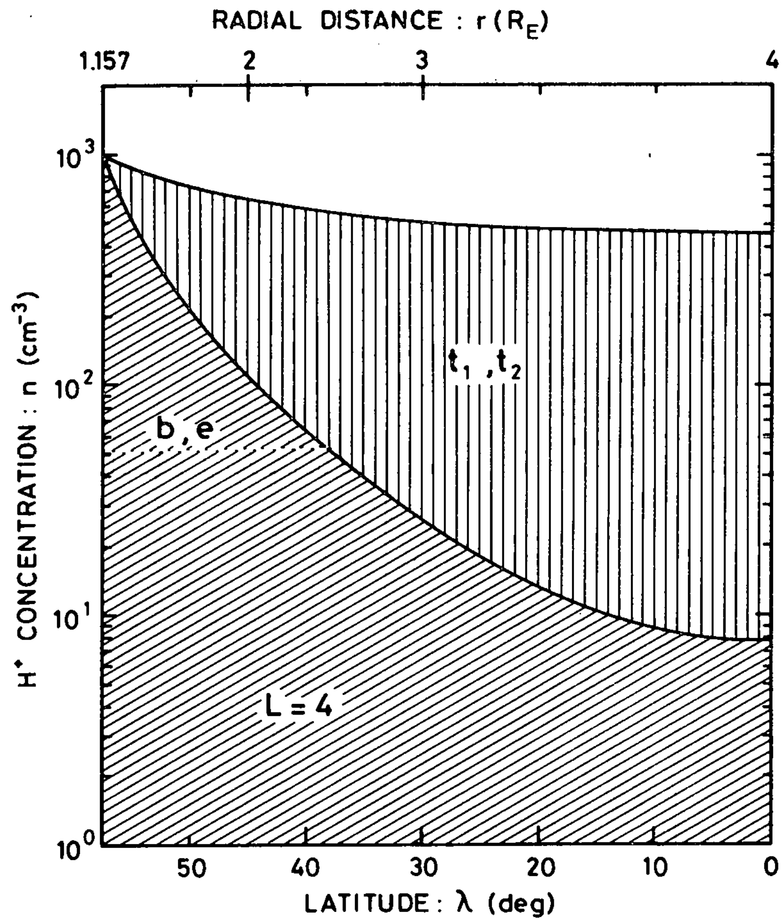

Fig. 5.- Hydrogen plasma density distributions as a function of latitude (λ) along the dipole magnetic field line L = 4. The upper solid line corresponds to the Diffusive Equilibrium (DE) model for N_o = 10^3 cm^{-3}, T_o = 3000 K at the reference level altitude : h_o = 1000 km. The lower solid line represents the Exospheric Equilibrium (EE) kinetic model for symmetrical boundary conditions at h_o in both hemispheres. The ion-exosphere is rotating with the Earth's rotation velocity (Ω_E). The abundance of trapped (t_1, t_2) particles in the DE model compared to the ballistic (b) and escaping (e) particles is shown by the different shadings.

the magnetic flux tubes at $L \geqq 4$ are depleted and all charged particles suddenly removed these flux tubes refill first with escaping (e) and ballistic (b) particles in a short period of time corresponding to the free flight time of ions from one hemisphere to the other ($t_F \cong 110$ minutes for a thermal H^+ ion at $L = 4$; see Table F2 in Appendix F). After this short transient period of time a new dynamical regime is expected to prevail with very low densities corresponding to the EE distributions and gradually building up higher densities by the continous addition of trapped particles (t_2 and t_3) as a result of Coulomb collisions and pitch angle diffusion. Eventually, over a period of several days corresponding to the characteristic refilling time, a flux tube reaches diffusive equilibrium. The trapped, ballistic and escaping particles are then in a steady state equilibrium; detailed balance is then achieved among all phase space densities.

Such a gradual refilling scenario is of course idealized. Indeed, it is based on the assumptions that the ionization fluxes from both hemispheres are exactly equal and that no hydrodynamic shock wave is formed and propagating upwards in the empty flux tubes as observed under certain conditions in laboratory vacuum expansion experiments or in numerical simulations (Samir et al. 1983; and Singh and Schunk, 1982).

As a result of eq. (2.5), the electron and H^+ ion densities given by eqs. (2.18) and (2.19) are strictly equal. Charge neutrality is therefore satisfied everywhere along the magnetic field line when this condition is verified at the reference level i.e. when $(N_o)_{ion} = (N_o)_e$ at the exobase h_o. Note also that at the exobase $n_o^{(b,e)} = N_o$ and that $n_o^{(t_1,t_2)} = 0$.

So far we have concentrated our attention on plasma distributions along magnetic field lines which do not traverse the ZPF surface. Along field lines for which L is larger than L_c, the expression (2.18) for the EE density is still valid at all altitudes below the ZPF surface. At a point B, beyond this surface, within the equatorial potential well, a more complicated expression must, however, be used to calculate the density of the escaping (e) particles

$$n_B^{(e)} = N_o\, e^{-\psi_B} \cdot \{1 - 2\, K_2(V_M) -$$

$$- (1 - \eta_B)^{1/2}\, e^{-\eta_B \psi_B/(1-\eta_B)} \cdot [1 - 2\, K_2(Y_M)]$$

$$- (1 - \mu_B)^{1/2}\, e^{-[\mu_B(\psi_B - \psi_M)/(1 - \mu_B)]} \cdot [2\, K_2(X_M) - 2\, K_2(X'_M)]\} \tag{2.20}$$

where

$$\mu_B = \frac{\eta_B}{\eta_M} = \frac{B_B}{B_M} \tag{2.21a}$$

$$V_M^2 = \psi_M - \psi_B \tag{2.21b}$$

$$Y_M^2 = \frac{\psi_M}{1 - \eta_M} - \frac{\psi_B}{1 - \eta_B} \tag{2.21c}$$

$$X_M^2 = \frac{\psi_M - \psi_B}{1 - \mu_B} + \frac{\eta_M \psi_M}{1 - \mu_M} \tag{2.21d}$$

$$(X'_M)^2 = \frac{\psi_M - \psi_B}{1 - \mu_B} \tag{2.21e}$$

and where the functions $K_m(x)$ are defined by

$$K_m(x) = \frac{2}{\sqrt{\pi}} \int_0^x e^{-t^2} t^m \, dt \tag{2.22a}$$

The function $K_m(x)$ can be expressed in terms of the error function and in terms of the exponential function. Indeed, partial integration yields the following recurrence formula,

$$K_m(x) = \frac{1}{2} (m - 1) K_{m-2}(x) - \frac{x^{m-1}}{\sqrt{\pi}} e^{-x^2} \tag{2.22b}$$

with

$$K_0(x) = \mathrm{erf}(x) \tag{2.22c}$$

$$K_1(x) = \frac{1 - e^{-x^2}}{\sqrt{\pi}} \tag{2.22d}$$

$$K_2(x) = \frac{1}{2} \mathrm{erf}(x) - \frac{x}{\sqrt{\pi}} e^{-x^2} \tag{2.22e}$$

The lower solid line in Fig. 6 shows the EE density distribution along the dipole magnetic field line L = 6 as calculated from eqs (2.18) and (2.20) respectively below and above the ZPF surface. The solid line has been calculated for the same boundary conditions as above : i.e. for $N_o = 10^3$ cm^{-3}, T_0 = 3000 K at the reference level h_0 = 1000 km, and for $\Omega = \Omega_E$. This field aligned EE density distribution is slightly smaller than that corresponding to the non-rotating ion-exosphere studied by Eviatar et al. (1964), and shown by the lower dashed line in fig. 6 (see also Bauer, 1973).

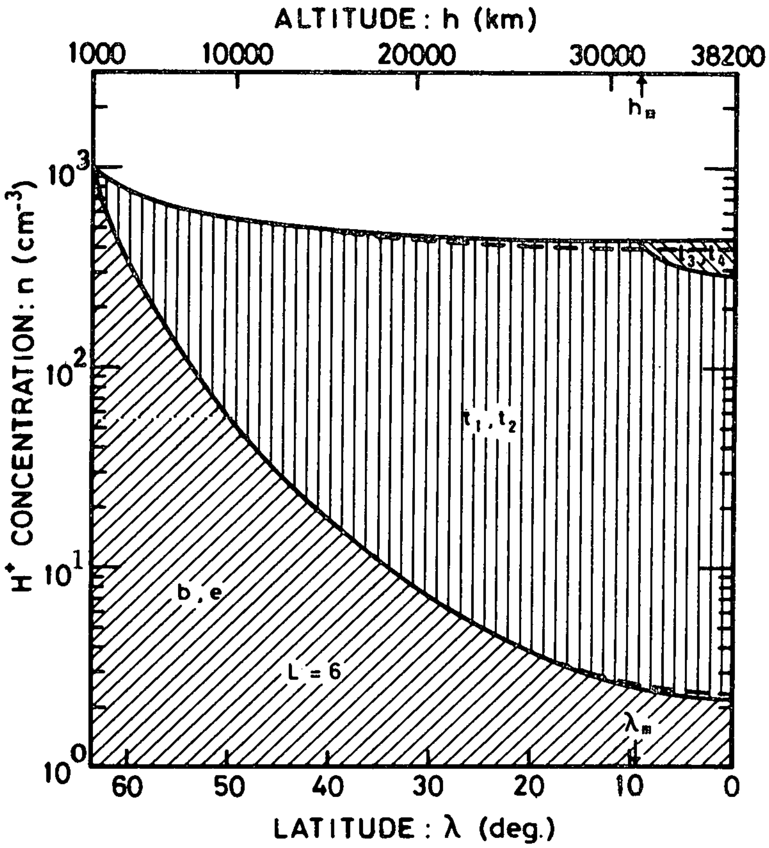

Fig. 6.- Hydrogen plasma density distributions as a function of latitude (λ) along the dipole magnetic field line L = 6. The upper solid line corresponds to the Diffusive Equilibrium (DE) model for $N_o = 10^3$ cm^{-3}, T_o = 3000 K at the reference level altitude : h_o = 1000 km. The lower solid line represents the Exospheric Equilibrium (EE) kinetic model for symmetrical boundary conditions at h_o in both hemispheres. The dashed lines correspond to non-rotating ion-exospheres. In this latter case there are no trapped particles of type t_3 and t_4. The DE density has a minimum value at the latitude λ_m = 9° where the magnetic field line penetrates through the ZPF surface. Note the large density contributed by trapped particles to the DE distribution.

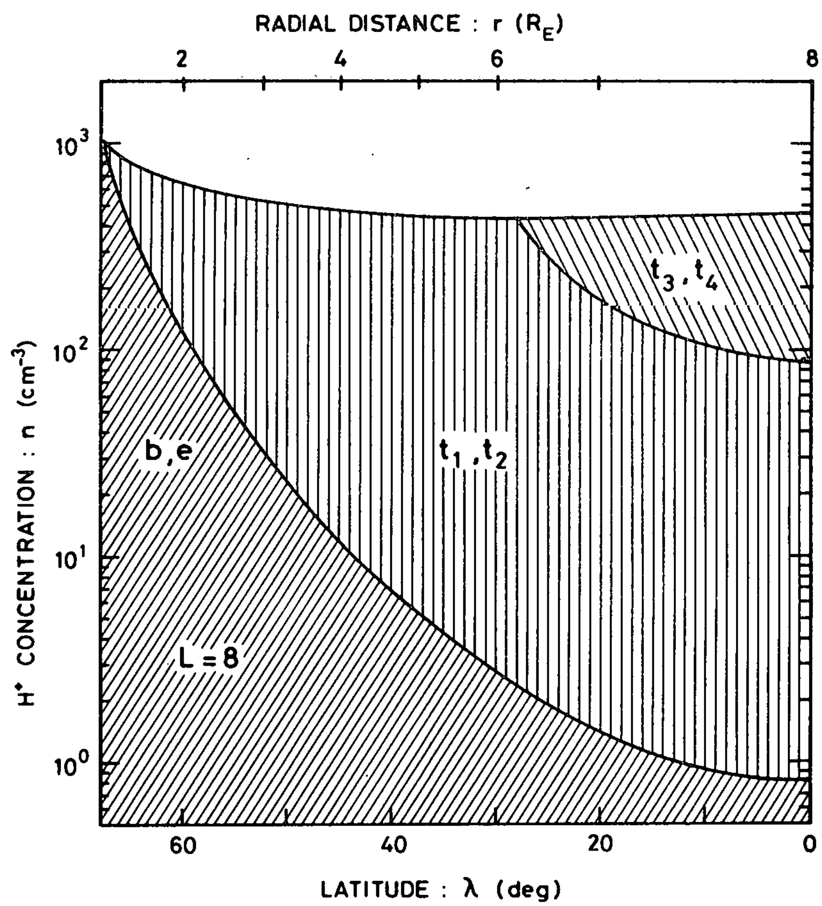

Fig. 7.- Same as in fig. 6 but for a dipole field line L = 8 penetrating across the ZPF surface for $\Omega = \Omega_E$ at $\lambda_m = 27°$ and $r_m = 6.27$.

It has been shown by Lemaire (1976b) that these EE density distributions are well approximated by the empirical R^{-4} density distribution often used to determine equatorial density from VLF whistler waves propagating in depleted magnetic flux tubes.

The upper solid line in figure 6 represents the field aligned density distribution corresponding to DE and given by eq. (2.19). The corresponding DE density distribution for the case of a non-rotating exosphere is shown by the dashed line. It can be seen that the values of the DE density are larger when the angular velocity Ω is not equal to zero. When $\Omega = \Omega_E$, the DE density distribution along the field line L = 6 has minimum value at the latitude $\lambda_m = 9°$ and $r_m = 5.83\ R_E$, where this field line penetrates through the ZPF surface. Beyond this altitude the number density $n^{(b,e,t_1-t_4)}$ given by eq. (2.19) increases as a function of altitude along the field line and has a maximum value at higher altitudes in the equatorial plane. This unusual situation is the consequence of the existence of the equatorial potential well where a large number of particles of class (t_4) can be trapped. This equatorial potential well does not exist along field lines at $L < L_c$, nor in the case of non-rotating ion-exospheres considered by Eviatar et al., (1964), indeed when $\Omega = 0$ it can be seen from eq. (2.9) that $L_c = \infty$.

When the angular velocity Ω is enhanced and made equal to $3\ \Omega_E$ the value of L_c becomes equal to 2.78 instead of 5.78. The ZPF surface approaches then closer to the Earth, the DE density distribution along the field line L = 8 has then a minimum value at $\lambda_m = 48°$ and at a radial distance of $r_M = 3.62\ R_E$. Note also that the equatorial density maximum for L = 8 is enhanced by a factor of 2.9 when the angular velocity is multiplied by 3 (see fig. 8).

Fig. 7 shows the DE and EE density distribution along the field line L = 8 for $\Omega = \Omega_E$. Note that the fraction of particles (t_4) trapped in the equatorial potential well is larger for L = 8 than for L = 6 (compare fig. 6 and 7); the relative abundance of these particles is enhanced when Ω increases (see fig. 8).

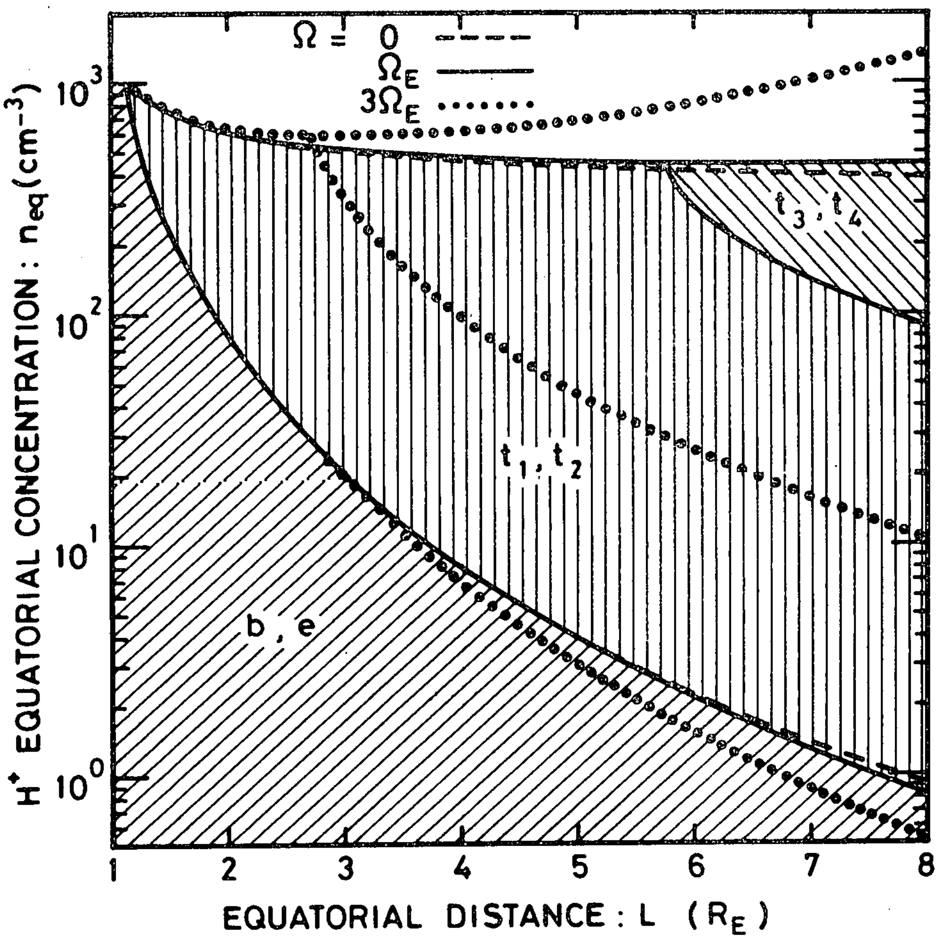

Fig. 8.- Equatorial plasma density distribution in rotating ion-exosphere models. As in figs. 6 and 7 the different shadings illustrate the abundances of different classes of particles spiraling along magnetic field lines for L varying from L = 1.2 to L = 8. The dashed lines correspond to a symmetric non rotating ion-exosphere ($\Omega = 0$); the solid lines correspond to a corotating H^+ ion-exosphere; the dotted lines show the same distributions for the case of fast rotation when $\Omega = 3\ \Omega_E$. It can be seen that the position of the minimum equatorial density at $L = L_m$ varies from $L_m = \infty$, to 6.6 and to 3.17 when Ω changes from $\Omega = 0$, to Ω_E and to $3\ \Omega_E$.

2.7. Formation of a Light Ion Trough (LIT)

A. In the previous subsections we have shown that, in a rotating ion-exosphere, the DE distribution of plasma along magnetic field lines which traverse the ZPF surface is characterized by a density decreasing as a function of altitude below the ZPF surface; but this density increases with altitude beyond the ZPF surface and has a maximum value in the equatorial plane. The larger the rotational speed in the ion-exosphere the smaller is the minimum distance of the ZPF surface, and the larger is the amount of trapped particles t_3 and t_4 which can be stored in the equatorial potential well beyond L_c.

We have also seen in section (2.3) that the ZPF surface is not cylindrically symmetric. Indeed, the convection velocity in the magnetosphere departs from ideal corotation already at $L \geqq 4$ in the night side region. The equatorial section of the ZPF surface is shown in fig. 4 for the case when magnetospheric convection can be approximated by the E3H electric field model described in Appendix B; the convection velocities are then, equal to the vectors shown in fig. 11. Note the enhanced eastward convection velocity for L > 4-5 in the post-midnight sector. For instance at φ = 0030 LT the radial distribution of $\Omega = v_\varphi/R$ has a maximum value $\Omega_{max} = 3.6\ \Omega_E$ at $r = 5.7\ R_E$. As a consequence it is in this local time sector that the ZPF surface is closest to the Earth. This is illustrated in fig. 4. The minimum minimorum equatorial distance of the ZPF is $L_c = 4.57$ at φ = 0142 LT.

The central shaded area in fig. 4 corresponds to the region of the plasmasphere where the convection streamlines donot traverse the ZPF surface. All equatorial plasma elements convecting outside this central region traverse this surface twice : once at a local time between 1800 and 0142 LT and a second time between 0142 LT and 1000 LT. Figs. B3 and B4 in Appendix B show the ZPF surface for two slightly different electric field models.

Let us consider an equatorial plasma element convecting along the streamline which coïncides with the equipotential -8 kV in fig. 4. Along the dayside and dusk portion of the -8 kV equipotential, the magnetic field lines do not cross the ZPF surface, and consequently the field aligned plasma distribution has a single minimum in the equatorial plane. Let us also assume that the magnetospheric electric field has been steady for more than 8 or 10 days, i.e. long enough to guarantee that the field aligned density distribution has been able to reach diffusive equilibrium (DE). The equatorial distance of this flux tube is 8 R_E at 1800 LT. The density and pressure gradients along the magnetic field line are everywhere negative. However, once the convecting flux tube enters the region beyond the ZPF surface, a potential well develops near the equatorial plane. Within this potential well trapped particles of the class (t_4) can pile up.

B. The net field aligned force per unit volume $\rho[\underline{g} + \underline{\Omega}\times(\underline{\Omega}\times\underline{r})]_{\parallel}$ is directed outwardly along the portion of the magnetic field line beyond the ZPF surface. The field aligned density and pressure gradients ($\underline{\nabla}_{\parallel} n$ and $\underline{\nabla}_{\parallel} p$) within the plasma element remain negative as they were in the duskside. Therefore, the pressure gradient force ($- \nabla_{\parallel} p$) in the momentum equation cannot be balanced by the parallel component of the external force since both vectors are directed outwardly. As a consequence hydrostatic equilibrium fails to be satisfied. Indeed, to satisfy hydrostatic equilibrium the field aligned pressure gradient must become positive beyond the ZPF surface. In the equation of motion

$$\rho\left(\frac{\partial}{\partial t} + \underline{v}_{\parallel} \cdot \underline{\nabla}_{\parallel}\right) \underline{v}_{\parallel} = - \underline{\nabla}_{\parallel}\, p + \rho\, [\, \underline{g} + \underline{\Omega} \times (\, \underline{\Omega} \times \underline{r})]_{\parallel} \qquad (2.23)$$

both vectors in the right hand side are directed outwardly. This forces the plasma to become accelerated outwardly along the magnetic flux tube. In other words, even if the plasma was in hydrostatic equilibrium while it convected in the duskside, its field aligned density distribution becomes convectively unstable as soon as the angular speed Ω is enhanced on the post-dusk portion of its drift path. When the tip of the magnetic field line extends beyond the ZPF the right hand side of eq. (2.23) is definitely positive and consequently $\left(\frac{\partial}{\partial t} + v_{\|} \cdot \nabla_{\|} \right) v_{\|} > 0$ above the ZPF surface. Although at low altitude the total external force (: last term in eq. 2.23) is dominated by the gravitational pull, its field aligned component is reduced because of the enhancement of the angular speed Ω. Since the centrifugal force $\rho \underline{\Omega} \times (\underline{\Omega} \times \underline{r})$ is enhanced, while the other terms in the right hand side of eq. (2.23) are unchanged, the right and left hand side of this equation will assume a positive value; this corresponds to outward acceleration of the plasma.

As a matter of consequence, field aligned plasma distributions with negative density and pressure gradients become convectively unstable when the plasma element traverses the ZPF surface. Therefore, the innermost streamline which is tangent to the ZPF surface defines a limit which has been associated, previously, with the equatorial plasmapause, but which is more closely related with the position of the Light Ion Trough (LIT) observed at midlatitudes in the topside ionosphere (Lemaire, 1974). Indeed, plasma elements circulating beyond this limit which coïncides in fig. 4 with the equipotential line -10 kV, are never in an equilibrium state, since flows of ions and electrons move always up or down along the magnetic field lines to reajust the plasma density distribution.

C. The reason for the upwelling of thermal plasma along magnetic field lines and light ion depletion of the midlatitude can also be presented in following terms : because of the enhancement of the angular rotation velocity in the post-dusk sector a deeper equatorial potential well is forming beyond the ZPF surface, as the flux tube proceeds toward post-midnight local time sector where the azimuthal convection velocity is up to three times larger than corotation; more and more particles can be piled up on t_4-trapped orbits. Coulomb collisions, and possibly other pitch angle scattering mechanisms are responsible for this irreversible piling up of particles near the equatorial plane. The accumulation of particles near the developing potential well, generates the upwelling of fresh new plasma out of the topside ionosphere at mid-latitudes.

The upward field aligned flux of light ions depletes the nightside ionosphere thus forming at mid-latitudes the Light Ion Trough observed by Taylor et al. (1969). The potential barrier which ions have to overcome is smaller for the lightest H^+ and He^+ ion than for the more massive O^+ or N^+ ions. The equation of motion for the ions is given by

$$n_i m_i \left(\frac{\partial}{\partial t} + \underline{v}_{\parallel i} \cdot \underline{\nabla}_{\parallel} \right) \underline{v}_{\parallel i} = - (\underline{\nabla} \cdot p_i)_{\parallel}$$

$$+ n_i m_i \left[\underline{g} + \underline{\Omega} \times (\underline{\Omega} \times \underline{r}) \right]_{\parallel} + n_i Z_i e \underline{E}_{\parallel} - \text{(frictional drag)} \qquad (2.24)$$

When Ω is enhanced, other terms remaining unchanged - including the mass independent partial pressure force $(- \underline{\nabla} . p_i)_{\parallel}$ - it results from eq. (2.24) that the acceleration of the ions is indeed upwards. It should be pointed out that the parallel electric field pointing outwards exceeds then the Pannekoek-Rosseland field derived from equation (2.2) for the case of hydrostatic equilibrium, when $v_{\parallel i} = 0$. The enhanced electric force contributes then also to accelerate ions out of the LIT topside ionosphere.

The Coulomb interactions which are relatively rare, but not negligible, deflect the lighter ions onto trapped orbits. The particles of smallest kinetic energy are deflected first, since the Coulomb collision frequency is strongly energy dependent ($\nu_i \propto E_i^{-3/2}$). Therefore, the trapped orbits (t_4) and ballistic orbits (b) corresponding to the lowest energies in velocity space will be populated first (see panels A and B in fig. 3). But this implies also that the equatorial potential well forming beyond the ZPF surface fills up rather quickly with particles of the lowest energies.

D. All these theoretical results concour to the conclusion that the ZPF surface and the innermost streamline tangent to the ZPF surface are associated with (i) upwelling of the ions of lowest energies, (ii) their piling up in the potential well beyond the ZPF surface, and (iii) the depletion of light ions from the topside ionosphere at mid-latitudes.

In conclusion, we suggest that the formation of the Light Ion Trough at midlatitudes is associated with the post-dusk enhancement of the azimuthal component of the convection velocity which determines the increase of the centrifugal force. This means that there should be no significant field aligned upwelling of light ions in the inner region of the plasmasphere where the angular velocity does not vary significantly along the drift path and where the centrifugal force is small. It is only at larger L- values, where the parallel component of the centrifugal force becomes predominant and where the streamlines have a large dawn-dusk asymmetry, that the post-dusk enhancement of the local angular velocity plays a significant role in the depletion of light ions out from the topside ionosphere. This upwelling is expected along magnetic field lines for L- values smaller than those where the equatorial plasmapause knee is observed in the equatorial plasma density distribution (see chapter 4).

E. These theoretical results are applicable both for steady state as well as for time dependent the magnetospheric electric field distributions i.e. during quiet and disturbed geomagnetic conditions. But during the recovery phase, after a magnetic substorm, there is an additional factor contributing to drive a "Polar Wind" like flux of up-welling light ions along the field lines located in the outer region of the plasmasphere. Indeed, after a substorm associated enhancement of the nightside convection velocity, the outer region of the plasmasphere is depleted. The magnetic flux tubes are nearly empty and the ion partial pressure in eq. (2.24) is drastically reduced at high altitude. As a consequence the pressure gradient term in this equation is larger than in the DE models illustrated in figs. 5, 6 and 7. This larger pressure gradient forces the light H^+ and He^+ to flow out of the ionosphere and to deplete it. This is why, during the recovery phase after an isolated substorm event, the formation of a Light Ion Trough is due to the combination of two distinct physical effects (i) the enhancement of the centrifugal force discussed above (ii), and secondly, the partial pressure reduction at high altitudes in recently depleted flux tube of the outer plasmasphere.

2.8 Comparison with the observations

A. The two complementary mechanisms contributing to the formation of Light Ion Trough at mid-latitude are consistent with the observations reviewed by Taylor (1972) and others. There is now plenty of evidence that the equatorial edge of the Light Ion Trough is located along magnetic field lines which are at one L-value equatorward from those corresponding with the equatorial plasmapause (Titheridge, 1976; Foster, et al., 1978; Grebowsky, et al., 1976) The first mechanism presented above, indeed, predicts that the streamline tangent to the ZPF surface is located at lower L-values (L_c = 4.56 in fig. 4) than the equatorial plasmapause whose position will be discussed in chapter 4. Furthermore, the intermediate region of depleted flux tube is always located at lower L-values than the new plasmapause forming at larger equatorial distance during the quiet recovery phase after a substorm event (see chapters 4 and 5).

B. The equatorward edge of the Light Ion Trough is found at positions which do not much depend on local time (Brace and Theis, 1974; Ahmed et al., 1979). This confirms our theoretical result that there should be no significant upwelling flux of light ions in the inner part of the plasmasphere (i) where the angular velocity of the plasma does not significantly depart from corotation and where all streamlines are almost symmetric and circular; (ii) where catastrophic depletions of magnetic flux tubes are rather rare.

C. It has also been found experimentally that the LIT forms at more equatorward latitudes when K_p increases (Taylor et al., 1975; Rycroft and Thomas, 1970; Rycroft and Burnell, 1970; Ahmed et al., 1979). These observations are also consistent with this theory which predicts that L_c decreases when Ω increases i.e. a deeper penetration of the ZPF surface in the plasmasphere, where Ω is enhanced during periods of high geomagnetic activity. The deeper penetration of the ZPF surface implies an equatorward shift of the low latitude edge of the LIT as observed during periods of increasing K_p.

D. The sharpest low latitude edges of the Light Ion Trough have been observed during night-times, when satellites crossed the region where the eastward convection velocity and the angular velocity Ω are largest (Taylor and Walsh, 1972; Ahmed et al., 1979) According to our theory this is precisely the local time where the LIT is formed by the field aligned instability driven by centrifugal effects and by large plasma pressure gradients.

E. Furthermore, these low latitude edges of the LIT are also becoming sharper when geomagnetic activity increases (Ahmed et al., 1979). Under these conditions (larger K_p-index) the gradients of the observed eastward convection velocities in the nightside local time sector are also enhanced. As a consequence there are also sharp gradients in the latitudinal distribution of the field aligned centrifugal force. The upward field aligned acceleration and flux of light ions driven by enhanced centrifugal effects have then also the steepest latitudinal gradients. Therefore, according to this theory the low latitude edge of the nightside LIT is likely to be sharper for high K_p values than for low ones. This is precisely what is reported in the literature.

F. Finally the smoother gradient observed in the dayside latitudinal H^+ and He^+ density distributions can be considered as resulting from the much smaller and smoother variation of the angular velocity as a function of L. But it is also the consequence of the LIT broadening by diffusion at lower altitude and by charge exchange processes.

3. TRANPORT OF PLASMA IN THE PLASMASPHERE

So far we have examined the centrifugal effects of non-uniform angular velocities and two mechanisms for the formation of a nightside LIT along geomagnetic field lines which traverse the ZPF surface. There are other dynamical effects resulting (i) from diurnal contractions and expansions of magnetic flux tubes convecting inside the plasmasphere, and (ii) from flux tube refilling after a period of large geomagnetic activity. These effects are examined in this chapter.

We start in this section with the question of diurnal variations of the equatorial density inside a plasma element convecting along a drift path which is not necessarily parallel to a geomagnetic L-shell. Ignoring cross-B diffusion processes as well as plasma interchange motion, the MHD theorem of conservation of magnetic flux tells us that the equatorial cross section (S_{eq}) of a field aligned plasma element varies as B_{eq}^{-1} along its drifts trajectory. As a consequence of the dawn-dusk asymmetry of its drift path, the cross section of this plasma element shrinks when it penetrates in a region of higher magnetic field intensity. During this adiabatic contraction, the plasma density and temperature increase. Conversely, when these plasma elements move outwardly toward lower magnetic regions, their equatorial cross-section and their density are respectively increasing and decreasing as

$$S_{eq}(L) \propto B_{eq}^{-1} \qquad (3.1)$$

$$n_{eq}(L) \propto V^{-1} \qquad (3.2)$$

Where V(L) is the volume of the plasma element which is almost equal to the volume of the magnetic flux tube containing this field aligned element.

3.1. The variation of the equatorial density as a result of the contraction of plasma elements in the post-dusk sector

The equatorial cross section (S_{eq}) of a dipole flux tube whose magnetic flux is equal to 1 Weber is given by

$$S_{eq}(L) = \frac{1}{B_{eq}} = 3.12 \times 10^8 L^3 \text{ [in cm}^2\text{]} \qquad (3.3)$$

The distribution of $S_{eq}(L)$ is illustrated by the upper solid line in fig. 9. Also shown is the perpendicular cross section (S_o) of the same magnetic flux tubes at the altitude of the reference level h_o = 1000 km (lower solid line)

$$S_o(L) = 4.8 \times 10^8 / (4 - 3. \frac{R_E + h_o}{LR_E})^{1/2} \text{ [in cm}^2\text{]} \qquad (3.4)$$

The volume of dipole magnetic flux tubes integrated above the Earth's surface is given by

$$V(L) = \frac{2}{7} \frac{R_E}{(B_{eq})_o} L \sin \Lambda \left[1 + \frac{6}{5\cos^2 \Lambda} + \frac{8}{5\cos^4 \Lambda} + \frac{16}{5\cos^6 \Lambda}\right] \qquad (3.5)$$

or

$$V(L) = 5.87 \times 10^{16} L(1 - \frac{1}{L})^{1/2} \left[1 + \frac{6}{5} L + \frac{8}{5} L^2 + \frac{16}{5} L^3\right] \text{ [in cm}^3\text{]} \qquad (3.6)$$

where Λ is the invariant latitude of the magnetic field line L :

$$\cos^2 \Lambda = 1/L \tag{3.7}$$

The volume of 1 Weber magnetic flux tubes is shown by the dashed line in fig. 9.

Fig. 8 shows the equatorial density distribution $n_{eq}(L)$ as a function of L for three different values of the angular speed Ω. The upper solid line corresponds to DE models with $\Omega = \Omega_E$, the dashed lines for $\Omega = 0$ and the dotted curves refer to $\Omega = 3\ \Omega_E$, i.e. to convection velocities comparable to those observed in the post-midnight local time sector beyond L = 5-6. The corresponding equatorial densities are also given for the Exospheric Equilibrium models discussed above.

Let us now consider a field aligned plasma element drifting for instance along the equipotential surface -8 kV shown in fig. 4. At dusk the equatorial distance is 8 R_E. At this distance the equatorial cross section (S_{eq}) and volume (V) of a 1 Weber magnetic flux tube are respectively $S_{eq} = 1.6 \times 10^{11}$ cm^2 and $V = 7.2 \times 10^{21}$ cm^3 (see fig. 9). From figs. 11 and 12 it can be seen that the plasma in this flux tube drifts with an angular velocity slightly below corotation ($\Omega \leqq \Omega_E$). Let us assume, furthermore, that the plasma is in diffusive equilibrium. The equatorial plasma density is then equal to 450 cm^{-3} for $n_o = 10^3$ cm^{-3} and T_o = 3000 K at h_o = 1000 K (see fig. 8).

Let us now transport this magnetic flux tube with its plasma content to L = 4.8 at φ = 0130 LT where the angular velocity has increased by a factor of 2 ($\Omega = 2\ \Omega_E$). If the magnetic flux encompassed within this plasma element has been conserved along its drift path, the transformation is adiabatic and the equatorial cross section has then shrinked from 1.6×10^{11} cm^2 to 0.35×10^{11} cm^2 (it has decreased by a factor 4.6), while the volume of the plasma element has decreased by a

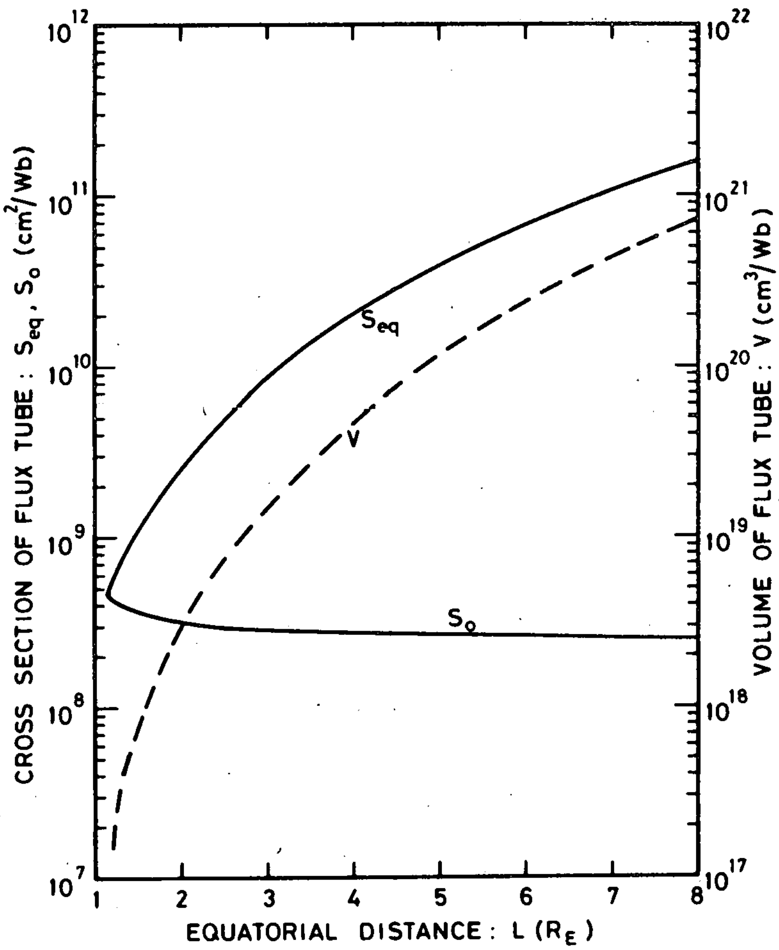

Fig. 9.- Equatorial cross section of 1 Weber dipole magnetic flux tubes (S_{eq}) as a function of their equatorial distance (L). Cross section of these same flux tubes at the reference altitude of 1000 km (S_o). The volume of the same magnetic flux tube integrated above the Earth's surface.

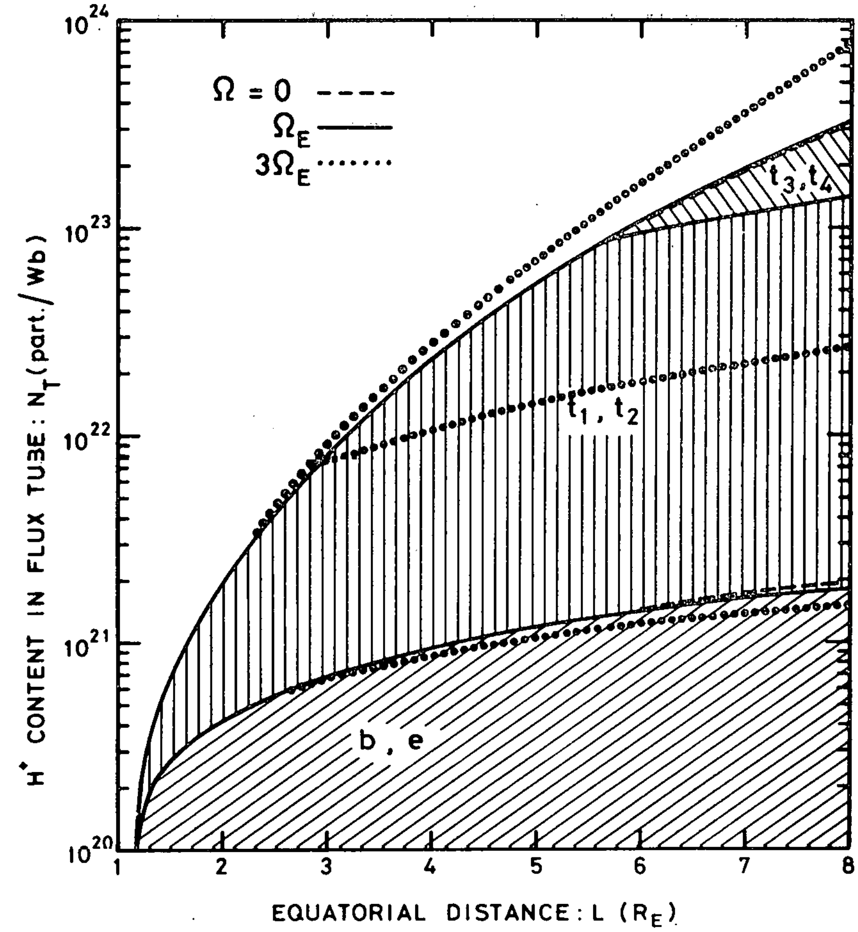

Fig. 10.- Total H^+ ions content in 1 Weber dipole flux tubes above the reference level altitude, h_o = 1000 km. The total particle contents are given for non-rotating ion-exospheric models (dashed lines); for corotating exospheric models (solid lines); the dotted lines show the distribution of N_T as a function of equatorial distance L for the case of fast rotation when $\Omega = 3\ \Omega_E$. As in fig. 8 the different shadings illustrate the contribution of the different classes of particles spiraling along magnetic field lines. Note that at L = 8 the total content of ballistic (b) and escaping (e) of the EE model is 200 times smaller then the total content in the DE model including the trapped particles (t_1, t_2, t_3 and t_4).

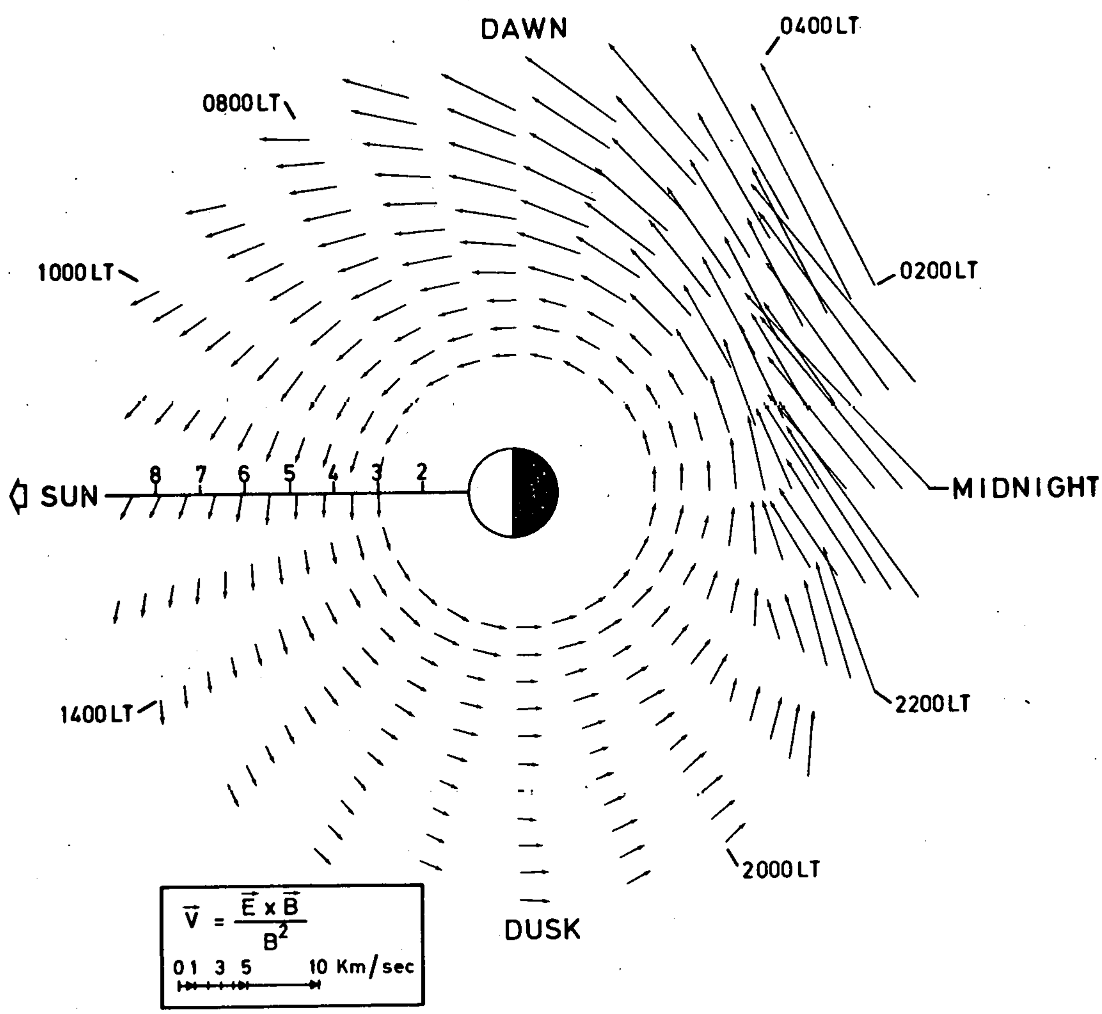

Fig. 11.- Equatorial convection velocities corresponding to the electric and magnetic field models E3H and M2, in a fixed frame of reference. The M2 and E3H models are described respectively in the Appendices A and B. Note the large eastward velocity component in the nightside sector corresponding to super-rotation of magnetospheric plasma.

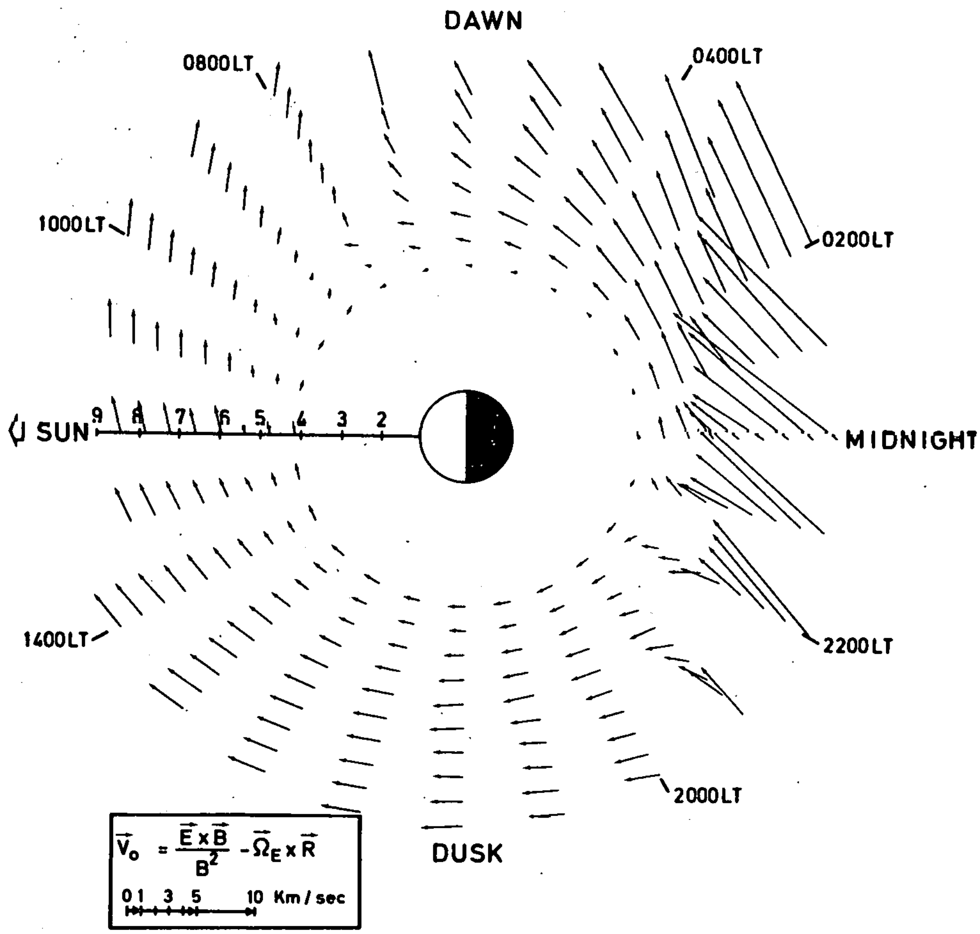

Fig. 12.- Equatorial convection velocities corresponding to the electric and magnetic field models E3H and M2 in a corotation frame of reference. The E3H and M2 models are described respectively in the Appendices B and A. Note the change in the azimuthal velocity component, respectively, at 2230 LT and at 0830 LT. The westward velocities in the dayside are probably due to atmospheric drag (Baumjohann et al. 1985).

factor 7.5 i.e. from 7.2×10^{21} cm^3 to 0.96×10^{21} cm^3. According to eq. (3.2) the equatorial density must have increased by the same factor 7.5, if the total number of particles (N_T) in this flux tube has been conserved. After this adiabatic transformation conserving the total particle content (N_T), the equatorial particle density (n_{eq}) has increased to 3375 cm^{-3}.

Note, already, that both the parallel and perpendicular temperatures increase also during this fast adiabatic compression. But we will come back to this question in section 3.5.

Let us next consider an isothermal transformation and assume that the drift time from dusk (1800 LT) to midnight is long enough to achieve thermal and diffusive equilibrium at any instant of time. This would of course imply characteristic drift times of several days from 1800 LT to 0130 LT to let Coulomb collisions and pitch angle scattering establish field aligned distributions in DE equilibrium all along the drift trajectory. During this slow transformation the temperature in the plasmasphere would remain equal to that of the ionospheric thermal source (i.e. at T_o = 3000 K). In this ideal isothermal transformation the ionosphere constitutes a large isothermal reservoir for charged particles and kinetic energy.

In the course of such an isothermal transformation the DE equatorial density given by eq. (2.19) increases because the field aligned potential given by eq. (2.12) decreases when L becomes smaller and when Ω becomes larger. As a result of both effects the DE equatorial density increases only by a factor of 1.13 from 450 cm^{-3} at L = 8 to 510 cm^{-3} at L = 4.8 if $\Omega = 2\ \Omega_E$ at 0130 LT.

However, the actual magnetospheric convection velocity is neither slow enough to let isothermy and DE equilibrium to be maintained during the transformation, nor is it fast enough to guarantee the transformation to be purely adiabatic and conserving the total content of particles. Therefore the post-dusk evolution of equatorial densities will be an intermediate one between these two extremes. Consequently n_{eq} near L = 4.8 is expected to range between the values 660 cm^{-3} and 3375 cm^{-3} corresponding respectively to the two extreme cases discussed above.

This result is well confirmed by the observations which indicate that equatorial densities are higher at late nightside local times than in the afternoon and dusk local time sectors (Chappell _et al._, 1970a, b; Chappell, 1972).

In section 3.6 we describe the results of a numerical simulation for the diurnal variation of the equatorial density.

3.2. The variation of the total particle content

In the adiabatic transformation the total particle content $N_T(L) \cong V(L).n_{eq}(L)$ is conserved when the flux tube drifts from L = 8 to L = 4.8. When the corotating plasma distribution is initially in diffusive equilibrium and in thermal equilibrium with the ionosphere (T_o = 3000 K, $n_o = 10^3$ cm^{-3} at h_o = 1000 km), it can be seen from fig. 10 that $N_T = 3.6 \times 10^{23}$ ions/Wb at L = 8.

In the ideal case of an isothermal transformation it can be seen from fig. 10 that N_T varies from 3.6×10^{23} ion/Wb at L = 8 to $N_T = 0.46 \times 10^{23}$ ion/Wb at L = 4.8 if Ω would have remained equal to Ω_E. This corresponds then to decrease by a factor 7.8. But since the angular velocity is enhanced by a factor of 2 in the post-midnight local time the centrifugal effects become significant and a larger number of particles can be stored in the equatorial potential well as already emphasized in section 2.6. Therefore, $N_T = 0.52 \times 10^{23}$ ions/Wb at L = 4.8 when $\Omega = 2\,\Omega_E$. This corresponds to a net decrease of N_T by a factor 7.

As a matter of consequence when field aligned plasma elements move toward the Earth in the post-dusk local time sector, the total particle content N_T can decrease by large factors except in the ideal case of an adiabatic transformation. Since the magnetospheric convection velocities are neither large enough for this transformation to be adiabatic, nor small enough to be isothermal, it can be concluded that N_T decreases by some factor varying between 7 and 1 when a field aligned plasma element is initially in DE and when it drifts in the post-dusk local time sector between 1800 LT and 0130 LT along the equi-potential surface -8 kV in fig. 4. As a consequence, a fraction of the total flux tube content at L = 8 is available for escape out of the flux tube. It is generally admitted that during the post-dusk compression of magnetic flux tubes the excess plasma density stored at high altitudes returns to the nightside ionosphere where it maintains the ionization density despite the absence of any photoionization process. The plasma pumped up in the plasmasphere during the day is precipitated along the nightside field lines to aliment the upper ionosphere during the night when the ions recombine or exchange charges with neutral atoms.

The maximum fraction of the DE total particles content which is available for precipitation and for recombination in the night-time ionosphere is equal to 86% of the 3.6×10^{23} ion/Wb which can be stored above the altitude of 1000 km in a 1 Weber magnetic flux tube at L = 8. The cross-section of this flux tube at an altitude of 1000 km is 2.7×10^8 cm^2. The total number of ions available in a flux tube with a cross section of 1 cm^2 at 1000 km altitude is then at most 1.1×10^{15} particles/cm^2. Considering that all plasmaspheric particles are evacuated by downward ionization flow in the period of time of 6 hours needed for the plasma to drift from dusk to midnight, the maximum precipitation is then 5×10^{10} ion/cm^{2}s. The total ionospheric content below the altitude of 1000 km is of the order of 5×10^{12} ion/cm^2 and the average F_2 layer loss coefficient 10^{-4} s^{-1} (Davies et al., 1979). Therefore, the minimum downward ionization flux needed during the night to maintain this ionospheric content is 5×10^8 ion/cm^2 s; this is two order of magnitude less than the maximum downward flux available at L = 8 and 1800 LT when the plasma is in DE. This order of magnitude calculation shows that if all magnetic flux tubes at L = 8 were in DE there would be too many particles stored in the outer plasmasphere than actually is needed to aliment the nightside ionosphere and to maintain its ionization density during the whole night.

Davies et al. (1979) have shown that the squeezing of plasmaspheric flux tubes at L = 2 with much smaller total particles content, can account not only for the maintainance of the nightside ionosphere, but can even explain the observed nocturnal ionization enhancement and the associated variation in the height of the F layer peak.

3.3. Upper limits for the total particle content in plasmaspheric flux tubes

In the order of magnitude calculations presented above we assumed that the magnetic flux tubes at L = 8 and 1800 LT were all filled up and saturated with corotating plasma in DE. The total content N_T at L = 8 and 1800 LT, just before the flux tube contraction, has to be smaller than the DE values by a factor 100 : i.e. 3.6×10^{21} ions/Wb.

As a result of the dawn-dusk asymmetry of the convection trajectories for L > 4, their total content varies with local time and is limited by the effect of periodic squeezing in the post-dusk sector, which is then followed by a flux tube expansion and dilatation in the dayside sector. To demonstrate that the alternation of contractions and dilatations of flux tubes is a limiting factor for N_T let us again consider the asymmetric drift path in fig. 4 which coïncides for example with the -8 kV equipotential line in the E3H model. Let us assume that all flux tubes along this equipotential line are no longer in DE but that they have been depleted during a recent substorm event. After a short period of time of the order of t_F, given in Table F1 (see Appendix F) and, corresponding to the average flight time for thermal ions to bounce from one hemisphere to the other, the escaping (e) and ballistic

(b) particles from the ionosphere have invaded the flux tube. The field aligned plasma distribution is then well represented by the exospheric equilibrium (EE) models which are illustrated by the lower curve in fig. 7. The total particle content $N_T(L)$ has then a minimum value which is equal to $N_T^{(b,e)} = 1.7 \times 10^{21}$ ions/Wb. As time goes on, more and more particles of the classes t_1, t_2, t_3 and t_4 become trapped in the ion-exosphere. Pitch angle diffusion is a consequence of Coulomb collisions and possibly also of wave-particle interactions. The latter mechanism might contribute, but only when the energy density of electrostatic or electromagnetic waves is large enough in the appropriate frequency ranges for wave-particle interactions to be an efficient source of pitch angle scattering. Whether or not wave-particle interactions are important or not for the bulk of thermal electrons and ions of less than 1 eV is not the point of our discussion. What is certain at least, is that Coulomb collisions between ions (and electrons) of energies smaller than 0.5 eV is a very efficient scattering mechanism, even at high altitudes in the low-density plasmasphere. This collision process is responsible for continual increase of the total particle content in depleted magnetic flux tubes.

In the inner plasmasphere at $L < 3$ where the drift path of corotating plasma elements is nearly circular : there is no significant volume contraction, nor squeezing, nor an expansion, nor a dilatation of the flux tubes. The total particle content can then build up until diffusive equilibrium (DE) is reached. The fluxes of escaping particles and precipitating particles are then nearly balanced all the time. However, for flux tubes drifting along an asymmetric trajectory at higher L values, the total content N_T builds up until it reaches a stationary upper limit $N_T^!$ at (L_{max}, φ_{max}) where the volume V(L) is maximum. In a steady state regime this upper limit for $N_T^!$ must be determined in such a way that the fraction of $N_T^!(L_{max}, \varphi_{max})$ which is dumped into the ionosphere during the night-time squeezing phase, is balanced by the total number of particles flowing out of the ionosphere and refilling the magnetic flux tube in the dayside, when it is expanding again. The balance between the total number of particles which are dumped downwards and those which diffuse upwards during the dayside part of the drift trajectory can be expressed by the following equation

$$N'_T(L_{max}, \varphi_{max}) = N'_T(L_{min}, \varphi_{min}) + 2\int_{t_{min}}^{t_{max}} F_{\parallel}\, S_o\, dt \qquad (3.18)$$

where $N'_T(L_{min}, \varphi_{min})$ is the maximum total content of particles in the same flux at L_{min} and φ_{min} where its volume has contracted to a minimum value; $F_{\parallel}$ is the field-aligned flux of light ions diffusing upwards across a unit surface located at h_o = 1000 km; S_o is the perpendicular cross section of the 1 Weber flux tube at the altitude of 1000 m (see eq. (3.4) and fig. 9); t_{min} and t_{max} are the universal times when the plasma element passes across the meridional planes at φ_{min} and φ_{max} respectively :

$$\varphi_{max} - \varphi_{min} = \int_{t_{min}}^{t_{max}} \frac{LR_E}{(V_E)_{\varphi}}\, d\varphi \qquad (3.19)$$

where $(V_E)_{\varphi}$ is the azimuthal velocity along the convection trajectory. The expression of $(V_E)_{\varphi}$ as a function of electric potential distribution $\phi(L, \varphi)$ and equatorial magnetic field intensity $B_{eq}(L,\varphi)$ is given in the Appendix C. For known analytical models of $\phi(L,\varphi)$ and $B_{eq}(L,\varphi)$ the values of $(V_E)_{\varphi}$ can be determined at each points (L,φ). In the case of the corotation electric field $(V_E)_{\varphi} = \frac{\Omega_E}{2\pi} LR_E$ and $\varphi_{min} - \varphi_{max} = \frac{2\pi}{\Omega_E}(t_{max} - t_{min})$.

The factor 2 in front of the integral in eq. (3.18) comes from the fact that magnetic flux tubes are filling up from both hemispheres. The upward flux $F_{\parallel}$ of ions ranges between zero and the maximum Polar Wind flux :

$$(F_{\parallel})_{PW} = \frac{1}{4} N_o C_{th} \tag{3.20}$$

(Lemaire, 1972) where N_o is the exobase density and c_{th} the average thermal ion speed at the altitude of the exobase. For H^+ ions

$$C_{th,H^+} = (8 \ k \ T_{H^+}/\pi m_H)^{1/2} \tag{3.21}$$

When the plasma is distributed according to the Exospheric Equilibrium (EE), the equatorial density is small and $F_{\parallel}$ can be approximated by eq. (3.20). On the contrary when the plasma is almost in diffusive equilbrium (i.e. when the equatorial density is maximum) the net field aligned diffusion flux $F_{\parallel}$ must vanish. In all intermediate cases, when the equatorial plasma density $n_{eq}(L)$ ranges between the minimum EE value and the maximum DE density $n_{eq}^{DE}(L)$, a useful approximation for $F_{\parallel}$ is

$$F_{\parallel} = \frac{1}{4} N_o C_{th} \left[1 - \frac{n_{eq}(L)}{n_{eq}^{DE}(L)}\right] \tag{3.22}$$

with

$$n_{eq}^{DE}(L) = N_o \ e^{-\psi_{eq}} \ . \tag{3.23}$$

It can be verified that $F_{\parallel} = 0$ for $n_{eq} = n_{eq}^{DE}$, and, that $F_{\parallel}$ is almost equal to the maximum Polar Wind value given by eq. (3.20) when n_{eq} is close to the small value corresponding to Exospheric Equilibrium (n_{eq}^{EE}).

Equation (3.18) can also be transformed into

$$N'_T(L_{max}) \cdot \left[1 - \frac{N'_T(L_{min})}{N'_T(L_{max})}\right]$$

$$= 2\int_{\varphi_{min}}^{\varphi_{max}} \frac{N_o}{4}\, C_{th} \cdot \left[1 - \frac{n_{eq}(L)}{n_{eq}^{DE}(L)}\right] \cdot S_o\, \frac{R_E L}{(V_E)_\varphi}\, d\varphi \qquad (3.24)$$

The bracket in the left hand side of eq. (3.24) represents the fraction of the total content of particles at dusk which is dumped into the ionosphere by squeezing of the magnetic flux tube in the post-dusk sector. This fraction is equal to zero when the post dusk transformation is conserving the total number of particles in the flux tube. However, when the transformation is isothermal we have estimated above that as much as 86% has to be dumped between 1800 LT and 0130 LT along the drift path.

On the other hand for $N_o = 10^3$ cm^{-3}, $T_{H^+} = 3000$ K, it results from eqs. (3.21), (3.20) and (3.4) that $C_{th} = 8$ km s^{-1}, $F_{\parallel PW} = 2 \times 10^8$ ions/cm^{2}s and $S_o = 2.5 \times 10^8$ cm^2. Since $n_{eq}(L) << n_{eq}^{DE}(L)$, $F_\parallel \cong F_{\parallel PW}$; with $t_{max} - t_{min} \cong 25$h the right hand side of eq. (3.18) is equal to 9×10^{21} ions/Wb. From eq. (3.18) we find $N'_T(L_{max}) = 9 \times 10^{21} : 0.86 = 10^{22}$ ions/wb. This is 30 times smaller than the maximum DE value of $N_T(L)$ at L = 8 (see fig. 10).

3.4. Variation of the equatorial temperatures as a result of the post dusk contraction of plasma elements

A. We have seen that the adiabatic contraction and squeezing of plasma elements in the post-dusk local time sector produces the observed enhancement of equatorial densities in the night local time sector. This adiabatic compression of magnetic flux tubes has also other consequences : the enhancement of the perpendicular and parallel plasma temperatures in the outer part of the plasmasphere, where the drift trajectories have the largest asymmetries i.e. where L_{max} is most different from L_{min}.

As a consequence of the adiabatic conservation of the magnetic moment

$$\mu = \frac{mv_{\perp}^{2}}{2B} \tag{3.25}$$

the perpendicular kinetic energy increases when a charged particle drifts into a region of higher field intensity. This adiabatic variation of the perpendicular kinetic energy of all charged particles is similar to the betatron acceleration process. The grad-B drift velocity which is proportional to the perpendicular kinetic energy of the particles is small for thermal (0.3 eV) ions and electrons compared to the $\underline{E} \times \underline{B}/B^2$ electric drift velocity. However, as a consequence of this small additional drift the electrons and ions are slightly deviating from equipotential trajectories : They move from one equipotential surface to another and lose electric potential energy. The loss of electric potential energy is equal to the kinetic energy gained by the particles.

Let us assume that the mean perpendicular kinetic energy of the ions and electrons of a plasma element at L_{max} = 8 and φ_{max} = 1800 MLT is equal to 0.26 eV. This corresponds to a perpendicular temperature of 3000 K. When all these particles are drifting from L_{max} = 8 at φ_{max} = 1800 MLT to L_{min} = 4.8 at φ_{min} = 0130 MLT, their mean energy and their perpendicular temperature is increased by a factor $B_{eq}(L_{min})/ B_{eq}(L_{max})$ = 4.63 :

$$\frac{[\frac{1}{2}\, m\overline{v_{\perp}^{2}}]_{L_{min}}}{[\frac{1}{2}\, m\overline{v_{\perp}^{2}}]_{L_{max}}} = \frac{T_{\perp}(L_{min})}{T_{\perp}(L_{max})} = \frac{B_{eq}(L_{min})}{B_{eq}(L_{max})} = \left(\frac{L_{max}}{L_{min}}\right)^{3} \tag{3.26}$$

As a consequence of the adiabatic contraction of magnetic flux tubes, the perpendicular temperature of the plasma is increased from 3000 K (0.26 eV) at 1800 MLT and L = 8 to 14,000 K (≅ 1 eV). The larger the ratio of L_{max}/L_{min}, the larger is the perpendicular temperature in the post-midnight local time sector.

In the inner plasmasphere, below L = 3, the drift path of plasma elements is almost symmetric ($L_{max} \cong L_{min}$), while closer to the plasmapause the trajectories of cold plasma elements become more asymmetric and quasi-adiabatic contraction in the post-dusk sector leads to larger perpendicular temperatures in the night-time sector.

At the onset of major geomagnetic perturbations when the drift path of plasma elements is most asymmetric this temperature enhancement in the nightside should be most important.

B. The parallel temperature is also enhanced as a result of the post-dusk magnetic field line contraction. Indeed, when the field variations are small during a particle bounce period, the second adiabatic invariant of motion

$$J = 2 \int_{l_1}^{l_2} m \, v_{\parallel} \, d\ell \qquad (3.27)$$

is conserved (Northrup and Teller, 1960; Alfvèn and Fälthammar, 1963); The integral is taken along the magnetic field line between two conjugate mirror points at distances ℓ_1 and ℓ_2.

As a consequence of the $\underline{E} \times \underline{B}/B^2$ drift velocity, the grad-B and curvature drifts trapped ions and electrons are forced to bounce up and down along magnetic field lines which become shorter as L decreases from L_{max} to L_{min}. The distance between magnetic mirror points decreases with L. Since J is conserved the amplitude of parallel velocity ($v_{\parallel}$) varies roughly as L and the parallel temperature $T_{\parallel}(L)$ varies then as L^2 (Northurp, 1963).

Let us assume that the parallel temperature $T_{\parallel}(L_{max})$ at 1800 MLT and $L_{max} = 8$ is equal to 3000 K. When the plasma element has drifted to 0100 MLT and $L_{min} = 4.8$, the parallel temperature has increased by a factor $(L_{max}/L_{min})^2 = 2.8$ i.e.

$$\frac{\left[\frac{1}{2}\, m\overline{v_{\parallel}^2}\right] L_{min}}{\left[\frac{1}{2}\, m\overline{v_{\parallel}^2}\right] L_{max}} = \frac{T_{\parallel}\ (L_{min})}{T_{\parallel}\ (L_{max})} = \left(\frac{L_{max}}{L_{min}}\right)^2 \tag{3.28}$$

The final parallel temperature in the post-midnight local time at L = 4.8 is increased up to 8300 K by the adiabatic transformation which can be compared to the Fermi acceleration process. This is a factor 1.6 (i.e. L_{max}/L_{min}) smaller than the perpendicular temperature enhancement by the betatron acceleration process discussed above. This indicates that the perpendicular temperature of plasmaspheric ions can become higher than the parallel temperature. As a consequence "pancake" like pitch angle distributions should be observed, as they are indeed, in the outermost region of the plasmasphere (Horowitz and Chappell, 1979; Chappell et al. 1982; Horowitz et al., 1981a, 1981b, 1983; Chappell, 1982).

C. However, when the "initial" parallel temperature $T_{\parallel}(L_{max})$ at φ_{max} is larger than the perpendicular temperature $T_{\perp}(L_{max})$, as in EE models (see Lemaire, 1976b), the final anisotropy at φ_{min} and L_{min} may remain that corresponding to an elongated "cigar-shaped" pitch angle distribution. A preference for this latter type of distribution should be observed in largely depleted flux tubes immediately after a substorm during the recovery phase. On the contrary, the former type of temperature anisotropy should be observed later on in the recovery phase, when the "initial" pitch angle distribution eventually contains a significant amount of trapped particles.

The ratio of the perpendicular temperature and parallel temperature at L_{min} and at L_{max} are related by

$$\left(\frac{T_\perp}{T_\parallel}\right)_{L_{min}} = \left(\frac{T_\perp}{T_\parallel}\right)_{L_{max}} \cdot \frac{L_{max}}{L_{min}} \tag{3.29}$$

when the post-dusk transformation of the plasma elements is a quasi-adiabatic one i.e. conserving the first and second invariant of motion of charged particles trapped in an inhomogeneous magnetic field. The larger the dawn-dusk asymmetry of the drift trajectory the larger is L_{max}/L_{min} and the larger is the change of the anisotropy of the pitch angle distribution. This is why not only the highest temperature but also the largest anisotropies in the ion pitch angle distributions are expected in the nightside during periods of high geomagnetic activity when the dawn-dusk component of the magnetospheric electric field distribution is largest. Indeed, it is then that the electric equipotential surfaces have the largest dawn-dusk assymmetry and that, according to eq. (3.29), the largest temperature anisotropies should eventually build up near 0130 LT.

D. It should be mentioned, however, that the post-dusk transformation of plasma elements is not exactly adiabatic because of Coulomb collisions and possibly other irreversible processes (e.g. wave-particle interactions). As a consequence, the eqs. (3.25) to (3.27) based on the assumption of an ideal adiabatic transformation should be considered only as an indicative first order approximation.

The validity of this approximation depends on the time lapse between t_{max} and t_{min} compared to the average collision time given in Table F1in Appendix F. Since the convection velocity is larger in the nightside than in the dayside sector, the post-dusk contraction and squeezing rate is closer to adiabaticity than the slower expansion and dilatation of magnetic flux tubes along the dayside portion of their closed trajectory. Moreover, fresh cold plasma is pouring into the dayside flux tubes out from the ionosphere. This cyclic quasi-adiabatic compression and heating followed by a slower expansion and flux tube refilling in the dayside should result in a net enhancement of the average plasmaspheric temperatures. The final plasma temperature averaged over a whole trajectory, depends on several factors : the amplitude of the rate of the compression and dilation, the collision rate and the rate at which heat can be exchanged between the warm plasma in outer plasmasphere and the cold ionospheric plasma.

We will not calculate here the final thermal structure in the plasmasphere resulting from these successive contractions and slower dilatations of magnetic flux tubes. But even without detailed calculations, it can be concluded that this average plasma temperature is expected to increase with radial distance in the plasmasphere. Indeed, the asymmetry of the drift trajectories of plasma elements and the amplitude of the post-dusk compression increase with radial distance. An increase of ion temperatures with radial distance, up to 100,000 K at the plasmapause, has been deduced from the observations (see Gringauz and Bezrukikh, 1976; Gringauz, 1976, 1983; Horowitz and Chappell, 1979; Baugher et al., 1980; Horowitz et al., 1981a, 1981b; Decréau et al., 1982; Chappell, 1982).

Another source of plasma heating in the outer zone of the plasmasphere is dissipation of energy of the ring current as it decays during the recovery phase of a magnetic storm (Galeev, 1975), and, as ions from the plasmasphere are energized up to ring current energies (Balsiger et al., 1980 and Balsiger, 1981). The relative importance of these additional sources compared to that which is described above, depends on the efficiency of wave-particle interactions mechanisms proposed. A quantitative model calculation of these heating processes, including the new one suggested above, is needed before a final answer can be given to this interesting question of the origin of the "warm" outer zone of the plasmasphere. But such a simulation is beyond the grasp of the present study.

3.5. Simulation of the drift path of background plasma elements in the plasmasphere

Let us consider a field aligned plasma element at L = 8 and 1800 LT whose initial equatorial density is equal to 0.8 cm^{-3} corresponding almost to the value of the exospheric equilibrium model for $\Omega = \Omega_E$ (see fig. 7 or 8). The radial and azimuthal components of the convection velocity

$$\underline{V}_E = \underline{E} \times \underline{B}/B^2 \qquad (3.30)$$

can be determined at any point in the magnetosphere for a given electric field model ($\underline{E}$) and magnetic field model ($\underline{B}$) (see Appendix C).

The magnetic field model which will be used in the following simulation is McIlwain's M2 model described in Appendix A. This empirical B-field distribution takes into account magnetic field measurements at geostationary orbit (i.e. near L = 6.6) and is therefore appropriate to model the equatorial magnetic field intensity up to the outer edge of the plasmasphere.

The empirical electric field model E3H has also been deduced by McIlwain (1974) from ion and electrons spectrograms collected along the orbit of the geostationary satellite ATS 5, and, is therefore relevant also to model the plasmasphere and plasmapause region. Furthermore, since there are no singular points in this analytical model, it is also very suitable for numerical integration.

According to McIlwain (1974) these electric and magnetic field models represent satisfactorily the large scale distribution of $\underline{E}$ and $\underline{B}$ in the magnetosphere when geomagnetic activity is steady and low : i.e. for K_p ranging between 1 and 2. Lemaire (1982) has verified that under similar geomagnetic conditions the E3H and M2 models also fit the particles fluxes collected at the longitude of another geostationary satellite : ATS 6. The E3H electric potential distribution $\phi(L,\varphi)$ is described in Appendix B. The equatorial cross sections of the E3H equipotential surfaces are shown by the dashed lines in fig. 4.

The equatorial electric field and magnetic field intensities are computed in Subroutines called KZSET, BRG and EVBC in our numerical program (see Appendix H).

The drift velocities of cold background plasma elements are tangent to these equipotential curves since according to eq. (3.30), $\underline{V}_E$ is perpendicular to $\underline{\nabla}\phi$. Therefore, the streamlines of the background plasma are parallel to the equipotential lines of the stationary E-field distribution. The equations of motion of an equatorial plasma element are

$$\frac{dR}{dt} = (V_E)_R \tag{3.31}$$

$$R\,\frac{d\varphi}{dt} = (V_E)_\varphi \tag{3.32}$$

where R is the radial distance expressed in Earth's radii (R_E); φ is the azimuthal angle in local time (LT) hours ($\varphi = 0$ at local midnight); t is Universal Time (UT) in hours; $(V_E)_R$ and $(V_E)_\varphi$ are computed in Earth radii per hour UT (R_E/h) in the subroutine DBPDD (see Appendix H). These velocity components are functions of L which are given in the Appendix E. The expressions given in the Appendices A and B respectively for the M2 and E3H models, have been used below to calculate by numerical integration of eqs. (3.31) and (3.32) the positions R(t) and φ (t). The standard HAMIN method of integration is used in our computer program (see Appendix H).

The equatorial convection velocities calculated with the E3H + M2 models are illustrated in fig. 11 in a fixed frame of reference

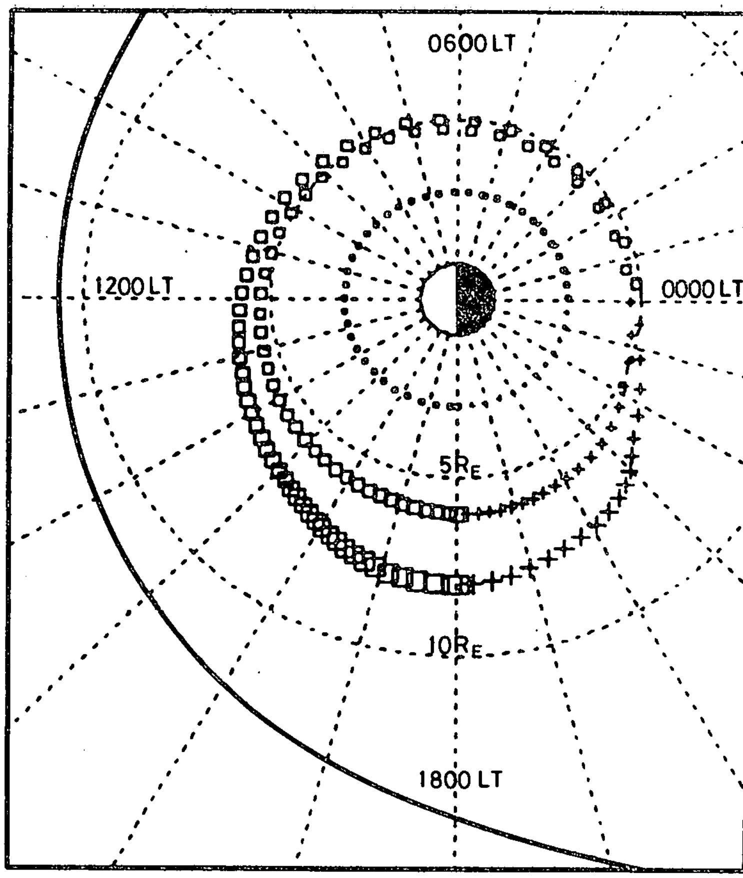

Fig. 13.- Drift path of three background plasma elements in the E3H and M2 electric and magnetic field distributions described in the Appendices A and B. The series of symbols indicate the successive positions each half hour interval of time. The size of these symbols changes along the drift path to indicate the variation of the equatorial cross section (S_{eq}) of the plasma element : $S_{eq}(L,\varphi)$ is inversely proportional to the equatorial magnetic field intensity $B_{eq}(L,\varphi)$. The type of symbols representing the plasma element changes when it traverses the midnight meridional plane (φ = 0000 LT, 2400 LT...). These closed drift trajectories are parallel to equipotential lines of the E3H electric field shown by dashed lines in fig. 4. The radial distances for these three trajectories are maximum in the dusk local time sector, respectively at 8 R_E, 6 R_E and 3 R_E. Note the large dawn-dusk asymmetry of the two outermost trajectories. The innermost plasma element is almost corotating with a period of revolution of 24 hours. The orbital period of the outermost one is 34 hours. The squeezing of magnetic flux tubes in the post-dusk sector can be appreciated from the decreasing sizes of the symbols.

and in fig. 12 in a corotating frame of reference. Note that for $L < 3$ the convection velocities are almost equal to the corotation speed (Ω_E R). Significant departures from corotation are observed at larger radial distances in the night-side. For instance in the post-midnight local time sector the eastward convection velocity exceeds the corotation speed by a factor 2 at $L = 4.8$ and 0130 LT. Between 0830 LT and 2230 LT atmospheric drag is likely to be responsible for the reduced rotational speed (Baumjohann et al., 1985).

Successive positions of three background plasma elements which were initially located respectively at $R = 8\ R_E$, $6\ R_E$ and $3\ R_E$ in the dusk sector, are given in fig. 13 by the three series of symbols (+ and □). Each of these positions are separated by half an hour drift time. It can be verified that the positions of these outermost series of symbols coïncide with the E3H equipotential line $\phi = -8$ kV shown in fig. 4. The distances between successive half-hour positions are inversely proportional to the convection velocity (V_E). It can be seen that along the post-dusk portion of this trajectory the convection velocity is significantly enhanced. Along the dayside and dusk portions of the two outermost trajectories the spacing between successive positions is smaller, indicating the slowing down of plasma elements. The enhanced convection velocity in the post-midnight sector indicates that magnetospheric convection is driven there by magnetospheric plasma streaming sunward down the magnetotail.

The size of the squares in fig. 13 is inversely proportional to the equatorial magnetic field intensity (B_{eq}) and indicates therefore how the equatorial cross-section of a plasma element varies along its trajectory when its magnetic flux is conserved (eq. 3.1). The diminishing size of the symbols along the post-dusk portion of the trajectory illustrates the contraction or squeezing of the plasma element as it drifts toward local midnight and closer to the Earth. The consequences of this flux tube contraction and squeezing on the equatorial content, on the perpendicular and parallel temperatures have already been discussed above in sections 3.1, 3.2, 3.3 and 3.4.

The innermost plasma element drifts around the Earth's in 24 hours along an almost circular trajectory. When K_p is less than 2, corotation prevails up to L = 4. The second plasma element orbiting at intermediate radial distances circulates around the Earth in 32 hours while the outermost one takes 34 hours to complete a revolution.

It is evident from these simulations that the trajectories of plasma elements located in the inner plasmasphere are nearly symmetric, while those circulating in the outermost part of the plasmasphere become increasingly asymmetric. We have already discussed the consequences of this increasing geometrical asymmetry for the total flux tube content (N_T), as well as for the average ion temperatures ($T_\perp$ and $T_\parallel$) and for temperature anisotropy ($T_\perp / T_\parallel$) (see sections 3.2 and 3.4).

From the numerical calculations in the following paragraphs, we will verify that the amplitude of the diurnal variations of the equatorial plasma density is indeed enhanced when the asymmetry of the drift trajectory is enlarged.

3.6. Simulation of the diurnal variation of the equatorial density and refilling of magnetic flux tubes

The rate of change of the equatorial plasma density is given by

$$\frac{dn_{eq}}{dt} = - \frac{n_{eq}}{V} \frac{dV}{dt} + \frac{S_o F_\parallel}{V} \tag{3.33}$$

where the last term represents the contribution due to the field aligned ion flow diffusing in or dumped out of a 1 Weber flux tube whose cross section (S_o) at 1000 km altitude is given by eq. (3.4) and whose volume (V) is given by eq. (3.5). Different expressions will be taken for the field aligned flux of ions ($F_\parallel$ in particles/cm^2 s) in the different simulations presented below.

The second term in eq. (3.33) represents the rate of change due to the expansion and contraction of the volume of the plasma element assuming its total content is conserved. The time derivative of the volume V(L) in this equation can be deduced from eq. (3.5)

$$\frac{d \ln V}{dt} = \left(\frac{1}{2L} + \frac{1}{2L - 2} + \frac{6 + 16L + 48L^2}{5 + 6L + 8L^2 + 16L^3} \right) \frac{dL}{dt} \qquad (3.34)$$

In the equatorial plane L can be replaced by R (expressed in Earth radii) and dL/dt is then equal to dR/dt given by eq. (3.31).

The right hand side of eq. (3.33) is a function of the unknown variables R, φ, and n_{eq}. It is calculated in the subroutine DBPDD of our numerical computer program (see Appendix H). The simultaneous numerical integration of eqs. (3.31), (3.32) and (3.33) is carried out by the standard HAMIN method. The initial conditions are determined in the subroutine TRAJB. The radial distance (R), the local time angle (φ) and the equatorial density (n_{eq}) are calculated as functions of Universal Time (t) and printed in the subroutine OUTP (see Appendix H).

A. Fig. 14 shows the diurnal variation of the equatorial density as a function of LT for three plasma elements orbiting in the E3H + M2 electric and magnetic field distributions along the three trajectories illustrated in fig. 13. The initial equatorial densities at 1800 LT are respectively equal to $n_{eq}(0) = 0.8 \text{ cm}^{-3}$ at $R_o = 8$, $n_{eq}(0) = 25 \text{ cm}^{-3}$ at $R_o = 6$, and $n_{eq}(0) = 410 \text{ cm}^{-3}$ at $R_o = 3$. The variable size of the symbols indicates again as in fig. 13 the variation of the equatorial cross section of the plasma element assuming the conservation of its magnetic flux ($S_{eq}.B_{eq} = c^{st}$): the larger the size of these symbols, the larger is S_{eq}.

In this first series of simulations we have assumed that there is no field aligned ion flow nor upward nor downward, the magnetic

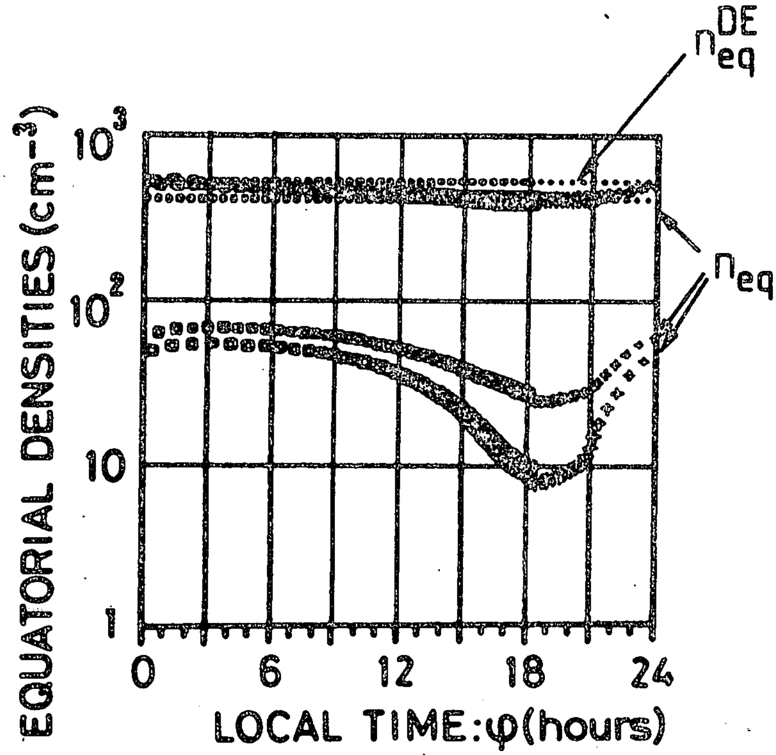

Fig. 14.- Equatorial density (n_{eq}) in three plasma elements drifting in the E3H + M2 electric and magnetic field distributions along their trajectories illustrated in fig. 13. The lowermost series of symbols indicate the successive values of n_{eq} as a function of local time (φ) for every half hour interval of Universal Time (t). The size of these symbols changes along the closed drift path to indicate the variation of the equatorial cross section (S_{eq}) of the plasma element. The type of symbols changes when the plasma element traverses the midnight meridional plane (φ = 0000 LT, 2400 LT...). The minimum equatorial density is located in the dusk local time sector where n_{eq} is respectively equal to 8 cm^{-3}, 25 cm^{-3} and 410 cm^{-3} in the three plasma elements. In this simulation it has been assumed that there is no field aligned flux tube refilling, i.e. $F_{\parallel} = 0$ in eq. (3.33). As a consequence of the conservation of the total number of particles in the squeezed magnetic flux tubes, the density increases in the post-dusk sector and reaches a maximum value in the post-midnight local time sector. The upper most symbols represent the equatorial density in the magnetic flux tubes if Diffusive Equilibrium (DE) would be achieved.

flux tube. In other words we have ignored here the effect of flux tube refilling by assuming $F_{\parallel} = 0$ in eq. (3.33). It can be seen that the equatorial density has then a periodic diurnal variation and that n_{eq} is minimum near dusk (1800 LT). As a result of the post-dusk adiabatic flux tube contraction, the equatorial density increases and becomes maximum in the post-midnight sector at (φ_{min}, L_{min}) where the volume V(L) has a minimum value. Note also that the amplitude of the diurnal variation of $n_{eq}(t)$ is largest for the plasma element circulating along the most distant drift trajectory, as already discussed in section 3.1; this results from the larger dawn-dusk asymmetry of the outermost trajectories.

The Diffuse Equilibrium values for the equatorial density (n^{DE}_{eq}) given by eq. (2.19) are also shown in the upper part of fig. 14. Note that n^{DE}_{eq} would be the equatorial plasma density in a flux tube if it would be saturated with plasma in isothermal and diffusive equilibrium with the ionospheric plasma. These DE values represent a sort of upper limit for n_{eq}. Indeed, when n_{eq} exceeds this limit, $F_{\parallel}$ becomes negative in eq. (3.33) (see eq. 3.22). The excess density flows then back to the ionosphere.

B. In the second series of simulations let us now allow ions to flow out of the ionospheric reservoir and refill the depleted plasma elements. Instead of forcing $F_{\parallel}$ to be equal to zero as in the previous simulation, we are now assuming that the field aligned flux of ions in eq. (3.33) is given by eq. (3.22) with $N_o = 10^3$ cm^{-3} T_o = 3000 K and $F_{\parallel\,PW} = 2 \times 10^8$ ions/cm^2/s. The result of the numerical integration of eqs. (3.31), (3.32) and (3.33) is illustrated in figs. 15a, b and c for three plasma elements drifting again on the trajectories illustrated in fig. 13. The numerical integration has been carried out from φ = 1800 LT up to φ = 1800 + 5 x 2400 LT corresponding to 5 consecutive revolutions around the Earth. The time to complete these 5 revolutions is 172 hours (7.17 days) for the outermost plasma element (fig. 15a); it is 155 hours (6.46 days) for the intermediate one (fig. 15b), and, 120 hours (5 days) for the innermost plasma element (fig. 15c). At t = 0

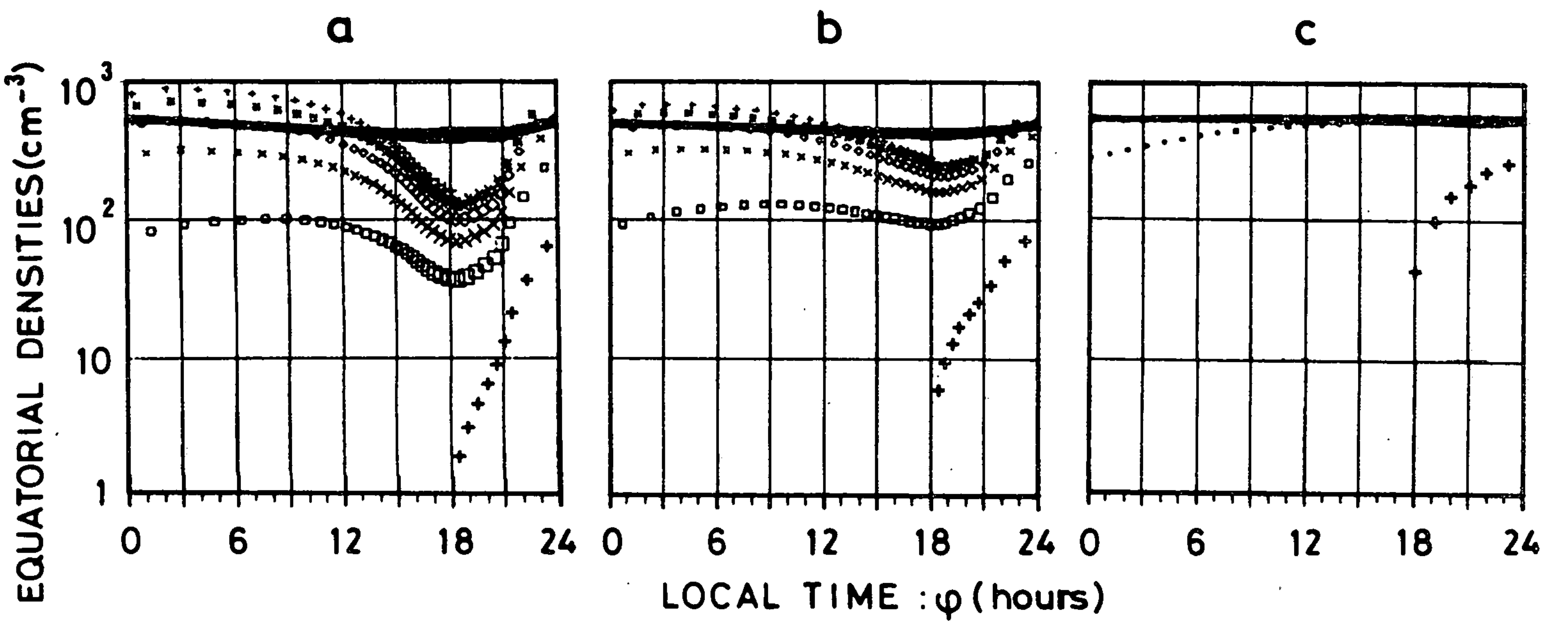

Fig. 15.- Equatorial density (n_{eq}) in three plasma elements drifting in the E3H + M2 electric and magnetic field distribution along the trajectories illustrated in fig. 13. The series of symbols indicate the successive values of n_{eq} as a function of local time (φ) for every hour interval of Universal Time (t). The size of these symbols changes along the closed drift path to indicate the variation of the equatorial cross section (S_{eq}) of the plasma element. The type of symbols representing the equatorial density changes each time when the plasma element traverses the midnight meridional plane (φ= 0000 LT, 2400 LT, 4800 LT,..). The solid line in each panel gives the equatorial density in the magnetic flux tube if Diffusive Equilibrium (DE) would be achieved. In this simulation the refilling flux $F_{\|}$ is given by eq. (3.22) : the ions flow upwards as long as n_{eq} is smaller than the DE value; (a) the left hand side panel illustrates the slow refilling rate superimposed on a large amplitude diurnal variation for a plasma element whose initial equatorial density is 0.8 cm^{-3} at L = 8 and 1800 LT; (c) n_{eq} = 41 cm^{-3} at t = 0 and L = 8, and 1800 LT (right hand side panel); (b) 2.5 cm^{-3} at t = 0 and at the same radial distance in the duskside. In all these simulations a stationary regime is obtained after a characteristic refilling time which increases with the radial distances of the drift trajectories.

the plasma elements were located at dusk respectively at $R = 8\ R_E$, $6\ R_E$ and $3\ R_E$; their initial densities were respectively $0.8\ cm^{-3}$, $2.5\ cm^{-3}$ and $41\ cm^{-3}$.

It can be seen from fig. 15c that the plasma element which corotates deep inside the plasmasphere at $R \cong 3\ R_E$ fills up very quickly. Indeed after one day the equatorial density has almost reached a stationary level close to D.E. The amplitude of the diurnal variation superimposed on the exponential refilling is relatively small : in the final stationary regime the maximum equatorial density is $581\ cm^{-3}$ at 1930 LT and the minimum value is $534\ cm^{-3}$ at 0220 LT. As a consequence of their small volumes magnetic flux tubes at low L-values are refilled in a short period of time. The small amplitude diurnal variation in the final stationary regime is a consequence of the small asymmetry of the drift trajectories at $L < 4$.

However, for the plasma elements which drift at larger radial distances along trajectories which are much more asymmetrical, it can be seen from figs. 15a and b, that the refilling time necessary to reach the final stationary regimes is longer than 7 days for the intermediate orbit at $L \cong 6$ and more than 8 days for the outermost trajectory at $L \cong 8$; these characteristic refilling times are comparable to the values deduced by Park (1970, 1974) from whistlers observations.

Furthermore, it can be seen that the upper limit for n_{eq} exceeds the diffusive equilibrium (DE) value as a result of the flux tube contraction in the post-dusk sector; n_{eq} has a broad maximum value ($\sim 930\ cm^{-3}$) at $L = 4.8$ in the post-midnight sector. On the contrary at dusk, where the trajectory has its maximum extent, the minimum equatorial density in the final stationary regime is equal to 134 $ions/cm^3$ at $L = 8$. This is a factor 4 smaller than the corresponding DE value at $L = 8$ i.e. $n_{eq}^{DE} = 455\ ions/cm^3$. Although the calculated values are minimum at dusk, as observed by Chappell et al. (1970a, b), they are still a factor 4 or 5 too high compared to the observed values at dusk. In order to reduce the equatorial density level at dusk one may assume that the plasmasphere is continously expanding like the solar corona, and that this continuous radial expansion forms at large radial distances a "plasmaspheric wind" similar to the solar wind. Indeed, as a consequence of such a radial plasmaspheric wind, the equatorial density would decrease faster with L then the DE value corresponding to hydrostatic equilibrium. From the equation of conservation of the total plasma content in flux tubes expanding outwardly in a dipole magnetic field, it results that the equatorial background (BG) density distribution should vary as L^{-4} : i.e. as the inverse of the flux tube volume V :

$$n_{eq}^{BG}(L) = D/L^4 \tag{3.35}$$

Such an L^{-4} equatorial density profile is often observed in the plasmasphere. The constant D in eq. 3.35 can be determined empirically from the observations which show that the background plasma density at L = 4 is often equal to 500 ions/cm^3. It results from eq. (3.35) that D = 1.28×10^5 ions/cm^3/R_E^4.

C. Considering now that the empirical density distribution (3.35) is a maximum mean value averaged over all local time angles, we have assumed, in the following third series of simulations, that the field aligned ion flux $F_{\parallel}$ in eq. (3.33) reverses sign when n_{eq} exceeds $n_{eq}^{BG}(L)$. Instead of using eq. (3.22), we assume now that $F_{\parallel}$ is given by

$$F_{\parallel} = \frac{1}{4} N_o \, C_{th} \left(1 - \frac{n_{eq}}{n_{eq}^{BG}}\right) \tag{3.36}$$

Figs. 16a, and b give the result of the numerical integration of equation (3.33) along the two outermost drift trajectories shown in fig. 13. The final stationary regime is reached much faster than in fig.

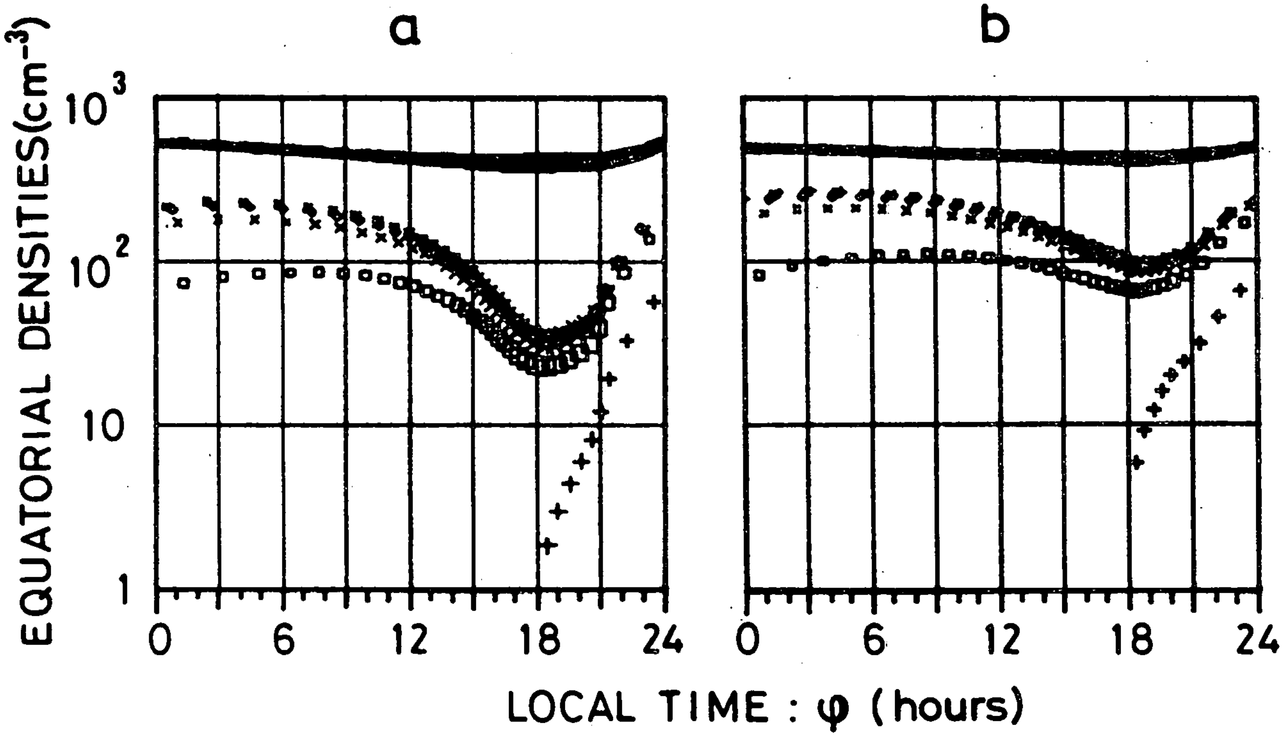

Fig. 16.- Equatorial density (n_{eq}) in a plasma element circulating along the two outermost trajectories illustrated in fig. 13 for the same initial conditions at 1800 LT and L = 8 (panel a) and L = 6 (panel b) as in fig. 15. The refilling flux $F_{\|}$ is given by eq. (3.36) : the ion flux $F_{\|}$ is upwards as long as n_{eq} is smaller than the background density $n_{eq}^{BG}(L)$ given by eq. (3.35). When n_{eq} becomes larger than n_{eq}^{BG}, the field aligned flux reverses direction. The type and size of symbols are the same as in figs. 14 and 15. The values of the equatorial densities in the stationary regime are lower than those obtained in fig. 15.

15a and b. The minimum densities are obtained again in the dusk local time sector where the flux tube has a maximum volume. The value of the minimum density is 33 ion/cm^3 at L = 8, and, 97 ion/cm^3 at L = 6. It can also be verified that these minimum equatorial density values vary approximately as L^{-4} in agreement with eq. (3.35). The values of $n_{eq}(L_{max})$ correspond better than those obtained in fig. 14 with those generally observed at these radial distances in the afternoon dusk sector (Chappell et al. 1970ab, b; Decréau, 1983; Higel and Wu, 1984).

The maximum densities $n_{eq}(L_{min})$ along the outermost trajectory is 237 ions/cm^3 at L = 4.8. The amplitude of the diurnal variation measured by $n_{eq}(L_{min})/n_{eq}(L_{max})$ is equal 7.0 for the outermost trajectory. It can be verified that this amplitude increases with radial distance because the asymmetry of the trajectories (measured by L_{max}/L_{min}) increases also with L.

D. This last series of simulations based on eq. (3.36) fit the observed local time (diurnal) and radial density distributions much better than the previous one based was based on eq. (3.22). Therefore the former dynamical simulation model can be used to calculate plasma density distribution in the plasmasphere under prolonged steady state conditions. The equilibrium density distribution $n_{eq}(L, \varphi)$ attained in the stationary regime is independent of the initial densities in each of the plasma elements. It has already been shown in section (3.1) that the local time variation of $n_{eq}(L, \varphi)$ is a sensitive function of the dawn-dusk asymmetry of the plasma streamlines i.e. of the equipotential surfaces of the magnetospheric electric field distribution. The radial dependence of $n_{eq}(L, \varphi)$ depends very much on the assumption made to limit the field aligned plasma flows. Indeed very different results have been obtained in figs. 14, 15 and 16 with different expressions for $F_{\parallel}$: $F_{\parallel}$ was chosen to be equal to zero in fig. 14, while it was given by eq. (3.22) and by eq. (3.36) respectively, in figs. 15 and 16.

Although the results obtained with eq. (3.36) simulate rather well the observations, it should be pointed out, however, that the equation (3.36) for $F_{\parallel}$ does not limit the total particle content in flux tubes as we described it in section 3.3. Indeed, it was shown in section 3.3 that the total number of particles squeezed out of a flux tube in the post-dusk must approximately be equal to the total number of particle recombining in the night side ionosphere. To take into account the regulatory effects of recombination in the nightside ionosphere which is a sink of particles, is a more demanding problem and has not yet been incorporated in our numerical program. With faster computers and additional modeling efforts it is possible, however, to simulate the coupling between the ionosphere and plasmasphere more accurately. We plan to undertake this new modelling effort in the future.

4. THE PLASMAPAUSE (PP)

4.1. Historical background

A. At the beginning of this century it was considered that the magnetic field above the Earth's atmosphere could be approximated by an ideal dipole field. But this ideal mathematical representation of the extended geomagnetic field distribution was found insufficient, already at the beginning of this century, when Störmer (1907) inferred the existence of a temporary ring current encircling the Earth at great equatorial distances.

Ground based surveys also indicated that the distribution of the surface magnetic field is far more complex than a simple dipole. High order spherical harmonic expansion series had to be introduced to give a more accurate representation of the Earth's surface magnetic field distribution (Chapman and Bartels, 1940; Cain, 1971).

Since 1960 satellites with magnetometers are prospecting the Earth's magnetic field in outer space. From such observations Ness et al. (1964) discovered for instance that high latitude geomagnetic field lines stretch far out from the Earth in the nightside forming a cometary-like magnetotail. To describe this and other non-dipole field perturbations, various empirical models have been proposed in terms of complex expansion series (McIlwain, 1972; Sugiura and Poros, 1973; Mead and Fairfield, 1975 and others; see also Walker, 1976, 1979, and Stern, 1976 for reviews).

B. A similar evolution, from the simplest idealized models to the more complex empirical ones, was also expected in modeling the magnetospheric electric field distribution. Surprisingly, however, in this area rather complex E-field models were proposed first by Axford and Hines (1961), Nishida (1966), Brice (1967). These first empirical models were based on observations. But basically for convenience and for the sake of simplicity, the more elementary and idealistic mathematical representation have been favoured by most theoreticians (Kavanagh, et al., 1968; Grebowsky, 1970, 1971; Chen and Wolf, 1972; Chen and Grebowsky, 1974; Volland, 1973, 1975; Rycroft, 1974; Stern, 1977; Grebowsky and Chen, 1976; Berchem, 1980; Berchem and Etcheto, 1981; Kaye and Kivelson, 1979). This has refrained, probably for more than a decade, the expected development of more complex and more realistic empirical geoelectric field model.

A recent analysis of GEOS 2 electric field measurements by Baumjohann et al. (1985) clearly indicates the limitations of simple analytical models and the need for more complex and of course less idealistic models for the E-field distribution in the magnetosphere based on direct observations.

C. Since 1966, most magnetospheric electric field modellers had been greatly influenced by the Brice's theory for the formation of the plasmapause. This theory is recalled in the Appendix G. Indeed, following a suggestion by Nishida (1966), Brice (1967) advanced the idea that the observed positions of the plasmapause coïncide with the Last Closed Equipotential (LCE) surface of the geoelectric field distribution. For instance Brice (1967) designed a "best estimate" electric field model whose Last Closed Equipotential precisely fitted the locations of the plasmapause knees derived by Carpenter (1966), and, illustrated in fig. 1c. The equatorial cross-section of the equipotential surfaces corresponding to this ad-hoc magnetospheric convection electric field model are reproduced in fig. 17. The position of the last closed equipotential in this theoretical model (shown by the closed dashed line in fig. 17) is determined by the existence and location of a stagnation point in the dusk local time sector. The electric field intensity is equal to zero at this stagnation point, and consequently the $\underline{E} \times \underline{B}/B^2$ convection velocity also vanishes there. This is why this mathematical point of singularity is called Stagnation Point (SP).

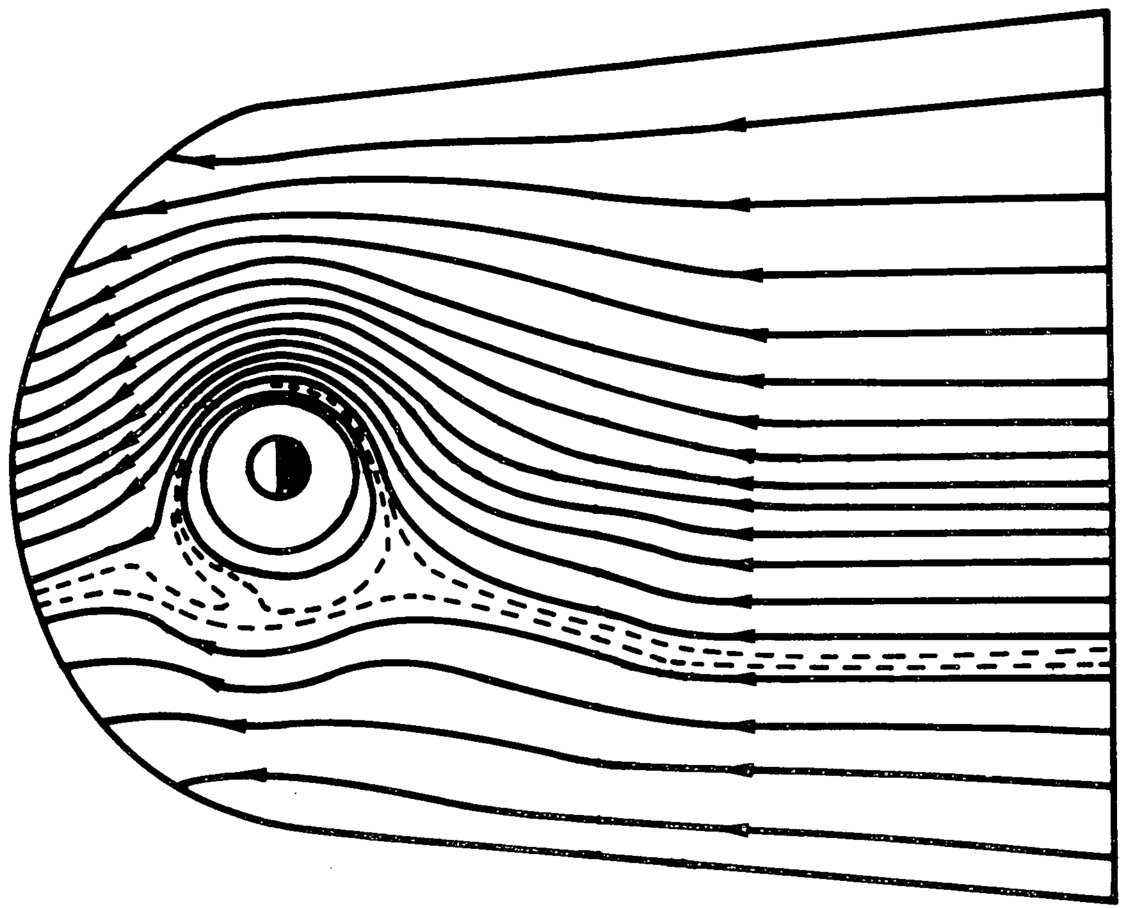

Fig. 17.- Equatorial cross section of equipotential surfaces corresponding to the "best estimate" geoelectric field models proposed by Brice (1967). The potential differences between solid lines are 3 kV. The dashed lines give intermediate equipotentials at 1 kV intervals. Equipotentials closed within the magnetosphere are inside the whistler knee. The last closed equipotential (dashed) gives the location of the knee observed by Carpenter (1966).

However, the existence of such a stagnation point, where equatorial plasma would indeed be stagnant for an extended period of time, has never been established from direct experimental observations in the equatorial plane. Nevertheless, most subsequent modelling efforts in the late 1960's and in the 1970's have been oriented toward ad-hoc magnetospheric electric field models which had the expected stagnation point in the dusk sector at the proper radial distance to fit the positions of the last closed equipotential with those of the observed plasmapause. Even numerical electric field models, like those produced by the Group of Rice University, have been influenced by the idea that the plasmapause surface should coïncide with the last closed equipotential of the magnetospheric electric field (Wolf, 1970, 1974; Jaggi and Wolf, 1973; Harel and Wolf, 1976; Harel et al., 1979, 1981).

Most other empirical electric field models like the E3 or E3H models (McIlwain, 1972, 1974) or Richmond's (1976) model which were deduced from observations, have been largely overlooked most likely because the expected stagnation point was missing in these empirical E-field models. This situation did not change when an alternative theory was proposed for the formation of the plasmapause where the whistlers knees had no longer to be assumed to coïncide with the last closed equipotential of the magnetospheric electric field (Lemaire, 1974, 1975, 1976a). This theory based on the mechanism of interchange motion is described in detail in the following sections. But let us already emphasize here, that it does not rely on the very existence of a point of singularity in the electric field model. As a consequence of this theory a plasmapause can be formed in the Earth's magnetosphere even when the E-field model has no stagnation point, as it is the case for instance in the corotation model, or in the E3H model which are both described in Appendix B.

Not only there is then no longer a need for a stagnation point in electric field models, but there are also additional reasons which led us to abandon the Brice's theory for the formation of the plasmapause.

These arguments indicating that the outer edge of the plasmasphere cannot be identified with the Last Closed Equipotential of the geoelectric field distribution are developed at the end of Appendix G.

4.2. Local dielectric and diamagnetic field perturbations

In chapter 3 we have discussed and simulated the drift motion of background plasma elements in given electric and magnetic fields produced by external sources. Indeed, the electric and magnetic fields acting on the ions and electrons contained in these plasma elements, are background fields caused by non-local electrical charge distributions and electrical current distributions. The small perturbations E- and B-fields produced in the vicinity of the dielectric-diamagnetic plasma elements have not yet been taken into account in the previous simulations. The effects of local charge densities and current distributions have neither been taken into account in the MHD theory for the formation of the plasmapause discussed in the Appendix G. But, as a result of charge separation and drift currents within plasma elements, the electric and magnetic fields inside and in their immediate vicinity can be quite different from the external background field described in the Appendices A and B. Indeed, the drift paths of the electrons and ions inside the plasma elements are determined by the actual electric and magnetic fields inside $\underline{E}_{in}$ and $\underline{B}_{in}$ which can differ significantly from the drift paths deduced in the framework of the ideal MHD theory. According to this theory, plasma elements drift with the velocity

$$\underline{V}_E = \frac{\underline{E} \times \underline{B}}{B^2} \tag{4.1}$$

where $\underline{E}$ and $\underline{B}$ are external background field distributions. However, unlike individual test particles which do not significantly perturb $\underline{E}_{ext}$ and $\underline{B}_{ext}$, a large collection of charged particles induce local and time dependent variations in these external fields which must be taken into account.

A. The magnetic perturbations are determined by diamagnetic currents, gradient-B or curvature currents which circulate inside the volume of these plasma elements or at their surface. These currents are driven by external forces or by gradients of the kinetic pressure, the magnetic pressure or by the curvature of magnetic field lines (Longmire, 1963). The amplitude of diamagnetic field perturbations depends on the values of β the ratio between the kinetic pressure ($\Sigma_i n_i k T_i$) and the magnetic pressure ($B^2/2\mu_o$). When the magnetic pressure is comparable to the kinetic pressure, as in the Plasma Boundary Layer near the Magnetopause, β is approaching unity; large amplitude magnetic field perturbations are then expected and indeed observed in association with engulfed solar wind plasma irregularities (Aubry, et al., 1970; Rijnbeek, et al., 1984; Saunders, 1983; Lemaire, 1977, 1984a, 1985).

In the plasmasphere and at its outer edge, the plasmapause region, the external magnetic field intensity is larger than 250 nT for L < 5; the equatorial plasma density is smaller than 300 cm^{-3} and the temperature of the background plasma of the order of 3000 K; the value β is then smaller than 5×10^{-4}. This order of magnitude calculation shows that, in the plasmapause region and within the plasmasphere, the external magnetic field cannot become significantly perturbed by the presence of diamagnetic density irregularities in the cold ambiant plasma background. Note, however, that substorm injections of hoter plasma clouds in the plasmapause region can well produce significant magnetic field perturbations when their kinetic pressure happens to be comparable to the local magnetic field pressure. But, gradients of the cold thermal plasma pressure in the plasmasphere are generally too small to produce significant (> 1%) diamagnetic perturbations of the external B- field. Therefore, the diamagnetic effects of plasma density irregularities will not be discussed any further in this study.

B. Because of the large dielectric constant in magnetized plasma, significant dielectric fields can, however, develop inside finite magnetospheric plasma elements. Accumulation of electric charges at the surface or in the middle of plasma clouds results from drifts of electrons and ions in opposite directions. For particles of non-zero energies, gradient-B and curvature drifts can contribute to build up opposite charge densities at the surfaces of plasma elements which have a finite extent in the direction perpendicular to $\underline{B}$ and grad B or ($\underline{B}$.grad)$\underline{B}$. The consequences of these drifts will be discussed below. These energy dependent drifts can be neglected in plasmas whose temperature is equal to zero or very small, i.e. when the ion and electron energies are smaller than 0.1 eV.

Accumulation of electrical charges at the surfaces of plasma clouds and polarization charges can also result from drifts in opposite directions induced by an external force (F) acting on the ions and electrons. The gravitational force ($\underline{F}$ = m $\underline{g}$) and the inertial force ($\underline{F}$ = m d$\underline{v}$/dt) produce drift velocities

$$\underline{V}_F = \frac{1}{Ze}\, \underline{F} \times \underline{B}/B^2 \qquad (4.2)$$

which depend on the sign of the electrical charge (Ze) of the particles but not on their kinetic energy. Therefore, the effects of these gravitational and inertial drifts donot vanish in the limit of cold (zero temperature) plasmas.

Although the acceleration of a plasma density element by the gravitational force is documented in classical plasma physics textbooks (Chandrasekhar, 1960; Longmire, 1963), its importance in geophysical plasmas has been widely overlooked. This comes partly from the fact that ideal case studies of unbounded plasmas - by contrast to finite scale plasma-elements have most often been considered, most probably for the sake of simplicity. Secondly, having been used for more than two decades to consider magnetospheric electrons and ions as individual test-particles which drift in given external E- and B- fields, the collective motion of these particles forming an entity (i.e. a plasmoïd, according to the definition by Bostick, 1956) has not yet been fully recognized. Therefore, it is not unnecessary to recall in the next section how the gravitational force can accelerate plasma clouds toward the Earth, across transverse geomagnetic field lines. In the following sections we show how the centrifugal force can drive detached plasma elements away from the Earth, as a consequence of plasma interchange velocity.

4.3. Plasma acceleration by gravitational and centrifugal forces

A. Let us consider a plasma density enhancement corotating with the Earth's angular velocity Ω_E, and examine first the effects induced by the gravitational force. Fig. 18 illustrates the equatorial section of this isolated plasma element at an equatorial distance smaller than 6.6 R_E where the gravitational force is larger than the centrifugal force. In a corotating frame of reference the protons confined in the density enhancement represented by the shaded area drift eastward with the velocity

$$\underline{V}_g = \frac{m_p \underline{g} \times \underline{B}}{eB^2} \qquad (4.3)$$

where m_p and e stand for the ion mass and charge. At L = 4 in the equatorial plane, V_g = 8 cm/s. Note that this velocity is much smaller than the corotation velocity at the same equatorial distance :

$$V_E = \Omega_E R = 1.8 \text{ Km/s}$$

The electrons drift in the opposite direction with a velocity smaller by a factor m_e/m_p. These opposite drift motions generate a polarization current inside the plasma element and contribute to build up a positive electric surface charge density on the eastward boundary

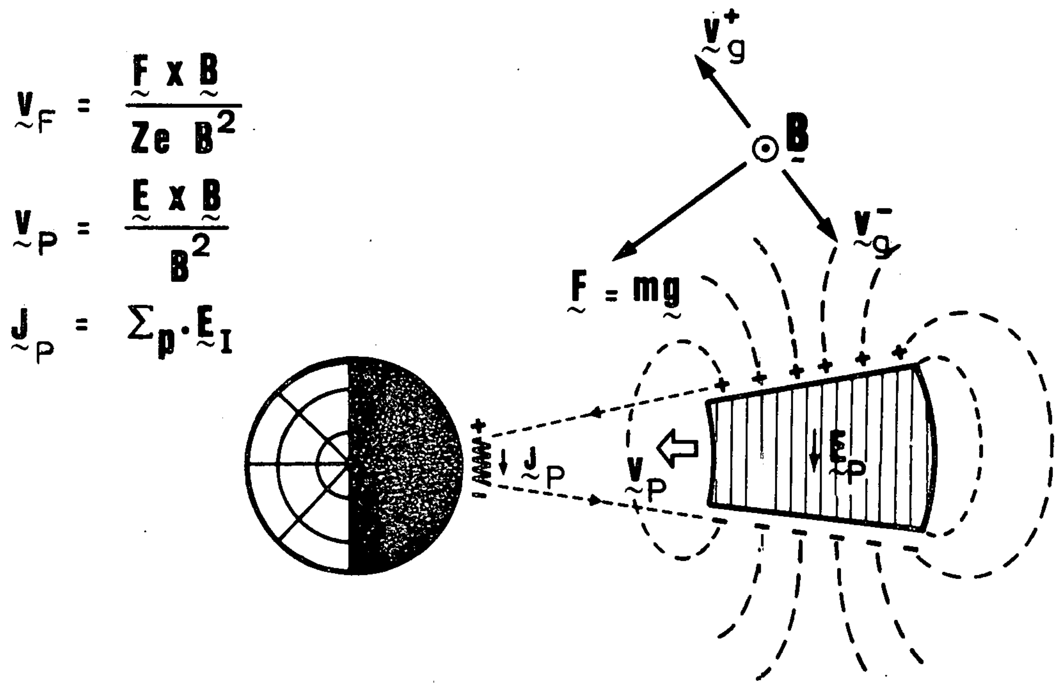

Fig. 18.- Illustration of a cold plasma element falling across geomagnetic field lines in the gravitational potential with a maximum interchange velocity V_P. The gravitational ions and electrons drifts give rise to a polarization electric field $\underline{E}_P$. The resulting electric drift $\underline{V}_P$ is parallel to the gravitational force.

of the plasma element and an equal surface density of negative charges on the westward edge. Due to this drift positive and negative charges originally together are separated by a distance Δx. The polarization $\underline{P}$ (i.e. the electric dipole moment per unit volume) is then

$$\underline{P} = ne\,\underline{\Delta x} \qquad (4.4)$$

where n is the number density of ions or electrons. The quantity $\underline{\Delta x}$ is determined from the gravitational drifts (4.3)

$$\underline{\Delta \dot{x}} = \underline{V}_{g,i} + \underline{V}_{g,e} \cong \frac{m_p \underline{g} \times \underline{B}}{eB^2} \qquad (4.5)$$

where the electron drift has been neglected since it is smaller than the ion drift by the mass ratio m_e/m_p. The polarization, $\underline{P}$, leads to the charge density

$$\rho_c = - \underline{\nabla} \cdot \underline{P} \qquad (4.6)$$

The electric field building up in the plasma element produces a counter-polarization, which tend to reduce $\underline{E}$. The counterpolarization is taken into account by using the plasma dielectric constant

$$\kappa = 1 + \frac{n\,m_p\,c^2}{B^2/\mu_o} \qquad (4.7)$$

where μ_o is the permeability of free space and c the velocity of light. It can be verified that for $n = 300\ cm^{-3}$, $B = 480\ nT$, $\kappa = 2 \times 10^5 >> 1$ since $nm_pc^2 >> B^2/\mu_o$ (Chandrasekhar, 1960; Longmire, 1963).

The resulting electric field is determined from Maxwell's equation

$$\underline{\nabla}.\kappa\underline{E} = \rho_c/\varepsilon_o \tag{4.8}$$

where ε_o is the permittivity of free space ($\varepsilon_o\mu_o = 1/c^2$). From eqs. (4.6) and (4.8) we obtain

$$\underline{\nabla}.\kappa\underline{E} = -\frac{1}{\varepsilon_o}\,\underline{\nabla}.\underline{P} \tag{4.9}$$

In addition, $\underline{E}$ must satisfy equation

$$\underline{\nabla} \times \underline{E} = 0 \tag{4.10}$$

indeed, we have assumed that $\underline{B}$ is constant in time and unperturbed by diamagnetic effects.

One solution of these equation is

$$\underline{E}_P = -\underline{P}/\kappa\varepsilon_o \tag{4.11}$$

or from eqs. (4.4) and (4.7)

$$\underline{E}_P = -\frac{ne\,\Delta x}{\epsilon_o\,(1 + nm_p c^2 \mu_o/B^2)} \tag{4.12}$$

Since $\mu_o nm_p c^2/B^2 >> 1$ eq. (4.12) becomes

$$\underline{E}_p = - \frac{eB^2}{m_p} \underline{\Delta x} \qquad (4.13)$$

This electric field gives rise to an electric drift

$$\underline{V}_P = \frac{\underline{E}_P \times \underline{B}}{B^2} = - \frac{e}{m_p} \underline{\Delta x} \times \underline{B} \qquad (4.14)$$

Since the surface charge density and the quantity $\underline{\Delta x}$ increases with time at a rate given by eq. (4.5), the rate of change of the drift velocity (4.14) is given by

$$\dot{\underline{V}}_P = - \frac{(\underline{g} \times \underline{B}) \times \underline{B}}{B^2} = \underline{g} \qquad (4.15)$$

since $\underline{g}.\underline{B} = 0$ in the equatorial plane.

Thus the plasma falls under gravity with the acceleration $\underline{g}$. The energy density required to separate the charges is the energy density of the electric field $\frac{1}{2} \varepsilon_o E_P^2$. The kinetic energy density of the falling element is that associated with V_P and is given by $\frac{1}{2}$ nm V_P^2; it is larger than $\frac{1}{2} \varepsilon_o E_P^2$ by a factor $\kappa \cong 2 \times 10^5$. Indeed

$$\frac{\frac{1}{2} nm_p V_P^2}{\frac{1}{2} \epsilon_o E_P^2} = \frac{\frac{1}{2} nm_p E_P^2/B^2}{\frac{1}{2} \epsilon_o E_P^2} = \frac{nm_p c^2}{B^2/\mu_o} = \kappa - 1 \cong \kappa \qquad (4.16)$$

Thus relatively little energy is needed to separate the charges in the plasma element, and the kinetic energy gained by the falling plasma element is equal to the gravitational potential energy lost. Through the polarization electric field (4.11), the particles exert forces on one another, and the plasma acts more like a rigid body than like a set of independent particles (Longmire, 1963).

In the preceeding demonstration the gravitational force can be replaced by the centrifugal force ($m\ \Omega^2\ R$), or more generally by the inertial force ($m\ d\underline{V}/dt$) associated with the guiding center of the particles.

B. When the particles inside the plasma element have a kinetic energy which is not negligibly small, grad-B and curvature drifts ($\underline{V}_B$ and $\underline{V}_G$) must be added to the gravitational drift (4.3)

$$\underline{V}_B + \underline{V}_G = \frac{m}{eBR_c} \left(v_{\parallel}^2 + \frac{1}{2} v_{\perp}^2\right) \underline{e}_{\varphi} \qquad (4.17)$$

(Longmire, 1963) where $\underline{e}_{\varphi}$ is the eastward azimuthal unit vector and R_c is the radius of curvature of the magnetic field line ($R_c \cong LR_E/3$ for a dipole magnetic field). For instance, at L = 4 in the equatorial plane, the grad-B and curvature drifts of a proton of 0.25 eV (T = 3000 K) are of the order of 30 cm/s in the westward direction while the corresponding drifts for electrons is in the eastward direction.

As above one can determine the polarization, $\underline{P}$, resulting from these drifts and replace eq. (4.5) by

$$\underline{\dot{\Delta x}} = \sum_{i,e} \frac{m_i}{Z_i e} \left(v_{\parallel}^2 + \frac{1}{2} v_{\perp}^2\right) \frac{\underline{e}_{\varphi}}{BR_c} \qquad (4.18)$$

Proceeding as above, it can be shown that the acceleration of the plasma element due to grad-B and curvature drifts is given by

$$\dot{\underline{V}}_E = \frac{\dot{\underline{E}} \times \underline{B}}{B^2} = \frac{\overline{v_\parallel^2} + \frac{1}{2}\overline{v_\perp^2}}{R_c}\ \underline{e}_\perp \tag{4.19}$$

where $\underline{e}_\perp = \underline{e}_\varphi \times \underline{B}/B$ is the outwardly directed unit vector normal to the L- shell and where $\overline{v_\parallel^2}$ and $\overline{v_\perp^2}$ are averages over the velocity distribution

$$\frac{1}{2}\, m\, \overline{v_\parallel^2} = \frac{1}{2}\, k\, T_\parallel \quad \text{and} \quad \frac{1}{2}\, m\, \overline{v_\perp^2} = k\, T_\perp \tag{4.20}$$

4.4. Maximum value of the plasma interchange velocity

A. The demonstrations presented in section 4.3 are based on the assumption that there are no inter-particle collisions impeding the gravitational and centrifugal drifts : i.e. that the ion collission frequency ($\nu_{c,i}$) is much smaller that the ion Larmor gyro frequency ($\nu_{L,i}$). This is generally the case in the plasmasphere where at L = 4 n_i = 300 cm^{-3} and $\nu_{c,i}/\nu_{L,i} = 2.6 \times 10^{-3}/7.2 = 3.6 \times 10^{-4}$ for 0.25 eV protons (T = 3000 K). In such highly collisionless plasmas the local transverse Pedersen electron conductivity (σ_P) is almost equal to zero, and no conduction current can flow in the direction of the electric field (4.11); consequently the polarization charge density (4.6) cannot be neutralized, and the potential difference ($\int_0^x E\, dx$) building up across the plasma element cannot be discharged by in-situ (local) transverse Pedersen currents ($\underline{J}_P = \sigma_P\, \underline{E}_I$).

However, when the magnetic field lines permeating the plasma elements traverse good conducting walls, like the ionosphere, the depolarization of the plasma element, can proceed via field aligned currents and distant Pedersen currents in the walls. Indeed, in collisional plasmas the electrical conductivity (σ_p) parallel to field lines is always very large and field aligned (Birkeland) currents are easy to drive the very small field aligned potential differences (Lemaire and Scherer, 1974b, 1983).

Furthermore, when the ionosphere is assumed to be an ideal super-conductor any potential difference between adjacent magnetic field lines are immediately short circuited. No polarization electric field (4.11) would then ever be able to build up in the plasma elements, and, their drift velocity (4.14) would remain strictly equal to zero in the corotating frame of reference.

But the transverse Pedersen conductivity is nor zero as implicitely assumed in the previous demonstration nor is it infinitely large, as assumed in the MHD theory for the formation of the plasma-pause. As a consequence of the finiteness of the collision frequency ($\nu_{c,i}$) of ions with neutral atoms in the ionospheric E-region (110 - 120 km), the transverse Pedersen conductivity (σ_P) assumes finite values depending on altitude, latitude, local time, solar and geomagnetic activity conditions. It is convenient to introduce the height integrated Pedersen conductivity

$$\Sigma_p = \int_{h_o}^{h_{eq}} \sigma_p \, dh \qquad (4.21)$$

which is measured in Siemens (S). The values of Σ_P range from 0.2 S during night, when ionospheric densities are minimum in the E- region, up to 20 S in the dayside local time sector, where photoionization by solar radiation increases the ion densities in the ionospheric regions.

Several empirical models describing the local time and latitudinal distribution of Σ_p can be found in the literature. In the following simulations we have used the Σ_p-model of Gurevitch et al. (1976). This empirical model has been deduced from a large number of observations and has been parametrized to take into account different levels of geomagnetic activity and solar activity. The values of $\Sigma_p(L, \varphi)$ obtained from this model are comparable in magnitude with those of the other published models. The Gurevitch et al's model is described in Appendix D. Let us first see how the value of Σ_p determines the value of the maximum interchange velocity of plasma density irregularities falling in the gravitational and centrifugal potentials.

B. Although in the equatorial plane in-situ transverse Pedersen currents cannot drive conduction currents parallel to $\underline{E}$, in the coupled ionospheric E-region such transverse currents can flow in the direction of the electric field $\underline{E}_I$ which is a projection of the magnetospheric electric field $\underline{E}$. Considering magnetic field lines as equipotential lines an East-West equatorial electric field $\underline{E}$ maps down into the ionosphere, along magnetic field lines, with an intensity $L^{3/2}$ times larger

$$E_I = L^{3/2} E \tag{4.22}$$

The height integrated Pedersen current density is defined by

$$\int_{h_o}^{h_{eq}} \underline{j}_p \, dh = \underline{J}_p = \Sigma_p E_I \tag{4.23}$$

These Pedersen currents carry the positive electric charges accumulating on the eastward side of the plasma element to the westward side of the plasma cloud (see fig. 18). In a stationary state the Pedersen currents are balanced by the polarization currents induced by gravity. The presence of Pedersen currents closing the electric circuit, limits the build up of polarization charges, and, consequently limits also the values of the magnetospheric and ionospheric electric fields ($\underline{E}$ and $\underline{E}_I$). The maximum value of $\underline{E}$ determines the maximum plasma interchange velocity

$$\underline{V}_{P,max} = \frac{\underline{E}_{max} \times \underline{B}}{B^2} \tag{4.24}$$

where $\underline{V}_{P,max}$ and $\underline{E}_{max}$ are measured in a corotating or comoving frame of reference

$$\underline{E}_{max} = - \underline{V}_{P,max} \times \underline{B} \tag{4.25}$$

In an inertial frame of reference fixed with respect to the Sun-Earth direction

$$\underline{V}' = \frac{\underline{E}_{ext} \times \underline{B}_{ext}}{B^2_{ext}} + \frac{\underline{E}_{max} \times \underline{B}_{int}}{B^2_{int}} \tag{4.26}$$

where the magnetic field in the interior ($\underline{B}_{int}$) is almost the same as outside ($\underline{B}_{ext}$) because of the low value of β (see section 4.2).

After a short period of transition, during which the plasma element is accelerated in the direction of $\underline{g}$ the fall (or interchange) velocity ($\underline{V}_P$) reaches the maximum asymptotic value $\underline{V}_{P,max}$. In this final stationary regime, the kinetic energy of the element is constant (since $\dot{V}_P = 0$), and the potential energy liberated by the falling element is dissipated by Joule heating in the lower ionosphere at a rate given by

$$\frac{d}{dt} Q_{Joule} = -\Sigma_p E_I^2 S_I = -\Sigma_p L^3 E_{max}^2 S_I \tag{4.27}$$

where S_I is the ionospheric section of the flux tube embracing the whole plasma element. Using eq. (4.25) to replace E_{max} in eq. (4.27), and

$$B = B_o/L^3 , \tag{4.28}$$

eq. (4.27) becomes

$$\frac{d}{dt} Q_{Joule} = - \Sigma_p V_{P,max}^2 B_o^2 S_I/L^3 \tag{4.29}$$

where B_o is the equatorial magnetic field at the Earth surface.

In the final stationary regime this quantity is equal to the potential energy liberated per second by the mass of the whole plasma element

$$- \int_{h_{min}}^{h_{eq}} S \; n \; m_p \underline{g} \cdot \underline{V}_{P,max} \; d\ell \tag{4.30}$$

where $S(\ell)$ is the section of the flux tube embracing the plasma element. In a dipole magnetic field

$$S(\lambda) = S_I \; B_o \; L^3 (4 - \frac{3}{L})^{1/2} \; \frac{\cos^6\lambda}{(1 + 3\sin^2\lambda)^{1/2}} \tag{4.31}$$

$$d\ell = R_E \cos\lambda \, (1 + 3\sin^2\lambda)^{1/2} \, d\lambda \tag{4.32}$$

The integral (4.30) along the field line between the equator (h_{eq}) and (h_{min}) the altitude of the lower edge of the plasma element, can be approximated by

$$- m_p \, g \, V_{P,max} \, N'_p \tag{4.33}$$

where N'_p is the number of protons contained in the plasma element whose projected cross section at ionospheric altitude is equal to S_I

$$N'_p = \int_{h_{min}}^{h_{eq}} n \, S \, d\ell \cong \bar{n} \, V' \tag{4.34}$$

where $\bar{n}$ is the average density in the plasma element and V' is the volume of the plasma element. Note that V' is approximately equal to $\gamma \, V \, S_I/S_o$ where V is given by eq. (3.5) and S_o by eq. (3.4); the plasma element occupies a fraction γ of the whole volume of the flux tube.

$$N'_p = \bar{n} \, \gamma \, V \, S_I/S_o \tag{4.35}$$

Equating the rate of potential energy liberated (4.33) and the rate of energy dissipated by Joule heating (4.29), one obtains also

$$V_{p,max} = \bar{n} \, m_p g \, \frac{\gamma \, V \, L^3}{\Sigma_p \, B_o^2 \, S_o} \tag{4.36}$$

So far we assumed that there is no plasma outside the plasma element. When the plasma element is embedded in a background plasma whose density (n^{BG}) is for instance given eq. (3.35) or (2.18), the value of $\bar{n}$ in eq. (4.36) must be replaced by

$$\Delta n_{eq} = \bar{n} - n^{BG} \tag{4.37}$$

Indeed, gravity produces polarization charges in the medium also outside the plasma element. The effect of these additional polarization charges is to reduce $\underline{E}_p$ inside the plasma element.

When the number density inside and outside the plasma element are equal, $\Delta n_{eq} = 0$. In this case, the value of $\dot{\underline{V}}_p$, of $\underline{V}_p$ and of $V_{p,max}$, the maximum plasma interchange velocity driven by the gravitational force, are all equal to zero. When the background density is larger than the plasma density $\bar{n}$, Δn_{eq} is negative. The electric field $\underline{E}_{max}$ is then reversed and the interchange velocity of such a "plasma hole" is in the direction opposite to the gravitational acceleration. Like a gas bubble in water, a plasma hole in a denser background plasma moves away from the Earth.

C. The maximum speed with which a bubble rises, or, with which a stone falls in a fluid is inversely proportional to the viscosity coefficient of the fluid. The maximum velocity is then determined by the balance between the rate at which potential energy is liberated, and the rate at which it is dissipated by viscous drag. In the case of a collisionless plasma viscous dissipation can be neglected compared to dissipation by Joule heating in the coupled ionospheric region which plays a key role by limiting the falling or rising velocity of a plasma element. When the electric conductivity in the ionosphere is low, the rate of dissipation by Joule heating is low and the plasma interchange velocity can increase to a large maximum value. On the contrary when the integrated Pedersen conductivity is large the plasma interchange velocity remains small. This inverse proportionality of $V_{P,max}$ and Σ_p in eq. (4.36), confirms that, in the limit of infinitely large ionospheric conductivities, the gravity induced interchange velocity would be vanishingly small for any positive or negative value of Δn_{eq}. In this case, which corresponds to the classical MHD approximation, any plasma density enhancement or plasma hole would only be able to move along the equipotential surface of the external convection electric field. Similarly, a bubble or a stone embedded in a fluid with infinitely large viscosity would be forced to follow the streamlines of the background viscous fluid.

Using actual values for Σ_p from the empirical model described in the Appendix D, one can estimate the order of magnitude of $V_{P,max}$. For instance in the post-midnight local time sector Σ_p has a minimum value of 0.2 Siemens; For a plasma element at L = 4 with an equatorial density of 200 cm^{-3} embedded in a background plasma density of 300 cm^{-3}, Δn_{eq} = -100 cm^{-3}; with g_{eq} = 0.61 m/s^2, V = 4.6×10^{19} cm^3/Wb, γ = 1, S_o = 2.8×10^8 cm^2/Wb, B_o = 3.1×10^{-5} T it comes from eq. (4.36) $V_{P,max}$ = 52 m/s = 0.03 R_E/h. This radial interchange velocity is relatively small compared to the corotation velocity ($\Omega_E . R$ = 1.8×10^3 m/s = 1.0 R_E/h at L = 4) but it will be shown below that it is sufficiently important to play a key role in peeling off the plasmasphere.

In the dayside sector, where the ionization density in the E-region is higher than in the nightside sector, the values of the integrated Pedersen conductivity is enhanced by a factor 75. Consequently, the maximum interchange velocity of a plasma density inhomogeneity - like those within which VLF whistler wave are ducted - is 75 times smaller in the dayside than in the nightside sector. This means that in the dayside any plasma element is almost forced to move parallel to the convection equipotential streamlines as supposed in the MHD theory. This fails, however, to be, a valid assumption in the nightside; where Σ_p is significantly reduced, and, where the physical process of plasma interchange motion should not be underestimated.

D. In section 4.3 we have shown that the grad-B and curvature drifts can accelerate finite plasma elements containing particles whose velocities are perpendicular and parallel to the magnetic field direction (or temperatures $T_\perp$ and $T_\parallel$) are not equal to zero (see eqs. 4.19 and 4.20). But as in the case of the gravitational acceleration, one can determine a maximum interchange velocity ($V_{P,max}$) which is inversely proportional to the integrated Pedersen conductivity. To determine this maximum interchange velocity one must proceed as above by considering that, in the final stationary regime, the rate of energy dissipation by Joule heating is equal to the rate at which free internal energy is made available as a result of the drift of the plasma element. The total thermal energy U of the electrons and protons contained in the plasma element is

$$U = \sum_{i,e} N_i' \, k(T_{\parallel,i} + 2\, T_{\perp,i})/2 \qquad (4.38)$$

The total number of protons and electrons (N_p', N_e' given by eq. 4.35) are equal; assuming that the total content of particles is conserved during the motion, the rate of change of the thermal energy is equal to

$$\frac{dU}{dt} = \sum_{i,e} N_i' \, k \, \underline{V}_{P,max} \cdot (\underline{\nabla}\, T_{\parallel,i} + 2\, \underline{\nabla}\, T_{\perp,i})/2 \qquad (4.39)$$

As a result of the conservation of the first adiabatic invariant the perpendicular kinetic energy ($\frac{1}{2}$ $mv_\perp^2$) and the temperature ($T_\perp$) of collisionless particle vary as B i.e. :

$$T_\perp(L) \propto B \propto L^{-3} \qquad \text{and} \qquad \nabla_\perp T_\perp = -\, 3\, T_\perp/LR_E \qquad (4.40)$$

The parallel kinetic energy ($\frac{1}{2} m_{\parallel} v^2$) and temperature ($T_{\parallel}$) change roughly as L^{-2} when the second invariant is conserved during the drift motion. It results then that

$$T_{\parallel}(L) \propto L^{-2} \quad \text{and} \quad \nabla_{\perp} T_{\parallel} = - 2T_{\parallel}/LR_E \tag{4.41}$$

Using eqs. (4.40) and (4.41) in eq. (4.39) it comes

$$\frac{dU}{dt} = - \sum_{i,e} V'\bar{n}_i \, k \, (T_{\parallel,i} + 3 \, T_{\perp,i}) \, \frac{E_{max}}{LR_E} \tag{4.42}$$

The work done per unit time by the pressure forces during the associated expansion of the volume (V') of the flux tube embracing the plasma element is given by

$$p \, \frac{dV'}{dt} = \sum_{i,e} \bar{n}_i \, k \, V' \, \frac{T_{\parallel,i} + 2T_{\perp,i}}{3} \, \underline{V}_{p,max} \cdot \underline{\nabla}_{\perp} V' \tag{4.43}$$

where p is the total kinetic pressure. Since V', the volume of a magnetic flux tube varies roughly as L^4 (see fig. 9 and eq. 3.5), it comes from eqs. (4.43) and (4.24)

$$p \, \frac{dV'}{dt} = \sum_{i,e} V' \, \bar{n}_i \, k \, \frac{4(T_{\parallel,i} + 2T_{\perp,i})}{3} \, \frac{E_{max}}{LR_E} \tag{4.44}$$

Therefore, the net energy made available for dissipation by Joule heating in the ionosphere is

$$\frac{dU}{dt} + p\,\frac{dV'}{dt} = -\sum_{i,e} V'\,\bar{n}_i\,k\,\frac{(T_{\perp,i} - T_{\parallel,i})}{3}\,\frac{E_{max}}{LR} \tag{4.45}$$

In the stationary regime, the right hand side of eq. (4.45) is equal to the rate of Joule dissipation

$$\frac{dQ}{dt} = -\sum_p E_I^2\,S_I \tag{4.46}$$

Taking into account eqs. (4.22), (4.25) and (4.35), the maximum interchange velocity is given by

$$V_{P,max} = \sum_{i,e} \bar{n}_i\,k\,(T_{\perp,i} - T_{\parallel,i})\,\frac{\gamma V L^2}{3\Sigma_p B_o S_o R_E} \tag{4.47}$$

This expression is the analogue of eq. (4.36) for interchange motion in plasmas with non-zero parallel and perpendicular temperatures. It can be seen that when the electron and ion velocity distributions are both isotropic $T_{\parallel} = T_{\perp}$ and $V_{p,max} = 0$. Furthermore, when a plasma element is embedded in a background plasma the sum $\sum_{i,e} \bar{n}_i\,k(T_{\perp,i} - T_{\parallel,i})$ must be replaced by

$$\begin{aligned} \Delta p_{\perp} - \Delta p_{\parallel} = {} & \sum_{i,e} (\bar{n}_i\,k\,T_{\perp i} - n_i^{BG}\,k\,T_{\perp i}^{BG}) \\ & - \sum_{i,e} (\bar{n}_i\,k\,T_{\parallel i} - n_i^{BG}\,k\,T_{\parallel,i}^{BG}) \end{aligned} \tag{4.48}$$

Indeed, the polarization produced in the background medium reduces the electric field inside the plasma element. When the parallel and perpendicular kinetic pressure of the electrons and of the ions inside and outside the plasma element balance each other exactly one has that $\Delta p_{\parallel} - \Delta p_{\perp} = 0$, and consequently $V_{p,max} = 0$. When the perpendicular plasma pressure is larger inside than outside the plasma element $\Delta p_{\perp}$ is positive; the plasma cloud is then accelerated in the outward direction : it is pushed out of the region of highest magnetic field intensity by the grad-B magnetic force. But while it is moving outwards, the volume of the element is increasing, and its density is decreasing as well as its perpendicular temperature and pressure. If during its outwardly directed interchange motion, the plasma element finds a stable position where the plasma pressure inside is balanced by the total plasma pressure outside the plasma interchange velocity tends then to zero. Overshooting of this equilibrium position because of the inertial forces would give rise to damped oscillations in the position of the center of mass of the plasma element; damped oscillations of the volume of the plasma element are then also expected. Whether this might be a source of the ULF waves observed in the magnetosphere and also detected with ground based magnetometers is an interesting question; but this problem is beyond the scope of the present study.

When a hot plasma cloud is injected into the geomagnetic field with a parallel temperature which is larger inside than in the ambiant plasma, $\Delta p_{\parallel}$ is positive, and, $V_{p,max}$ is directed inwards. As a result of plasma interchange motion driven by curvature drifts such a plasma element moves toward the Earth until it finds a position where Δp is equal to zero. Such a position does always exist, indeed the back-ground plasma pressure is increasing rapidly in the inner region of the geomagnetic field. Furthermore, the particles injected with pitch angles in the loss cones are precipitated in the atmosphere; these particles escape definitely out of the cloud, while those with large pitch angles remain trapped in the magnetosphere where the density is lowest. As a consequence of this loss cone precipitation $T_{\parallel}$ decreases necessarily. As a result of this reduction of $T_{\parallel}$ inside the injected hot plasma cloud the inward directed interchange velocity is also reduced. Except in the papers by Richmond (1973) and Sonnerup and Laird (1963) the role played by interchange motion in geophysical plasmas has so far been largely underestimated.

Although interchange motion due to curvature drifts or grad-B drift is an important mechanism in warm and highly anisotropic magnetospheric plasmas, in the case of the cold and almost isotropic thermal plasma forming the bulk of the plasmasphere, these effects can be neglected. Indeed, any offset in the total plasma pressure inside a thermal plasma cloud can rapidly be cancelled by an appropriate expansion or contraction of its volume, possibly accompanied by a few damped oscillations. For this reason we will restrict the following study to examine only the consequences of plasma interchange motion driven by gravity and inertial or centrifugal forces.

4.5. Zero Radial Force (ZRF) surface

A. In the previous section we have shown that the maximum interchange velocity due to gravity and inertial forces is given by

$$\underline{u} = \underline{V}_{p,max} = \Delta\rho \, g_{eff} \, \frac{\gamma V L^3}{\Sigma_p B_o^2 S_o} \tag{4.49}$$

where $\Delta\rho$ is the excess mass density; when $\Delta\rho$ is positive, the density inside the plasma element is higher than the background density : this element is called below a "plasma density enhancement"; when $\Delta\rho < 0$, the plasma element is a "plasma hole". In eq. (4.49) g_{eff} stands for the effective acceleration due to gravity and centrifugal or inertial forces

$$g_{eff} = g - \frac{d\underline{V}'}{dt} \tag{4.50a}$$

where $\underline{V}'$ is the sum of $\underline{u}$, the interchange velocity, and $\underline{V}_E$, the convection velocity determined by the E- and B- field models describing the streaming of the background plasma at large distances from the plasma element.

Since $u \ll V_E$ the total velocity $\underline{V}'$ and its time variation $d\underline{V}'/dt$ are almost equal to $\underline{V}_E$ and $d\underline{V}_E/dt$, respectively.

When the corotation electric field is a valid approximation, as in the inner magnetosphere for $L < 3$, the effective acceleration in the equatorial plane is given by

$$g_{eff} = \frac{g_o}{L^2} - \Omega^2 R_E L \tag{4.50b}$$

where g_o the gravitational acceleration at the surface of the Earth (g_o = 9.81 m/s^2). The interchange velocity $\underline{u}$ becomes equal to zero at the equatorial distance

$$L_m = \left(\frac{g_o}{R_E \Omega^2}\right)^{1/3} = \left(\frac{GM_E}{R_E^3 \Omega^2}\right)^{1/3} = \left(\frac{3}{2}\right)^{1/3} L_c \tag{4.51}$$

where the critical L_c value is given by eq. (2.9).

When the angular velocity Ω of the ion-exosphere is equal to the angular velocity of the Earth (Ω_E), L_c = 5.78 and one has L_m = 6.6; the radial component of the effective force acting on a plasma element becomes then equal to zero along a cylindrically symmetric surface whose equatorial cross-section coïncides with the geostationary orbit. This surface will be called the Zero-Radial-Force (ZRF) surface. This surface is located beyond the Zero-Parallel-Force (ZPF) surface introduced in chapter 2.

The ZRF surface separates the regions where the radial components of the interchange velocities are in opposite directions : Plasma density enhancements in the equatorial plane, at $L < L_m$, spiral inwardly (i.e. toward the Earth) until they reach a place where $\Delta\rho$ and u become both equal to zero. All plasma density enhancements located

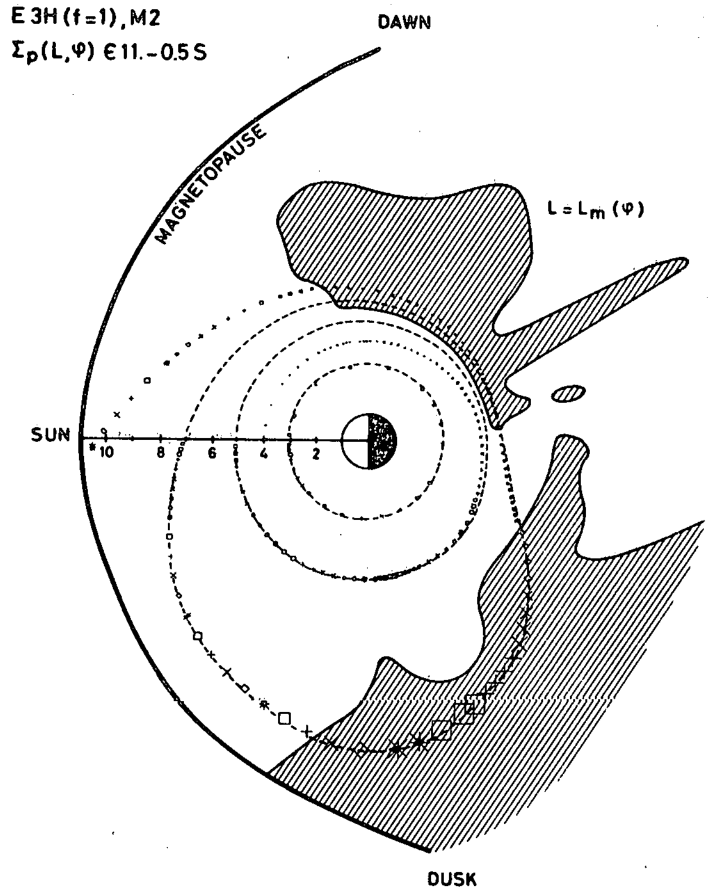

Fig. 19.- Equatorial cross section of the Zero Radial Force surface corresponding to the E3H + M2 electric and magnetic field models. In the shaded area the interchange velocity of all plasma density enhancements is directed away from the Earth. Elsewhere, it is pointing inwardly. The dashed closed curves are equipotential lines of the E3H field. These curves represent also streamlines of plasma density enhancements when interchange motion is ignored as in the MHD theory, or when the integrated Pedersen conductivity (Σ_p) is very large as in the dayside local time sector (Σ_p = 11 S). In the night side where Σ_p is significantly reduced (Σ_p = 0.5 S) the interchange velocity is strongly enhanced. The trajectories of three plasma density enhancements for which $\Delta n/n_{eq}^{BG}$ = 40% is shown by three series of the different symbols. The size of these symbols is proportional to the equatorial cross section of the drifting plasma elements. The type of symbols has been changed every new Universal Time hour. Note that the two plasma density enhancement starting at L = 3 and 5 donot penetrate across the ZRF surface : they spiral inwardly. The interchange velocity $\underline{u}$ decreases rapidly with L (see eq. 4.49). The outermost plasma density enhancement spirals away from the Earth in the shaded region beyond the ZRF surface.

beyond the ZRF surface, where the radial component of the centrifugal force exceeds the gravitational force, spiral outwardly. The interchange velocities of plasma holes on both sides of the ZRF surface are reversed in direction; equatorial plasma holes inside the ZRF surface bubble upwards, while beyond the ZRF surface they converge toward this surface.

B. It has already been emphasized that the corotation electric field is significantly perturbed by solar wind induced magnetospheric convection. The E3H electric field model described in the Appendix B, takes into account the sunward convection observed in the magnetotail. This E-field model also takes into account the enhanced eastward bulk velocity measured in the post-midnight local time sector. This electric field model and the M2 magnetic field model described in the Appendix A, have been used to calculate $\underline{V}_E$ (see fig. 11); they have also been used to calculate the components of $d\underline{V}_E/dt$ which is a good approximation for $d\underline{V}/dt$ in eq. (4.50).

Considering stationary or quasi-stationary field distributions one has

$$\frac{d\underline{V}_E}{dt} = (\underline{V}_E \cdot \underline{\nabla})\, \underline{V}_E \qquad (4.52)$$

The radial and azimuthal components of the vectors $\underline{V}_E$ and $d\underline{V}_E/dt$ have been derived in the Appendix C. For any electric and magnetic fields models, the Zero Radial Force surface can be obtained by determining the roots (L_m) of the equation :

$$(\underline{g} - d\underline{V}_E/dt) \cdot \underline{R}/R = 0 \qquad (4.53)$$

at all local time angles (φ).

For the corotation electric field, we have seen above that the roots of eq. (4.53) are all equal to L_m = 6.6; they are then independent of . But, for the E3H + M2 field models there are up to four different roots in certain local time sectors (0100 - 0150 LT), while in the dayside sector between 0900 LT and 1700 LT the equation (4.53) has no root at all : in this local time range the gravitational dominates the centrifugal or inertial force at all radial distances. The solid line at the border of the shaded area in fig. 19 corresponds to the equatorial cross section of the ZRF surface for the E3H + M2 model. The minimum equatorial distance of the ZRF surface is L_m = 4.70 at 0200 LT; this is slightly beyond the minimum ZPF surface L_c = 4.56 at 0150 LT.

McIlwain (1974) introduced a scale factor (f) in his empirical model to obtain better correspondence to K_p values outside the range 1 to 2. For f = 1 one recovers the E3H model for which fig. 19 has been calculated. The minimum minimorum equatorial distance of the ZRF surface for f = 2 and f = 0.75 are respectively L_m = 5.87 and L_m = 3.87; the former case corresponds to K_p smaller than 1; the latter one corresponds to K_p larger than 2.

4.6. The effect of plasma interchange motion on the drift path of cold plasma density irregularities

A. In fig. 13 we have illustrated the successive positions of three plasma elements in the equatorial plane of the magnetosphere. The trajectories represented in fig. 13 were obtained by integrating numerically the equations (3.31) and (3.32), where $\underline{V}_E$ is calculated from the E3H and M2 models; plasma interchange motion was, however, neglected in these simulations. These drift paths were parallel to equipotential lines; they represent therefore the drift paths of background plasma elements for which $\Delta\rho$ would be equal to zero everywhere along the closed streamlines. Indeed, according to eq. (4.49), $\underline{u}$ is then equal to zero, and the total drift velocity, $\underline{V}' = \underline{V}_E + \underline{u}$, coïncides with the background plasma velocity, $\underline{V}_E$. These closed trajectories coïncide also with the drift paths of plasma density irregularities for any arbitrary value of $\Delta\rho$, in the ideal case when the integrated Pedersen conductivity Σ_p is assumed to be infinitely large (i.e. in the MHD limit, when $\underline{u}$ is infinitely small).

The three drift trajectories shown in fig. 19 have been obtained by numerical integration of eqs. (3.31) and (3.32), where $\underline{V}_E$ has been replaced by $\underline{V}' = \underline{V}_E + \underline{u}$, with $\underline{u}$ given by eq. (4.49). These trajectories correspond to plasma density enhancements with an excess density of + 40% over the background plasma density : $\Delta n/n_{eq}^{BG} = +\ 40\%$; the equatorial background plasma density (n_{eq}^{BG}) assumed in this simulation is given by eq. (3.35). The values of the integrated Pedersen conductivity (Σ_p) were assumed to be 11 Siemens in the dayside local time sector (i.e. for φ = 0600 LT to 1800 LT), while in the night-time intervals, 0000 LT - 0600 LT and 1800 LT - 2400 LT, Σ_p has a reduced value of 0.5 S. The series of successive positions of the plasma elements are indicated by symbols whose size is proportional to their equatorial cross section, assuming conservation of magnetic flux. The type of symbols has been changed every new Universal Time hour. At the initial time, all three plasma elements were aligned along the noon equatorial radius respectively at R = 3 R_E, 5 R_E and 7 R_E.

It can be seen that in the dayside local time sector, where the values of Σ_p are large, the plasma interchange velocity is very small, and, the trajectories are almost parallel to equipotential lines as in fig. 13. But as soon as the elements penetrate in the nightside beyond 1800 LT where Σ_p is reduced by a factor 22, the values of $\underline{u}$ contribute significantly to the total velocity $\underline{V}$. In the shaded areas beyond the ZRF surface plasma density enhancements drift toward outer equipotential surfaces. In the unshaded area, where the gravitational force exceeds the centrifugal force, the plasma element slips earthward toward lower equipotential lines. The outermost trajectory starts at 7 R_E in the noon meridian, and it ends at the magnetopause (at 11 R_E)

after one whole turn around the Earth. On the contrary, the two innermost plasma density enhancements spiral inwardly toward a place where the internal plasma density is equal to the external background density, i.e. where $\Delta\rho$ is equal to zero on the average.

In fig. 20, the solid line spiraling outwardly corresponds to the trajectory of a plasma density enhancement ($\Delta n/n^{BG}_{eq}$ = + 20%) released at 7 R_E in the noon meridian plane, and drifting in the E3H (f=1) + M2 fields and in the same background density distribution as in the simulation shown in fig. 19. The interchange velocity $\underline{u}$ has been calculated, however, with different values for the integrated Pedersen conductivity; the model of Gurevitch et al. (1976), described in the Appendix D, has been used to obtain the trajectories illustrated in fig. 20. The squares along this solid line represent the positions of the plasma element after a drift time indicated in hours by the numbers shown nearby.

As a consequence of the different distribution for Σ_p, and, also because of the smaller excess density, it takes 2 turns around the Earth (70 hours) in fig. 20 - instead of 1 turn in fig. 19- before the plasma element reaches the magnetopause, where it is eventually lost.

The dashed line in fig. 20 shows the trajectory of a plasma hole for which $\Delta\rho/\rho^{BG}_{eq}$ = - 20%. This plasma density depression has also been released at 7 R_E in the noon meridian plane. While spiraling inwardly, it completes a first turn around the Earth in 36 hours. After four additional revolutions (i.e. after almost 190 hours), it has reached an asymptotic orbit.

C. The solid line and dashed line in Fig. 21 show again the drift paths of a plasma density enhancement and of a plasma hole, respectively. But, both elements are released at 5 R_E in the noon meridian plane, instead of 7 R_E. It can be seen that the plasma density enhancement spirals now inwardly in the dominant gravitational field. On the contrary, the plasma hole bubbles away from the Earth until it

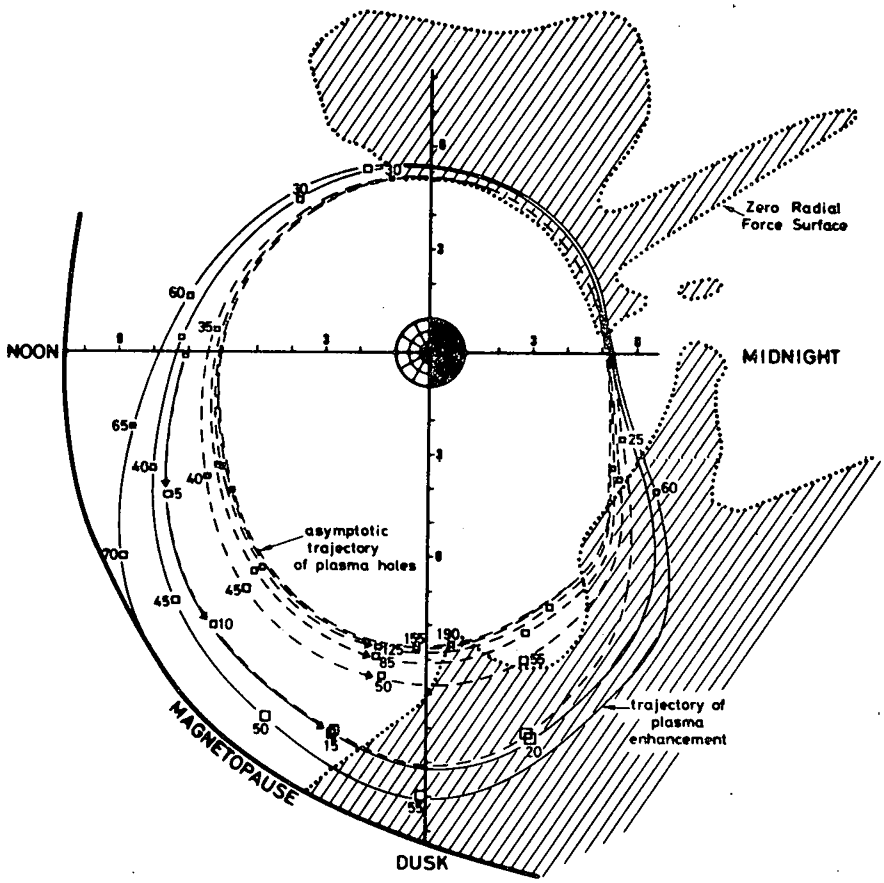

Fig. 20.- Equatorial cross section of magnetosphere showing the shaded region where the radial component of the inertial force exceeds gravitational force. The solid lines indicates the trajectory of a plasma density enhancement with an excess density of + 20% drifting in the ambiant E3H + M2 fields and in a background density distribution given by eq. (3.35). The numbers and squares along the trajectory indicate the positions after the given number of hours. The plasma hole reaches the magnetopause after 70h. The dashed line shows the inward spiraling trajectory of a plasma density depression ($\Delta\rho/\rho^{BG}_{eq}$ = - 20%) released at 7 R_E in the noon local time meridian plane. This plasma hole tends toward a stable asymptotic orbit after several revolutions around the Earth.

reaches the same asymptotic trajectory as the plasma hole illustrated in fig. 20. Along this asymptotic trajectory the interchange velocity ($\underline{u}$) averaged over one revolution around the Earth is equal to zero.

All plasma holes forming anywhere in the plasmasphere are converging toward this asymptotic trajectory whose position and shape depend on the E- and B-fields models used to approximate the actual DC electromagnetic field distribution. It can be seen from fig. 21 that this stable asymptotic drift path for plasma holes has the characteristic dawn-dusk asymmetry of the E3H field itself. The minimum radial distance of this trajectory is 4.8 R_E at 0230 LT. This is a distance of 0.1 R_E beyond the minimum radial distance of the ZRF surface.

In the case of the corotation electric field, this asymptotic trajectory of plasma holes would have been a circle at 6.6 R_E which coïncides with geostationary orbit, i.e. with the equatorial cross-section of the ZRF surface.

For asymmetric E- and B-field distributions and local time dependent values for Σ_p, the asymptotic trajectory does not coïncide with the ZRF surface : its minimum radial distance is then slightly larger than L_m.

D. The asymptotic trajectory is a stable drift path for plasma holes, but an unstable one for plasma density enhancements. Indeed, a small perturbation in the orbit of a plasma density enhancement deviates the element either on an outward or on an inward spiraling trajectory. On the contrary, plasma holes always drift back toward this unique asymptotic trajectory.

4.7. The formation of the equatorial plasmapause

From the results illustrated in figs. 19, 20 and 21 it can be concluded that all cold plasma density depressions - or holes- formed in the magnetosphere (by any kind of perturbation), converge toward an

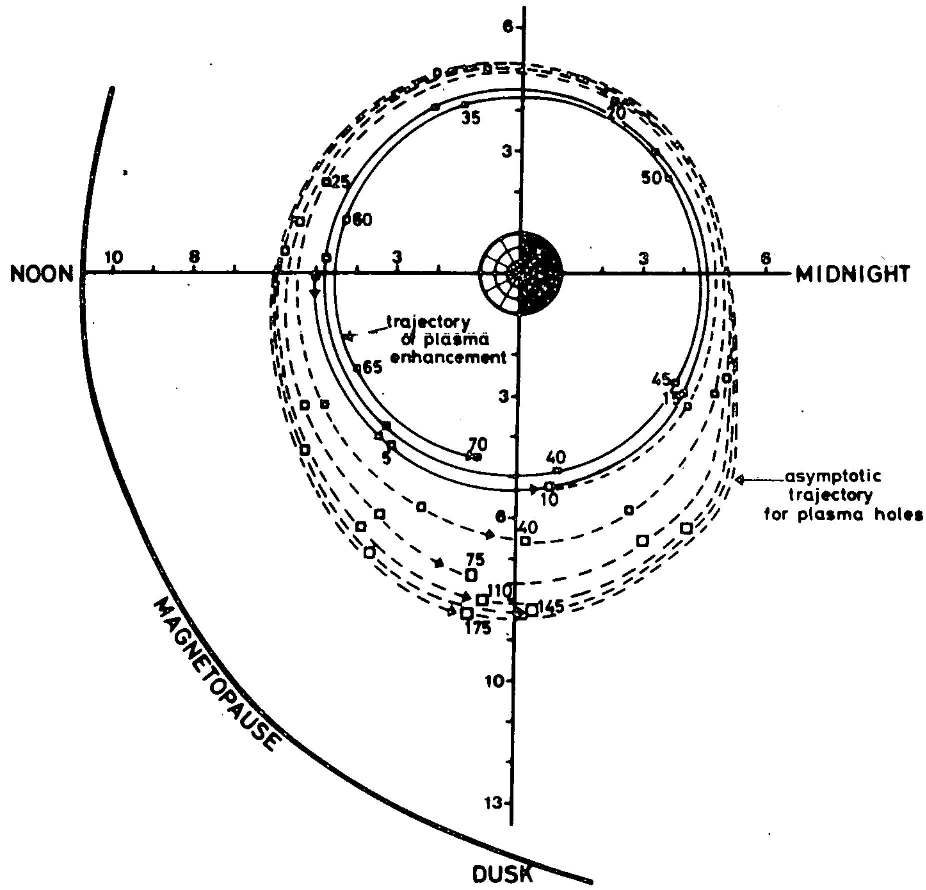

Fig. 21.- Same as fig. 20 except that the plasma density enhancement (solid line) and the plasma hole (dashed line) have both been released at 5 R_E (instead of 7 R_E) in the noon meridian plane. The plasma density enhancement ($\Delta\rho/\rho_{eq}^{BG}$ = + 20%) spirals now inwards while the plasma hole ($\Delta\rho/\rho_{eq}^{BG}$ = - 20%) drift toward the same asymptotic trajectory as in fig. 20.

asymptotic trajectory whose equatorial position depends on the electric and magnetic field distribution in the magnetosphere. Along this unique drift path, the mean interchange motion resulting from the gravitational force is equal to the mean interchange motion resulting from the radial component of the inertial force : in other words the gravitational force averaged over one revolution around the Earth, is balanced by the radial component of the inertial force averaged over the trajectory.

It must be pointed out that the value of integrated Pedersen conductivity determines the speed with which the plasma holes converge toward the asymptotic trajectory, but does not directly influence the position of this final orbit which is determined by the balance between two forces : the gravitational force and the centrifugal or inertial force.

The converging motion of plasma holes is also illustrated in the three panels of fig. 22. Two density depressions in the equatorial plasma distributions are shown at three successive instants of time, t_0, t_1 and t_2. In a corotating frame of reference the inner plasma hole bubbles upwards until it reaches the place where the interchange velocity ($\underline{u}$) vanishes, i.e. where the radial component of the gravitational and centrifugal forces balance each other. The outer plasma hole converges toward the same place which, in the case of the corotation E-field, coïncides with the geostationary orbit at 6.6 R_E. As a consequence of the convergence of all plasma holes toward the same asymptotic orbit, a trough develops at this position. The shell or block of plasma located beyond this trough is a plasma density enhancement which must drift outwardly and which finally detaches from the main plasma body on the left of the dashed line. This detached plasma element drifts toward the magnetopause where it is eventually lost. The inner edge of the trough corresponds to a knee in the equatorial density. This knee resembles the density gradients observed at the plasmapause.

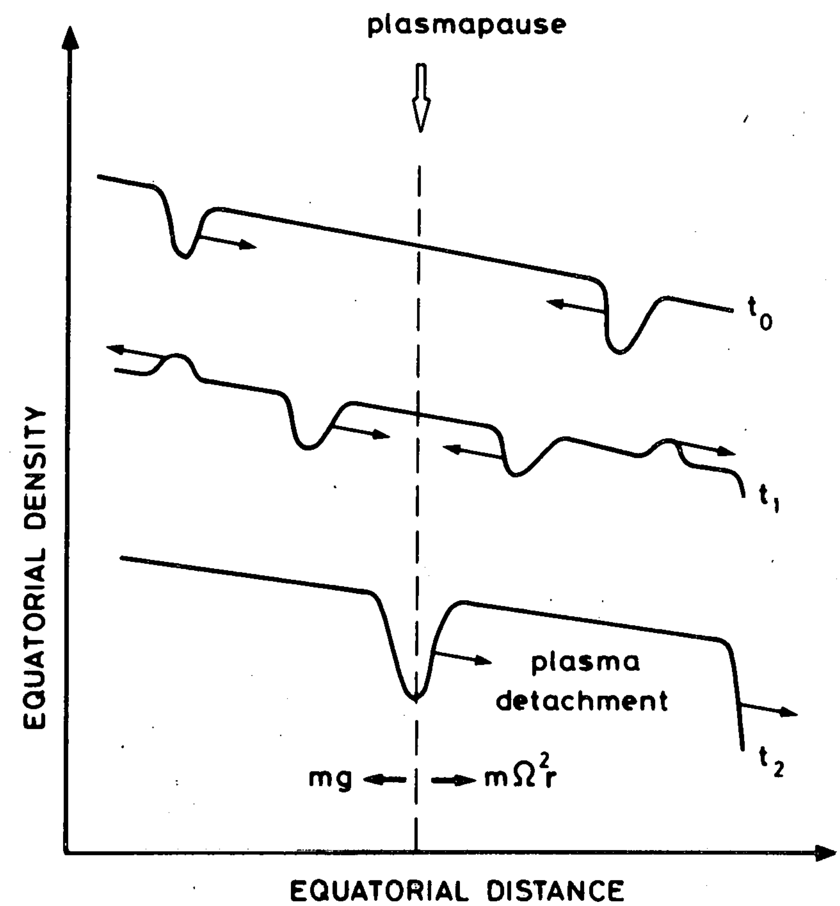

Fig. 22.- Equatorial density distribution with two plasma holes drifting toward a common asymptotic trajectory determined by the balance between the mean gravitational force and the radial component of the centrifugal force. All plasma holes collect along this trajectory. As a consequence a trough is developping there. The large plasma density enhancement formed beyond this trough, drifts away from the main plasmasphere, by interchange motion. Indeed beyond the dashed line the centrifugal force exceeds the gravitational force. A sharp "knee" in the equatorial density remains when the outer detached plasma block has separated from the plasmasphere which is confined within the gravitational potential well. This figure illustrates how a new plasmapause density gradient is formed by peeling off a shell of the plasmasphere by interchange motion.

4.8. Theoretical and observed positions of the inner and outer edges of the plasmapause region

A. When the geomagnetic activity remains very low for a prolonged period of time, corotation extends to larger radial distances in the magnetosphere and there is even a tendency for the thermal plasma to rotate around the Earth with a smaller angular velocity than Ω_E (Olsen, 1984, private communication; Baumjohann et al., 1985). Under such quiet condition the ZRF surface, the asymptotic trajectory of plasma holes and the location of formation of plasmapause are all displaced beyond geostationary orbit; geostationary satellites, like ATS 5 or 6, or as GEOS 2, remain then inside the high density plasmasphere at all local times. Although this has been observed a few times with GEOS 2 (Decreau, 1983) it is rare to find very quiet period of time lasting for more than one day.

Most of the time, however, GEOS 2 orbiting at $R = 6.6\ R_E$ crosses the plasmapause twice a day indicating that the minimum radial distance of the plasmapause is generally smaller than $6.6\ R_E$. These satellites observations support the numerical results obtained with the M2 + E3H models, and illustrated in fig. 21. Indeed, with these field models, the minimum radial distance of the asymptotic trajectory which we have identified with the outer edge of the plasmapause region, is located at $L = 4.8$, i.e. inside geostationary orbit. Furthermore, the theoretical plasmapause has its minimum radial extent in the post-midnight local time sector, as confirmed by the observations. The largest radial distance of the theoretical plasmapause is beyond geostationary orbit in the dusk local time sector where it was found, from whistler and in-situ satellite observations, that the plasmasphere has a bulge (Carpenter, 1966; Chappell, et al., 1970b; Decreau, 1983; Higel and Wu Lei, 1984).

B. The dashed line in fig. 23 shows the asymptotic trajectory of plasma holes in the E3H + M2 field models. The shaded area

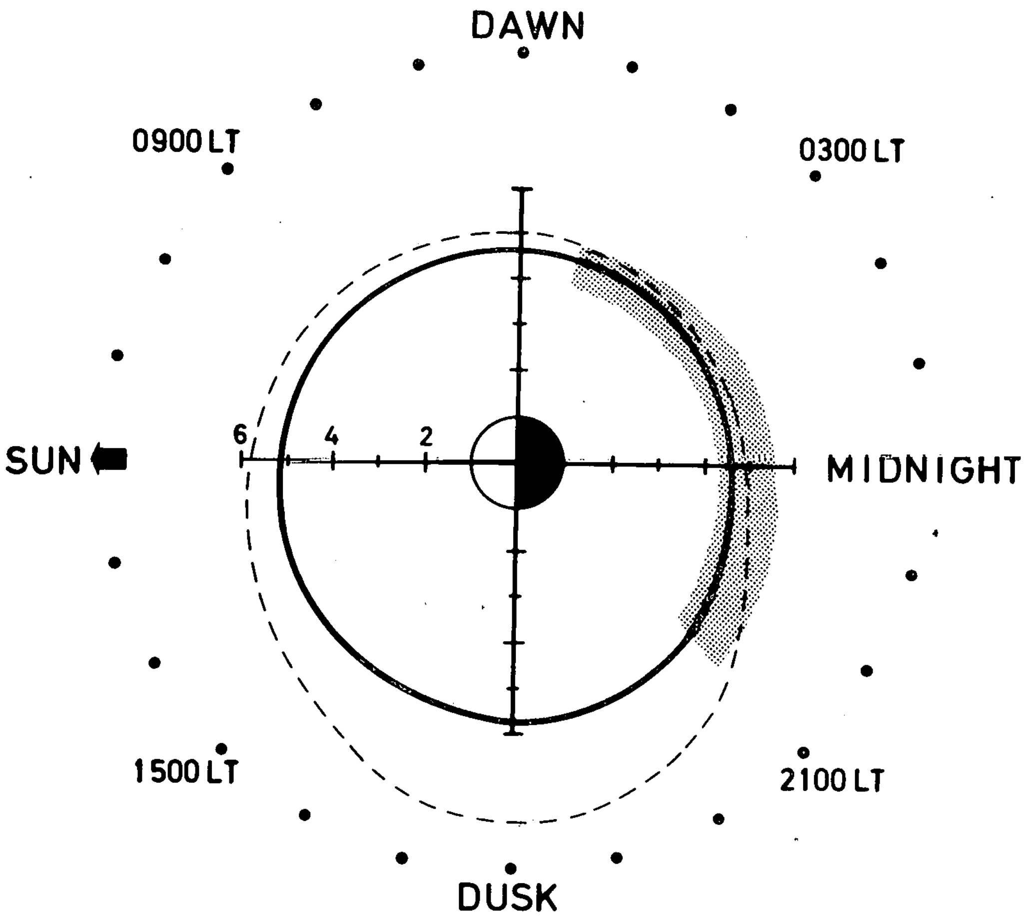

Fig. 23.- Equatorial cross section of a stationary plasmasphere model showing (i) the outer edge of the plasmapause region (dashed line) which, in this stationary model, coïncides with the asymptotic trajectory of plasma holes; (ii) the inner edge of the plasmapause region (solid line) which coïncides with E3H equipotential surface tangent to the ZRF surface. The shaded area corresponds to the region where the equatorial plasmapause is mostly observed when $K_p = 1$ according to a statistical study of whistler observations by Rycroft and Burnell (1970). The agreement between the theory and the observations is very satisfactory in this local time sector.

corresponds to the statistical limits within which Rycroft and Burnell (1970) observed the equatorial plasmapause positions between 2100 LT and 0500 LT, when $K_p = 1$. It can be seen that the theoretical results obtained with the E3H electric field model for f = 1, fit satisfactorily the statistical observations when $K_p \cong 1$-2.

C. The solid line in fig. 23 represents the equatorial cross section of the E3H equipotential surface which is tangent to ZRF surface at its minimum minimorum radial distance. We have identified this curve as the inner edge of the plasmapause region. Indeed, background plasma elements corotating inside this curve never traverse the ZRF surface : they are always stably confined in the gravitational potential well. Plasma density enhancements circulating outside, in the region between the solid line and dashed line, experience an outwardly directed interchange motion along the night side portion of their trajectory; but the net outward motion resulting from the centrifugal force is smaller than the average inward motion due to gravity. These plasma elements, if they become detached in the post-midnight sector, as illustrated in fig. 22, are recaptured in the gravitational potential well and fall back toward the plasmasphere at later local times; in this intermediate region plasma expands outwardly over a short radial distance but not far enough to escape up to the magnetopause. Therefore, the region between the solid line and dashed line can be identified with the plasmapause region. A plasma density gradient or "knee" develops there. Indeed, the partial outward expansion of the background plasma results there in a gradual density decrease like that actually observed in the plasmapause region.

It can be seen that in the post-midnight sector the plasmapause region is only 0.1 R_E thick, while at dusk the plasmapause density gradient extends over more than 3 R_E. Both whistler and satellite observations confirm this theoretical local time variation for the thickness of the plasmapause region. Indeed the sharpest density gradients have been observed after substorm events, in the post-midnight local time sector. The minimum observed thickness of the plasmapause is of the order of 0.15 R_E in good agreement with the model calculations illustrated in fig 23.

D. So far we have only discussed the position of the plasmapause region (i) in the case of the corotation E-field, and (ii) in the case of the E3H electric field when the scale factor f is assumed equal to 1.0. Fig. 24 shows the inner edge of the plasmapause region for values of f ranging between 0.7 and 1.3.

It can be seen that the plasmapause tends to become more symmetric and to extend at larger radial distances when the value of the scale factor f increases from 1 to 1.3. Note also the pronounced noon to midnight asymmetry obtained when f = 1.3. Such a noon-midnight asymmetry has, indeed, been observed by Gringauz and Bezrukikh (1976) and by Carpenter and Seely (1976) during prolonged quiet periods of time, when K_p was smaller than 1.

On the contrary when the value of the scale factor f is reduced from 1 to 0.7, the dawn-dusk asymmetry is enhanced and the bulge of the plasmasphere extends to larger radial distances in the dusk sector. Deformations of this kind are observed when the value of K_p is large and remains so for an extended period of time. Furthermore, when the geomagnetic activity increases it has been observed that the equatorial plasmapause in the post midnight region forms closer to the Earth. Rycroft and Burnell (1970) using whistler observations determined a statistical relation between the invariant latitude (Λ'_{pp}) of equatorial nightside plasmapauses and the values of the K_p index

$$\Lambda'_{pp} = 62.0 - 1.0\, K_p - 0.4\,\varphi \pm 1.8 \text{ [in degree]} \qquad (4.54)$$

where φ is the local time in hours for $-3h < \varphi < 5h$ and K_p the geomagnetic activity at the time of the measurements, with $0 < K_p < 5$. The

TABLE 1 : The invariant latitudes and equatorial positions of the plasmapause at 0100 LT, for different values of K_p, according to the statistical study by Rycroft and Burnell's (1970) (R.B. 70); by Carpenter and Park's (1973) : (C.P. 73).

K_p	0	1	2	5	9	Ref.
Λ'_{pp}	61.60°	60.60	59.60	56.60	(52.60)	R.B. 70
L_{pp}	5.11	4.80	4.52	3.82	(3.14)	R.B. 70
L_{pp}	5.7	5.23	4.76	3.35	(1.47)	C.P. 73

invariant latitude Λ'_{pp} is defined at an altitude of 1000 km : $L \cos^2 \Lambda' = 1 + 1000/6370 = 1.157$. The table 1 gives the values of Λ'_{pp} and L_{pp} at 0100 LT (φ = + 1) for different values of K_p.

Carpenter and Park (1973) have determined a similar relationship between the equatorial plasmapause position L_{pp} in the post-midnight local time sector and the maximum values of K_p during the 12 hours preceding the measurement. The predictions of this empirical relationship are also given in Table 1. We have used this relationship to determine a relation between the scale factor (f) of McIlwain's E3H electric field model, and, the value of K_p. Indeed, using the E3H(f) model one can determine the asymptotic trajectory of plasma holes for a series of E-field models characterized by different values of f. Considering that this asymptotic trajectory coïncides with the outer edge of the plasmapause region the following relation has been derived between f and L_{pp} at 0100 LT

$$L_{pp} = 0.24 + 5.96 \, f - 1.16 \, f^2 \tag{4.55}$$

Furthermore, since the empirical relationship (1.1) deduced by Carpenter and Park (1973) gives the equatorial plasmapause at post-midnight local time as a function of K_p, one can derive the following relationship between f and K_p

$$f = 2.55 - (1.85 + 0.403 \, K_p)^{1/2} \tag{4.56}$$

This relationship is also illustrated in fig. 25. It will be used in the next chapter to simulate time dependent electric field distributions. The variations of the three-hourly index K_p are available for any period of time. Therefore, at any instant of Universal Time the corresponding values of f can then be found from eq. (4.56), and the electric field model E3H(f) can then also be determined.

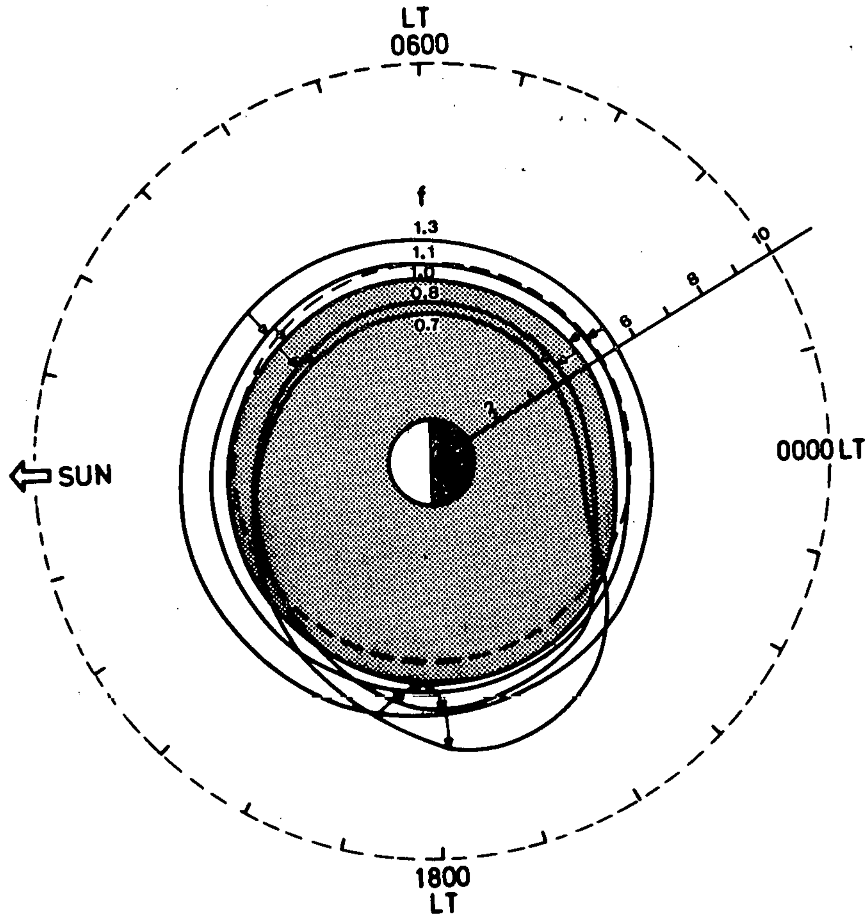

Fig. 24.- Equatorial cross section of the plasmasphere showing the calculated positions of the inner edge of the plasmapause region for a series of E3H type electric field models for different scale factors f ranging between 1.3 to 0.7. The inner edge of the equatorial plasmapause region has been identified with the equipotential surface tangent to the Zero Radial Force surface in the post-midnight sector. The shaded area corresponds to the portion of the plasmasphere which remains confined within the gravitational potential well

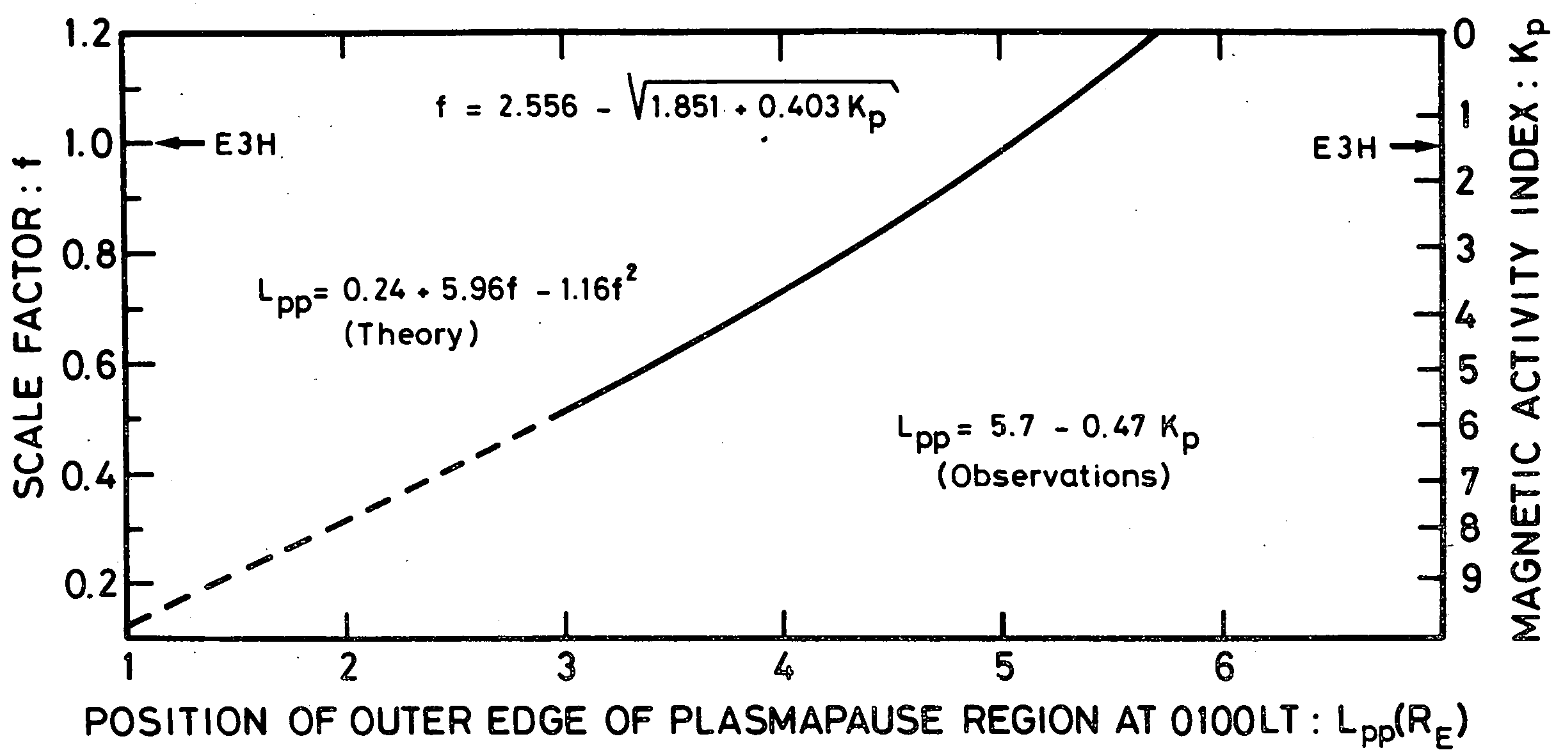

Fig. 25.- Empirical relation between the value of the K_p index and the scale factor f introduced by McIlwain (1974) in the E3H(f) model describing the magnetospheric electric distribution when K_p is outside the range from 1 to 2. The values of f are given by the left hand side scale; the corresponding values of K_p are given by the right hand side scale; the values of the post-midnight positions of the outer edge of the plasmapause region calculated with the E3H(f) model are given by the horizontal scale. When K_p increases, f decreases and the plasmapause at = 0100 LT forms at a smaller equatorial distance (L_{pp}).

Assuming that the E3H(f) family of models with variable f represent satisfactorily the actual magnetospheric electric field distribution at all radial distances and at all local times, the eq. (4.56) offers the interesting possibility to define a sequence of E-fields distributions corresponding to all values of K_p, and therefore for each Universal Time (t). This advantage will be used in the next chapter to study the deformation of the plasmapause for changing geoelectric field distributions.

But, before we present the numerical simulations for time dependent electric field models we discuss first, in the next sections, the formation of "multiple plasmapauses" and the smoothing out of plasma density gradients through the mechanism of interchange motion.

4.9. The formation of multiple plasmapauses

The formation of multiple plasmapauses, as reported in the literature, has often been observed after extended quiet times following periods of high geomagnetic activity (Corcuff, et al., 1972). The formation of multiple plasmapauses is explained as the consequence of the gradual outward displacement of the new plasmapause when the values of K_p steps down after a substorm; the corresponding values of the scale factor f increase then step by step. Indeed, when K_p is large a steep post-midnight plasmapause gradient is formed close to the Earth as indicated in Table 1. When subsequently the level of geomagnetic activity steps down to a lower contant values, the formation of a new plasmapause by the mechanism of plasma interchange motion operates at larger and larger radial distances in the post-midnight local time sector. The region between the old plasmapause (formed while K_p was high for a prolonged period of time) and the newly forming one has been depleted during the previous phase, i.e. when magnetospheric convection was strongly enhanced in the post-midnight sector. This depleted zone of the plasmasphere gradually refills by upward plasma diffusion from the topside ionosphere, as illustrated in fig. 26 and as described in chapter 3. The electric field would have to be stationary

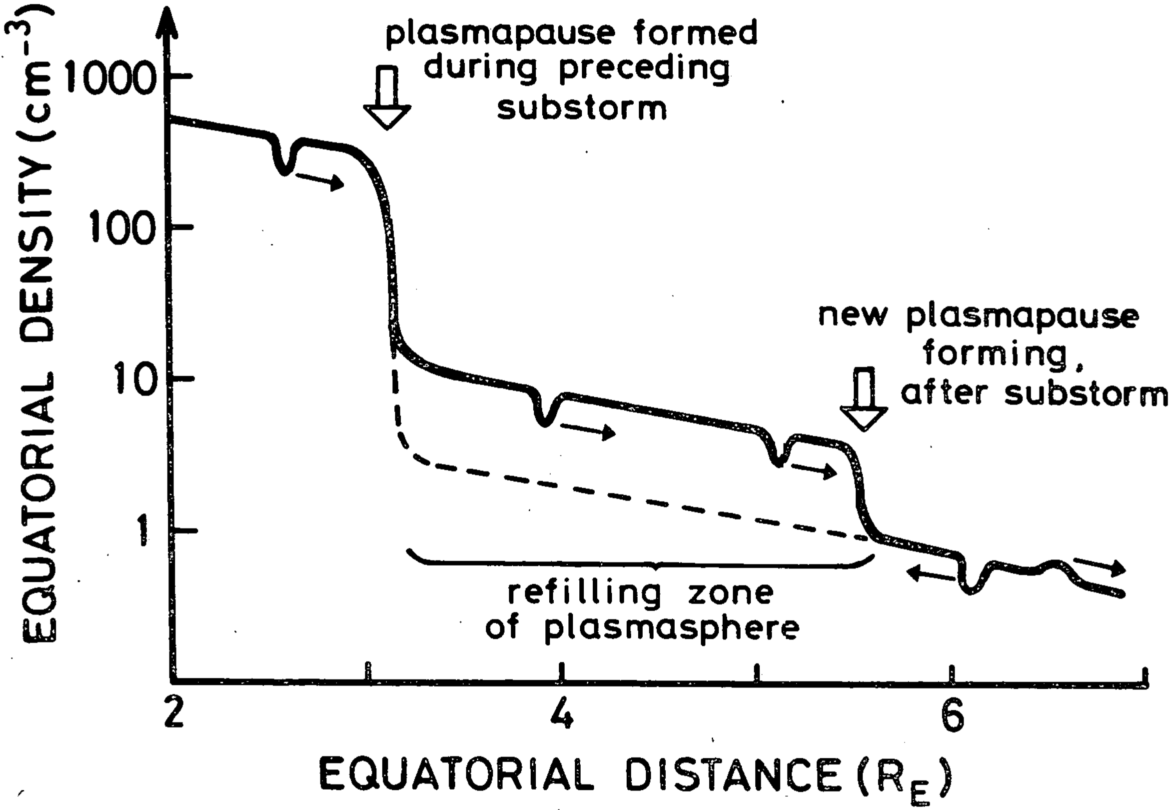

Fig. 26.- Illustration of the formation of "multiple plasmapauses" after an extended period of high geomagnetic activity. The gradual refilling of the depleted region between the old position of the plasmapause and the new one is shown by "steps" in the equatorial plasma density distribution. Only the outermost density "knee" determines the position of the actual plasmapause region.

for several days before the equatorial density has come back to its original level or to the diffusive equilibrium value corresponding to a sort of saturation level (see chapter 2).

According to this theory, step-shaped equatorial density distributions are expected for several days after prolonged periods of geomagnetic activity when the K_p values have been high. Such steps in the equatorial plasma density have often been observed and reported (Corcuff, et al, 1972; Chappell, et al., 1970a). The radial width and the height of these successive steps depend on the levels of geomagnetic activity, as well as on the time intervals of the successive phases in the recovery period during which the geomagnetic activity decreased step by step.

This sequence of successive events gives rise to the formation of multiple density gradients or knees in the equatorial plasma density distribution. These features have been interpreted as multiple plasmapauses. But, if the plasmapause is considered as the outer surface of a plasmasphere containing thermal plasma which is stably confined in the gravitational potential well, then it is preferable to avoid the improper expression : multiple plasmapauses; indeed, only the outermost density gradient - whatever small it can be - determines the location of the plasmapause region where the centrifugal force balances the gravitational force. The additional density knees inside the plasmasphere are just disappearing vestiges of former plasmapauses, but are no longer real plasmapauses.

4.10 Smoothing out of plasmapause density gradients

The plasma density decreases often by two orders of magnitude over a radial distance of less than 0.2 R_E in the plasmapause region. The steepest plasmapause gradients have been observed in the post-midnight and dawn sectors after geomagnetic activity enhancements (Chappell, et al., 1970a). This is precisely where the theory predicts that interchange motion is most efficient (i) because of the reduced values of the integrated Pedersen conductivity, and also (ii) because of the enhanced convection velocity in the post-midnight sector. But observations have also indicated that the thickness of the plasmapause region increases with the local time angle. It has been shown by Horwitz (1983b) that the observed broadening of the plasmapause region cannot be explained nor by Bohm diffusion nor by wave-particle interactions.

We have already seen in fig. 23 that the thickness of the plasmapause region increases from the post-midnight sector - where the plasmapause is formed - to the dusk sector where the separation between the inner and outer edge of the plasmapause region has a maximum extent sometimes larger then 3 R_E. This broadening and the associated smoothing out of the initial plasmapause gradient while it is convected around the Earth results from the divergence of the E3H equipotential lines in the dayside local time sector. This can be considered as adiabatic broadening of the initial plasmapause region. But, there is another physical mechanism which contributes to smooth away the sharp plasma density gradients observed at the equatorial plasmapause, as well as inside the plasmasphere itself. It is shown below that plasma interchange motion can contribute to this smoothing out effect much more efficiently than any other dissipation process examined so-far, e.g. Coulomb collisions, Bohm-diffusion or wave-particle interactions.

Fig. 27 shows a steep density gradient formed during an earlier period when geomagnetic activity was high. The new plasmapause forming during the following lower activity period, is located at much larger radial distances for the reason explained in section 4.9. The density gradients associated with the new and the older plasmapauses broaden and smooth out as a consequence of the plasma interchange process described in sections (4.3) and (4.4). Indeed, any plasma density depression formed in the intermediate refilling region moves outwardly toward the place where the new plasmapause is presently forming (fig. 26). Plasma density enhancements drift in the opposite

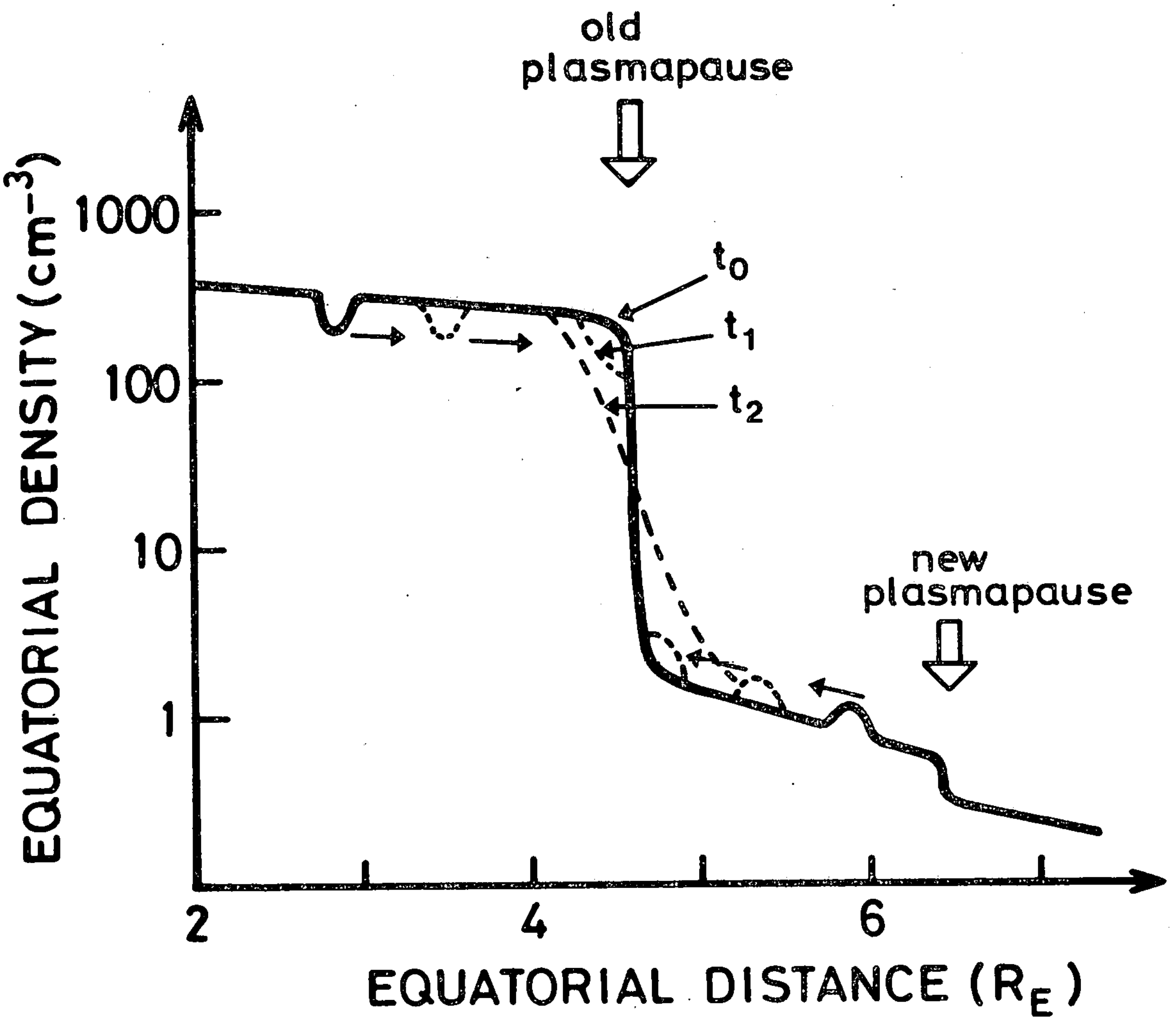

Fig. 27.- Illustration of the mechanism responsible for the broadening of the plasmapause region. The steep plasmapause density gradient, formed in the post-midnight sector, broadens rapidly by plasma interchange motion when it corotates to the dayside local time sector. Non-local diffusion and dissipation processes occuring in the collision dominated ionospheric regions coupled to the old plasmapause by field-aligned (Birkeland) currents determine the maximum rate of smoothing out of magnetospheric density gradients.

direction (fig. 27) with the maximum interchange velocity determined in section (4.4). This mechanism transports plasma to the outer edge of the old plasmapause; this fills in the magnetic flux tubes located just beyond the density knee.

Let us now consider a plasma hole formed closer to the Earth than the old plasmapause position. These plasma elements spiral upwards until they reach the inner edge of the first density knee and dissolve there where their density becomes equal to the background density. This contributes to decrease the equatorial density in magnetic flux tubes at the inner edge of the density knee. The dashed lines in fig. 27 illustrate the time evolution of the equatorial density distribution, and, show how the process of interchange motion broadens the old plasmapause region by decreasing the steepness of the density gradient. The same non-adiabatic process works of course also at the location of the new plasmapause.

The characteristic time constant for this non-adiabatic broadening of regions with sharp density gradients, depends on the value of the integrated Pedersen conductivity (Σ_p) in the ionosphere. Indeed we have seen in section 4.4 that the value of Σ_p determines the maximum plasma interchange velocity, u, and consequently the broadening time (t_B). If the values of Σ_p are large, as in the ideal MHD limit, interchange motion is slow and t_B is large. On the contrary when Σ_p is small the maximum interchange velocity due to gravity is enhanced; the time constant for t_B is then of the order of 33 h, which is rather comparable to the broadening time which can be deduced from observations.

It can therefore be concluded that the sharp density gradient formed in the post-midnight region at the onset of a substorm event, broadens not only because of the divergence of the plasma streamlines in the dayside local time sector, but also via an additional non-adiabatic process : plasma interchange motion.

Furthermore, from this conclusion it can be inferred that, after a sufficiently long period of time, with no substorms, all plasma density gradients should have been smoothed out. Indeed, if external factors would not perturb the magnetosphere over and over again, the plasma density distribution would eventually relax to a more uniform distribution, and all sharp density gradients would have been smoothed out. However, because of the non-stationary interaction of the magnetosphere with the gusty solar wind the plasmasphere is almost never in such an idealistic steady state for long enough time to achieve this smoothing out process completely. New plasmapause density gradients are formed closer to the Earth when the ZRF surface penetrates deeper into the plasmasphere at the onset of a magnetospheric substorm. Therefore, the existence and persistence of plasmapause regions with sharp plasma density gradients in planetary magnetosphere does not only depend on the existence of a ZRF surface and on low enough values for the integrated Pedersen conductivity, but it implies furthermore that the smoothing out process has a time constant which is large compared to the time between substorm associated convection electric field enhancements.

5. DEFORMATION OF THE PLASMASPHERE AND OF ITS OUTER BOUNDARY

5.1. Simulation of the deformation of the plasmapause by a ideal short duration enhancement of the geoelectric field intensity

So far we have used time independent electric field models in our numerical simulations. This has been useful to understand stationary transport phenomena inside the plasmasphere (chapter 3), and, to explain the mechanism of formation of the Light Ion Trough (chapter 2) and of the equatorial Plasmapause Region (chapter 4). In this chapter we make use of time dependent electric field models in order to simulate the deformations of the plasmasphere and of its outer boundary during typical substorm events.

We have seen that in the case of stationary electric fields the asymptotic trajectory of plasma holes can be used to trace the position of the outer edge of the plasmapause region. In the previous chapter we have also shown that this asymptotic trajectory changes when the electric field distribution changes as a function of K_p; We have for example used the E3H(f) models for different values of the scale factor f. In section 4.8, we have established a relationship between f and the K_p- index. This relationship is given by eq. (4.56). It will now be used to calculate f(t) for a period of several days when the values of the three-hourly index K_p are given as a function of universal time (t).

A. We will first examine the ideal case of a short duration enhancement of the geoelectric field associated with an impulsive enhancement of the geomagnetic activity index K_p. The universal time variation of K_p, with a peak value of 5 between t = 24h and 27h UT, is shown in the upper panel of fig. 28. Considering that the trajectories of plasma holes can again be used to trace the outer edge of the plasma-pause region, we have calculated the successive positions of a series of

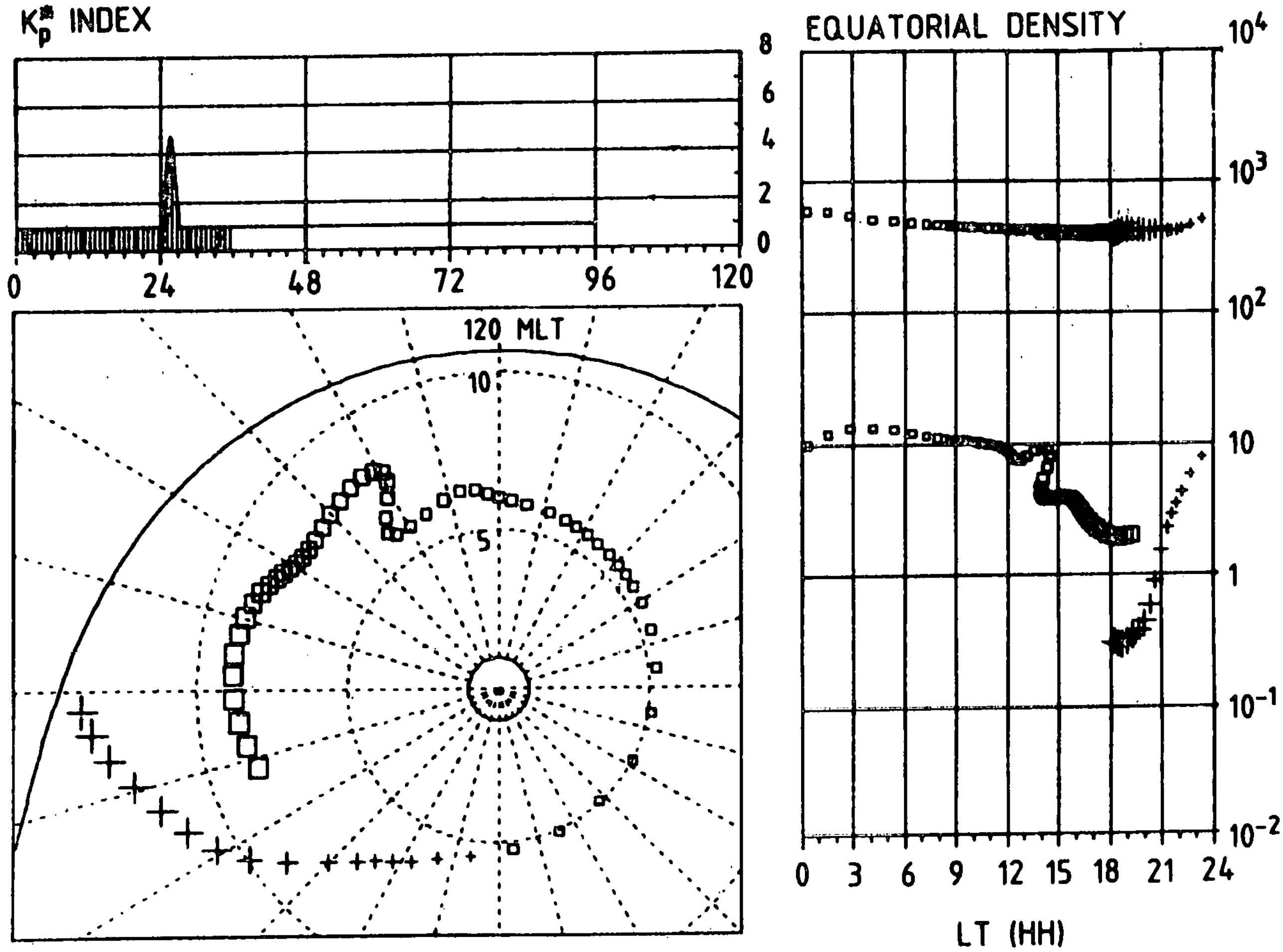

Fig. 28.- The lower left hand side panel is an equatorial cross section of the plasmasphere showing the position of the outer edge of the plasmapause region 12 hours after an ideal geoelectric field intensity enhancement which is indicated in the upper panel by a peak in the K_p index between t = 24h UT and 27h UT. The E3H(f) electric field model described in Appendix B is used with eq. (4.56) in this simulation. The values for the integrated Pedersen conductivity have been taken from the model of Gurevitch et al. (1976) to calculate the plasma interchange velocity and the successive positions of the plasma holes which identify the outer edge of the plasmapause region. The size of the symbols used to indicate the positions of the plasma elements is proportional to their equatorial cross section. The type of symbol change after the plasma element has traversed the midnight meridian plane. The right handside panel gives the (i) actual equatorial density in the drifting plasma assuming their initial density at φ = 1800 LT and R = 14 R_E is equal to 0.3 cm^{-3} (refilling of the magnetic flux tubes has not been taken into account in this simulation); (ii) the saturation values of the equatorial density corresponding to diffusive equilibrium. The tail-like structure in the afternoon sector is the deformation of the plasmapause consequent to the short duration enhancement of the dawn to dusk electric field component.

large plasma density depressions released successively each half-hour universal time at 1800 LT and R = 14 R_E. As a consequence of interchange motion, these plasma holes always tend toward the ZRF surface. In the nightside, all plasma holes released from anywhere in the magnetosphere converge rapidly in the post-midnight sector toward the same asymptotic trajectory because of the large plasma interchange velocity in this local time sector. The empirical model of Gurevitch, et al. (1976) described in the Appendix D has been used to calculate this maximum interchange velocity. See Apppendix H for a description of the computer program.

A series of different simulations have indicated that plasma holes released from very different radial distances in the dusk sector drift all in the post-midnight local time sector toward almost the same radial distance. Subsequently, they proceed together toward the dayside along nearly the same trajectory; in the dayside this trajectory coïncides approximately with an equipotential line of the E3H(f) field. Indeed, in the dayside the values of Σ_p are significantly greater, and, consequently the maximum interchange velocity is nearly equal to zero.

The lower left panel of fig. 28 indicates the positions of the 72 plasma holes released during the 36 previous UT hours. This snapshot shows the positions of the outer edge of the plasmapause region 12 hours after the beginning of the geoelectric surge. During the 24 first hours K_p was constant and equal to 1; the corresponding value of f was then equal to 1.05. When K_p increases from 1 to the maximum value of 5, f drops from 1.05 to 0.59 according to eq. (4.56); the convection velocity is then strongly enhanced in the post-midnight local time sector and the dawn to dusk component of the external electric field E3H(f) is also significantly enhanced. As a consequence, the sharp increase of K_p at 24h UT coïncides with a sunward drift of the whole plasmasphere, both in the nightside and dayside sectors. Furhtermore, because of the enhanced eastward convection velocity in the post-midnight sector, the centrifugal force balances the gravitational force at radial distances which are closer to the Earth; indeed, we have seen that the minimum radial distance of the ZRF surface is displaced toward the Earth when f becomes smaller (see figs. 24 and B4). At the onset of the K_p increase and until 25:30h UT, when K_p has reached its maximum value, the shell of plasma which is peeled off from the plasmasphere becomes increasingly thicker. When K_p culminates, the plasmasphere is peeled off at a minimum equatorial geocentric distance of 3 R_E in the post-midnight local time sector, i.e. where the centrifugal force is largest and where the integrated Pedersen conductivity is smallest. As soon as K_p decreases, the location where the plasmasphere is unstable with respect to plasma interchange motion retreats to larger radial distances. When K_p comes back to its pre-storm value (K_p = 1), the peeling off mechanism forms a new plasmapause at R = 4.97 R_E and 0230 LT.

It takes almost 12 hours for a plasmapause formed in the post-midnight sector to propagate into the post-noon local time sector. In fig. 28 the plasma holes which are located closest to the Earth at 1430 LT are precisely those corresponding to a plasmapause which has been formed in the post-midnight sector 10:30 hours earlier, i.e. at t = 25:30h UT when K_p was maximum.

The larger radial positions of the plasmapause between 1230 LT and 1430 LT result from the retreat of the peeling off location to larger radial distance as soon as K_p decreases after 25:30 UT. The tail like structure displayed in fig. 28 between 1400 LT and 1600 LT is a consequence of the combined effects of (i) the sunward expansion of the dayside plasmapause at the time of the substorm onset and (ii) the lower convection velocity at larger radial distances (i.e. due to differential angular velocities).

At subsequent universal times, K_p remains equal to 1.0, and, the ripple or tail-like deformation of the plasmasphere corotates toward dusk. At each short duration substorm event, a bulge is formed in the noon local time sector as a result of the general sunward expansion of the whole dayside plasmasphere. During the recovery phase, this bulge becomes sometimes a tail-like structure which eventually corotates into the afternoon and dusk sectors.

This characteristic behaviour of the plasmapause after a short-duration magnetic substorm, is well confirmed by whistler and satellite observations (Chappell et al., 1971; Corcuff et al., 1972; Corcuff and Corcuff, 1982; Decreau, 1983; Carpenter, 1970b, 1983).

B. The right handside panel of fig. 28 gives the local time distribution of the equatorial density in the plasma holes (lower series of symbols) as well as the corresponding densities (upper series of symbols) for diffusive equilibrium. The lower series of symbols represent the actual equatorial densities in plasma holes, just outside the plasmapause "knee". Their initial density at 1800 LT and R = 14 R_E is arbitrarily taken equal to 0.3 cm^{-3}. In this simulation we donot consider the additional process of flux tube refilling discussed in section 3.6. The size and the type of symbols which have been used to identify successive plasma holes is the same as in figs. 14 and 15 : their cross section is proportional to the size of these symbols, while the type of symbols is changed each time the local time angle becomes equal to 0000 LT, i.e. each time the plasma element returns to the local midnight meridional plane.

Notice that the equatorial density in plasma holes, just outside the plasmapause, is more than two orders of magnitude smaller than the corresponding diffusive equilibrium value shown in the upper part of this panel. The smallest equatorial densities are found in the bulge region.

At the onset of the K_p associated increase of the dawn to dusk component of the electric field, the nightside plasmasphere is compressed by the sunward drift of plasma. This compression is associated with an increase of the equatorial plasma density, and, is well simulated in our time-dependent model.

Furthermore, in the aftermath of temporally isolated substorms that follow relatively quiet periods of time, outward radial plasma drift has consistently been observed in the post-midnight sector (Carpenter, et al., 1972; Carpenter and Seely, 1976; Carpenter, 1983). This outward expansion of the post-midnight plasmasphere after an isolated substorm, is explained in this model, as a consequence of the decompression of the nightside plasma which had previously been compressed by the enhanced convection E-field.

The tail-like structure between 1400 LT and 1600 LT appears, in the right handside panel, as a density decrease associated with the sunward expansion of the dayside flux tubes which form a noon local time bulge at the onset of the geoelectric surge.

C. The amplitude, width and size of plasmapause deformations depend very much on the maximum value of K_p, on the total duration of the simulated substorm event, as well as on the steepness of the geomagnetic activity enhancement. When high geoelectric (and geomagnetic) activity is observed over longer periods of time than in the case illustrated in fig. 28, the tail-like bulge formed at 1200 LT, has broader azimuthal and radial extents. For levels of geomagnetic activity higher than 5 the radial extent of this tail is larger than that shown in fig. 28.

The simulation presented in this figure for a time dependent electric field model, illustrates how a bulge is formed at noon local time during each new substorm and how a tail-like structure develops subsequently due to differential convection velocities at different radial distances. The substorm associated ripple formed in the plasmapause surface corotates toward dusk during the recovery phase. This sequence of events is also well supported by observations indicating an eastward displacement of the plasmasphere bulge after periods of high geomagnetic activity (Carpenter, 1970, 1983).

5.2. Simulation of the event of 29 July 1977

A. Let us now consider an extended period of several days including 29 July 1977 when, after a period of several days of low geomagnetic activity, the K_p index increased suddenly to a maximum value of 7. The geomagnetic index for this period is shown in the upper panel of fig. 29. The equatorial positions of the outer edge of the plasmapause region are given in the lower left-hand side panel at 00h UT on 29 July, i.e. just before the explosive onset of the magnetic storm.

This simulation started at 00h UT on 27 July. From then on, and for a period of 48 hours, plasma density holes were released every half hour at 14 R_E in the dusk meridional plane. As explained before, the drift paths of these plasma holes determine the position of the outer edge of the plasmapause region.

During the first two days, the K_p index remained less than 2. During this prestorm period a series of three small amplitudes bulges were formed in the noon local time sector at each slight increase of K_p. Later on, these ripples corotated eastward toward the dusk sector as explained in the previous section; at 00h UT on 29 July these bulges are located near 1500 LT, 1730 LT and 1900 LT respectively (see fig. 29).

At the onset of the large magnetic storm, early 29 July, the nightside plasmasphere is compressed and the plasmapause is displaced earthward to R = 3 R_E, while the dayside plasmasphere and plasmapause move sunward under the action of the enhanced dawn to dusk component of the electric field. This rather explosive expansion of the dayside plasmapause is illustrated in fig. 30; it corresponds to a snapshot taken 6 hours after the beginning of the storm. The new plasmapause formed at midnight near 3 R_E propagates eastward almost with the corotation velocity. It takes almost 12 hours for this new plasmapause to reach the noon local time sector, and 18 hours to drift

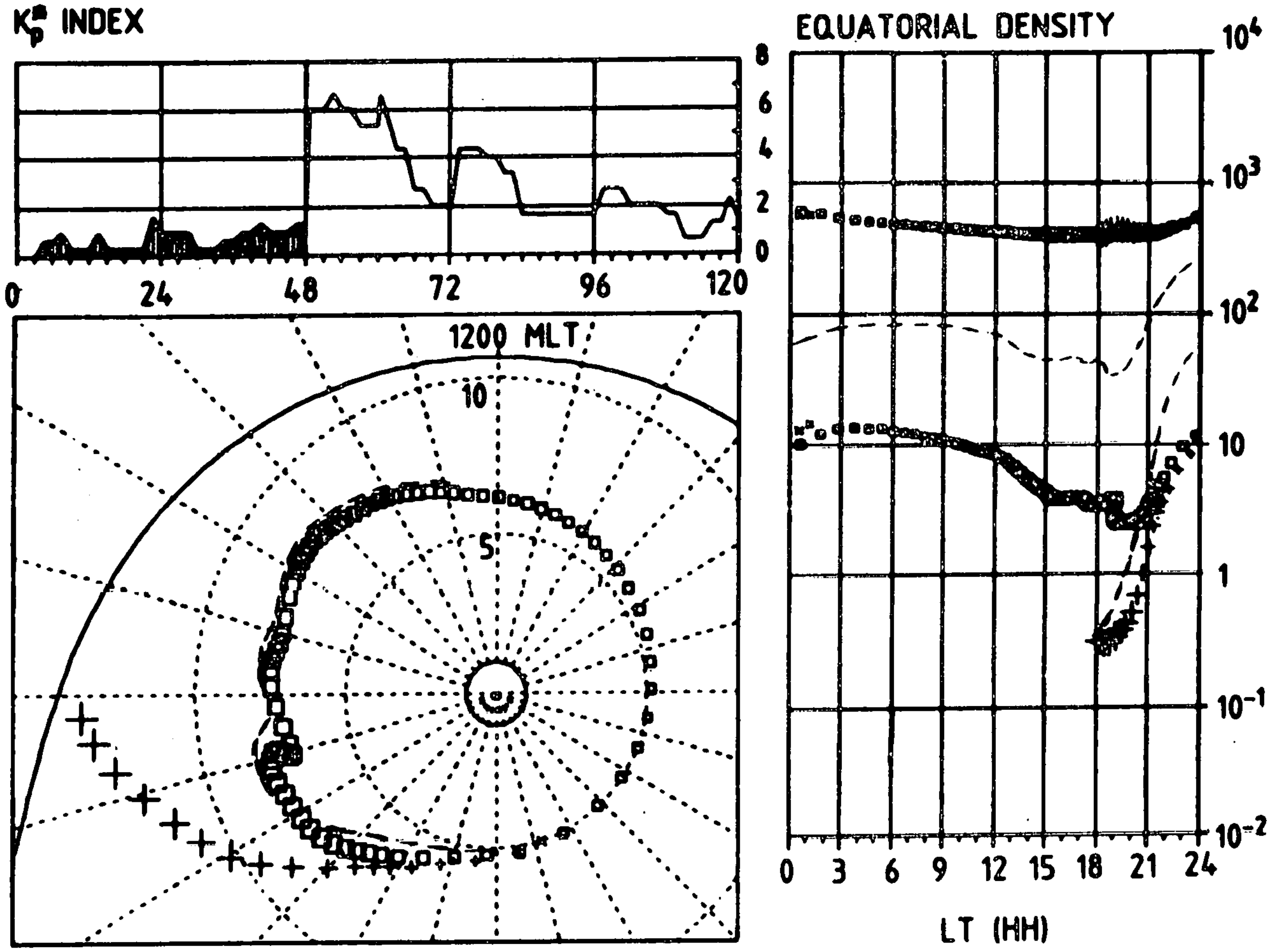

Fig. 29.- Equatorial plasmapause positions and densities as in fig. 28; this simulation illustrates the deformations of the plasmasphere at 00h UT on 29 July 1977 which have been produced during the previous 48h by small amplitude variations in the geomagnetic activity (see upper left panel). The dashed contours correspond to a similar simulation obtained by taking into account the effect of flux tube refilling.

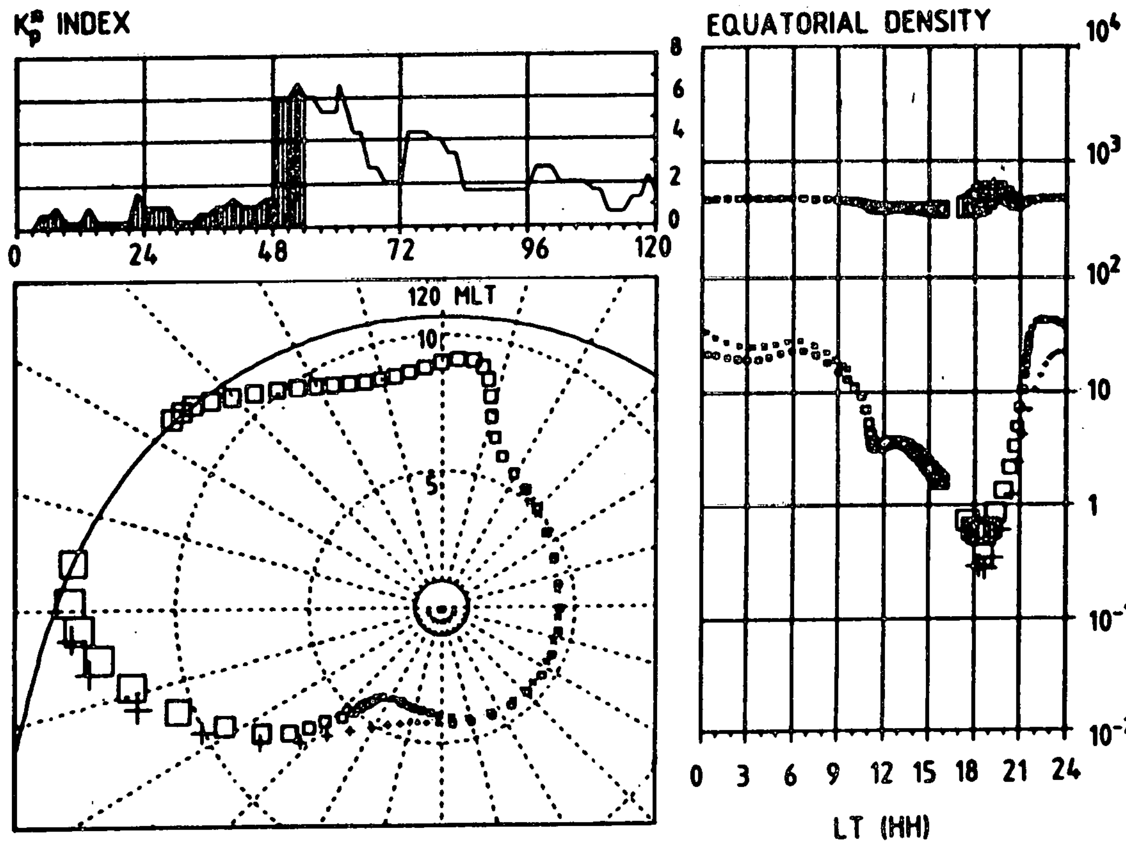

Fig. 30.- Equatorial plasmapause and equatorial densities as in fig. 29 but at 06h UT on 29 July 1977. This snapshot taken six hours after the onset of the major storm event illustrates (i) the inward motion of the plasmapause in the post-midnight local time sector when K_p is severely increased; (ii) the compression of the plasmasphere in this same LT sector; (iii) the explosive sunward expansion of the dayside plasmasphere.

into the duskside one. A few hours later, the outward propagating front of dayside plasmapause will encounter the magnetopause; the afternoon and dusk plasmasphere extends up to the outer edge of the magnetosphere. As a consequence of this explosive radial expansion the equatorial plasma density distribution is drastically reduced, and, decreases nearly as L^{-4}. On the contrary, the plasma in the nightside is highly compressed; its density is strongly increased, there.

B. As in fig. 28, the right handside panel of fig. 30 displays the equatorial densities in flux tubes located just outside the plasmapause region, as well as the corresponding diffusive equilibrium values. In this simulation the refilling of the plasma density depressions has not been taken into account. The multiple density values seen in this panel do not, therefore, correspond to effect of flux tube refilling, but to the difference in radial distances of plasma holes after the first revolution around the Earth.

Refilling of deeply depleted plasma elements has been shown to be a slow process (sections 3.2 and 3.6). The dashed lines in fig. 29 indicate the results for a similar simulation except that refilling of flux tubes is taken into account in the numerical calculations. It can be seen that the slight differences seen in the dusk and post-dusk positions correspond to plasma holes which have already drifted for at least one full day and whose density has significantly increased. Consequently the refilling rate of a highly depleted plasma hole does not influence a great deal their position, nor that of the plasmapause in the post-midnight sector, where both simulations give the same results. Note also that the minimum radial distance of the ZRF surface, where interchange instability is driven by the centrifugal force, is of course independent of the process of refilling of magnetic flux tubes.

C. In a recent article Corcuff, et al. (1985) have compared the positions of the plasmapause predicted by this dynamical model, and the positions of observed plasma density gradients deduced from whistler as well as from satellite measurements.

Figs. 31 and 32 show the geocentric distances of the outer edge of the plasmapause region as a function of Universal Time, in three sets of local time sectors, and for two different time dependent electric field models : the right handside panels correspond to the E3H(f) model already used in previous simulations. The results with Volland-Stern's model, for $\gamma = 2$ (also described in the Appendix B), are shown in the left handside panels. The results for the local time sectors 00-01, 06-07, 09-10, 12-13, 15-16 and 18-19 LT are shown in the panels a, b, c of figs. 31 and 32. The solid lines represent the theoretical plasmapause positions as calculated with the two time-dependent E-field models, and, with plasma interchange velocities calculated for the Σ_p-model of Gurevitch et al. (1976). The various circles in these panels show the results deduced from the analysis of whistler observations which propagated near the plasmapause and which have been recorded at Kerguelen (L = 3.7), and, at General Belgrano (L = 4.5) in Antarctica. Their ordinates represent the L-values of the whistler ducts; their type and size indicate, according to the scale on the right hand side, the order of magnitude of the equatorial electron density. Solid circles correspond to the dense plasmasphere, and open circles to the tenuous region beyond the plasmapause; dots inside open circles and stars coïncides with the plasmapause or to expanding plasmasphere regions which are characterized by relatively low densities or which are in the process of refilling with cold ionospheric plasma.

The small triangles in fig. 32 illustrate, in a similar way, the values of the equatorial electron density deduced from in-situ measurements made with the relaxation sounder flown on the GEOS-1 satellite (Etcheto and Bloch, 1978). Because of experimental and orbital limitations, only densities below 75 cm^{-3}, measured between 4 and 7.5 R_E, are available from GEOS-1 data. Furthermore, in July 1977, the satellite apogee was located in the afternoon sector; therefore, GEOS-1 data are shown only in figs. 32a, b and c for the noon, afternoon and dusk local time sectors, respectively.

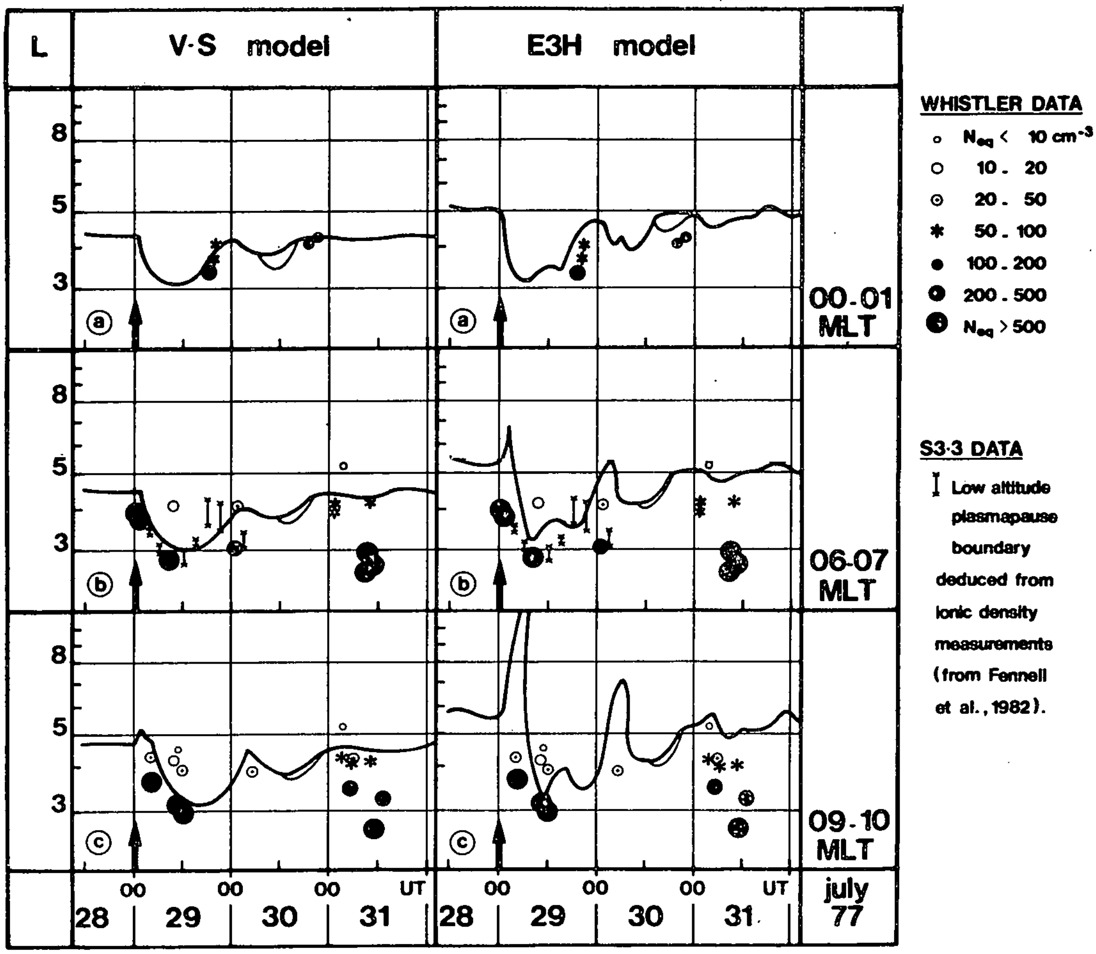

Fig. 31.- Radial distances of the equatorial plasmapause in different local time sectors versus Universal Time, between 12 UT on July 28 and 24 UT on July 31, 1977. The time dependent Volland-Stern's (on the left hand side) and McIlwain's E3H (on the right hand side) electric field distributions have been used in these model calculations which take into account the effect of plasma interchange motion. The different symbols show the results deduced from S3-3, GEOS-1 and whistler observations; their type and size indicate the order of magnitude of the equatorial electron density according to the scale on the right hand side. Panels a, b and c correspond to the 00-01, 06-07 and 09-10 local time sectors respectively (after Corcuff et al., 1985).

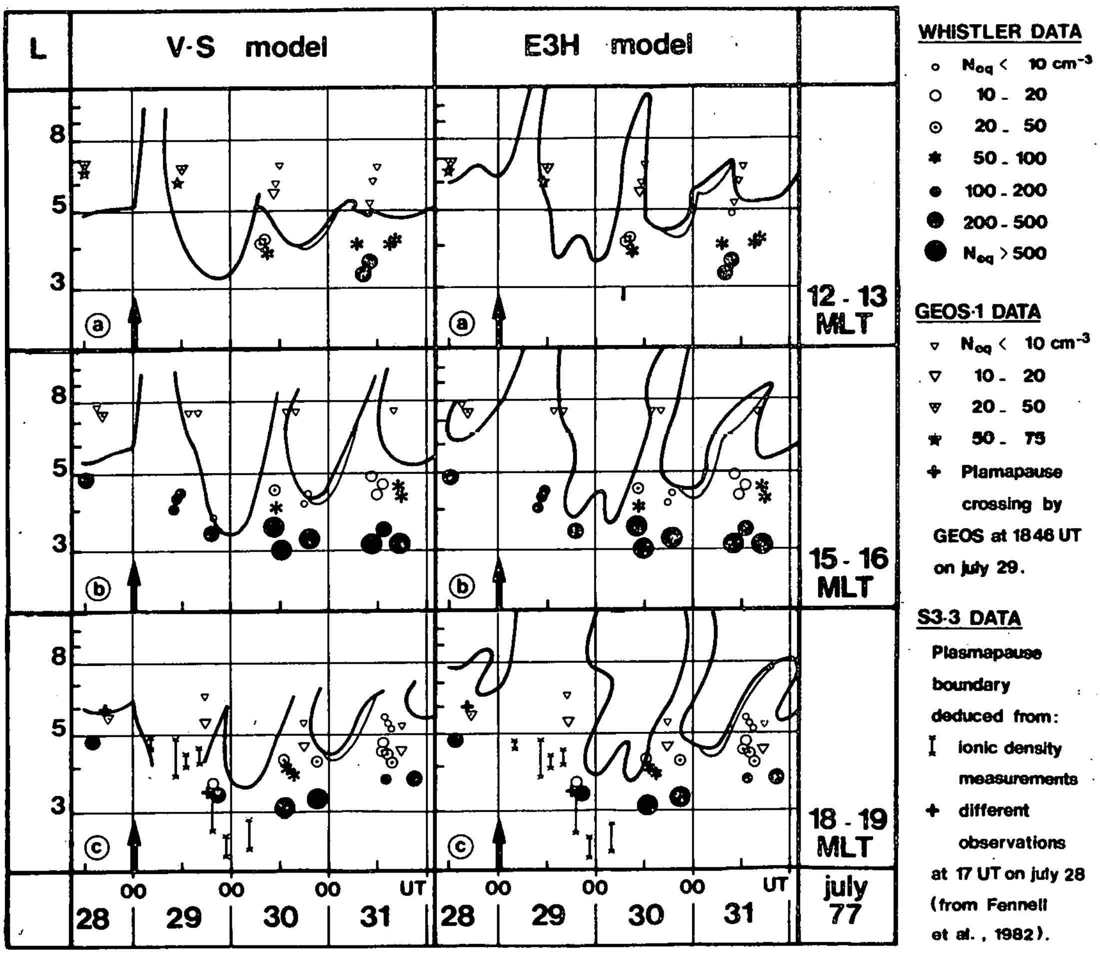

Fig. 32.- The same as in figure 31, but for other magnetic local time sectors : 12-13 LT (a), 15-16 LT (b) and 18-19 LT (c) (after Corcuff et al., 1985).

The Light Ion Trough (LIT) boundary deduced by Fennell, et al. (1982) from ionic density measurements made with the satellite S3-3, between 1000 and 4000 km altitude near dawn and dusk, are indicated by vertical bars in figs. 31 and 32; the length of some bars is relatively great because the density data on July 29 showed often a very slow variation with invariant latitude.

In figure 32c, the cross at 17 UT on July 28 locates the low-altitude LIT boundary obtained from different S3-3 observations; the cross at 1846 UT on July 29 corresponds to the equatorial plasmapause crossing by GEOS. It is worthwhile to note the good agreement between the dusk plasmapause positions deduced from knee-whistlers ($3.4 < L_{pp} < 3.6$ at 1955 UT), GEOS-1 ($L_{pp} = 3.4$ at 1846 UT) and S3-3 ($2.6 < L_{pp} < 3.5$ at 1930 UT) data.

a) From figures 31 and 32, it can be seen that, according to both simulations, the plasmasphere experiences large radial displacements in all local time sectors as a consequence of the intense substorm activity during the first 15 hours of July 29. However, the amplitude of these deformations and the response time of the plasmasphere depend very much on the magnetic local time and on the assumed geoelectric field distribution.

In the post-midnight local time sector (fig. 31a), there is an immediate compression of the plasmasphere when K_p increases : the plasmapause moves from beyond 4 R_E to a minimum position of 3 R_E in less than six hours. This is consistent with current ideas about plasmapause dynamics based on experimental evidence (Chappell et al., 1970a; Carpenter and Park, 1973; Corcuff, 1975).

At the same time, the noon plasmapause moves outward immediately after the Storm Sudden Commencement (SSC) which is indicated by an arrow at 00 UT on July 29 (fig. 32a). The relatively high values of the equatorial electron densities ($N_{eq} \sim 65$ and 45 cm^{-3}) measured by GEOS-1 in this local time sector, at 11 and 12 UT on July

29, nicely confirm the radial expansion of the dayside plasmasphere predicted in both model calculations.

In both simulations the inward displacement of the post-midnight plasmapause, appears in the dayside with a time delay which increases linearly with local time. The experimental data confirm these theoretical results, especially in the dawn sector (fig. 31b) where the data from the S3-3 satellite are in good agreement with those deduced from whistlers and from GEOS-1 observations. In this sector the plasmapause moves closer the the Earth with a short time delay after the SSC; it reaches a minimum radial distance of 3 R_E around 12 UT on July 29, in good agreement with both model calculations (Corcuff, et al., 1985).

b) According to the experimental data in figure 32c the plasmapause also moves closer to the Earth in the dusk sector just after the SSC : two distinct successive inward motions can be identified. The first inward motion brings the duskside plasmapause from a pre-SSC position close to 6 R_E to a post SSC position at 4.8 R_E. This inward motion is rather well simulated by the calculations based on the Volland-Stern's model (fig. 32c, left hand side panel). In this E-field model the stagnation point moves closer to the Earth when the dawn-dusk E-field component increases, i.e. when K_p is enhanced. The outer part of the duskside plasmasphere is then ripped off by an enhanced westward convection velocity.

A rather different evolution of the plasmapause position is shown in the right hand side panel of figure 32c obtained with the time dependent E3H model. According to this model, the duskside plasmasphere and its outer edge expand radially, up to the magnetopause beyond 10 R_E, immediately after the onset of the SSC. As a consequence, the equatorial density distribution in the dusk sector is reduced. Also possibly, as a result of this radial expansion, another "knee" can be formed closer to the Earth at the boundary between the dense inner corotating part of the plasmasphere and an outer expanded one.

It can therefore already be concluded that in the dusk local time sector the position of the outer edge of the plasmasphere obtained with the time dependent model of Volland-Stern differs drastically from that calculated with the E3H(f) model. In the former case this boundary moves closer to the Earth and the sheared plasmasphere should terminate rather steeply, while in the latter case the duskside plasmasphere is widely expanded after the onset of the SSC. At a first glance, the experimental data shown in figures 32c, between 00 UT and 24 UT on July 29, seem to support better the former elementary E-field model than the latter one. However, these observations can equally well be used in support of the E3H model calculations and can be interpreted as the inner edge of an expanded outer plasmasphere region. Indeed, the density profile in the afternoon and dusk sectors obtained from GEOS-1 between L = 7.7 and L = 4, resembles there an L^{-4} density distribution; this is typical of the expanded plasmaspheres which are often observed in these local time sectors (Chappell et al., 1970b; Berchem and Etcheto, 1981; Décréau et al., 1982; Corcuff and Corcuff, 1982). The relatively low values of n_{eq} measured in this region show that this expanded part of the plasmasphere is partly depleted, as indeed predicted from the E3H model calculations. A clear cut answer to these two alternatives scenario would require, however, detailed multistation and coordinated observations including plasma bulk velocity measurements (Corcuff, et al., 1985).

c) A second large amplitude inward displacement of the duskside plasmapause starts at 18 UT on July 29, i.e. almost 18 hours after the SSC; as already discussed above, this delay corresponds approximately to the time required for a plasma element to be convected from the midnight to the dusk sectors. The observed geocentric distance of the equatorial plasmapause decreases then in less than 6 hours from 4.8 R_E to 3.4 R_E.

These experimental results support those found by Décréau et al. (1982), Higel and Wu Lei (1984), and Décréau (1983), who studied the dynamical response of the thermal plasma parameters measured by GEOS-1 and GEOS-2 as a function of the level of geomagnetic activity. These observations are in favour of the mechanism of formation of the plasmapause described in this study; according to this theory, there is a peeling off, and, an earthward motion of the post-midnight plasmasphere when substorm activity increases. The peeling off mechanism by plasma interchange motion leads to the formation of a new plasmapause closer to the Earth in the post-midnight local time sector. Subsequently, this new boundary corotates toward the dayside; the time delay after which the inward motion is observed in the dayside is approximately proportional to the local time corresponding to the corotation propagation time (see chapter 4).

According to our two model simulations, it takes approximately 18 hours for the new plasmapause formed near midnight to corotate around the Earth and to reach the duskside. The minimum plasmapause position shown in figures 32c, near 00 UT on July 30, is a direct consequence of this corotation effect. The other two minima in the theoretical duskside plasmapause positions, seen respectively at ∿ 09 UT on July 30 and at ∿ 03 UT on July 31, correspond to the plasmapauses formed near midnight during the two enhancements of geomagnetic activity at 12 UT on July 29 and at 00 UT on July 30 (see upper left hand side panel in fig. 30).

Consequently, the theory for the formation of a new plasmapause at each new substorm enhancement fits the observed corotation time delays observed by GEOS 1, as well as those deduced from OGO 5 observations by Chappell, et al. (1971). The agreement with the observations clearly indicates that the plasmapause peeling off takes place near midnight local time, and not near dusk as a result of shearing near the stagnation point in the Volland-Stern's model (Corcuff, et al., 1985).

d) Immediately after the onset of the substorm events of July 29 and 30, we have obtained, with the E3H model, a rapid and short duration increase in the equatorial distance of the plasmapause at 06 and 09 LT (figs. 31b and 31c). The experimental data do not indicate, however, such a radial expansion of the plasmasphere as early as 06 LT : they show that, at 04 and 05 UT, the plasmapause is located at geocentric distances close to 4 R_E, i.e. at a radial distance almost coincident with the positions predicted by the Volland-Stern's model; on the contrary, with the time dependent E3H(f) model, the corresponding plasmapause distances are significantly greater.

This is another major difference between the results obtained with the two E-field models. While in the Volland-Stern's model, only the dawn-dusk component of the electric field is enhanced when K_p increases, in the E3H(f) model there is an additional enhancement of the eastward component in the morning and dayside sectors from 06 LT to 18 LT. This result from the E3H(f) model calculation is not supported by the experimental results at 06 and 09 LT. It is likely that the factor, f, scaling the electric field components in the dawn and dayside sectors ought not to be the same as in the post-midnight sector where eq. (4.56) fits the observations rather well (Corcuff <u>et al</u>., 1985).

The fairly good fits obtained with the Volland-Stern's time dependent electric field model indicate that this elementary model is a rather satisfactory first approximation of the actual E-field distribution in the dawn sector of the magnetosphere.

Although it is not possible with such elementary models to describe in great details the complex magnetospheric electric field distribution, their simplicity constitutes, however, an advantage over the E3H model; indeed, this latter empirical model is represented by a series of 120 terms which have been deduced by McIlwain from independent observations made along the geostationary orbit of the satellite ATS 5. From this point of view, the E3H model is not so much a fetch model as the more elementary analytical models were at their origin. Indeed, originally most of these earlier elementary electric field models had been designed with an ad-hoc "stagnation point" in the duskside. The existence of this singular point in the E-field model has long been considered to be essential in order to define the plasmapause as the Last Closed Equipotential (LCE) surface (Brice, 1967). In Appendix G, we have pointed out some of the difficulties with this definition of the plasmapause. Furthermore, it is shown in chapter 4 of this study that the existence of a stagnation point is not at all essential to explain the formation of a plasmapause in the Earth magnetosphere. Indeed, it has been demonstrated above that plasma interchange motion driven by the centrifugal force leads naturally to the formation of a plasmapause, even when the electric field model has no stagnation point, like the E3H model or the corotation electric field model.

e) The solid dots in figs. 31 and 32 correspond to observed densities greater than 100 cm^{-3}. They are all located earthward of the theoretical plasmapause positions in both simulations. None of these points corresponding to high plasmaspheric densities is located beyond the calculated outer edge of the plasmapause region.

Furthermore, all intermediate plasma densities ($20 < N_{eq} <$ 100 cm^{-3}; indicated by solid stars in figs. 31 and 32) are also observed during the recovery phase of July 30 and 31, inside the positions of the plasmapause. Remember that all the positions have been calculated by taking into account the effects of plasma interchange motion.

However, when interchange motion is neglected, or inhibited by setting $\Sigma_p = \infty$ in the numerical calculations, we have obtain the plasmapause positions which are shown in the right hand side panels of fig. 33a, b and c, for Volland-Stern's field model. This time dependent model calculation is then analogous to that obtained in the ideal MHD approximation by Grebowsky (1970, 1971).

The intermediate plasma density data, also represented by solid stars in fig. 33, correspond to expanded afternoon plasmaspheric regions or to post-dawn magnetic flux tubes in the process of refilling. These flux tubes are expected to be located inside the outer edge of the plasmapause. This is precisely the case in the left hand side panels

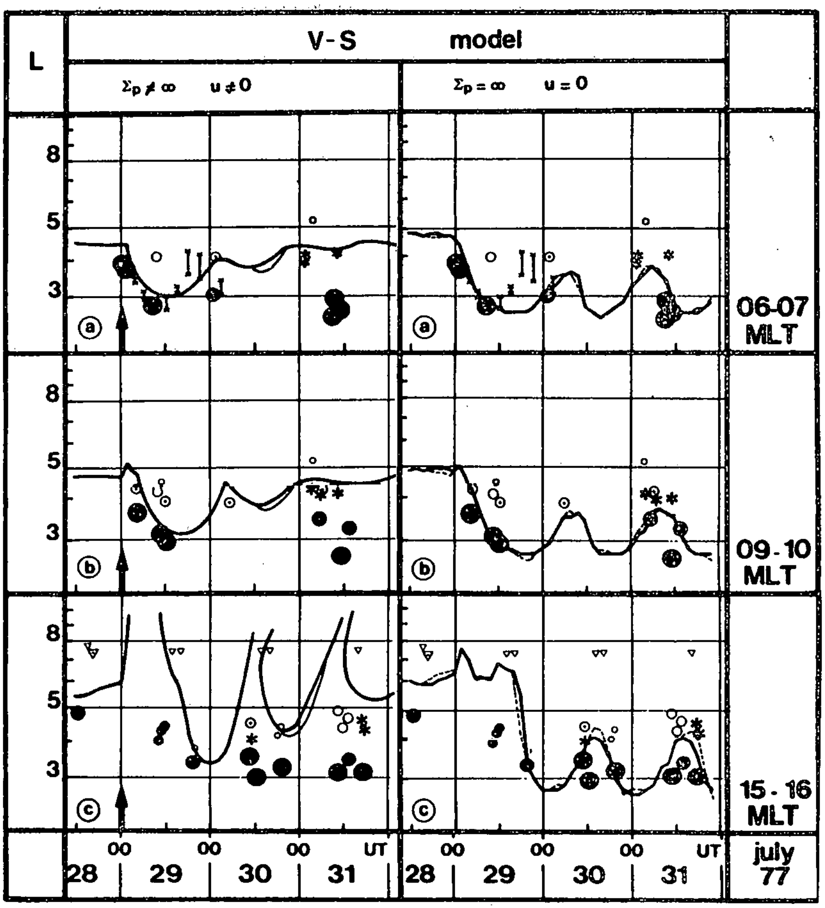

Fig. 33.- Radial distances of the outer edge of plasmapause region in three different local time sectors as a function of Universal Time from July 28 to July 31, 1977. The time dependent Volland-Stern electric field distribution has been used in all these simulations. In the left hand side panels realistic values for the integrated Pedersen have been used to calculate the plasma interchange velocity. In the right hand side panels plasma interchange velocity is assumed to be equal to zero as in the MHD theory for the formation of the plasmapause (after Corcuff et al., 1985).

of fig. 33, where realistic values for the integrated Pedersen conductivity have been used to compute the maximum interchange velocity as in figs. 31 and 32. In the right hand side panels of fig. 33, however, the solid stars are located outside the plasmapause which, in this instance, is determined by using the ideal MHD theory : i.e. without interchange motion. This comparison indicates that, after major substorm events the positions of the plasmapause calculated with plasma interchange motion are much more consistent with the observations, than those obtained without this physical mechanism; indeed, in the latter case the plasmapause remains at too low L-values after a large geomagnetic perturbation. On the contrary, the theory described in the previous chapter, predicts that the plasmapause rapidly re-forms itself at larger radial distances during recovery phases, as confirmed by all available observations (Corcuff, et al., 1985).

5.3. Further comparison with observations

Kowalkowski and Lemaire (1979) have examined 285 ion density distributions collected with the satellite OGO 5 between 7 March 1968 and 26 February 1969 in all local time sectors. The objective of their study was to verify wether there is evidence in these observations of plasma detachment in the post-midnight local time sector.

Fig. 34 shows one of the density profiles considered in their studies. It has been measured in the midnight local time sector. The arrow indicates a detached plasma element or plasmatail. But, since the maximum density in this element is lower than the critical threshold

$$n_S = 100(4/L)^4 \qquad (\mathrm{cm}^{-3}) \qquad (5.1)$$

used by Chappell (1974) to identify detached plasma elements, the density irregularity indicated by the arrow in fig. 34, has not been taken into account in his statistics of the local time distribution of

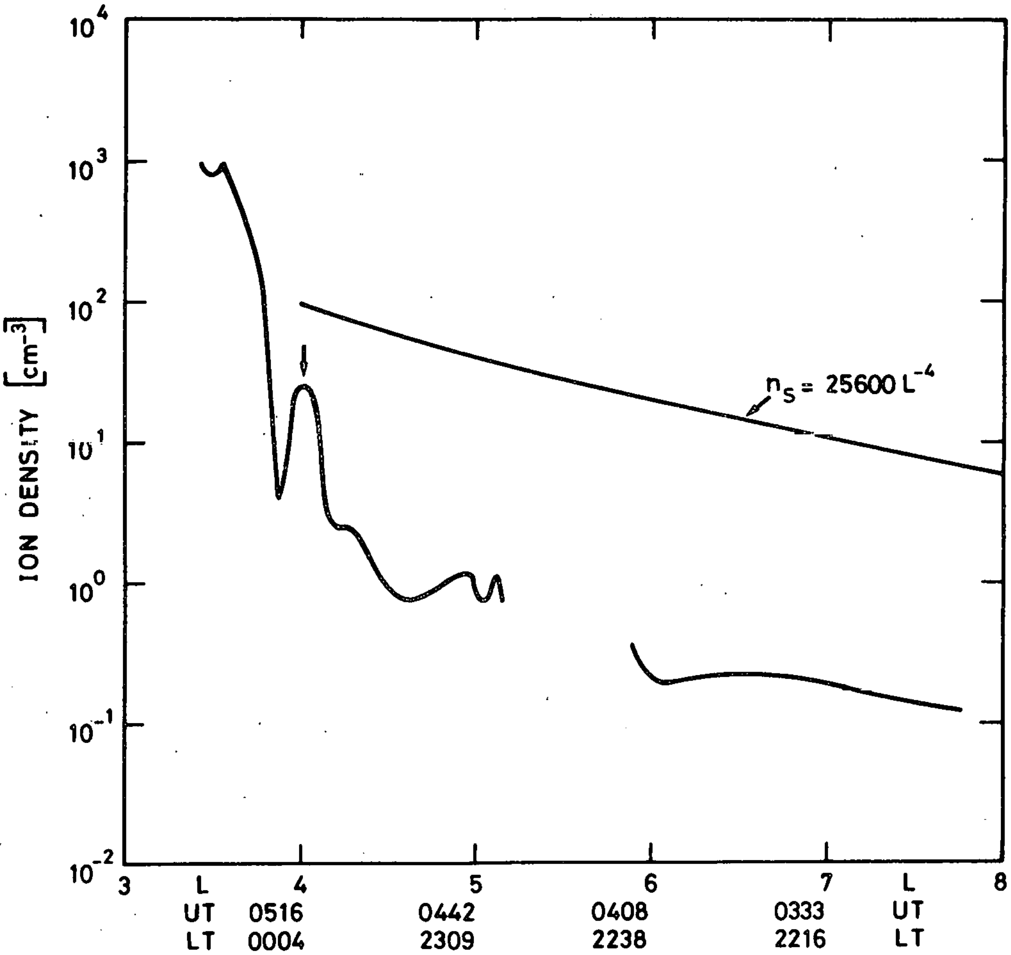

Fig. 34.- Ion concentration versus McIlwain's parameter (L) measured along the orbit of the OGO 5 satellite in the midnight local time sector. The smooth line (n_S) represents an L^{-4} density profile. The arrow corresponds to a detached plasma element or tail just beyond the plasmapause (after Kowalkowski and Lemaire, 1979).

detached plasma elements. Similarly, the detached plasma elements for which the minimum density between the plasmapause and the inner edge of the density enhancement, is larger than the threshold value (n_S), have not been included in Chappell's (1974) statistical study of detached plasma elements.

Instead of using the threshold criteria given by eq. (5.1) Kowalkowski and Lemaire (1979) examined each density profile available and determined "de visu" the presence or absence of detached plasma elements such as that shown in fig. 34. The number of occurrences in all local time sectors have been determined for different values of the K_p index at the Universal Time t' where

$$t' = t - \varphi$$

where t and φ are the Universal Time and local time when and where the observations were made.

The solid line histograms in fig. 35 represent the local time distributions of the observed number of detached plasma elements (d_i) in all LT sectors. These numbers were determined for $K_p \leqq 2$ and for $K_p > 2$ by the visual method, which is less precise but probably more accurate than the "threshold method". Since the orbits for which data sets were available are not evenly distributed in all local time sectors, a theoretical distribution was constructed under the "null hypothesis" that p, the probability of occurrence of a plasma element in any LT range is independent of the local time sector. The expected mean number (m_i) of detached plasma elements in the i^{th} LT sector is then given by

$$m_i = N_i \; p \qquad (5.2)$$

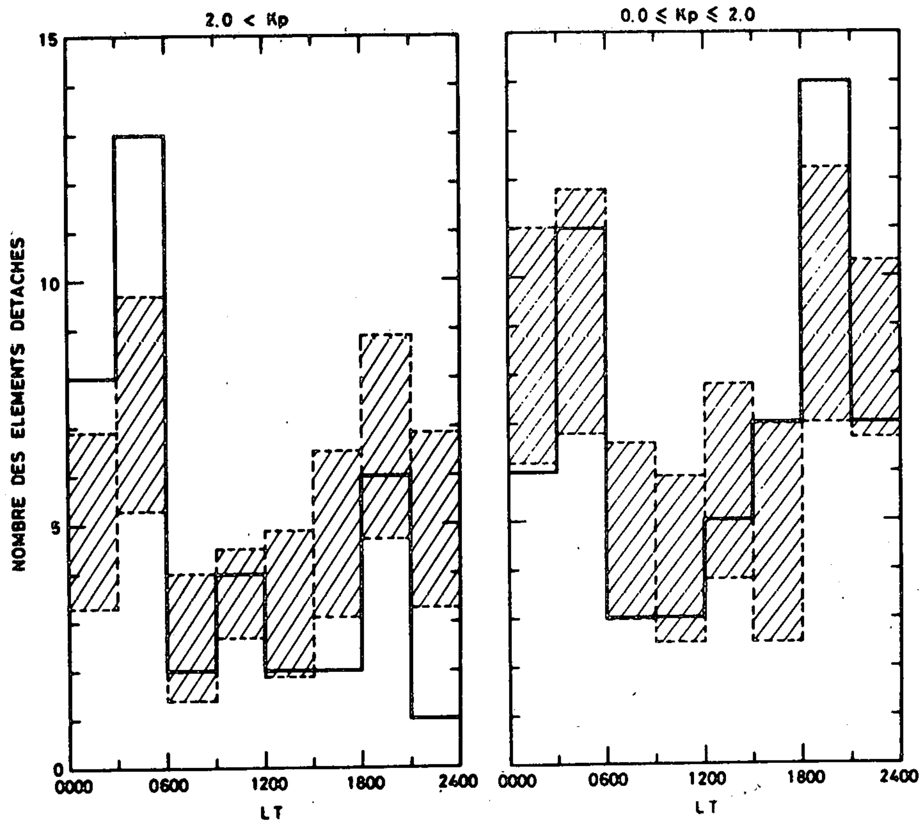

Fig. 35.- Number of detached plasma elements found in different local time sectors a) for $K_p > 2$ (left hand side panel, and b) for $K_p \leqslant 2$ (right hand side panel). The shadings correspond to the confidence range for a theoretical local time distribution.

where N_i is the number of data sets available for that same i^{th} sector. The standard devivation for this binomial distribution in the i^{th} local time sector is given by

$$\sigma_i = \left[N_i \, p(1 - p) \right]^{1/2} \tag{5.3}$$

The value of p is determined from the samples themselves :

$$p = \frac{\Sigma_i \; d_i}{\Sigma_i \; N_i} \tag{5.4}$$

where $\Sigma_i \, d_i$ is the total number of detached plasma elements observed for all sectors, and $\Sigma_i \, N_i$ the total number of profiles, for a given range of K_p. For $K_p \leqq 2$, $\Sigma_i d_i = 56$ and $\Sigma_i \, N_i = 172$, $p = 0.32$. For $K_p > 2$, $\Sigma_i d_i = 37$, $\Sigma_i \, N_i = 113$, $p = 0.33$. In each LT sector of fig. 35, the shadings correspond to the range between $m_i - \sigma_i$ and $m_i + \sigma_i$. Any value of d_i outside this range has a low probability to be a statistical fluctuation about the mean of the theoretical distribution.

It can be seen from fig. 35 that, when $0.0 \leqq K_p \leqq 2.0$, the maximum observed in the post-dusk sector is outside the range of one standard deviation (right panel); but the peak between 0300 LT and 0600 LT can possibly be due to statistical fluctuations. The large maximum found between 1800 LT and 2100 LT may be related to the peak obtained in the afternoon sector by Chappell (1974) with a different criteria and from a different statistical analysis. Note, however, that the peak in Kowalkowski and Lemaire's histogram is located in the post-dusk sector and not in the pre-dusk sector.

An even larger number of detached plasma elements is found after midnight local time, when the geomagnetic activity index K_p is larger than 2 (see left panel of fig. 35). This indicates that under perturbed geomagnetic conditions the number of detached plasma elements between 0300 LT and 0600 LT is abnormally large; it cannot be accounted for as a statistical fluctuation about the theoretical distribution based on the assumption of equiprobability in all LT sectors. This deviation is definitely too larger to be a simple statistical fluctuation about the theoretical mean. A "Chi-square test" confirms that the "null hypothesis" from which this theoretical distribution was derived, must therefore be rejected (at the probability threshold of 15%).

Note also that the pre-midnight number of occurrences is abnormally small, while the post-dusk maximum is very close to the expected mean value (m_i), at least when K_p is larger than 2 (left panel).

These statistical results fully support the theory for the formation of the plasmapause which is described in chapter 4. Indeed, when geomagnetic activity is enhanced, the eastward convection velocity is also enhanced in the post-midnight sector and plasma interchange motion is driven unstable closer to the Earth by the larger centrifugal force. A thick shell of high density plasma is then peeled off from the post-midnight plasmasphere. This occurs mainly when $K_p > 2$. This leads to the conclusion that a significantly larger number of detached plasma elements is expected in the formative post-midnight sector when the geomagnetic activity level is high, as actually found in the left panel of fig. 35. We donot see, however, any plausible explanation for such a post-midnight peak in the framework of the ideal MHD theory, for the formation of the plasmapause described in Appendix G.

Since these newly detached plasma elements are convected eastward one should expected very few of them in the pre-noon local time sector. This is consistent with the minimum found in the histogram of the left hand side panel between 2100 LT and 2400 LT.

When geomagnetic activity is small (i.e. $K_p < 2$; see right hand side panel), less peeling off is expected in the post-midnight local time sector at $L < 6$. The plasmapause is forming at larger radial distances and thinner plasma shells are expected to be peeled off as a result of smaller amplitude variations in K_p. Therefore, it is not surprising that the expected number of detached plasma elements observed in the post-midnight sector is smaller when $K_p < 2$, as actually found in the right hand side panel of fig. 35.

But the significant peak observed in the post-dusk sector during quiet geomagnetic conditions fits also into the framework of the theory presented in this monograph. Indeed, in all the simulations which we made for periods of small geomagnetic activity we found that small amplitude variations in the values of K_p produce small bulges in the noon LT sector as for instance illustrated in fig. 29. These bulges corotate then eastward toward dusk. Because of the differential convection velocity at different radial distances these bulges develop into small tail-like structures in the post-dusk sector. These tail-like structures can account for the abnormally large peak between 1800 LT - 2100 LT in the right hand panel of fig. 35. It looks more difficult to find a simple explanation for this post-dusk peak in the framework of the ideal MHD theory for the formation of the plasmapause.

Finally fig. 36 shows a density distribution which has also been measured in the post-midnight sector along OGO 5's orbit. The absolute value of the densities might be biased by spacecraft charging, but the qualitative variations of such density profiles are nevertheless useful and instructive. For instance this profile corresponds to a period when K_p has remained small for an extended period of time, and increased to $K_p = 3$ an hour before the measurement of the density depression (or plasma hole) indicated by the arrow. The trough which is seen at 3.4 R_E corresponds to the density depression which devellops closer to the Earth, when K_p increases as schematically illustrated in fig. 22. Furthermore, the shape of the plasma density enhancement beyond the trough suggests that a plasma shell is in the process of detaching from the post-midnight plasmasphere as explained in chapter

4 and as illustrated in fig. 22. As this block of plasma becomes detached, the equatorial density decreases as L^{-4} indicating that the total number of particles is conserved while the volume is increasing. Examples like that shown in fig. 36 are not uncommon in the sample of OGO 5 density profiles analysed by Kowalkowksi and Lemaire (1979). Such troughs form precisely where the theory predicts the formation of a new plasmapause; we consider them as direct evidence in support of the theory presented in chapter 4 of this monograph.

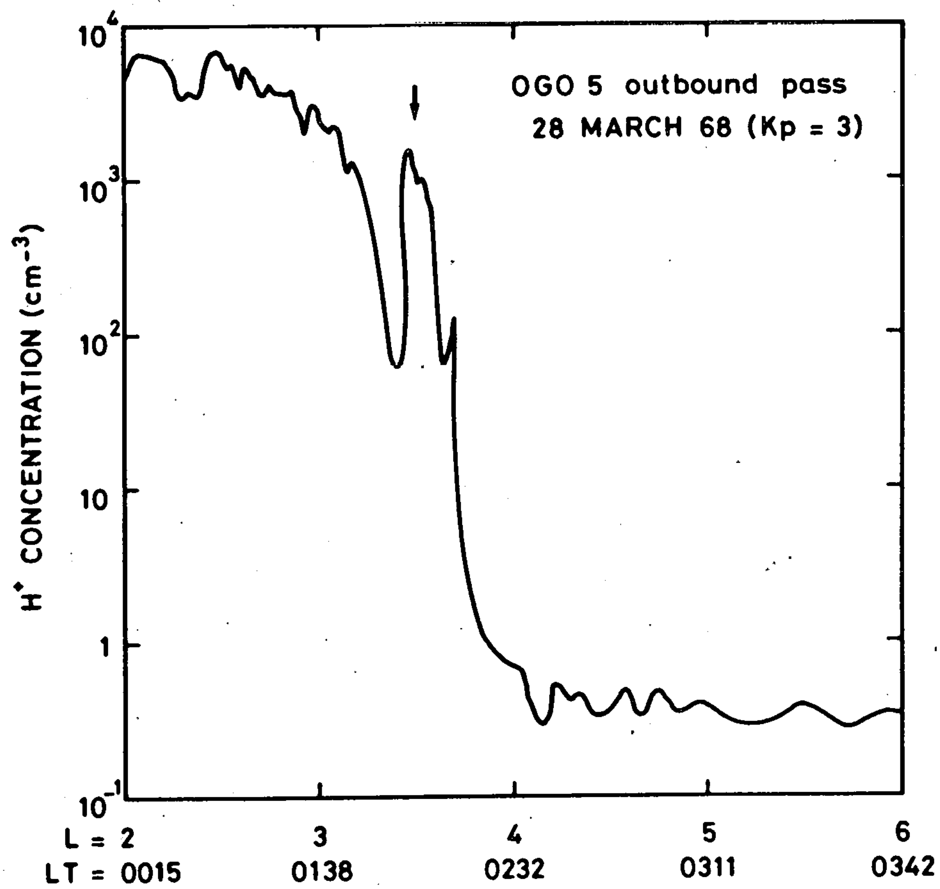

Fig. 36.- Ion concentration versus L as measured by OGO 5 on 28 March, 1968. The arrow indicates a plasma element or tail becoming detached from the post-midnight plasmasphere.

6. GENERAL CONCLUSIONS

A. Soon after it had been found by Carpenter (1966) that the equatorial plasmapause has a bulge in the dusk local time sector during the prolonged recovery phases of a series of weak to moderate magnetic storms, it was proposed that this characteristic boundary corresponds to the Last Closed Equipotential (LCE) of the magnetospheric electric field distribution. Indeed, according to the MHD theory, plasma streamlines are parallel to the equipotential surfaces of this electric field distribution. Therefore, all magnetic flux tubes drifting along closed equipotential lines inside the LCE can fill up and saturate with plasma of ionospheric origin, while those which convect outside this LCE surface are continuously emptied when they reach "open" magnetic field lines at the magnetopause (see figs. B1 and G1). Consequently, large equatorial plasma densities all expected on the innerside of the LCE, but not on its outerside. This has been presented as the first explanation for the formation of the observed "knee" in the equatorial plasma density (Brice, 1967). The LCE of the "best estimate" electric field model shown in fig. 17 was precisely taylored to fit the observed plasmapause positions illustrated in fig. 1c.

A number of other different elementary E-field models describing the presumed distribution of the magnetospheric convection electric fields were then proposed in the late 1960's. The simplest of these elementary models was that proposed by Kavanagh, et al. (1968) and illustrated in fig. B1. This model is the result of a vacuum superposition of the radial corotation electric field ($\underline{E}_c$) and a uniform electric field ($\underline{E}_o$) directed from dawn to dusk. The intensity of $\underline{E}_o$ was varied to fit, as well as possible, the positions of the LCE surface of the E-field model to the observed positions of the equatorial plasma density knee. The uniform dawn-dusk field model became most popular, and, the ideal MHD theory for the formation of the plasma, on which it was based, became soon widely accepted.

Slightly more general analytical E-field models with two free adjustable parameters (q and γ), instead of one (E_o), were proposed subsequently by Volland (1973, 1975) and Stern (1973, 1977) (a description of these models is given in Appendix B). It was hoped that the LCE corresponding to these two-parameters models would fit more accurately the observed positions of the plasmapause.

Time dependent E-field models, for which E_o or q were assumed to vary with the level of geomagnetic activity index K_p, were also constructed by a few modellers. Numerical E-field models were also calculated for various assumed boundary conditions by the Rice group. A variety of model simulations using these time dependent E-field models proliferated in the literature of the 1970's. In all these dynamical models the plasmapause was identified with the LCE of the electric field model at the initial time (t_o) of the numerical simulation.

B. In the Appendix G, we point out a few difficulties with this early definition of the plasmapause and with the time dependent simulations which are based on it. For instance, in these models the calculated plasmapause positions depend on the choice of the initial time (t_o) at which the simulation is started. Furthermore, in all of these time dependent simulations the plasmapause coïncides with a LCE only a brief instant of time, at $t = t_o$, but at no later moment will the presumed plasmapause coïncide again with an equipotential surface of the variable electric field distribution. This indicates the inconsistency of this definition of the plasmapause and of the ideal MHD theory on which it is based.

C. In 1974, McIlwain determined an empirical electric field model from observations collected at geostationary orbit by the satellite ATS 5. Unlike previous modellers, McIlwain did not adjust the 120 different terms defining his E3 model, and later his E3H electric field model, in order to fit a "best estimate LCE" with an observed shape of the plasmapause. He adjusted the equatorial electric field model in the different local time sectors and at different radial distances, in order to fit actual characteristic structures which he identified in the ions and electrons spectrograms that he observed near the equatorial plane, at 6.6 R_E. The absence of a stagnation point in the E3H electric field model, as well as in the model deduced from radar observations by Richmond (1976), have been considered by the MHD space community as a major deficiency of these independent empirical models. Indeed, in these empirical E-field models the LCE, and consequently, the plasmapause extends up to the magnetopause, which is too far out, according to Carpenter's (1966) observations shown in fig. 1c.

The dilemma was then either to reject all electric field models without the expected stagnation point, or to abandon the ideal MHD theory for the formation of the plasmapause. As noted recently by Carpenter (1983, p. 918), "progress in study of the plasmasphere-plasmapause system may well have been hindered by over acceptance of the relatively simple descriptive pictures that emerged from the earliest research". But, as time went on, an increasing number of people became aware that a more convincing explanation was needed to account for the large amount of observations collected since the time when the plasmapause region was discovered by Gringauz <u>et al</u>. (1960) and by Carpenter (1963).

D. The alternative theory for the formation of the plasmapause, which is described in chapter 4 of this monograph, does not rely on the very existence of a mathematical singularity point in the magnetospheric electric field distribution; on the contrary, it is based on a physical mechanism which had been overlooked or neglected in the earlier MHD theory. This mechanism is plasma interchange motion which is driven unstable beyond a surface called the Zero-Radial-Force (ZRF) surface, as described in chapter 4 and illustrated in figs. 18, 20 and 22. Beyond this surface the centrifugal force acting on corotating (or super-rotating) thermal plasma becomes larger than the gravitational force. Any plasma density enhancement located beyond this ZRF surface drifts outwardly across magnetic field lines and across the equipotential lines of the external electric field.

The interchange velocity of plasma density irregularities has been determined and discussed in sections 4.3 and 4.4. Its maximum value has been found to be inversely proportional to the integrated Pedersen conductivity (Σ_p) which plays here a similar role than the viscosity coefficient (η) in classical fluid hydrodynamics. When Σ_p (or η) is large - as it is the case in the dayside local time sector - the maximum interchange velocity is small, and the streamlines of plasma density enhancements are almost parallel to the equipotential surfaces of the external electric field distribution. The plasma flow is then almost identical to that obtained in the ideal MHD approximation. The electric field inside the dielectric plasma elements is equal to the ambiant electric field intensity. However, in the nightside ionosphere the value of Σ_p is drastically reduced. Plasma interchange velocities become then significantly larger, and the plasma elements which are located beyond the ZRF surface can become detached from the plasmasphere, as illustrated in figs. 22 and 36. It has also been pointed out in section 4.7 that this peeling off mechanism is most efficient, and most unstable, in the post-midnight local time sector where (i) the integrated Pedersen conductivity has a minimum value (as shown in the Appendix D), and (ii) where the magnetospheric convection velocity has a maximum eastward velocity (see fig. 11) i.e. where the centrifugal force is also most enhanced.

At each large substorm associated enhancement of the radial component of the post-midnight electric field intensity, the ZRF surface is displaced closer to the Earth; a large plasma shell is then peeled off from the plasmasphere in the post-midnight local time sector. As illustrated in fig. 22, this detachment leads to the formation of a trough which becomes broader as time goes on. When the plasma element is completely detached from the plasma stably trapped in the gravitational potential well, an equatorial plasma density "knee" is left over at the outer edge of the plasmasphere.

E. The dynamical simulations presented in sections 5.1 and 5.2 show how the new plasmapause forms closer to the Earth in the post-midnight sector, and how it subsequently propagates with the corotation velocity toward noon and toward the dusk local time sector. These simulations also illustrate the formation of ripples and bulges in the noon local time sector for each small enhancement of geomagnetic activity. It is found from these model calculations that these ripples corotate eastwards toward dusk, where they develop into small tails.

F. At the onset of a prolonged period of high geomagnetic activity, the simulation presented in section 5.2 shows that the dayside plasmapause moves explosively toward the dayside magnetopause (see fig. 30). The post-midnight plasmasphere is then strongly compressed toward the Earth and a new plasmapause forms at $L = 2.5$ for $K_p = 7$.

All these theoretical results are well confirmed by presently available observations, including those concerning the major magnetic storm event of 29 July 1977, and reported in section 5.2. Further statistical observations concerning the local time distribution of detached plasma elements are presented in section 5.3. They confirm also that the plasmapause is formed in the post-midnight sector as predicted by the theory described in chapter 4.

G. The formation of "multiple plasmapauses"(i.e. step-like equatorial density profiles) is described in section 4.9, as a consequence of major peelings off followed by flux tube refilling processes during following quieter periods of time.

H. It is suggested in section 4.10 that plasma interchange motion can also contribute to the smoothing out of the sharp density gradients inside the plasmasphere, as well as at its outer frontier. But the diffusion time due to interchange motion is relatively long compared to the time between successive substorm onsets. Therefore, density gradient rarely have the time necessary to be washed out completely before new ones are formed at the onset of new geomagnetic perturbations.

I. The maximum interchange velocity is proportional to the difference between the density inside a plasma irregularity and the density of the background plasma. Plasma density depressions, or plasma holes, move therefore in directions which are opposite to those of plasma density enhancements. All plasma holes in a corotating electric field converge therefore towards a common asymptotic trajectory which coïncides with geostationary orbit, or toward a more complicated ZRF surface when the external E-field distribution departs significantly from the symmetric corotation electric field, as it the case for the E3H field model. We have used this E3H field model in the time independent simulations illustrated in figs. 20 and 21. The E3H(f) field model, with a variable scale factor f (described in Appendix B) has been used in the time dependent simulations illustrated in figs. 28, 29, 30, 31, 32 and 33. In all these simulations we make use of the property that all plasma holes converge toward a common asymptotic trajectory. This provides a direct and practical method to determine the instantanous positions of the ZRF surface and consequently of the outer edge of plasmapause region at all local time. This has proven to be very useful to study the dynamical deformations of the plasmasphere and of its outer frontier under different geomagnetic conditions.

J. The Light-Ion-Trough (LIT) is another characteristic frontier of the plasmasphere. At the LIT the H^+ ion concentration in the topside ionosphere decreases rapidly over a short range of latitudes. The LIT is formed along midlatitude magnetic field lines located inside the plasmasphere, at almost one L-value equatorwards of the equatorial plasmapause.

In section 2.7 we have suggested that the LIT is related to the existence of a Zero-Parallel-Force (ZPF) surface which has been defined in section 2.3. Beyond this ZPF surface the total gravitational and centrifugal potential distribution along a magnetic field line, has a minimum in the equatorial plane instead of a maximum (see section 2.2 and fig. 2). In a corotating ion-exosphere the ZPF surface is located at $L_c = 5.7$ i.e. almost one L value inside the ZRF surface : $L_m = 6.6$.

This is therefore consistent with the observations indicating that the LIT is along field lines at lower L values than the equatorial plasmapause.

Along field lines traversing the ZPF surface, an upward H^+ flow is expected to fill up the equatorial potential well. Indeed, it has been shown in section 2.6 that an exospheric equilibrium density distribution necessarily tends to evolve toward a diffusive equilibrium one; the ions and electron evaporated from the topside ionosphere are continously scattered by Coulomb collisions outside the pitch angle source cones. This slow pitch angle diffusion populates more and more high altitude trapped orbits with ionospheric ions. The equatorial potential well, resulting from the centrifugal force in a rotating ion-exosphere, constitutes therefore a sink where a large number of light ionospheric ions can be pilled up temporarily on trapped orbits. Thus, when at the onset of substorm associated enhancements of the magnetospheric convection velocity the ZPF surface penetrates deeper into the plasmasphere, a polar wind like flow of light ions is pumped upward along the magnetic field lines along which an equatorial potential minimum has developped as a consequence of the enhanced angular rotational speed. It is shown in section 2.8 that this explanation for the formation of the LIT is consistent with the observations.

K. In the third chapter of this monograph we have discussed various aspects of plasma transport in the plasmasphere. In section 3.1, it has been emphasized that the diurnal variation of the equatorial density observed in the outer magnetosphere is a consequence of the cyclic contractions and expansions of the volume of field aligned plasma elements which convect along very asymmetric drift paths. This diurnal variation has been illustrated in section 3.6, using numerical model simulations (see figs. 13 and 14). The minimum in the equatorial densities is consistently found in the 1800 LT sector, where the volume of the flux tube is maximum. This is in fair agreement with the satellite observations.

L. Refilling of magnetic flux tubes has also be simulated in the numerical model. The characteristic refilling times deduced are consistent with those derived from whistler observations and with those evaluated in the Appendix E.

M. Another consequence of the cyclic contractions and expansions of the plasma elements which convect along highly asymmetric drift trajectories, is the diurnal variation of the perpendicular and parallel ion temperatures. Heating of the plasma in the outer plasmasphere can result from repetitive fast quasi-adiabatic compressions in the post-dusk sector, followed by slower quasi-isothermal expansions in the dayside. Wether this process of quasi-adiabatic compression followed by a quasi-isothermal decompression can account for the observed increase of plasmaspheric temperatures as a function of L, warrants more attention and needs to be modeled quantitatively in the future. The recent measurements from the Retarding Ion Mass Spectrometer (RIMS) on the Dynamic Explorer satellite (DE 1) are most adequate and apposite to resolve this interesting question.

N. The theories for the formation of an equatorial Plasmapause Region, and for the formation of a low-altitude Light Ion Trough, which have been presented in this monograph, bring to light the effects of the centrifugal forces in rotating ion-exosphere, and emphasize their role in the process of formation of these two frontiers of the plasmasphere. Changes in the distribution of these forces associated with substorm enhancements of the magnetospheric convection velocities, have profound effects on the dynamical distribution of thermal ionospheric plasma, both along midlatitude geomagnetic field lines, as well as across them. These are the major conclusions which emerge from this study of the plasmasphere and of its frontiers.

APPENDIX A : MAGNETIC FIELD MODELS

The geomagnetic field can be approximated by a dipole magnetic field. In this zero order approximation the equatorial magnetic field intensity (in nT) is given by

$$B_{eq} = 31000/R^3 \tag{A1}$$

where R is the radial distance in Earth's radii; R is also equal to McIlwain's parameter L (McIlwain, 1961).

Near geostationary orbit (R = 6.6) and at larger radial distances significant noon-midnight distorsions or asymmetry are observed. These distorsions result from large scale currents circulating in the Ring Current region, in the plasmasheet, and at the magnetopause.

Olsen and Pfitzer (1974) have modeled the perturbations produced by these currents in terms of a polynomial expansion in the cartesian GSM coordinates system (x, y, z). Although this model is very useful to organize data, we will use another crude representation which has originally been introduced by McIlwain (1972). This model is known as the M2 model. It has been constructed to fit (a) the field observed at 6.6 R_E by Cummings, et al. (1971), (b) the field just inside the magnetopause (Fairfield, 1968), and (c) the field in the neutral sheet of the magnetotail. The equatorial magnetic field intensity (in nT) is given by

$$B = \frac{31000}{R^3} + 6 - 24 \cos \varphi + \frac{18 \cos^2 \varphi}{1 + 1728/R^3} \tag{A2}$$

where φ is the local time in radian; φ = 0 and π correspond to midnight, and noon respectively. This field is symmetric with respect to the noon-midnight meridian plane.

Fig. A1 shows (on the dusk side of the noon-midnight meridian plane), the magnetic field isointensity contours for the M2 model. The corresponding isointensity contours calculated for Olson and Pfitzer's model are shown on the dawn side. The shaded zones indicate where the two models differ by more than 20%. It can be seen that in the whole plasmasphere, up to R = 7, the two models agree well enough for the purpose of the calculations presented in this work.

Although, there is plenty observational evidence that the magnetic field intensity change during substorm events or solar wind plasma injection events, we have assumed in our model calculation that the magnetic field is independent of time. Inside the whole plasmasphere such transient magnetic field variations rarely exceed 30-40% and we can ignore them in a first order of approximation. Anyway, time dependent empirical B-field models depending on K_p or on other geophysical activity indexes are not yet available. Furthermore, the time variation of B due to the wobbling of the geomagnetic dipole around the axis of rotation of the Earth are also relatively small for R < 6-8 (Block and Carpenter, 1974; Mroz, et al., 1979). Therefore, accepting a tolerance of 30-40% in modeling the magnetic field is the best that can be done for the time being.

In order to calculate in the Appendix C the components of convection velocity, $\underline{V}_E = \underline{E} \times \underline{B}/B^2$, as well as their gradients in the radial and local time directions it is necessary to evaluate first order and second order derivatives of $B(R,\varphi)$

$$\nabla_R B = - \frac{93000}{R^4} + \frac{93312 \cos^2 \varphi}{R^4(1 + 1728/R^3)^2} \qquad \text{(A3)}$$

$$\nabla_{\varphi} B = 24 \sin\varphi - \frac{36 \sin\varphi \cos\varphi}{1 + 1728/R^3} \quad \text{(A4)}$$

$$\nabla_R^2 B = \left[\frac{372000}{R^5} + \frac{373248 \cos^2\varphi}{R^5(1 + 1728/R^3)^2}\left(\frac{2592}{R^3(1 + 1728/R^3)} - 1\right)\right] \quad \text{(A5)}$$

$$\nabla_{\varphi}^2 B = 24 \cos\varphi - \frac{36(\cos^2\varphi - \sin^2\varphi)}{1 + 1728/R^3} \quad \text{(A6)}$$

$$\nabla_{\varphi} \nabla_R B = -\frac{186624 \cos\varphi \sin\varphi}{R^4(1 + 1728/R^3)^2} \quad \text{(A7)}$$

When the geomagnetic field is approximated by a dipole these equations become

$$\nabla_{\varphi} B = 0 \; ; \; \nabla_{\varphi}^2 B = 0 \; ; \; \nabla_{\varphi} \nabla_R B = 0 \quad \text{(A8a)}$$

$$\nabla_R B = -\frac{93000}{R^4} \quad ; \quad \nabla_R^2 B = \frac{372000}{R^5} \quad \text{(A8b)}$$

where these gradients are expressed in nT/R_E, nT/R_E^2, nT/rad, nT/rad^2 and $nT/R_E/rad$, respectively.

The magnetic field intensity at the position of the magnetopause illustrated in fig. A1 is given by

$$B_{MP} = 16 - 35 \cos\varphi + 12 \cos^2\varphi \quad \text{(A9)}$$

(McIlwain, 1972).

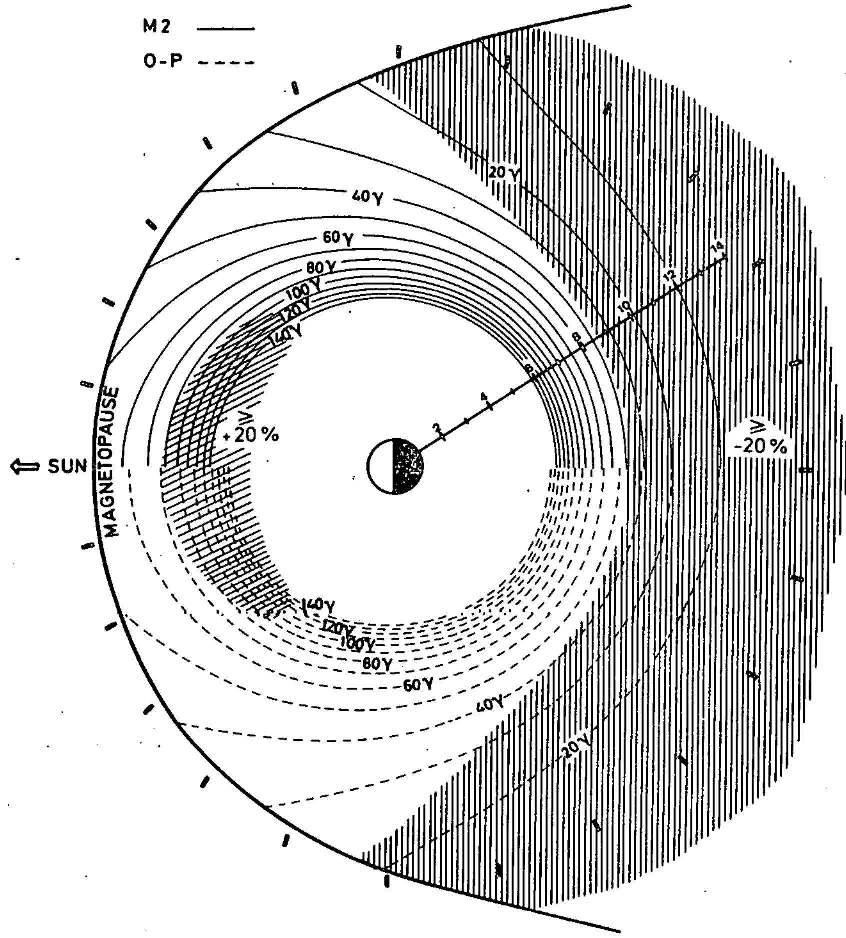

Fig. A1.- Equatorial cross-sections of surfaces of constant magnetic field intensity for McIlwain's (1974) M2 magnetic field model (solid lines) and for the Olson-Pfitzer (1974) magnetic field model. The shaded areas correspond to regions where the difference between these two field intensities exceeds $\pm$ 20%.

The radial distance of the magnetopause (R_{MP}) can be obtained from eq. (A2) by the following algorithm

$$A = 18 \cos^2 \varphi$$

$$G = B_{MP} - 6 + 24 \cos \varphi$$

$$H = G - A \quad , \text{ if } \quad H < 0 \rightarrow R_{MP} = 999$$

$$C = (17.94 + G)^2 - 71.76\ A \quad , \text{ if } \quad C < 0 \rightarrow R_{MP} = 999$$

$$D = 864\ (17.94 - G + (\sqrt{C})/H$$

$$R_{MP}(\varphi) = D^{1/3} \qquad \text{(A10)}$$

APPENDIX B : ELECTRIC FIELD MODELS

The corotation electric field is the electric field distribution which has to be applied in the direction perpendicular to the magnetic field $\underline{B}(R, \varphi, \lambda)$, such that the electric drift velocity is precisely equal to the corotation velocity $\underline{\Omega}_E \times \underline{R}$, where Ω_E is the angular velocity of the Earth and $\underline{R}$ the radial vector. The equatorial potentials corresponding to the corotation E-field are given in kV by

$$\phi = - 92(B/31000)^{1/3} \qquad \text{(B1)}$$

where B is the equatorial magnetic field intensity in nT : B = B(R, φ, λ = 0). In the case of a symmetric dipole B-field (see eq. A1), ϕ varies as R^{-1}; the electric field is radial and falls off as R^{-2}.

$$E_\varphi = - \frac{\partial\phi}{R\partial\varphi} = 0 \;;\; E_r = - \frac{\partial\phi}{\partial R} = - \frac{\partial\phi}{\partial B} \cdot \frac{\partial B}{\partial R} = - \frac{92}{R^2} \qquad \text{(B2)}$$

where E is in kV/R_E and R in Earth radii.

The corotation E-field is a very good approximation in the inner magnetosphere for L < 3, and is obtained by mapping the ionospheric electric field up into the magnetosphere, assuming (i) that magnetic field lines are equipotential ($\underline{E} \cdot \underline{B} = 0$), and (ii) that the ionospheric ions and electrons are dragged around the axis of rotation of the Earth with the azimuthal speed of the neutral atmosphere

$$\underline{V}_E = \frac{E \times B}{B^2} = \underline{\Omega}_E \times \underline{R} \qquad \text{(B3)}$$

At radial distances larger then 3-4 R_E, the magnetospheric and ionospheric electric field depart from the simple corotation field as a consequence of the magnetospheric convection induced near the magnetopause by the solar wind. The electric field in the middle of the magnetotail has a dawn-dusk component which becomes more important than the corotation E-field at large distances.

The most popular E-field model with a dawn-dusk component at large distances, is the one introduced by Volland (1973, 1975) and Stern (1975) independently. In this simple analytic model the equatorial electric potential is given in kV by

$$\phi = - 92\ (B/31000)^{1/3} + q\ \left(\frac{B}{31000}\right)^{-\gamma/3} \sin\ \varphi \qquad \text{(B4)}$$

where q and γ are constants which have often be choosen by adjusting the dimensions and shape of the last closed equipotential (LCE) to those of the observed plasmapause illustrated in fig. 1c.

Fig. B1 illustrates such a model for $\gamma = 1$. The LCE resembles a "tear drop" with a bulge in the dusk local time sector, like the equatorial plasmapause positions determined experimentally by Carpenter (1966) from whistler observations, or, by Chappell (1972) from OGO 5 satellite measurements.

To calculate the electric field E = - grad ϕ and convection velocity, $\underline{E} \times \underline{B}/B^2$, for a given magnetic field distribution (like the simple dipole or the M2 model described in Appendix A, it is necessary to calculate first the following derivatives :

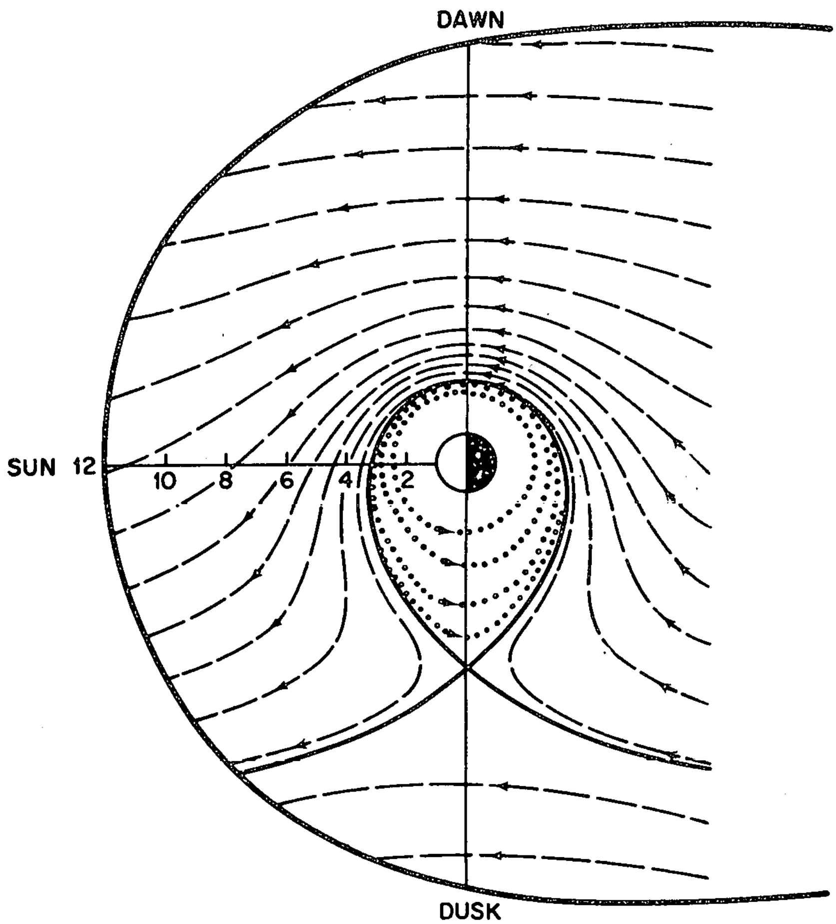

Fig. B1.- The equatorial cross sections of equipotential surfaces (dashed lines) corresponding to a uniform dawn-dusk electric field distribution (after Kavanagh et al., 1968). This corresponds also to a Volland-Stern type field for $\gamma = 1$. The value of q or E_0, the intensity of the dawn-dusk component of the electric field has been selected to place the Stagnation Point (SP) at 7 R_E in the 1800 LT meridian plane : $q = E_0 = 0.29$ mV/m. The arrows indicate the direction of plasma streaming parallel to equipotential surfaces. The solid line passing through the SP is the Last Closed Equipotential (LCE) identified with the Plasmapause in the MHD theory for the formation of this magnetospheric boundary.

$$\frac{\partial\phi}{\partial\varphi} = q^* \, B^{-\gamma/3} \cos\varphi \tag{B5a}$$

$$\frac{\partial\phi}{\partial B} = -\frac{a^*}{3} B^{-2/3} - \frac{\gamma q^*}{3} B^{-(3+\gamma)/3} \sin\varphi \tag{B5b}$$

$$\frac{\partial \ \phi}{\partial\varphi^2} = - q^* \, B^{-\gamma/3} \sin\varphi \tag{B5c}$$

$$\frac{\partial \ \phi}{\partial B^2} = \frac{2a^*}{3} B^{-5/3} + \frac{\gamma(3+\gamma)q^*}{9} B^{-(6+\gamma)/3} \sin\varphi \tag{B5d}$$

$$\frac{\partial \ \phi}{\partial B \partial\varphi} = -\frac{\gamma q^*}{3} B^{-(3+\gamma)/3} \cos\varphi \tag{B5e}$$

where

$$a^* = 92/(31000)^{1/3} \quad \text{and} \quad q^* = q(3100)^{\gamma/3} \tag{B5f}$$

The uniform dawn-dusk E-field originally introduced by Kavanagh, et al. (1968) is obtained by setting $\gamma = 1$ and $q = E_o$ where E_o is the dawn to dusk convection electric field intensity in the magnetotail expressed in kV/R_E.

More than ten years ago McIlwain (1972, 1974) introduced a different type of magnetospheric E-field model with 120 ajustable parameters which he determined to match the ions and electrons spectrograms observed along ATS 5 geostationary orbit, for geomagnetic activity conditions ranging between 1 and 2. In McIlwain's E3H model the equatorial electric potential is given in kV by

TABLE B1 : Coefficients for electric field model.

j	A_{ij}	A_{2j}	A_{3j}	A_{4j}	A_{5j}	A_{6j}	φ_j	C_j
1	6.49	3.26	2.30	1.12	- 0.24	0.17	4	2
2	1.37	0.83	0.38	0.48	- 0.17	0.13	6	2
3	1.73	0.84	0.36	0.50	- 0.26	0.08	8	2
4	0.69	- 0.13	- 0.31	0.16	- 0.28	- 0.03	10	2
5	0.90	- 0.49	- 0.53	- 0.09	- 0.41	- 0.17	12	2
6	0.06	- 1.04	- 0.88	- 0.37	- 0.46	- 0.26	14	2
7	- 0.96	- 1.78	- 1.11	- 0.64	- 0.62	- 0.38	16	2
8	- 2.30	- 1.78	- 1.28	- 0.53	- 0.60	- 0.32	18	2
9	- 3.20	- 2.13	- 1.75	- 0.89	- 0.83	- 0.43	20	2
10	- 0.78	- 1.09	- 0.06	- 0.63	0	- 0.17	21	1
11	1.00	- 1.10	- 0.29	- 0.49	- 0.27	- 0.19	22	1
12	0.59	0.07	- 0.04	0.03	- 0.16	- 0.05	22.5	0.5
13	1.20	0.28	0.17	0.13	- 0.20	- 0.05	23	0.5
14	2.24	0.77	0.57	0.29	- 0.29	- 0.08	23.5	0.5
15	2.64	1.13	0.94	0.40	- 0.23	- 0.06	0	0.5
16	3.47	1.67	1.38	0.53	- 0.22	- 0.06	0.5	0.5
17	2.48	1.27	1.05	0.38	- 0.12	- 0.03	1	0.5
18	2.00	1.04	0.84	0.30	- 0.08	- 0.02	1.5	0.5
19	5.67	2.92	2.28	0.76	- 0.13	- 0.02	2	1
20	2.23	1.00	0.72	0.30	- 0.03	0.06	3	1
i	1	2	3	4	5	6		
B_i	0	40	100	180	280	400		
d_i	30	50	70	90	110	130		

$$\phi = 10 - 92 \left(\frac{B}{31000} \right)^{1/3} + \sum_{i=1}^{6} \sum_{j=1}^{20} A_{ij} \exp \{- a_i (B - B_i)^2 - b_j \, [1 - \cos(\varphi - \varphi_j)]\} \tag{B6}$$

where B is the equatorial magnetic field in nT, and, φ is the local time (LT). The first term is an arbitrary constant set to make the potential vary around zero at geostationary orbit. The second term is the corotational field. The last term is a set of 120 functions with approximately gaussian forms (i) centered at $B = B_i$ and $\varphi = \varphi_j$, and (ii) with shapes given by the values of the a_i and b_j coefficients. The values which were preselected for B_i, $a_i = \ln 2/d_i^2$, φ_j and $b_j/(1 - 2 \cos c_j)$ are included in Table B1 where B_i are in nT, while φ_j and c_j are angles measured in hours.

It has been verified that under similar geomagnetic conditions this E3H model fits also the observations made with another geostationary satellite : ATS 6 (Lemaire, 1982).

Again in order to calculate the electric field intensity, as well the convection velocity and its spatial derivatives, it is necessary to calculate first the following quantities :

$$\frac{\partial \phi}{\partial \varphi} = - \sum_{i=1}^{6} \sum_{j=1}^{20} A_{ij} \, e^{-\alpha_i - \beta_j} \, b_j \sin(\varphi - \varphi_j) \tag{B7}$$

$$\frac{\partial \phi}{\partial B} = - \frac{a^*}{3} B^{-2/3} - 2 \sum_{i=1}^{6} \sum_{j=1}^{20} A_{ij} \, e^{-\alpha_i - \beta_j} \, a_i (B - B_i)$$

$$\frac{\partial^2 \phi}{\partial \varphi^2} = \sum_{i=1}^{6} \sum_{j=1}^{20} A_{ij} \, e^{-\alpha_i - \beta_j} \, [b_j^2 \sin^2(\varphi - \varphi_j) - b_j \cos(\varphi - \varphi_j)]$$

$$\frac{\partial^2\phi}{\partial B^2} = \frac{2a^*}{9} B^{-5/3} + 2 \sum_{i=1}^{6} \sum_{j=1}^{20} A_{ij}\, e^{-\alpha_i - \beta_j} \left[2\, a_i^2 (B - B_i)^2 - a_i\right]$$

$$\frac{\partial^2\phi}{\partial\varphi\partial B} = 2 \sum_{i=1}^{6} \sum_{j=1}^{20} A_{ij}\, e^{-\alpha_i - \beta_j}\, a_i\, b_j (B - B_i) \sin(\varphi - \varphi_j)$$

where $a^* = 92/(31000)^{1/3}$, $\alpha_i = a_i(B - B_i)^2$ and $\beta_j = b_j\,[1 - \cos(\varphi - \varphi_j)]$.

These derivatives are given in the (B, φ) coordinates system. To obtain the derivatives of $\phi[B(R, \varphi), \varphi]$ in the (R, φ) coordinate system the following transformations must be made. Henceforth, we denote these derivatives by the operators ∇_R, ∇_φ, ∇_φ^2, $\nabla_R \nabla_\varphi \ldots$

$$\nabla_\varphi \phi = \frac{\partial\phi}{\partial\varphi} + \frac{\partial\phi}{\partial B} \cdot \frac{\partial B}{\partial\varphi} \tag{B8a}$$

$$\nabla_R\, \phi = \frac{\partial\phi}{\partial B} \cdot \frac{\partial B}{\partial R} \tag{B8b}$$

$$\nabla_\varphi^2\, \phi = \frac{\partial^2\phi}{\partial\varphi^2} + 2\, \frac{\partial^2\phi}{\partial B\partial\varphi}\, \frac{\partial B}{\partial\varphi} + \frac{\partial^2\phi}{\partial B^2} \cdot \left(\frac{\partial B}{\partial\varphi}\right)^2 + \frac{\partial\phi}{\partial B} \cdot \frac{\partial^2 B}{\partial\varphi^2} \tag{B8c}$$

$$\nabla_R^2\, \phi = \frac{\partial^2\phi}{\partial B^2} \left(\frac{\partial B}{\partial R}\right)^2 + \frac{\partial\phi}{\partial B} \cdot \frac{\partial^2 B}{\partial R^2} \tag{B8d}$$

$$\nabla_\varphi \nabla_R\, \phi = \frac{\partial^2\phi}{\partial B\partial\varphi} \cdot \frac{\partial B}{\partial R} + \frac{\partial^2\phi}{\partial B^2}\, \frac{\partial B}{\partial\varphi} \cdot \frac{\partial B}{\partial R} + \frac{\partial\phi}{\partial B} \cdot \frac{\partial B}{\partial R\partial\varphi} \tag{B8e}$$

where the derivatives of $B(R, \varphi)$ are given by eqs. A(3)-(7), for the M2 magnetic field model, and, by eq. (A8) for a dipole magnetic model.

The electric field component in (R, φ) coordinate system are given by

$$E_R = - \frac{1}{B} \nabla_R \Phi \tag{B9}$$

$$E_\varphi = - \frac{1}{RB} \nabla_\varphi \Phi \tag{B10}$$

Fig. B2 shows the equatorial sections of equipotential surfaces corresponding to the E3H electric field model. The magnetic field model M2 described in Appendix A has been used in eq. (B6).

This field is time independent and was derived from ATS 5 observations for steady geomagnetic activity conditions with K_p ranging between 1 and 2. A whole family of solutions can be generated from eq. (B6) through the conversion

$$B_i' = B_i/f^3 \;,\; a_i' = a_i\, f^6 \text{ and } A_{ij}' = A_{ij}/f \;; \tag{B11}$$

where f is a variable scale factor. It has been suggested by McIlwain (1974) that this conversion could be used to obtain better correspondence to ATS 5 observations when K_p values are outside the range of 1 to 2. Fig. B2 is obtained for f = 1.0. Fig. B3 corresponds to f = 1.2. It can be seen that in the latter case the corotation electric field, with nearly circular equipotential lines extends at larger radial distance. This model ressembles the electric field distribution when geomagnetic activity is very low, i.e. for K_p smaller than 1. On the contrary when f is taken larger than 1.0, the magnetospheric convection electric field components are enhanced and penetrate closer to the Earth, as observed when K_p increases (see fig. B4).

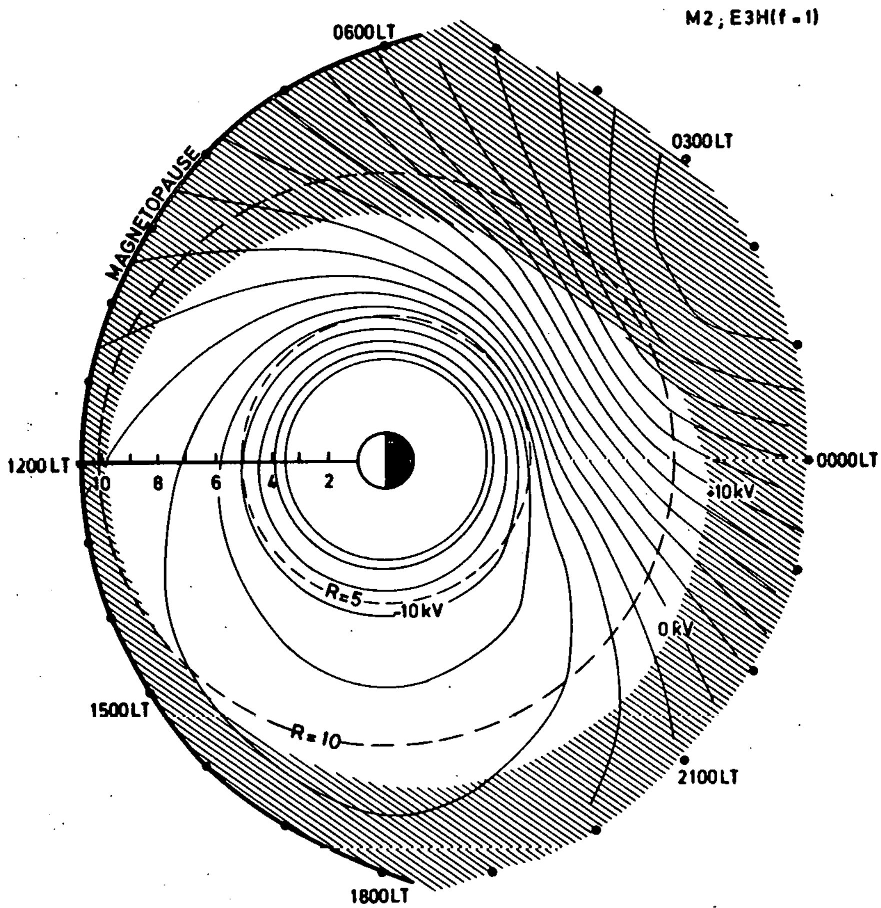

Fig. B2.- Equatorial cross sections of equipotential surfaces corresponding to McIlwain's (1974) E3H electric field model. This empirical E-field distribution has been derived from ATS 5 particle flux measurements along geostationary orbit for periods of time when the geomagnetic activity index ranged between 1 and 2. The hatched area corresponds to the region beyond geostationary altitude where there is no reason to expect the model to be of useful accuracy. Note that corotation is a good approximation up to L = 4. But in the post-midnight local time sector the radial component is significantly enhanced beyond L = 5.

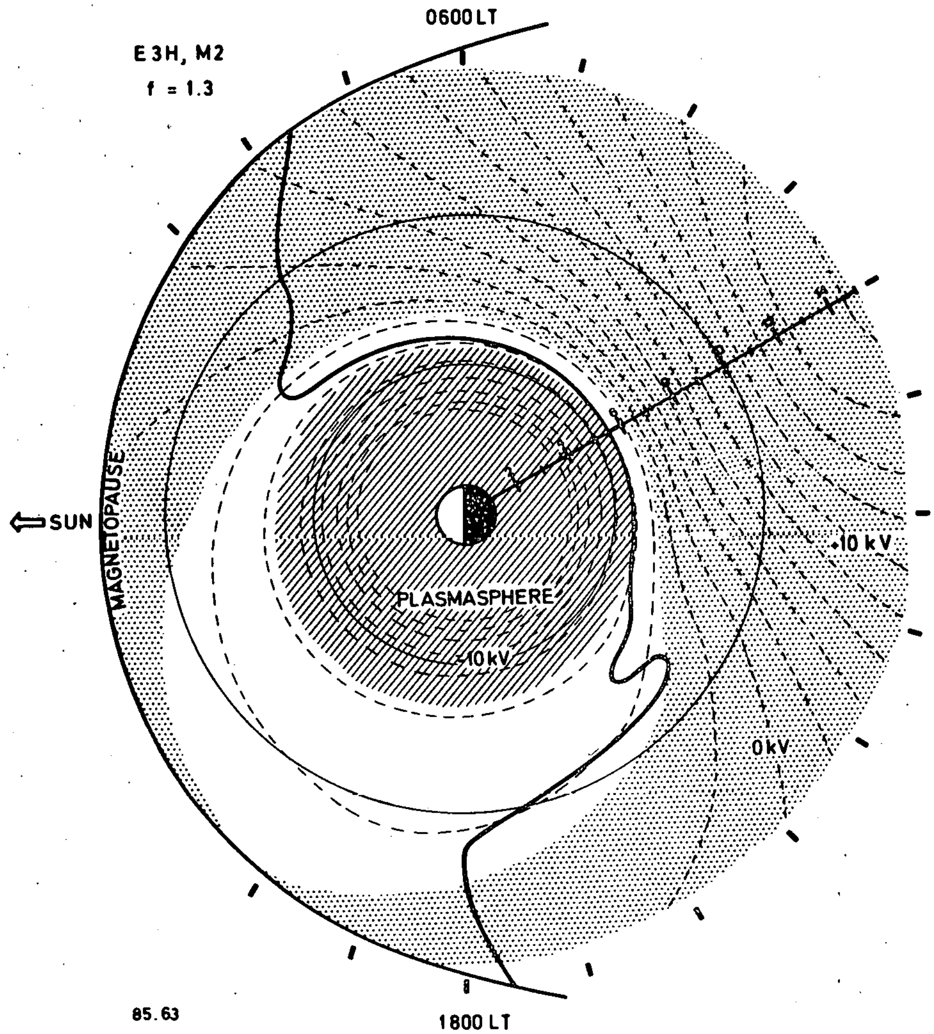

Fig. B3.- The dashed lines represent the Equatorial cross section of equipotential surfaces corresponding to McIlwain's (1974) E3H(f) electric field model when the scale factor f is set equal to 1.3. The solid line corresponds to the equatorial cross-section of the Zero-Parallel-Force (ZPF) surface. The inner nearly circular region where corotation is predominant up to L = 6 corresponds approximately to the plasmasphere under very low geomagnetic activity conditions (Kp < 1). The plasmasphere extends at larger radial distances in the noon local time sector than in the post-midnight region. The outer hatched area corresponds to the equatorial regions of the magnetosphere where equipotential surfaces are open and where plasma streamlines extend up to the magnetopause. The inner edge of this area is the Last Closed Equipotential (LCE) for this E-field model.

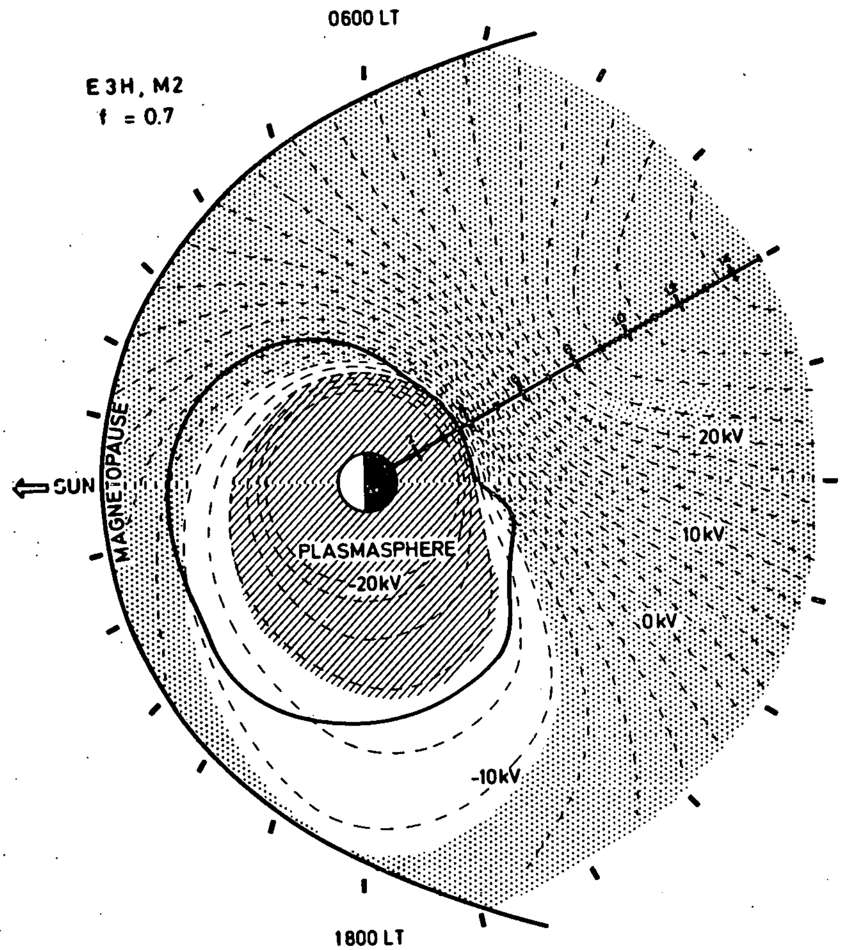

Fig. B4.- Same as in fig.B3, but the scale factor f is set equal to 0.7 in this case. This electric field model E3H (f = 0.7) is representative of the convection electric field in the equatorial plane of the magnetosphere when Kp is of the order of 4. Note the large dawn-dusk asymmetry of the equipotential lines and of the plasmasphere (innermost shaded zone) which develops when the value of f is reduced below f = 1, i.e. when geomagnetic activity is enhanced.

An important feature of the E3H(f) electric field models is that the radial E-field intensity (corresponding to eastward convection) is significantly enhanced beyond R = 4-5, in the post midnight local time sector between 0000 LT and 0600 LT. When f is decreasing (i.e. K_p increasing), the region of enhanced radial E-field (corresponding to super-rotation) penetrates deeper into the plasmasphere (i.e. closer to the Earth) (Lemaire, 1976a).

Another major difference between Volland-Stern's models and the family of E3H models is that in the latter case there is no "stagnation point" where the electric field intensity and the convection velocity are equal to zero. Of course, such a stagnation point may possibly exist in the shaded region in fig. B2, where McIlwain (1974) claims that there is no reason to expect the model to be of useful accuracy. From fig. B2 it can be seen the "last closed equipotential" of the E3H electric field model extends beyond 10 R_E, far into the shaded region, beyond the observed positions of plasmapause.

The electric field models described so far are stationary; they are supposed to simulate the actual magnetospheric E-field when geomagnetic activity remains at a constant level. Except for the numerical E-field models produced by Harel, et al (1976, 1979, 1981), most time dependent E-field models have been constructed by assuming that the intensity of the dawn-dusk component (q) in Volland-Stern's models is modulated as a function of K_p, in an ad-hoc manner, to match observed plasmapause positions in the post-midnight region (Chen and Wolf, 1972; Grebowsky, 1971; Berchem, 1980) or the polar cap potential differences. The same procedure can be used to modulate the value of the scale factor f as a function of K_p. Using the model E3H(f), we have calculated the plasmapause positions (L_{pp}) at 0130 LT, for different values of the scale factor f (Lemaire, 1976a). Since the observed plasmapause positions (L_{pp}) are a function of the maximum value of K_p during the 12 previous hours

$$L_{pp} = 5.7 - 0.47\ K_p \tag{B12}$$

(Carpenter and Park, 1973), we have been able to determine an empirical relationship between f and K_p. This led us to the following empirical relation

$$f = 2.55 - (1.85 + 0.403\ K_p)^{1/2} \tag{B13}$$

This relationship is illustrated in fig. 25. Although, the validity of Carpenter and Park's relation (eq. B12) is restricted to values of K_p smaller than 5, we have used eq. (B13) beyond this limit to simulate the time dependent magnetospheric electric field during the large substorm event of 29 July 1977, when K_p reached a peak value of 7.

APPENDIX C : CONVECTION VELOCITY

The convection velocity $\underline{V}_E$ of plasma in an externally imposed electric field $\underline{E}$ (R,φ) which is perpendicular to a magnetic field $\underline{B}(R,\varphi,\lambda)$ is given by

$$\underline{V}_E = \underline{E} \times \underline{B}/B^2 \tag{C1}$$

When $\underline{E} \cdot \underline{B} = 0$, the radial and azimuthal components of $\underline{V}_E$ in the equatorial plane are respectively

$$(V_E)_R = \frac{E_\varphi}{B} = -\frac{1}{BR}\frac{\partial\phi(R,\varphi)}{\partial\varphi} \tag{C2}$$

$$(V_E)_\varphi = -\frac{E_R}{B} = +\frac{1}{B}\frac{\partial\phi(R,\varphi)}{\partial R} \tag{C3}$$

When the electric potential $\phi(B,\varphi)$ is given in the (B,φ) coordinate system, the following expressions apply

$$\frac{dR}{dt} = (V_E)_R = -\frac{1}{BR}\nabla_\varphi\phi\ [B(R),\varphi] \tag{C4}$$

$$R\frac{d\varphi}{dt} = (V_E)_\varphi = \frac{1}{B}\nabla_R\ \phi[B(R),\varphi] \tag{C5}$$

where the "nabla" notation $\nabla_\varphi\phi$ and $\nabla_R\phi$ are used instead of $\partial\phi/\partial\varphi\,_R$ and $\partial\phi/\partial R\big|_\varphi$. These derivatives are given in the Appendix B by eqs. (B8a-e).

To calculate the polarization drift ($\underline{V}_p$) acting on the ions and electrons resulting from non-uniformity in the convection flow, it is necessary to calculate

$$\frac{d\underline{V}_E}{dt} = (\underline{V}_E \cdot \text{grad})\, \underline{V}_E + \frac{\partial \underline{V}_E}{\partial t} \tag{C6}$$

Considering that $\underline{E}$ and $\underline{B}$ are independent on time, or vary slowly as a function of t, the last term has been ignored, at first approximation. Of course, this might fail to be a satisfactory approximation when $\partial \underline{E}/\partial t$ or/and $\partial \underline{B}(R,\varphi,t)/\partial t$ become large. Except, during rare catastrophic events these time derivatives can be neglected. As a consequence, $\partial \underline{V}_E/\partial t$ has been assumed to be equal to zero or much smaller than the other terms in eq. (C6). With these restrictions, the radial and azimuthal components of the acceleration are respectively given by

$$\left(\frac{d\underline{V}_E}{dt}\right)_R = (\underline{V}_E)_R\, \nabla_R (\underline{V}_E)_R + \frac{(\underline{V}_E)_\varphi}{R}\, \nabla_\varphi (\underline{V}_E)_R - \frac{(V_E)_\varphi^2}{R} \tag{C7}$$

$$\left(\frac{d\underline{V}_E}{dt}\right)_\varphi = (\underline{V}_E)_R\, \nabla_R (\underline{V}_E)_\varphi + \frac{(\underline{V}_E)_\varphi}{R}\, \nabla_\varphi (\underline{V}_E)_\varphi + \frac{(V_E)_R\, (V_E)_\varphi}{R} \tag{C8}$$

where $(V_E)_R$ and $(\underline{V}_E)_\varphi$ are given above by eqs. (C2) and (C3), or (C4) and (C5), while the derivatives of these velocities are given in the (R,φ) coordinates system by

$$\nabla_R (\underline{V}_E)_R = \frac{1}{BR^2} \nabla_\varphi \phi + \frac{1}{B^2 R} \nabla_R B \cdot \nabla_\varphi \phi - \frac{1}{BR} \nabla_R \nabla_\varphi \phi \tag{C9}$$

$$\nabla_\varphi (\underline{V}_E)_R = \frac{1}{B^2 R} \nabla_\varphi B . \nabla_\varphi \phi - \frac{1}{BR} \nabla_\varphi^2 \phi \tag{C10}$$

$$\nabla_R \, (\underline{V}_E)_\varphi = - \frac{1}{B^2} \nabla_R \, B.\nabla_R\phi + \frac{1}{B} \nabla_R^2 \, \phi \tag{C11}$$

$$\nabla_\varphi \, (\underline{V}_E)_\varphi = - \frac{1}{B^2} \nabla_\varphi \, B.\nabla_R\phi + \frac{1}{B} \nabla_\varphi \nabla_R \, \phi \tag{C12}$$

Note that the derivatives of ϕ and B used in these formulae are given, respectively in the Appendix B and A, for two different empirical electric and magnetic field models.

APPENDIX D : INTEGRATED PEDERSEN CONDUCTIVITY

To calculate the maximum interchange velocity of plasma density enhancements or depressions permeated by magnetic field lines, it is essential to know the values of the electric conductivity along these field lines.

In the magnetosphere and in the upper ionosphere σ_0, the conductivity parallel to the magnetic field direction is large. Indeed σ_0, given by

$$\sigma_0 = \frac{e^2 N}{m_e \nu_{en} + \nu_{ei}} \qquad \text{(D1)}$$

is inversely proportional to the total electron collision frequency ($\nu_{en}+\nu_{ei}$) with neutrals (n) and with ions (i) (Fejer, 1953). Since these collision frequencies decrease exponentially with altitude σ_0 reaches extremely large values for altitudes larger than 250 - 300 km. For this reason magnetic field lines are expected to be almost electric equipotential lines i.e. $\underline{E}.\underline{B} \cong 0$. Note however that even in the collisionless limit, the gravitational field induces a charge separation electric field which has a component parallel to the magnetic field direction (see section 2.2). The MHD condition $\underline{E}.\underline{B} = 0$ is therefore never exactly satisfied in planetary ion-exospheres.

The Pedersen and Hall conductivities σ_1 and σ_2 are the two other components of the σ-tensor. The Pedersen conductivity is relative to a direction perpendicular to $\underline{B}$, and, parallel to the electric field $\underline{E}$.

Let us consider first the distributions of the Pedersen conductivity as a function of altitude, and, then its field aligned integrated value

$$\Sigma_p = \int_{h_o}^{\infty} \sigma_1 \, dh \tag{D2}$$

Unlike for σ_0, ions-neutral collisions contribute significantly to σ_1 which is given by

$$\sigma_1 = \frac{e^2 N}{m} \cdot \frac{\upsilon_{en} + \upsilon_{ei} + \Omega_i \, \omega/\upsilon_{in}}{(\nu_{en} + \nu_{ei})^2 + \omega^2 \left(1 + 2 \frac{m \, \nu_{ei}}{M_i \, \nu_{in}} + \frac{\Omega_i^2}{\nu_{in}^2}\right)} \tag{D3}$$

where m_e and M_i are the electron and ion masses respectively; - e and N are the electron charge and number density respectively; Ω_i and ω are the ion and electron gyrofrequencies. The Pedersen conductivity is also often noted σ_p instead of σ_1. The height distribution of σ_p is given in figs. D1a,b for noon and midnight local times and for a series of geomagnetic latitudes. These curves have been calculated by Soboleva (1971) from a model ionosphere obtained by averaging a series of electron density profiles, N(h), corresponding to winter conditions, for minimum solar activity, and for quiet geomagnetic conditions ($K_p < 2$).

In the daytime (see fig. D1a), the altitude distribution of σ_p has one maximum in the E-region (110-120 km) where the ion-neutral collision frequency υ_{in} becomes almost equal to the ion gyrofrequency Ω_i. At higher altitude σ_p decreases very rapidly to zero, while σ_0 increases steadily. During daytime the E-region maximum maximorum value of $\sigma_p(h)$ is at noon local time (φ = 1200 LT) at equatorial latitudes ($\lambda \cong 0$). During nighttime σ_p is maximum maximorum at high latitudes ($\lambda > 75°$).

It can also be seen from figs. D1a,b that the nightside Pedersen conductivity is significantly smaller than the dayside one. This is also true for the values of the integrated Pedersen conductivities (eq. D2), which, at midlatitudes (λ = 50°) decrease from 8-9 mhos at noon local time, to less than 0.3 mho near local midnight (Soboleva, 1971).

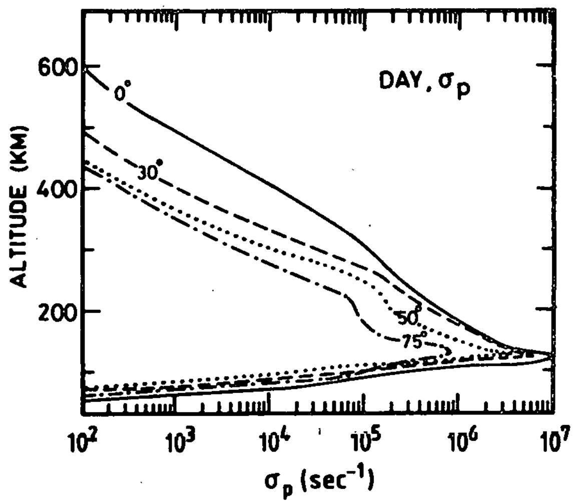

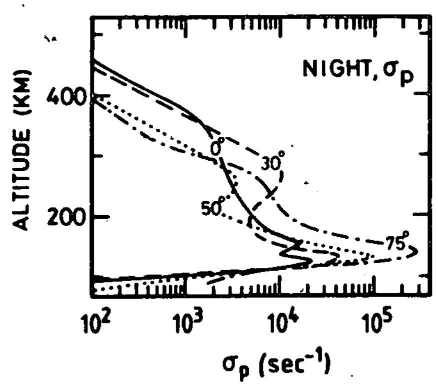

Fig. D1.- Distribution of the Pedersen conductivity (σ_p) versus altitude at noon local time (panel a) and at midnight (panel b) derived by Soboleva (1971) for quiet geomagnetic conditions and solar activity minimum and for different geomagnetic latitudes. The corresponding values of the geomagnetic latitude are indicated on the different curves.

Local time and latitudinal distributions of Σ_p have been modelled by several authors. In our calculations we have adopted the empirical model proposed by Gurevitch, et al. (1976). Indeed this model is based on a large series of observations. Furthermore, in addition to the diurnal, latitudinal and seasonal variations, it takes into account the dependence of Σ_p on geomagnetic activity (K_p), and on the level of solar activity.

The height integrated value of the Pedersen conductivity appears in the form of a sum of two terms $\Sigma_p^s(\theta, \varphi)$ and $\Sigma_p^d(\theta, \varphi)$ describing respectively the conductivity determined by solar photo-ionization and the conductivity enhancement resulting from corpuscular ionization sources at geomagnetic latitudes higher then $\theta > 50°$

$$\Sigma_p^s(\theta, \varphi) = \Sigma^D(\theta) \exp \{f(\theta) F(\varphi)\} \tag{D4a}$$

with

$$f(\theta) = \ln [\Sigma^D(\theta)/\Sigma^N(\theta)] \tag{D4b}$$

where $\Sigma^D(\theta)$ and $\Sigma^N(\theta)$ describe respectively the variation of Σ_p^s in the noon and midnight meridians

$$\Sigma^D(\theta) = (a_e^D - a_p^D) \cos^{3/2} \theta + a_p \tag{D4c}$$

$$\Sigma^N(\theta) = a_e^N + (a_p^N - a_e^N) \sin^\lambda \theta \tag{D4d}$$

Here $a_e^{D,N}$ and $a_p^{D,N}$ are the values of $\Sigma^{D,N}(\theta)$ at the equator (e) and at the geomagnetic pole (p). The values of a's and λ are found by comparison of $\dot{\Sigma}$ values deduced from these empirical formulae with observational results

$$a_e^D = 18 \text{ mho}, \quad a_e^N = 0.2 \text{ mho}$$

$$a_p^D = a_p^N = a_p = 2 \text{ mho} \tag{D4e}$$

$$\lambda = 6$$

The function $F(\varphi)$ describes the longitudinal dependence of Σ^S

$$F(\varphi) = -1 + 0.5 \left[1 + \frac{(\pi - |\varphi_o|)(|\varphi| - |\varphi_{om}|)}{\pi - |\varphi|} \right]^{-\lambda_m}, \quad \varphi_{om} > \varphi > -\pi$$

$$= -0.5 \left[1 + \frac{\varphi_{om}(|\varphi_{om}| - |\varphi|)}{\varphi} \right]^{-\lambda_m}, \quad 0 > \varphi > \varphi_{om}$$

$$= -0.5 \left[1 + \frac{\varphi_{oe}(\varphi_{oe} - \varphi)}{\varphi} \right]^{-\lambda_e}, \quad \varphi_{oe} > \varphi > 0$$

$$= -1 + 0.5 \left[1 + \frac{(\pi - \varphi_{oe})(\varphi - \varphi_{oe})}{\pi - \varphi} \right]^{-\lambda_e} \quad \pi > \varphi > \varphi_{oe} \tag{D4f}$$

$F(\varphi)$ is a smooth function which changes from $F = 0$ at noon LT, to $F = -1$ at midnight ($\varphi = \pm\pi$). Here φ_{om} is the value of the longitude when $F = -0.5$, i.e. where $\Sigma^S(\theta) = [\Sigma^D(\theta)\, \Sigma^M(\theta)]^{1/2}$ in the morning local time sector; φ_{oe} is the corresponding value of φ in the evening local time sector. The parameter λ_m and λ_e determine the variation of $\Sigma^S(\theta,\varphi)$ in the morning and evening local time sectors.

TABLE D1 :Values of the constants θ_1, θ_2, θ_m, b_θ , a_p and b_m for low, medium and high magnetic activity.

Magnetic activity	θ_1 (deg)	θ_2 (deg)	θ_m (deg)	b_θ $(deg)^2$	a_p	b_m (mho)
Night						
low	50	81	66	848	1.79	1.8
medium	50	81	66	848	2.12	5
high	50	81	66	848	2.82	15
Day						
low	50	86	75	877	1.2	1
medium	50	86	75	877	1.2	2
high	50	86	75	877	1.2	3

The quantities φ_{om}, φ_{oe}, λ_m and λ_e are functions of the latitude θ. However, a comparison between results obtained with this model and observations indicate that at a first approximation these quantities can be regarded as constant

$$\varphi_{om} = -0.45\pi \; ; \; \varphi_{oe} = 0.5\pi$$

$$\lambda_m = \lambda_e = 2 \qquad \text{(D4g)}$$

The shift of the value φ_{om} relative to the meridian $\pi/2$ describes the half-hour LT lag of the Σ^S maximum.

The coefficients a (see D4.e,c,d) correspond to conditions of minimum solar activity. For conditions of moderate activity the values of the a's (and the values of Σ^S) are a factor 1.5 larger while for maximum solar activity they should be multiplied by a factor of 2 Gurevitch, et al. (1976).

Fig. D2 shows isointensity contours for Σ^S (in mho) as determined from the eqs. D4a-g (1 mho = 1 Siemens).

This model corresponds to equinox conditions, when the angle α between the geomagnetic pole and the twilight line is equal to zero. Under such conditions $\Sigma^S(\theta, \varphi)$ is symmetric with respect to the geomagnetic equator $\theta = 0$. This is no longer correct when $\alpha \neq 0$, i.e. when the twilight line does not pass across the geographic and geomagnetic poles. To obtain the corresponding values of $\Sigma^S(\theta, \varphi)$ in the northern and southern hemispheres it has been shown by Gurevitch, et al. (1976) that one must replace θ and φ by $\bar{\theta}$ and $\bar{\varphi}$ in the previous expressions

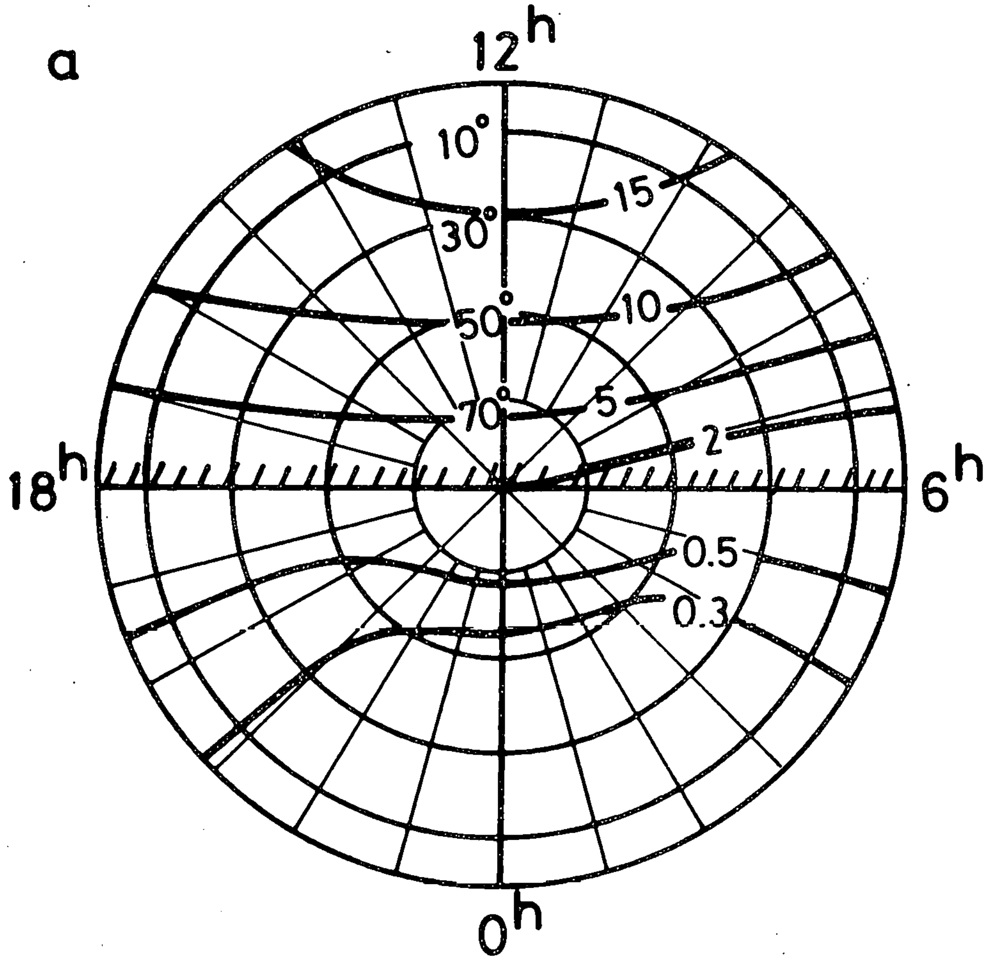

Fig. D2.- Isocontours of the integrated Pedersen conductivity resulting from solar photoionization in Siemens for equinox conditions ($\alpha = 0$). (After Gurevitch et al.,1976).

$$\bar{\theta} = \arcsin\,[\cos\alpha\,\sin\theta - \cos\theta\,\sin\alpha\,\cos\varphi] \qquad \text{(D5a)}$$

$$\bar{\varphi} = \arccos\,\frac{\sin\alpha\,\sin\theta + \cos\alpha\,\cos\theta\,\cos\varphi}{\left[1 - (\cos\alpha\,\sin\theta - \cos\theta\,\sin\alpha\,\cos\varphi)^2\right]^{1/2}} \qquad \text{(D5b)}$$

Fig. D3a,b illustrate the values of $\Sigma_p^s(\bar{\theta}, \bar{\varphi})$ in the northern summer and southern winter hemispheres, respectively, for $\alpha = 17°$.

So far we have modelled the distribution of Σ_p^s resulting from photoionization. Corpuscular radiation from the magnetosphere is another source to ionize the upper atmosphere and to enhance the value of the integrated Pedersen conductivity in the auroral precipitation zones. To model this high latitude conductivity enhancement Gurevitch, et al. (1976) suggest the same function has in eq. (D4a) : i.e.

$$\Sigma_p^d(\theta, \varphi) = \Sigma_p^{dD}(\theta)\,\exp\,\{f(\theta)\,F(\varphi)\} \qquad \text{(D6a)}$$

where $f(\theta)$ and $F(\varphi)$ are given by eq. (D4b) and (D4f) with

$$\lambda_e = \lambda_m = 2 \qquad \text{(D6b)}$$

$$\varphi_{oe} = \frac{\pi}{2}\;\frac{(1 - 2\theta/\pi)}{(0.58 - \theta/\pi)}$$

$$\varphi_{om} = -\frac{\pi}{4}\,[1 + \cos^4 5(\theta - 75°)]$$

The noon and midnight latitudinal variations of $\Sigma^d(\theta,\varphi)$ are given by

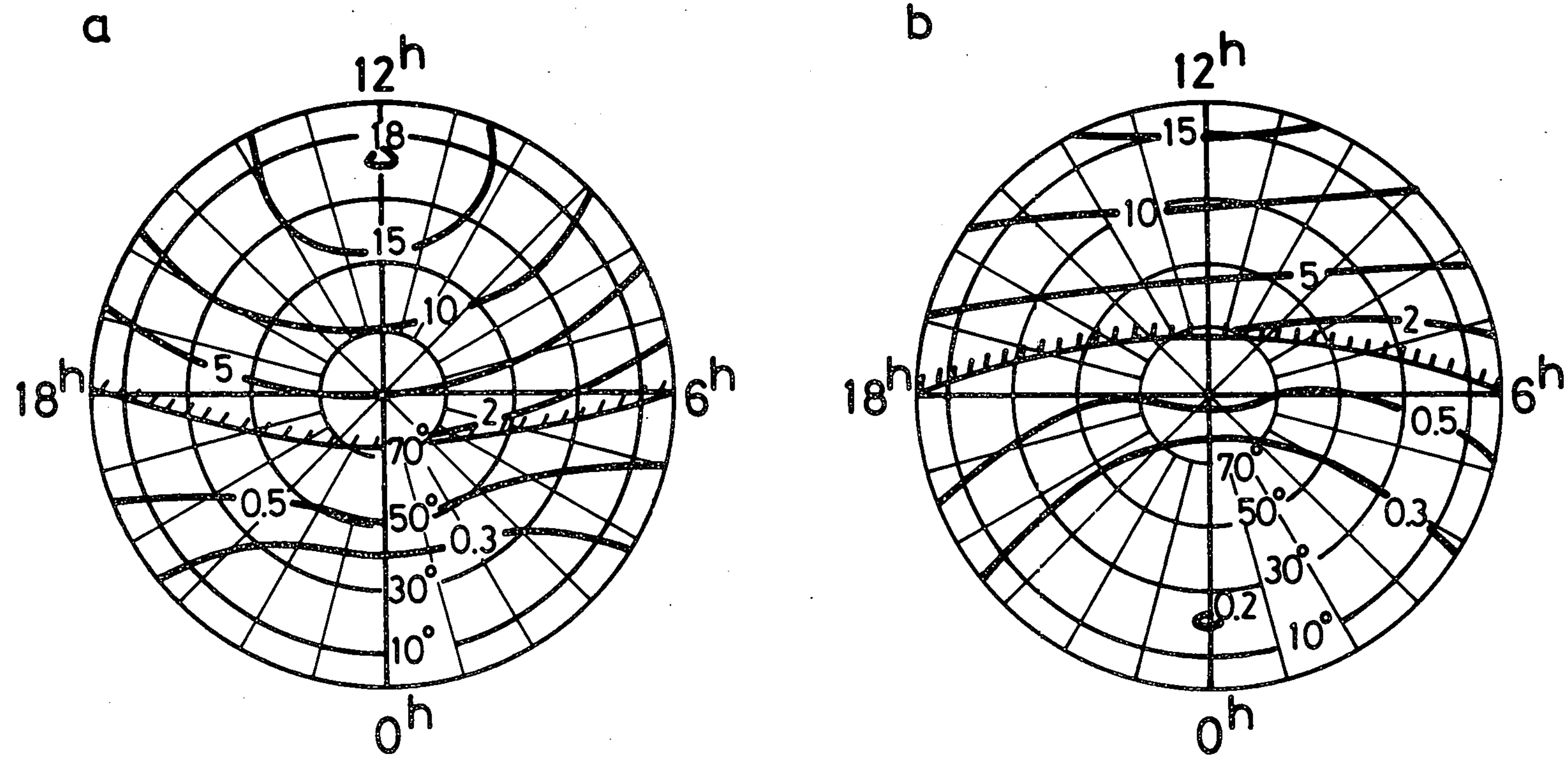

Fig. D3.- Isocontours of the integrated Pedersen conductivity Σ_p^S in Siemens a) for northern summer conditions (a = 17°); b) for the southern winter hemisphere (a = 17°).

$$\Sigma_p^{dD}(\theta) = b_m \, E(\theta_1, \frac{\pi}{2}) \times$$

$$\times \exp \left\{ - \frac{b_\theta \, (\theta - \theta_m)^2}{(\theta - \theta_1)^2 \, (\theta - \theta_2)^2 \, E(\theta_1, \theta_2) + \frac{b_\theta}{a_p} \, (\theta - \theta_m)^2 \, E(\theta_m, \frac{\pi}{2})} \right\} \tag{D6c}$$

with a similar expression for $\Sigma_p^{dN}(\theta)$

$$a_p = \ln (b_m/b_p) \tag{D6d}$$

$$E(\theta_1, \theta_2) = 1 \quad \text{for } \theta_1 < \theta < \theta_2 \tag{D6e}$$

$$= 0 \quad \text{for } \theta < \theta_1 \text{ or } \theta > \theta_2$$

b_m is the maximum value of Σ_p^d in the auroral region (at $\theta = \theta_m$); b_θ is a constant determining the width of the enhanced conductivity region; θ_1 and θ_2 correspond to the boundaries of the region, and, θ_m gives the latitude of the maximum of $\Sigma_p^{dD}(\theta)$ and $\Sigma_p^{dN}(\theta)$; b_p gives the value of Σ_p^d at the geomagnetic pole. The values of these constants are given in table D1 for different levels of magnetic activity.

Fig. D4 illustrates the distribution of $\Sigma_p^d(\theta, \varphi)$ calculated according to equations (D6a-d) for quiet geomagnetic conditions.

The maximum maximorum values for Σ_p^d is located in the auroral zone just after midnight local time. However at plasmapause latitudes ($\theta \leqq 60°$), the local time distribution of the total integrated Pedersen conductivity $\Sigma^d + \Sigma^s$, has an absolute minimum near midnight local time and a maximum at 1230 LT.

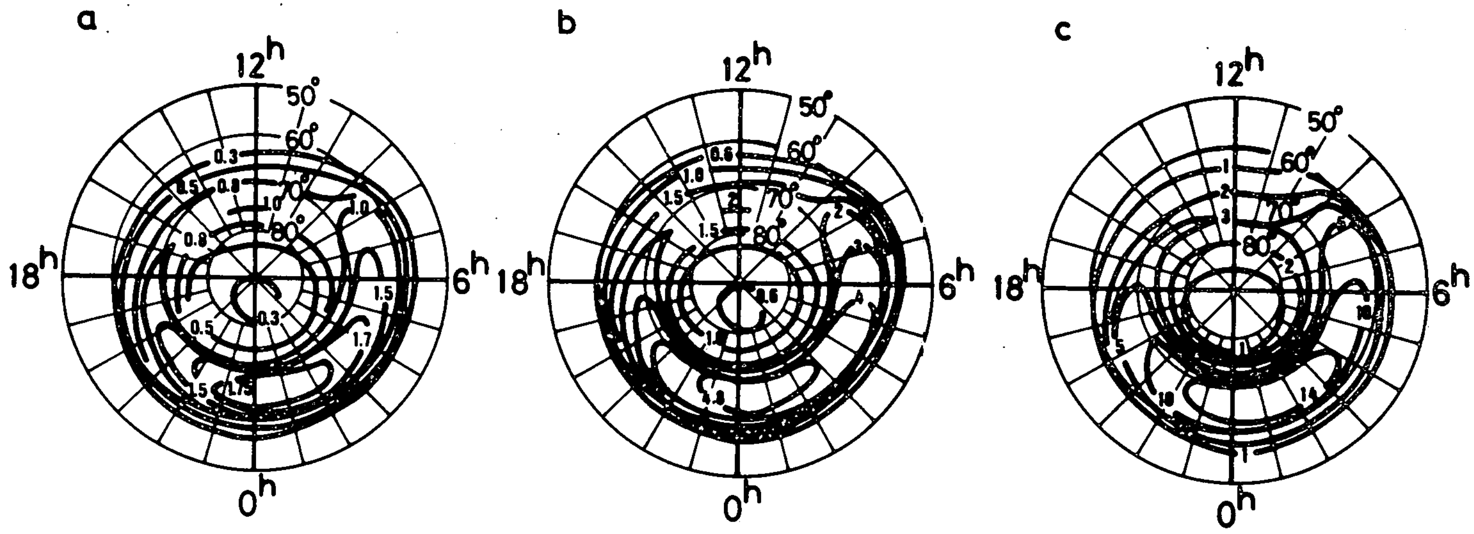

Fig. D4.- Isocontours of the integrated Pedersen conductivity Σ^{s}_{p} resulting from corpuscular ionization (in Siemens) a) for quiet geomagnetic conditions; b) mean geomagnetic activity and c) high activity

APPENDIX E : REFILLING TIME OF EMPTY FLUX TUBES

Let us consider a depleted magnetic flux tube. If F is the constant ionization flux escaping out of the topside ionosphere trough the surface S_o, the characteristic time (t_N) necessary to recover the total flux tube particle content (N_T^{DE})corresponding to diffusive equilibrium, is given by

$$t_N = \frac{N_T^{DE}}{FS_o} \tag{E1}$$

The maximum upward flux is equal to the free evaporation flux at the exobase where the mean free path of the particles becomes equal to the local plasma density scale height. Lemaire and Scherer (1970, 1974) have shown that for the polar wind the maximum upward flow of H^+ ions is of the order of

$$F_{pw} = \frac{1}{4} n_o \left(\frac{8kT_o}{\pi m_H}\right)^{1/2} \tag{E2}$$

where m_H is the mass of Hydrogen; n_o and T_o are respectively the density and temperature at the exobase. Assuming that n_o = 1000 cm^{-3} and T_o = 3000 K, it results from eq. (E2) that $F_{pw} = 2 \times 10^8$ cm^{-2} s^{-1}.

For L = 4, $N_T^{DE}/S_o = 8.4 \times 10^{13}$ particles/cm^2, F = 2 x 10^8 cm^{-2} s^{-1}, one obtains t_N > 115 hours : i.e. more than 4 days. The refilling time (t_N) necessary to recover a diffusive equilibrium density distribution increases rapidly with L. For instance at L = 8, t_N is of the order of 1600 hours (66 days). Other intermediate values for t_N are reported in Table E1. These order of magnitude calculations agree with the refilling times estimated from whistler observations and with the simulations presented in fig. 15.

TABLE E1 :Flux tube refilling times (t_N) for different values of L. A maximum polar wind flux of 2×10^8 cm^{-2} s^{-1} is assumed to flow at a constant rate to increase the total flux tube content from the minimum (EE) value to their maximum value (DE).

L	2	4	6	8	R_E
t_N	9.4	115	544	1587	hours
t_N	-	4.7	22.7	66.1	days

These calculations indicate also that the refilling process by diffusion or by ionospheric evaporation is a relatively slow process, especially for L > 4 where t_N exceeds 4 days. Since the time between two successive substorms rarely exceeds 4 days, it can be concluded that beyond L = 4 a magnetic flux tube which is depleted during a substorm event rarely has time to fill up to the stage of diffusion equilibrium before the next substorm depletes it again. This conclusion had already been reached by Park (1974) and Corcuff, et al. (1972) from detailed studies of whistler observations over periods of several days.

APPENDIX F . FREE FLIGHT TIMES OF THERMAL IONS AND COLLISION TIMES

A The characteristic time necessary to build up the minimum Exospheric Equilibrium density distribution shown by the lower curves in figs. 5, 6 and 7. corresponds to the lapse time (t_F) necessary for a thermal proton to spiral along the magnetic field line from the ionosphere up to the equatorial plane

$$t_F = \int_{1000 \text{ km}}^{\text{equator}} \frac{dl}{v_\parallel} \tag{F1}$$

where $v_\parallel$ is the velocity component parallel to the magnetic field direction. For a proton with an initial pitch angle of 45° at 1000 km altitude and an initial velocity equal to the mean thermal speed $(8\,kT_o/\pi m)^{1/2}$, the free flight times are given in Table F1 for T_o = 3000 K. Note that t_F is much shorter than t_N, the refilling time calculated in Appendix E

After the lapse of time t_F, the class of "escape trajectories" (e) and of "ballistic orbits" (b) are populated with particles which have the same energy as those of the topside ionosphere, but their pitch angle tends to be depleted for large pitch angles, i.e. outside the source cones illustrated in fig. 3. Indeed, trapped orbits (t_1, t_2, t_3 or t_4) can only become populated via collisional processes.

B. Coulomb collisions between ions with energies less than 1 eV cannot be completely ignored in the plasmasphere; indeed, they are actually frequent enough to change significantly the pitch angles of the spiraling ions and scatter them outside the source cone.

TABLE F1 : Free Flight time (t_F) of a thermal proton spiraling along the magnetic field line (L) from an altitude of 1000 km up to the equatorial plane. The proton has an energy of 0.25 eV (T_o = 3000 eV) and an initial pitch angle of 45° at 1000 km altitude; its field aligned velocity is calculated along the field line by assuming conservation of the magnetic moment of the particle (eq. 3.25) and conservation of the sum of kinetic energy and potential energy given by eq. 2.8 and illustrated in fig. 2; t_S is the Coulomb collision time of a thermal proton (0.25 eV, T ≅ 3000 eV) gyrating in the equatorial plane; the background plasma density is assumed to be equal to that of the minimum exospheric equilibrium model (n_{eq}^{EE}) illustrated in fig. 8.

L	2	4	6	8
t_F	42 m	1.9 h	3.6 h	5.2 h
t_S	16 m	2.8 h	10 h	28 h
n_{eq}^{EE}	80 cm^{-3}	8.1 cm^{-3}	2.2 cm^{-3}	0.82 cm^{-3}

As a result of Coulomb interactions, the trapped orbits become gradually populated. Pitch angle diffusion refills the velocity distribution outside the loss cone. The orbits corresponding to the smallest energies and to the smallest equatorial pitch angles (i.e. to the lowest mirror altitudes) become populated first. It takes a much longer time to refill the pitch angles near 90° because these particles mirror at higher altitudes where the density is smallest and the collision frequency lowest. The mean collision for a thermal proton gyrating in the equatorial plane with a pitch angle of 90°, is given by

$$t_S = 0.5 \frac{T^{3/2}}{n} \quad [\mathrm{sec}] \tag{F2}$$

Spitzer (1956), where T and n are the temperature (in K) and density (in cm^{-3}) of the background hydrogen plasma, respectively. In the exospheric equilibrium density model illustrated in Fig. 5, 6 or 7, the equatorial density is $n_{eq} = 8\ cm^{-3}$ at $L = 4$, with $T = 3000$ K it results from eq. F2 that $t_S = 2.8$ h. In the case of diffusive equilibrium the equatorial density at $L = 4$ is 60 times larger, and t_S is 60 times smaller ($t_S = 2.8$ min). At $L = 8$, where the equatorial plasma density in the exospheric model is only $0.8\ cm^{-3}$, t_S is equal to more than 1 day. Table F1 gives the values of t_S as a function of L for the minimum exospheric equilibrium density model.

From tables E1 and F1, it can be concluded that, t_F, the time to build up a collisionless ion-exosphere density distribution in a magnetic flux tube, is at least one order of magnitude smaller than t_N, the characteristic refilling time necessary to established barometric equilibrium. For $L > 3$, t_F is also smaller than t_S, the equatorial Coulomb collision time, which corresponds to the pitch angle diffusion time necessary to smooth an anisotropic pitch angle distribution. Therefore, along magnetic field lines with large L-values, it takes less time to establish the highly anisotropic velocity distribution corresponding to the Exospheric Equilibrium model, than for pitch angle diffusion to smooth out this large anisotropy in the proton velocity distribution. In other words, in newly depleted flux tubes outside the plasmapause, anisotropic pitch angle distributions can be maintained in the ion thermal energy range for several hours before binary Coulomb collisions eventually make it become isotropic.

Recent observations with the Retarding Ion Mass Spectrometer on Dynamic Explorer, indicate that after large substorm events highly anisotropic field aligned ion flows are present during several hours, in significantly depleted flux tubes (Horwitz, et al. 1984). These observations confirm the order of magnitude calculations and the discussion presented above.

C. As a result of Coulomb collisions the time for a thermal proton to diffuse from the ionosphere to the equatorial plane is longer than the average than (t_F) estimated in table F1. A thermal proton escaping at the altitude of 1000 km from the upper ionosphere experiences usually more than one 90° pitch angle deflection, before it can reach the equatorial plane. The expected number of collisions of a particle spiralling along a field line L is given by

$$q = \int_{o}^{t_F} \frac{dt}{t_S} \tag{F3}$$

where t_F is the time required for the particle to travel from the exobase to the equatorial plane; t_F is given by eq. (F1), t_S is a characteristic collision time given by eq. (F2).

If $v_{\parallel}(\lambda)$ is the component of the velocity parallel to the magnetic field direction, eq. (F3) becomes

$$q = \int_{R_o}^{R_{eq}} \frac{dl(\lambda)}{t_S(\lambda)\; v_{\parallel}(\lambda)} \tag{F4}$$

where dl is the element of magnetic field line. For a dipole magnetic field

$$dl = L\,R_E \cos\lambda \sqrt{1 + 3\sin^2\lambda}\; d\lambda \qquad \text{(F5)}$$

If θ is the local pitch angle of the test particle

$$v_{\parallel} = v\cos\theta \qquad \text{(F6)}$$

Considering that the magnetic moment and the total energy are conserved between two collisions

$$v_{\parallel} = \sqrt{\frac{2kT_F}{m}\left(V_o^2 - \psi - \frac{B}{B_o} V_o^2 \sin^2\theta_o\right)} \qquad \text{(F7)}$$

where T_F is the temperature of the field particles; m_F the mass and $Z_F e$ charge of these particles; V_o is the normalized velocity of the test particle at the exobase : $V_o = v_o/(2\,k\,T_F/m\,)^{1/2}$; θ_o is the initial pitch angle at the exobase; $\psi(\lambda)$ is the normalized potential energy distribution

$$\psi(\lambda) = -\frac{m_F + m_e}{2}\,\frac{GM\,m}{LR_E\,kT_F}\left[\frac{1}{\cos^2\lambda} - \frac{1}{\cos^2\lambda_o} + \frac{\Omega^2 R_E^3 L^3}{2\,GM}\left(\cos^6\lambda - \cos^6\lambda_o\right)\right] \qquad \text{(F8)}$$

TABLE F2 : Expected number of Coulomb collisions for protons (p^+) and electrons (e^-) injected at 1000 km with a pitch angle (θ_o), an initial velocity (v_o), i.e. an initial energy (K_o); q_1 is the expected number of collisions for a background plasma density distribution in Diffusive Equilibrium (T_F = 3000 K and n_F = 10^3 cm^{-3} at 1000 km, $v_T^2 = 2\,kT_F/m$; q_2 is the expected number of collisions when the background density distribution is in Exospheric Equilibrium for the same exobase conditions; t_F is the free flight time of the test particle from the 1000 km level up to the equatorial plane along the field line L = 4.

Test particle	Field particle	v_o/v_T -	K_o [eV]	θ_o [Deg]	q_1 -	q_2 -	t_F [s]
p^+	p^+	1	0.26	45	55.0	6.7	6790
p^+	p^+	1	0.26	0	52.0	5.8	6450
p^+	e^-	1	0.26	45	35.3	4.9	6790
p^+	p^+	1.5	0.58	45	13.5	2.0	3190
p^+	p^+	3.0	2.33	45	0.81	0.13	1410
p^+	p^+	10	25.8	45	0.0059	0.001	409
e^-	p^+	1	0.26	45	5.15	0.36	159
e^-	p^+	1.5	0.58	45	0.24	0.032	74
e^-	p^+	3.0	2.33	45	0.0095	0.0016	33
e^-	p^+	10	25.8	45	0.000068	0.000012	9.5
e^-	e^-	1	0.26	45	55.0	6.7	159

TABLE F3 : Same as in Table F2 but for the magnetic field line L = 8.

Test particle	Field particle	v_o/v_T	K_o [eV]	θ_o [Deg]	q_1 -	q_2 -	t_F [s]
p^+	p^+	1	0.26	45	138.	7.3	18900
p^+	p^+	1	0.26	0	134.	6.3	18400
p^+	e^-	1	0.26	45	82.	5.2	18900
p^+	p^+	1.5	0.58	45	28.	2.1	7400
p^+	p^+	3.0	2.33	45	1.57	0.14	3160
p^+	p^+	10	25.8	45	0.001	0.001	913
e^-	p^+	1	0.26	45	23.9	0.5	441
e^-	p^+	1.5	0.26	45	0.54	0.034	173
e^-	p^+	3.0	2.33	45	0.018	0.0016	74
e^-	p^+	10	25.8	45	0.00013	0.000012	21
e^-	e^-	1	0.26	45	138.	7.3	441

(Lemaire, 1974); $B(\lambda)$ and B_o are the magnetic field intensities respectively at λ and λ_o

$$\frac{B(\lambda)}{B_o} = \frac{\sqrt{1 + 3 \sin^2 \lambda}}{\sqrt{1 + 3 \sin^2 \lambda_o}} \quad \frac{\cos^6 \lambda_o}{\cos^6 \lambda} \tag{F9}$$

The Coulomb collision time that we will consider is the slowing-down characteristic time as defined by Spitzer (1956, p. 79). It is related to the rate at which the mean velocity of the test particle (m, Ze) decreases as a result of encounters with the field particles

$$t_S = \frac{v}{\left(1 + \frac{m}{m_F}\right) A_D \frac{m_F}{2kT_F} \quad G\left(\sqrt{\frac{m_F v^2}{2kT_F}}\right)} \tag{F10}$$

$$G(x) = \frac{1}{2x^2} \left[\frac{2}{\sqrt{\pi}} \int_o^x e^{-y^2} dy - \frac{2xe^{-x^2}}{\sqrt{\pi}}\right] \tag{F11}$$

$$A_D = \frac{8\pi e^4 n_F Z^2 Z_F^2 \ln\Lambda}{m^2} \tag{F12}$$

$$\Lambda = \frac{3}{2ZZ_F e^3} \left(\frac{k^3 T_F^3}{\pi n_F}\right)^{1/2} \tag{F13}$$

The expected number of collisions of a test particle spiraling upwards between the exobase (1000 km) and the equator is given by

$$q(v_o) = \frac{m_F + m}{m} \quad \frac{8\pi e^4}{(2kT_F)^2} \quad LR_E \cdot$$

$$\cdot \int_o^{\lambda_o} \frac{\cos \lambda \sqrt{1 + 3 \sin^2 \lambda}}{v_o^2 \left(1 - \frac{B}{B_o} \sin^2 \theta_o\right) - \psi} \quad G\left[\frac{m_F}{m} (v_o^2 - \psi)\right] \ln \Lambda \, . \, n_F \, d\lambda \tag{F14}$$

When the field particles (thermal H^+ ions and electrons) are in diffusive equilibrium $n_F(\lambda)$ is given by eq. (2.19), and, the expected number of collisions is then given by q_1 in Table F2. The value of q_2 corresponds to the contribution of the ballistic and escaping particles obtained by assuming that $n_F(\lambda)$ is given by eq. (2.18), corresponding to the exospheric equilibrium model with T_F = 3000 K and $n_F = 10^3$ cm^{-3} at the reference level of 1000 km.

The test particles considered in the calculation spiral along a magnetic field line at L = 4; different initial pitch angles (θ_o), velocities (v_o) and kinetic energies (K_o) have been chosen at the reference level of 1000 km. The field particles are considered to be either protons (p^+) or thermal electrons (e^-).

It can be seen that a thermal proton or electron experiences several collisions on its upward motion toward the equator along the magnetic field L = 4. When the field particle density corresponds to diffusive equilibrium the expected number of collisions is almost 10 times larger than for exospheric equilibrium. For supra-thermal energies (K_o = 13 eV, v_o/v_T = 10) the values of q_1 and q_2 decrease rapidly below unity. This drastic reduction results from the sensitivity of the Coulomb collision cross section to the energy of the incident charged particles. Therefore, it can be deduced that larger departures from isotropic pitch angle distributions are expected for suprathermal protons with energies larger than 5-10 eV.

Note also that protons (p^+) are more efficiently deflected by collisions with other protons than with the field electrons. A test electron is much more efficiently scattered by the field electrons than by field protons of the same mean energy.

The electrons travel to the equatorial plane 43 times faster than the protons of same energy but these electrons experience almost the same number of collisions than the protons. Therefore, it can be concluded that Coulomb collisions will restore isotropy of the electron velocity distribution much faster than for the thermal ions in the plasmasphere.

Comparison of Tables F2 ($L = 4$) and F3 ($L = 8$) indicates that the number of collisions q_2 in an exospheric equilibrium model (i.e. without $t_1 - t_4$ trapped particles) is almost independent of L, i.e. of the length of the magnetic field line. For a background density distribution in Diffusive Equilibrium the expected number of collisions (q_1) is almost two times larger along $L = 8$ than along $L = 4$. The free flight times (t_F) are a factor 2.8 larger for $L = 8$ than for $L = 4$.

APPENDIX G : THE IDEAL MHD THEORY FOR THE FORMATION OF A PLASMAPAUSE

A. Inspired by the observations of Carpenter (1963, 1966), an ideal MHD theory for the formation of a plasmapause was first suggested by Nishida (1966) and subsequently developed by Brice (1967). It is this model which is discussed in this Appendix. A discussion of the limitations and drawbacks of this model will also be presented.

According to the MHD theory the "knee" in the equatorial plasma density distribution is supposed to be the boundary between (i) plasma that drifts along closed electric equipotential surfaces, and (ii) plasma that somewhere along its drift path ends up onto a open magnetic field lines (i.e. polar cusp or polar cap field lines which extend deep into the magnetotail). The solid lines in Fig. G1 illustrate the drift paths of plasma elements on both sides of this boundary for a uniform dawn-dusk electric field model (i.e. a Volland-Stern model with γ = 1, see Appendix B). Inside this boundary indicated by a thick line, plasma remains trapped on closed field lines; the plasma density is expected to be large, close to the saturation value corresponding to Diffusive Equilibrium. Outside this limit, however, the ambient plasma escapes along open magnetotail field lines interconnected with those of the interplanetary medium.

This limit coïncides with the Last Closed Equipotential (LCE) surface passing through the stagnation point at L = 5 in the dusk meridional plane; The LCE determines the positions of the plasmapause. As a matter of fact, on the inner side of this surface plasma elements drift indefinitely along closed trajectories; they can refill until they eventually reach high equatorial densities. On the outerside of the LCE, all plasma elements drift to the magnetopause in less than 24 h, a period of time much shorter than the magnetic flux tube refilling times;

therefore, the slow refilling mechanism is unable to build up, fast enough, high values for the equatorial density just outside the LCE. As a consequence, under steady state conditions, and after a period of 24 hours a density gradient is expected to be formed along the LCE. This density gradient was identified by Nishida (1966), Brice (1967), Kavanagh et al. (1968), Volland (1973, 1975) and others as the steady state plasmapause.

B. The "tear-drop" shape of the LCE mimics the dawn-dusk asymmetry of the whistlers knee observed by Carpenter (1966). Indeed, like the observed plasmapause illustrated in fig. 1c, the LCE shown by the thick line in fig. G1 has a bulge at 1800 LT. An ad-hoc adjustments of the intensity of the uniform dawn-dusk electric field intensity (E_o), enabled MHD modelers to place the stagnation point where needed to "explain" (i.e. to fit approximately) the observed plasmapause positions. Table G.1 gives the equatorial distances of the stagnation point for a series of values E_o. From this table it can be seen that the range of variation of E_o is rather narrow (from 0.1 to 5.0 mV/m). Indeed, for values of E_o smaller than 0.1 mV/m the dusk side plasmapause (i.e. the LCE) would extend too far out beyond the magnetopause. On the contrary, for E_o > 5.0 mV/m the plasmapause, at 1800 LT, would shrink closer to the Earth than ever observed.

This indicates that the plasmapause position is a very sensitive function of the value assumed for E_o. This is also illustrated in fig. G1. Indeed, the dashed line represents the LCE when E_o is decreased from an initial value of 0.58 mV/m (thick solid line) to 0.28 mV/m (dashed line; see also Table G1). It can be seen that dividing E_o by a factor of two changes the equatorial distance of the stagnation point from 4.9 R_E to 7.2 R_E. Since magnetospheric electric fields have been found to vary rapidly and over much wider ranges of amplitudes, the stagnation point is expected to wander often beyond the magnetopause as well as down to L = 1 (i.e. into the surface of the Earth)!

TABLE G1 :Equatorial distance of the Stagnation Point (L_{sp}) for a minimum dawn-dusk convection electric field (E_o) and for a dipole magnetic field.

E_o	0	0.1	0.28	0.58	1.0	5.0	mV/m
L_{SP}	∞	12.2	7.3	4.9	3.85	1.72	R_E

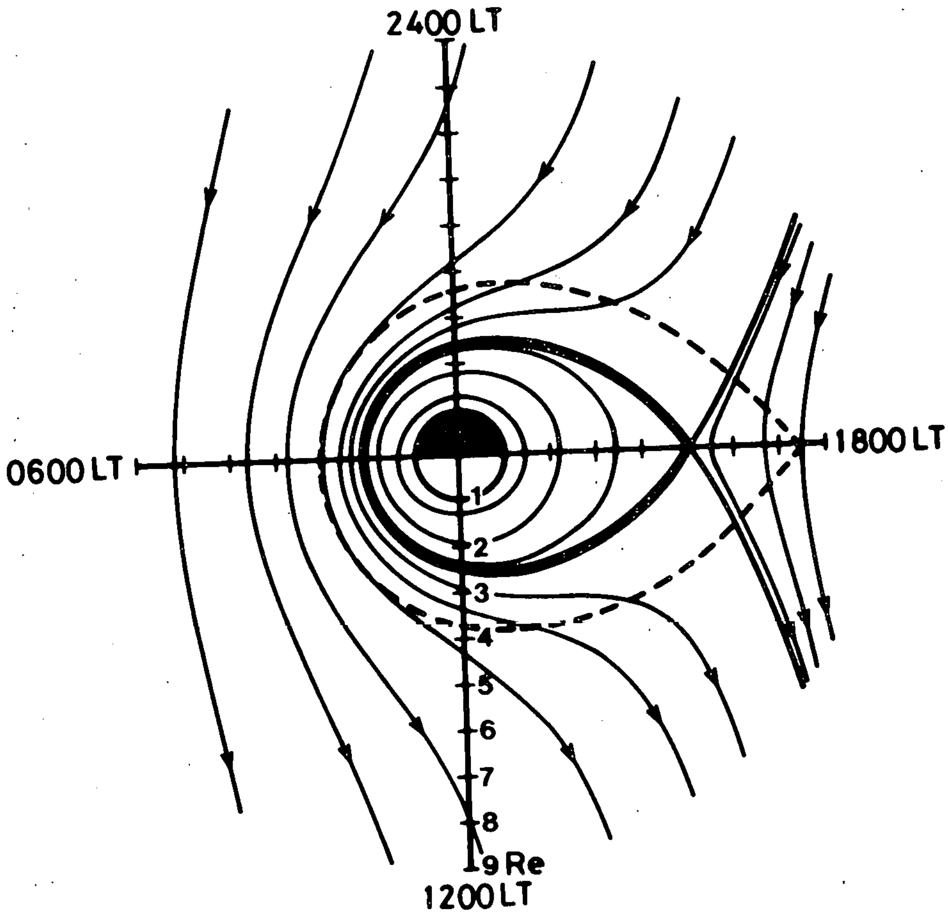

Fig. G1.- Equatorial cross section of equipotential surface corresponding to the uniform dawn-dusk convection electric field of Kavanagh et al. (1968) for E_o = 0.58 mV/m (solid lines). The thick solid line depicts the Last Closed Equipotential (LCE) for this electric field model. The LCE is identified with the plasmapause in the MHD theory for the formation of this boundary. The dashed curve indicates the LCE when the intensity of the dawn-dusk field (E_o) is equal to 0.28 mV/m and the Stagnation Point at 7.2 R_E in the 1800 LT meridian plane (after Grebowsky, 1970). The arrow indicate the direction of the plasma streaming parallel to the equipotential surfaces.

In many instances, time dependent "tear-drop" electric field models have been used with variable intensities for E_o, to simulate the deformation of the plasmapause during non-stationary geoelectric conditions (Grebowsky, 1970; Chen and Wolf, 1972; Chen and Grebowsky, 1974).

A number of other types of idealized electric field models, with stagnation points at various locations, have also been proposed by Grebowsky (1971), Volland (1973, 1975), Rycroft (1974), Stern (1977), Raspopov (1970), Kivelson and Southwood (1975), Cowley and Ashour-Abdalla (1975), Ejiri (1978), Southwood and Kaye (1979); Grebowsky and Chen (1976), Berchem (1980)and Hultqvist et al. (1981, 1982). The remarks made above, and limitations discussed below apply to all these "Stagnation Point Models" as well.

C. Although the ideal MHD definition of the plasmapause has been handy and useful to a certain extent, it has now become hard to hold that the plasmapause coïncides precisely with the Last Closed Equipotential of any ad-hoc large scale electric field distribution.

To demonstrate that this definition is unsatisfactory let us consider for instance a variable dawn-dusk electric field model for which E_o decreases suddenly from 0.58 mV/m to 0.28 mV/m. The two dashed curves in fig. G2 represent the LCE of the initial and final E-field distributions respectively. Let us first assume that the initial plasmapause coïncides at $t = t_o$ with the outermost dashed line. Since the electric field is stationnary at any subsequent time ($t > t_o$), all plasma elements located at the plasmapause drift along this LCE. Consequently, the plasmapause does not change position as time goes on.

Let us now assume, instead, that the initial plasmapause coïncided at $t = t_o$ with the innermost dashed line corresponding to the LCE for E_o = 0.58 mV/m. The subsequent positions of the plasmapause can again be determined by following the $\underline{E} \times \underline{B}/B^2$ drift path of plasma

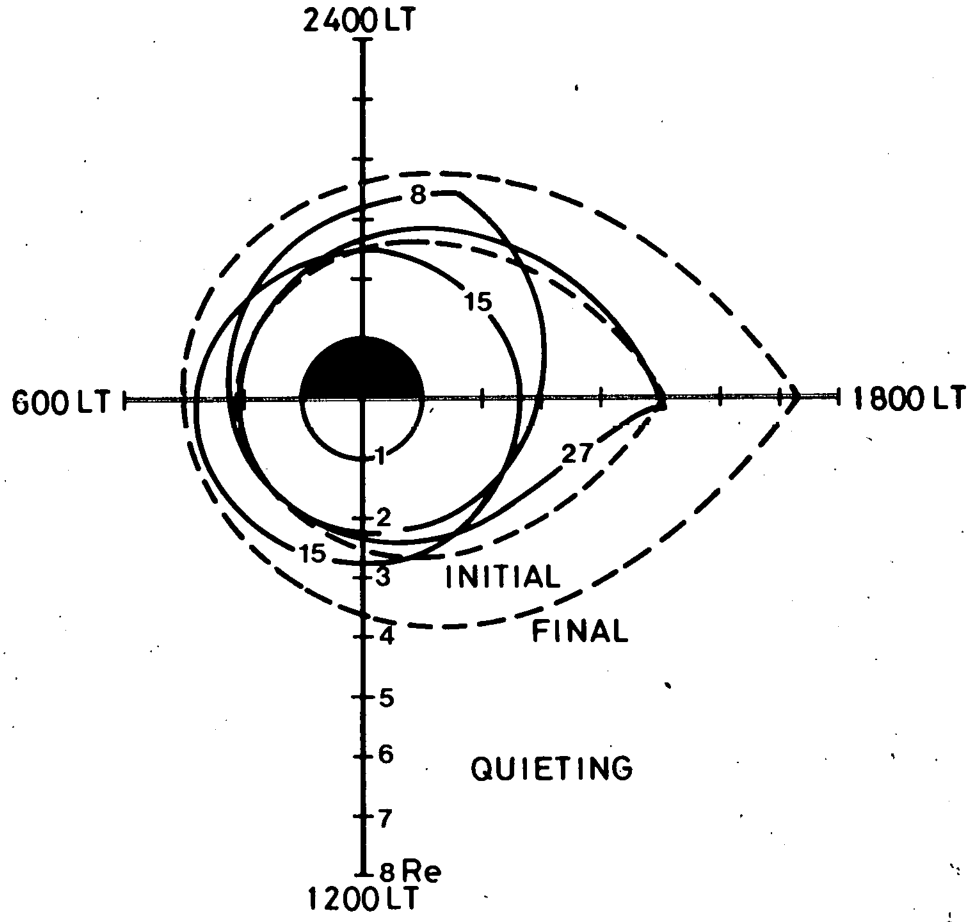

Fig. G2.- Successive equatorial positions of the plasmapause considered to be the last closed equipotential (LCE) of an initial uniform dawn-dusk electric field E_o = 0.58 mV/m, at $t = t_o$. For $t > t_o$ the plasma elements forming the plasmapause are moving in a uniform dawn-dusk field whose intensity is 0.28 mV/m and whose LCE is shown by the outermost dashed curve (after Grebowsky, 1970).

elements originally located along the initial plasmapause. The three solid curves in fig. G2 correspond then to the plasmapause locations at t_o + 8h, t_o + 15h and t_o + 27h respectively. These calculations have been made by Grebowsky (1970). It can be seen that while the plasmapause position changes it will never coïncide with the outermost dashed line which is the actual LCE for $t > t_o$.

This example illustrates clearly that for a time dependent electric field the plasmapause does not remain the last closed equipotential, even if it coïncided at some initial time t_o with such an ideal LCE surface. Why then identify the plasmapause at some brief instant of time (t_o) with a last closed equipotential, when this definition is no longer valid at any later instant of time?

The example illustrated in fig. G2 demonstrates also that the plasmapause positions at the time (t) are not independent of the choice of t_o, the initial time when plasmapause was assumed to coïncide with the LCE. Indeed, when t_o is taken before or after the sudden decrease of E_o, the resulting positions of the plasmapause, at $t > t_o$, are completely different. A satisfactory theory for the formation of the plasmapause must, of course, predict positions for the plasmapause which are not dependent of the particular choice of the initial time of the numerical simulation (t_o).

D. Furthermore, when t_o is choosen when E_o has a minimum minimorum value the initial LCE has then a maximum maximorum extent. It has been verified numerically that in less then 36 hours all the plasma elements forming originally the plasmapause have drifted to the magnetopause. Indeed, for $t > t_o$, $E_o(t)$ is necessarily larger then $E_{o,min}$; as a consequence, the stagnation point and all subsequent LCE's are located inside the initial plasmapause surface; therefore, all plasma elements forming the original plasmapause drift along open trajectories, and eventually, they reach the magnetopause surface where they are lost less than 36h after t_o.

E. Spiro, et al. (1981) also pointed out that, according to their recent numerical simulations with time dependent electric fields, the observed plasmapause positions for September 16, 1976 are closer to their theoretical model calculation when the "initial plasmapause" is not choosen to be the last closed equipotential at t_o = 0900 h UT on that date. The best agreement with the observations was obtained for some other arbitrary initial circle defining the positions of the plasmapause at $t = t_o$. This results coroborates that the plasmapause should never again be regarded as a Last Closed Equipotential of any magnetospheric convection electric field.

The main program (TROJA) calculates the equatorial position (R, radial distance and φ, local time angle) as well as the equatorial density (n_{eq}) of a plasma density element along its drift path in the magnetosphere as a function of time (t). The equations of motion (3.31) and (3.32) and the equation for the time evolution of the equatorial plasma density (3.33) are integrated simultaneously by the standard HAMIN predictor-corrector numerical method. These differential equations are contained in the subroutine DBPDD.

The total velocity of the plasma elements ($\underline{V}' = \underline{V}_E + \underline{u}$) is the sum of (i) the electric drift, $\underline{V}_E$ (eq. 4.1) determined by the electric and magnetic field distributions E(R, φ, t)) and B(R, φ, t), (ii) the plasma interchange velocity, $\underline{u}$ (eq. 4.49) which is set equal to be equal to zero in the ideal MHD approximation as for the simulations illustrated in figs. 13, 14, 15 and 16.

The magnetic field model (described in Appendix A) and the electric field model (described in Appendix B) which have been used to calculate $\underline{V}_E$ are contained in subroutines called BRG and KZSET, respectively. The spatial derivatives of these B-field and E-field components are calculated in the subroutines BGRAD and GRAD, respectively. The electric field model E3H(f) depends on a scale factor f which has been changed as function of time (t) for the simulations illustrated in figs. 28, 29, 30, 31 and 32. The scale factor f(t) is determined by eq. (4.56) (in subroutine FACK) as a function of the geomagnetic index $K_p(t)$. The three-hourly values of $K_p(t)$ for a period of time of two months are stored in a Data File called LEMAIREAP.

The instantaneous value of $\underline{u}(t)$, the maximum plasma interchange velocity, given by eq. (4.49) is calculated in the subroutine DBPDD; (i) $\Sigma_p(R, \varphi, K_p)$, the integrated Pedersen conductivity described in Appendix D, is calculated as a function of R, φ and K_p in subroutine PEDER; (ii) g_{eff}, the effective gravitational plus centrifugal acceleration is given by eqs. (4.50) and (4.52) and is calculated in the subroutine DBPDD; (iii) $\Delta\rho$ the excess density in the plasma element, $S_o(R,\varphi)$ and $V(R,\varphi)$, the section at reference altitude, and volume of a 1 Weber magnetic flux tube are given by eqs. (3.4) and (3.5) and are all calculated in the subroutine NT.

The integration of the three differential equations starts at a given initial value (R_o, φ_o, n_o) at a given initial time (t_o), for a given day (DD) in the period of two months for which the K_p values have been stored in the file LEMAIREAP. The numerical integration is stoped either after a given lapse of Universal Time (Δt), or when φ exceeds a maximum Local Time angle, (φ_{max}) or when R becomes larger than the radial distance of the magnetopause $R_{MP}(\varphi)$ (defined by eqs. A9 and A10).

In the subroutine OUTP the results are printed; they are stored in a data file for later use by the ploting program : TRAJO.

REFERENCES

AHMED, M., SAGALYN, R.C., WILDMAN, P.J.L. and BURKE, W.J., Topside ionospheric trough morphology : occurrence frequency and diurnal, seasonal and altitude variations, J. Geophys. Res., 84, 489-498, 1979.

ALFVEN, H. and C.-G. FALTHAMMAR, Cosmical electrodynamics, 2d., ed. Oxord University Press, London and New York, 1963.

ANGERAMI, J.J., Whistler duct properties deduced from VLF observations made with the OGO 3 satellite near the magnetic equator, J. Geophys. Res., 75, 6115-6135, 1970.

ANGERAMI, J.J. and CARPENTER, D.L., Whistler studies of the plasmapause in the magnetosphere. 2. Electron density and total tube electron content near the knee in magnetospheric ionization, J. Geophys. Res., 71, 711-725, 1966.

ANGERAMI, J.J. and THOMAS, J.O., Studies of planetary atmospheres. 1. The distribution of electrons and ions in the Earth's exosphere, J. Geophys. Res., 69, 4537-4560, 1964.

AUBRY, M.P., RUSSELL, C.T. and KIVELSON, M.G., Inward motion of the magnetopause before a substorm, J. Geophys. Res., 75, 7018-7031, 1970.

AXFORD, W.I. and HINES, C.O., A unifying theory of high-latitude geophysical phenomena and geomagnetic storms, Canad. J. Phys., 39, 1433-1464, 1961.

BAILEY, G.J. and HEELIS, R.A., Ion temperature troughs induced by a meridional neutral air wind in the night-time equatorial topside ionosphere, Planet. Sp. Sci., 28, 895-906, 1980.

BAILEY, G.J., MOFFETT, R.J., HANSON, W.B. and SANATANI, S., Effects of interhemisphere transport on plasma temperatures at low latitudes, J. Geophys. Res., 78, 5597-5610, 1973.

BAILEY, G.J., MOFFETT, R.J. and MURPHY, J.A., A theoretical study of night-time field-aligned O^+ and H^+ fluxes in a mid-latitude magnetic field tube at equinox under sunspot maximum conditions, J. Atmos. Terr. Phys., 39, 105-110, 1977.

BAILEY, G.J., MOFFETT, R.J. and MURPHY, J.A., Interhemispheric flow of thermal plasma in a closed magnetic flux tube at mid-latitudes under sunspot minimum conditions; Planet. Space Sci., 26, 753-765, 1978.

BAILEY, G.J., MOFFETT, R.J. and MURPHY, J.A., Calculated daily variations of O^+ and H^+ at mid-latitudes. II. Sunsport maximum results, J. Atmos. Terr. Phys., 41, 417-429, 1979.

BALSIGER, H., Composition of hot ions (0.1 - 16 keV/e) as observed by the GEOS and ISEE mass spectrometers and inferences for the origin and circulation of magnetospheric plasmas, Adv. Space Res., 1(1), 289-303, 1981.

BALSIGER, H., EBERHARDT, P., GEISS, J. and YOUNG, D.T., Magnetic storm injection of 0.9- to 16-keV/e solar and terrestrial ions into the high-altitude magnetosphere, J. Geophys. Res., 85, 1645-1662 and 6080, 1980.

BANKS, P.M. and HOLZER, T.E., The polar wind, J. Geophys. Res., 73, 6846-6854, 1968.

BAUER, S.J., Physics of planetary ionospheres, 230 pp., Springer-Verlag, Berlin, 1973.

BAUGHER, C.R., CHAPPELL, C.R., HORWITZ, J.L., SHELLEY, E.G. and YOUNG, D.T., Initial thermal plasma observations from ISEE-1, Geophys. Res. Lett., 7, 657-660, 1980.

BAUMJOHANN, W., HAERENDEL, G. and MELZNER, F., Magnetospheric convection observed between 06 and 21 LT : variations with K_p, submitted to J. Geophys. Res., 1985.

BEGHIN, C., CERISIER, J.C., RAUCH, J.L., BERTHELIER, J.J., LEFEUVRE, F., DEBRIE, R., MOLCHANOV, O.A., MALTSEVA, O.A. and MASSEVITCH, N.I., Experimental evidence of ELF ducts in the ionospheric trough and in the auroral zone, presented at Cospar symposium 9, Graz, 1984.

BEGHIN, C., PANDEY, R. and ROUX, D., North-south asymmetry in quasi-monochromatic plasma density irregularities observed in the night-time equatorial F- region, presented at Cospar symposium 9, Graz, 1984.

BERCHEM, J., Etude de la convection magnétosphérique à l'aide des données de plasma froid fournies par les satellites GEOS 1 et ISEE 1, Thèse de doctorat 3ème Cycle, Univ. Paris VI, 1980.

BERCHEM, J. and ETCHETO, J., Experimental study of magnetospheric convection, Adv. Space Res., 1, (1) 179-184, 1981.

BERTIN, F. and PAPET LEPINE, J., Latitudinal variation of total electron content in the winter at middle latitudes, Radio Science, 5, 899-906, 1970.

BEWERSDORFF, A.B. and SAGALYN, R.C., Spatial and temporal variations of the thermal plasma between 3000 and 5700 kilometers at L = 2 to 4, J. Geophys. Res., 77, 4734-4745, 1972.

BINSACK, J.H., Plasmapause observations with the M.I.T. experiment on IMP2, J. Geophys. Res., 72, 5231-5237, 1967.

BIRMINGHAM, T.J. and NORTHROP, T.G., Diffusion of cold magnetospheric ions, J. Geophys. Res., 86, 8971-8976, 1981.

BLOCK, L.P. and CARPENTER, D.L., Derivation of magnetospheric electric fields from whistler data in a dynamic geomagnetic field, J. Geophys. Res., 79, 2783-2789, 1974.

BOSTICK, W.H., Experimental study of ionized matter projected across a magnetic field, Phys. Rev., 104, 292-299, 1956.

BRACE, L.H., REDDY, B.M. and MAYR, H.G., Global behavior of the ionosphere at 1000 kilometer altitude, J. Geophys. Res., 72, 265-283, 1967.

BRACE, L.H. and THEIS, R.F., The behavior of the plasmapause at mid-latitudes : ISIS 1 Langmuir probe measurements, J. Geophys. Res., 79, 1871-1884, 1974.

BRICE, N.M., Bulk motion of the magnetosphere, J. Geophys. Res., 72, 5193-5211, 1967.

BULLOUGH, K. and SAGREDO, J.L., Longitudinal structure in the plasmapause : VLF goniometer observations of knee-whistlers, Nature, 225, 1038-1039, 1970.

CAIN, J.C., Geomagnetic models from satellite surveys, Rev. Geophys. Space Phys., 9, 259-273, 1971.

CARPENTER, D.L., New experimental evidence of the effect of magnetic storms on the magnetosphere, J. Geophys. Res., 67, 135-145, 1962.

CARPENTER, D.L., Whistler evidence of a "knee" in the magnetospheric ionization density profile, J. Geophys. Res., 68, 1675-1682, 1963.

CARPENTER, D.L., Whistler studies of the plasmapause in the magnetosphere. 1. Temporal variations in the position of the knee and some evidence on plasma motions near the knee, J. Geophys. Res., 71, 693-709, 1966.

CARPENTER, D.L., Relations between the dawn minimum in the equatorial radius of the plasmapause and Dst, K_p and local K at Byrd station, J. Geophys. Res., 72, 2969-2971, 1967.

CARPENTER, D.L., Remarks on the ground-based whistler method of studying the magnetospheric thermal plasma, Ann. Géophys., 26, 363-370, 1970a.

CARPENTER, D.L., Whistler evidence of the dynamic behavior of the duskside bulge in the plasmasphere, J. Geophys. Res., 75, 3837-3847, 1970b.

CARPENTER, D.L., OGO 2 and 4 VLF observations of the asymmetric plasmapause near the time of SAR arc events, J. Geophys. Res., 76, 3644-3650, 1971.

CARPENTER, D.L., Whistlers and VLF noises propagating just outside the plasmapause, J. Geophys. Res., 83, 45-57, 1978.

CARPENTER, D.L., VLF observations of magnetospheric dynamics near the plasmapause, in Proceedings of International Workshop on Selected Topics of Magnetospheric Physics, Tokyo, March 1979.

CARPENTER, D.L., A study of the outer limits of ducted whistler propagation in the magnetosphere, J. Geophys. Res., 86, 839-845, 1981.

CARPENTER, D.L., Some aspects of plasmapause probing by whistlers, Radio Science, 18, 917-925, 1983.

CARPENTER, D.L. and CHAPPELL, C.R., Satellite studies of magnetospheric substorms on August 15, 1968. 3. Some features of magnetospheric convection, J. Geophys. Res., 78, 3062-3067, 1973.

CARPENTER, D.L. and PARK, C.G., On what ionospheric workers should know about the plasmapause-plasmasphere, Rev. Geophys. Space Phys., 11, 133-154, 1973.

CARPENTER, D.L., PARK, C.G., TAYLOR, H.A. and BRINTON, H.C., Multi-experiment detection of the plasmapause from EOGO satellites and Antarctic ground stations, J. Geophys. Res., 74, 1837-1847, 1969.

CARPENTER, D.L. and SEELY, N.T., Cross-L plasma drifts in the outer plasmasphere : quiet time patterns and some substorm effects, J. Geophys. Res., 81, 2728-2736, 1976.

CARPENTER, D.L. and SMITH, R.L., Whistler measurements of electrons density in the magnetosphere, Rev. Geophys., 2, 415-441, 1964.

CARPENTER, D.L. and STONE, K., Direct detection by a whistler method of the magnetospheric electric field associated with a polar substorm, Planet. Space Sci., 15, 395-397, 1967.

CARPENTER, D.L., STONE, K., SIREN, J.C. and CRYSTAL, T.L., Magnetospheric electric fields deduced from drifting whistler paths, J. Geophys. Res., 77, 2819-2834, 1972.

CARPENTER, D.L., WALTER, F., BARRINGTON, R.E. and McEWEN, D.J., Alouette 1 and 2 observations of abrupt changes in whistler rate and of VLF noise variations at the plasmapause- A satellite ground study, J. Geophys. Res., 73, 2929-2940, 1968.

CHANDRASEKHAR, S., Plasma physics, University of Chicago Press, Chicago, 1960.

CHAPMAN, S. and BARTELS, J., Geomagnetism, Oxford University Press, New York, 1940.

CHAPPELL, C.R., Recent satellite measurements of the morphology and dynamics of the plasmasphere, Rev. Geophys. Space Phys., 10, 951-979, 1972.

CHAPPELL, C.R., Detached plasma regions in the magnetosphere, J. Geophys. Res., 79, 1861-1870, 1974.

CHAPPELL, C.R., Cold plasma distribution above a few thousand kilometers at high latitudes, paper presented at Nobel symposium problems in high latitude magnetospheric-ionospheric plasma physics and strategies for their solution, Kiruna, Sweden, 1982.

CHAPPELL, C.R., BAUGHER, C.R. and HORWITZ, J.L., The new world of thermal plasma research, Rev. Geophys. Space Phys., 18, 853-861, 1980.

CHAPPELL, C.R., GREEN, J.L., JOHNSON, J.F.E. and WAITE, J.H., Jr., Pitch angle variations in magnetospheric thermal plasma - Initial observations from Dynamics Explorer 1, Geophys. Res. Letters, 9, 933-936, 1982.

CHAPPELL, C.R., HARRIS, K.K. and SHARP, G.W., A study of the influence of magnetic activity on the location of the plasmapause as measured by OGO 5, J. Geophys. Res., 75, 50-56, 1970a.

CHAPPELL, C.R., HARRIS, K.K. and SHARP, G.W., The morphology of the bulge region of the plasmasphere, J. Geophys. Res., 75, 3848-3861, 1970b.

CHAPPELL, C.R., HARRIS, K.K. and SHARP, G.W., The dayside of the plasmasphere, J. Geophys. Res., 76, 7632-7647, 1971.

CHAPPEL, C.R., OLSEN, R.C., GREEN, J.L., JOHNSON, J.F.E. and WAITE, H.J., The discovery of nitrogen ions in the Earth's magnetosphere, Geophys. Res. Letters, 9, 937-940, 1982.

CHEN, A.J. and GREBOWSKY, J.M., Plasma tail interpretations of pronounced detached plasma regions measured by OGO 5, J. Geophys. Res., 79, 3851-3855, 1974.

CHEN, A.J., GREBOWSKY, J.M. and TAYLOR, H.A., Dynamics of mid-latitude light ion trough and plasma tails, J. Geophys. Res.. 80, 968-976, 1975.

CHEN, A.J. and WOLF, R.A., Effects on the plasmasphere of a time-varying convection electric field, Planet. Space Sci., 20, 483-509, 1972.

COMFORT, R.H., BAUGHER, C.R. and CHAPPELL, C.R., Use of the thin sheath approximation for obtaining ion temperatures from the ISEE-1 limited aperture RPA, J. Geophys. Res., 87, 5109-5123, 1982.

COMFORT, R.H. and HORWITZ, J.L., Low energy ion pitch angle distributions observed on the dayside at geosynchronous altitudes, J. Geophys. Res., 86, 1621-1627, 1981.

CORCUFF, P., CORCUFF, Y., CARPENTER, D.L., CHAPPELL, C.R.. VIGNERON, J. et KLEIMENOVA, N., La plasmasphère en période de recouvrement magnétique. Etude combinée des données des satellites OGO 4, OGO 5 et des sifflements reçus au sol, Ann Géophys., 28, 679-695, 1972.

CORCUFF, Y., Probing the plasmapause by whistlers, Ann. Géophys., 31 53-67, 1975.

CORCUFF, Y. et CORCUFF, P., Structure et dynamique de la plasma-pause-plasmasphère les 6 et 14 juillet 1977 : étude à l'aide des données de sifflements reçus au sol et de données des satellites ISIS et GEOS 1, Ann. Geophys., 38, 1-24, 1982.

CORCUFF, Y., CORCUFF, P. and LEMAIRE, J., Dynamical plasmapause positions during the July 29-31, 1977, storm period : a comparison of observations and time dependent model calculations, accepted for publication in Ann. Geophysicae, 1985.

COWLEY, S.W.H. and ASHOUR-ABDALLA, M.A.M., Adiabatic plasma convection in a dipole field variation of plasma bulk parameters with L, Planet. Space Sci., 23, 1527, 1975.

CUMMINGS, W.D., COLEMAN, P.J. Jr. and SISCOE, G.L., Quiet day magnetic field at ATS 1, J. Geophys. Res., 76, 926-932, 1971.

DALY, R.A. and HUGHES, W.J., The effects of hydromagnetic waves on the shape of the plasmapause boundary, preprint 1983.

DAVIES, K., ANDERSON, D.N., PAUL, A.K., DEGENHARDT, W., HARTMANN, G.K. and LEITINGER, R., Nighttime increases in total electron content observed with the ATS 6 radio beacon, J. Geophys. Res., 84, 1536-1542, 1979.

DECREAU, P., Fonctionnement d'une sonde quadripolaire sur satellite magnétosphérique (expérience GEOS). Contribution à l'étude du comportement du plasma froid au voisinage de la plasmapause équatoriale, Thèse de Doctorat d'Etat en Sciences Physiques, Université d'Orléans, 1983.

DECREAU, P.M.E., BEGHIN, C. and PARROT, M., Electron density and temperature as measured by the mutual impedance experiment on board GEOS-1, Space Sci. Rev., 22, 581-595, 1978.

DECREAU, P.M.E., BEGHIN, C. and PARROT, M., Global characteristics of the cold plasma in the equatorial plasmapause region as deduced from the GEOS 1 mutual impedance probe, J. Geophys. Res., 87, 695-712, 1982.

DECREAU, P.M.E., CARPENTER, D.L., CHAPPELL, C.R., COMFORT, R.H., GREEN, J.L., GURNETT, D.A., OLSEN, R.C. and WAITE, J.H., Jr., Latitudinal plasma distribution in the dusk plasmaspheric bulge : refilling phase and quasi-equilibrium state, 1984.

DECREAU, P.M.E., ETCHETO, J., KNOTT, K., PEDERSEN, A., WRENN, G.L. and YOUNG, D.T., Multi-experiment determination of plasma density and temperature, Space Sci. Rev., 22, 633-645, 1978.

EJIRI, M., Trajectory traces of charged particles in the magnetosphere, J. Geophys. Res., 83, 4798, 1978.

EJIRI, M., HOFFMAN, R.A. and SMITH, P.H., The convection electric field model for the magnetosphere based on Explorer 45 observations, J. Geophys. Res., 83, 4811, 1978.

ETCHETO, J. and BLOCK, J.J., Plasma density measurements from the GEOS-1 relaxation sounder, Space Sci. Rev., 22, 597-610, 1978.

EVANS, J.V., Observations of F-region vertical velocities at Millstone Hill. 2. Evidence for fluxes into and out of the protonosphere, Radio Science, 6, 843-854, 1971.

EVIATAR, A., LENCHEK, A.M. and SINGER, S.F., Distribution of density in an ion-exosphere of a non rotating planet, Phys. Fluids, 12, 455-462, 1964.

FAHR, H.J. and SHIZGAL, B., Modern exospheric theories and their observational relevance, Rev. Geophys. Space Phys., 21, 75-124, 1983.

FAIRFIELD, D.H., Average magnetic field configuration of the outer magnetosphere, J. Geophys. Res., 73, 7329-7338, 1968.

FAIRFIELD, D.H. and MEAD, G.D., Magnetospheric mapping with a quantitative geomagnetic field model, J. Geophys. Res., 80, 535-542, 1975.

FAIRFIELD, D.H. and VINAS, A.F., The inner edge of the plasma sheet and the diffuse aurora, J. Geophys. Res., 89, 841-854, 1984.

FEJER, J.A., Semidiurnal currents and electron drifts in the ionosphere, J. Atmos. Terr. Phys., 4, 184-203, 1953.

FENNELL, J.F., JOHNSON, R.G., YOUNG, D.T., TORBERT, R.B. and MOORE, T.E., Plasma and electric field boundaries at high and low altitudes on July 29, 1977, J. Geophys. Res., 87, 5933-5942, 1982.

FOSTER, J.C., An empirical electric field model derived from Chatanika radar data, J. Geophys. Res., 88, 981-987, 1983.

FOSTER, J.C., BANKS, P.M. and DOUPNIK, J.R., Electrostatic potential in the auroral ionosphere derived from Chatanika radar observations, J. Geophys. Res., 87, 7513-7524, 1982.

FOSTER, J.C., DOUPNIK, J.R. and STILES, G.S., Large scale patterns of auroral ionospheric convection observed with the Chatanika radar, J. Geophys. Res., 86, 357-371, 1981.

FOSTER, J.C., DOUPNIK, J.R. and STILES, G.S., Ionospheric convection and currents in the midnight sector on November 8, 1979, J. Geophys. Res., 86, 2143-2148, 1981.

FOSTER, J.C., PARK, C.G., BRACE, L.H., BURROWS, J.R., HOFFMAN, J.H., MAIER, E.J. and WHITTEKER, J.H., Plasmapause signatures in the ionosphere and magnetosphere, J. Geophys. Res., 83, 1175-1182, 1978.

GALEEV, A.A., Plasma turbulence in the magnetosphere with special regard to plasma heating, in "Physics of the Hot Plasma in the Magnetosphere", eds. B. Hultqvist and L. Stenflo, Plenum Press, New York, pp. 251-270, 1975.

GEISS, J., BALSIGER, H., EBERHARDT, P., WALKER, H.-P., WEBER, L., YOUNG, D.T. and ROSENBAUER, H., Dynamics of magnetospheric ion composition as observed by the GEOS mass spectrometer, Space Sci. Rev., 22, 537-566, 1978.

GEISS, J. and YOUNG, D.T., Production and transport of O^{++} in the ionosphere and plasmasphere, J. Geophys. Res., 86, 4739-4750, 1981.

GREBOWSKY, J.M., Model study of plasmapause motion, J. Geophys. Res., 75, 4329-4333, 1970.

GREBOWSKY, J.M., Time-dependent plasmapause motion, J. Geophys. Res., 76, 6193-6197, 1971.

GREBOWSKY, J.M. and CHEN, A.J., Effects on the plasmasphere of irregular electric fields, Planet. Space Sci., 24, 689-696, 1976.

GREBOWSKY, J.M., HOFFMAN, J.H. and MAYNARD, N.C., Ionospheric and magnetospheric "plasmapauses", Planet. Space Sci., 26, 651-660, 1978.

GREBOWSKY, J.M., MAYNARD, N.C., TULUNAY, Y.K. and LANZEROTTI, L.J., Coincident observations of ionospheric troughs and the equatorial plasmapause, Planet. Space Sci., 24, 1177-1185, 1976.

GREBOWSKY, J.M., RAHMAN, N.K. and TAYLOR, H.A., Jr., Comparison of coincident OGO 3 and OGO 4 hydrogen ion composition measurements, Planet. Space Sci., 18, 965-976, 1970.

GREBOWSKY, J.M., TAYLOR, H.A. and LINDSAY, J.M., Location and source of ionospheric troughs, Planet. Space Sci., 31, 99-105, 1983.

GREBOWSKY, J.M., TULUNAY, Y.K. and CHEN, A.J., Temporal variations in the dawn and dusk midlatitude trough and plasmapause position, Planet. Space Sci., 22, 1089-1099, 1974.

GREEN, J.L. and HORWITZ, J.L., Magnetospheric processes in the plasmapause, EOS, 65, 110-111, 1984.

GREENWALD, R.A., Electric fields in the ionosphere and magnetosphere, Space Sci. Res., 34, 3, 305-315, 1983.

GRINGAUZ, K.I., The structure of the ionized gas envelope of earth from direct measurements in the USSR of local charged particle concentrations, Planet. Space Sci., 11, 281-296, 1963.

GRINGAUZ, K.I., The cold plasma throughout the magnetosphere, in "Physics of Solar Planetary Environments", ed. D.J. Williams, A.G.U. publication, pp. 672-684, 1976.

GRINGAUZ, K.I., Plasmasphere and its interaction with the ring current, Space Sci. Rev., 34, 245-257, 1983.

GRINGAUZ, K.I. and BEZRUKIKH, V.V., Asymmetry of the Earth's plasmasphere in the direction noon-midnight from Prognoz and Prognoz-2 data, J. Atmos. Terr. Phys., 38, 1071-1076, 1976.

GRINGAUZ, K.I., KURT, V.G., MOROZ, I. and SHKLOVSKII, I.S., Results of observations of charged particles observed out to R = 100,000 km, with the aid of charged-particle traps on Soviet space rockets, Soviet Astronomy-AJ., 4, 680-695, 1960.

GUREVICH, A.V., KRYLOV, A.L. and TSEDILINA, YE.YE., Electric fields in the earth's magnetosphere and ionosphere, Space Sci. Rev., 19, 59-160, 1976.

HANSON, W.B. and ORTENBURGER, I.B., The coupling between the protonosphere and the normal F region, J. Geophys. Res., 66, 1425-1435, 1961.

HANSON, W.B. and PATTERSON, T.N.L., The maintenance of the night-time F-layer, Planet. Space Sci., 12, 979-997, 1964.

HAREL, M. and WOLF, R.A., Convection, in "Physics of Solar Planetary Environments" vol. 2 edited by D.J. Williams, AGU, Washington D.C., pp. 617-629, 1976.

HAREL, M., WOLF, R.A. and REIFF, P.H., Computer modeling of events in the inner magnetosphere, in "Quantitative Modeling of the Magnetospheric Processes", Geophys. Monogr. Ser., vol. 21, edited by W.P. Olson, pp. 499-512, AGU, Washington D.C., 1979.

HAREL, M., WOLF, R.A., REIFF, P.H., SPIRO, R.W., BURKE, W.J., RICH, F.J. and SMIDDY, M., Quantitative simulation of a magnetospheric substorm. 1. Model logic and overview, J. Geophys. Res., 86, 2217-2241, 1981.

HAREL, M., WOLF, R.A., SPIRO, R.W., REIFF, P.H., CHEN, C.-K., BURKE, W.J., RICH, F.J. and SMIDDY, M., Quantitative simulation of a magnetospheric substorm. 2. Comparison with observations, J. Geophys. Res., 86, 2242-2260, 1981.

HARRIS, K.K., SHARP, G.W. and CHAPPELL, C.R., Observations of the plasmapause from OGO 5, J. Geophys. Res., 75, 219-224, 1970.

HARTLE, R.E., Ion-exosphere with variable conditions at the baropause, Phys. Fluids, 12, 455-462, 1969.

HARTLE, R.E., Model for rotating and non-uniform planetary exospheres, Phys. Fluids, 14, 2592-2598, 1971.

HELLIWELL, R.A., Exospheric electron density variation deduced from whistlers, Ann. Géophys., 17, 76-81, 1961.

HIGEL, B. and WU LEI, Electron density and plasmapause characteristics at 6.6 R_E : a statistical study of the GEOS 2 relaxation sounder data, J. Geophys. Res., 89, 1583-1601, 1984.

HILL, T.W., Inertial limit on corotation, J. Geophys. Res., 84, 6554-6558, 1979.

HO, D. and CARPENTER, D.L., Outlying plasmasphere structure detected by whistlers, Planet. Space Sci., 24, 987-994, 1976.

HOCH, R.J., Stable auroral red arcs, Rev. Geophys. Space Phys., 11, 935-949, 1973.

HOCH, R.J. and SMITH, L.L., Location in the magnetosphere of field lines leading to SAR arcs, J. Geophys. Res., 76, 3079-3086, 1971.

HOFFMAN, J.H., DODSON, W.H., LIPPINCOTT, C.R. and HAMMACK, H.D., Initial ion composition results from the ISIS satellite, J. Geophys. Res., 79, 4246-4251, 1974.

HONES, E.W. and BERGESON, J.E., Electric field generated by a rotating magnetized sphere, J. Geophys. Res., 70, 4951-4958, 1965.

HORWITZ, J.L., Conical distributions of low-energy ion fluxes at synchronous orbit, J. Geophys. Res., 85, 2057-2064, 1980.

HORWITZ, J.L., ISEE 1 observations of O^{++} in the magnetosphere, J. Geophys. Res., 86, 9225-9229, 1981.

HORWITZ, J.L., The ionosphere as a source for magnetospheric ions, Rev. Geophys. Space Phys., 20, 929-952, 1982.

HORWITZ, J.L., Major questions on the interchange of thermal plasmas between the ionosphere and plasmasphere, J. Atmos. Terr. Phys., 45, 765-775, 1983a.

HORWITZ, J.L., Plasmapause diffusion, J. Geophys. Res., 88, 4950-4952, 1983b.

HORWITZ, J.L., BAUGHER, C.R., CHAPPELL, C.R., SHELLEY, E.G. and YOUNG, D.T., Pancake pitch angle distributions in warm ions observed with ISEE 1, J. Geophys. Res., 86, 3311-3320, 1981a.

HORWITZ, J.L., BAUGHER, C.R., CHAPPELL, C.R., SHELLEY, E.G., YOUNG, D.T. and ANDERSON, R.R., ISEE 1 observations of thermal plasma in the vicinity of the plasmasphere during periods of quieting magnetic activity, J. Geophys. Res., 86, 9989-10001, 1981b.

HORWITZ, J.L. and CHAPPELL, C.R., Observations of warm plasma in the dayside plasma trough at geosynchronous orbit, J. Geophys. Res., 84, 7075-7090, 1979.

HORWITZ, J.L., CHAPPELL, C.R., REASONER, D.L., CRAVEN, P.D., GREEN, J.L. and BAUGHER, C.R., Observations of low energy plasma composition from the ISEE-1 and SCATHA satellites, in "Energetic Ion Composition in the Earth's Magnetosphere", edited by R.G. Johnson, 263-286, Terra Scientific Publishing Company, Tokyo, 1983.

HORWITZ, J.L., COMFORT, R.H. and CHAPPELL, C.R., Thermal ion composition measurements of the formation of the new outer plasmasphere and double plasmapause during storm recovery phase, Geophys. Res. Letters, 11, 701-704, 1984.

HULTQVIST, B., APARICIO, B., BORG, H., ARNOLD, R. and MOORE, T.E., Decrease of keV electron and ion fluxes in the dayside magnetosphere during the recovery phase of magnetospheric disturbances, Planet. Space Sci., 29, 107-126, 1981.

HULTQVIST, B., HOLMGREN, L.A., REME, H., BAHNSEN, A., JESPERSEN, M. and KREMSER, G., Quiet-time convective electric field properties derived from keV electron measurements at the inner edge of the plasma sheet by means of GEOS-2, Planet. Space Sci., 30, 261-283, 1982.

JAGGI, R.K. and WOLF, R.A., Self-consistent calculation of the motion of a sheet of ions in the magnetosphere, J. Geophys. Res., 78, 2852-2866, 1973.

KAISER, R.R. and BULLOUGH, K., VLF and ELF émissions, Ann. Géophys., 31, 137-141, 1975.

KAVANAGH, L.D., Jr., FREEMAN, J.W., Jr. and CHEN, A.J., Plasma flow in the magnetosphere, J. Geophys. Res., 73, 5511-5519, 1968.

KAYE, S.M. and KIVELSON, M.G., Time dependent convection electric fields and plasma injection, J. Geophys. Res., 84, 4183-4188, 1979.

KHAZANOV, G.V., KOEN, M.A., KONIKOV, Yu. V. and SIDOROV, I.M., Simulation of ionosphere-plasmasphere coupling taking into account ion inertial and temperature anisotropy, Planet. Space Sci., 32, 585-598, 1984.

KINTNER, P.M. and GURNETT, D.A., Evidence of drift waves at the plasmapause, J. Geophys. Res., 83, 39-44, 1978.

KIVELSON, M.G., Magnetospheric electric fields and their variation with geomagnetic activity, Rev. Geophys. Space Phys., 14, 189-197, 1976.

KIVELSON, M.G. and SOUTHWOOD, D.J., Local time variations of particle flux produced by an electric field in the magnetosphere, J. Geophys. Res., 80, 56, 1975.

KLEIMENOVA, N.G., KOVNER, M.S. and KUZNETSOVA, V.A., VLF-ground observations near the plasmapause projections, J.Atmos. Terr. Phys., 38, 1215-1216, 1976.

KLOBUCHAR, J.A., AARONS, J. and HOSSEINIEH, H.H., Midlatitude nighttime total electron content behavior during magnetically disturbed periods, J. Geophys. Res., 73, 7530-7534, 1968.

KOONS, H.C., Plasmapause crossings determined by using the oblique plasma resonance excited by a satellite-borne RF antenna, J. Geophys. Res., 79, 2526-2528, 1974.

KOPAL, Z., A study of the Roche model, Jodrell Bank Ann., 1 (3), 37-57, 1954.

KOWALKOWSKI, L. et LEMAIRE, J., Contribution à l'étude des éléments de plasma détachés dans la magnétosphère, Bull. Classe Sci., Acad. Royale Belgique, 65, 159-173, 1979.

LANZEROTTI, L.J., FUKUNISHI, H. and CHEN, L., ULF pulsation evidence of the plasmapause. 3. Interpretation of polarization and spectral amplitude studies of Pc 3 and Pc 4 pulsations near L = 4, J. Geophys. Res., 79, 4648-4653, 1974.

LANZEROTTI, L.J., FUKUNISHI, H., HASEGAWA, A. and CHEN, L., Excitation of the plasmapause at ultralow frequencies, Phys. Rev. Letters, 31, 624-628, 1973.

LANZEROTTI, L.J., MACLENNAN, C.G. and WEBB, D.C., Comparisons of inferred total plasmasphere content with measured plasma density profiles, J. Geophys. Res., 84, 2648-2650, 1979.

LANZEROTTI, L.J. and WOLFE, A., Hydromagnetic wave observations in the vicinity of a magnetospheric plasma density gradient, J. Geophys. Res., 86, 2447-2450, 1981.

LEMAIRE, J., O^+, H^+ and He^+ ion distributions in a new polar wind model, J. Atmos. Terr. Phys., 34, 1647-1658, 1972.

LEMAIRE, J., The "Roche-Limit" of ionospheric plasma and the formation of the plasmapause, Planet. Space Sci., 22, 757-766, 1974.

LEMAIRE, J., The mechanisms of formation of the plasmapause, Ann. Géophys., 31, 175-189, 1975.

LEMAIRE, J., Steady state plasmapause positions deduced from McIlwain's electric field models, J. Atmos. Terr. Phys., 38, 1041-1046, 1976a.

LEMAIRE, J., Rotating ion-exosphere, Planet. Space Sci., 24, 975-985, 1976b.

LEMAIRE, J., Impulsive penetration of filamentary plasma elements into the magnetospheres of the Earth and Jupiter, Planet. Space Sci., 25, 887-890, 1977.

LEMAIRE, J., The interpretation of protons and electrons observations from ATS 6 satellite within the frame of McIlwain's electric field model, Bull. Classe Sci., Acad. Royale Belgique, 68, 821-834, 1982.

LEMAIRE, J., Formation and deformation of the plasmapause, Video-montage, Institut d'Aéronomie Spatiale, Bruxelles, 1983.

LEMAIRE, J., Simulation of solar wind-magnetosphere interaction, in Proceedings of NATO Advances Research Workshop on "The Morphology and Dynamics of the Polar Cusp" (eds. J. Holtet and A. Egeland), D. Reidel Publishing Company, Dordrecht, Holland, 1984a.

LEMAIRE, J., Formation and deformation of the plasmapause during a substorm event, in Proceedings of Conference on "Résultats du projet ARCAD 3 et des programmes récents en physique de la magnétosphère et de l'ionosphère", Ed. CNRS, Toulouse, 1984b.

LEMAIRE, J., Plasmoid motion across a tangential discontinuity (with application to the magnetopause) (accepted for publication in J. Plasma Phys., 1985).

LEMAIRE, J. and KOWALKOWSKI, L., The role of plasma interchange motion for the formation of a plasmapause, Planet. Space Sci., 29, 449-478, 1981.

LEMAIRE, J. et SCHERER, M., Le champ électrique de polarisation dans l'exosphère ionique polaire, Compt. Rend. Acad. Sci. Paris, 269, 666-669, 1969.

LEMAIRE, J. and SCHERER, M., Model of the polar ion-exosphere, Planet. Space Sci., 18, 103-120, 1970.

LEMAIRE, J. and SCHERER, M., Kinetic models of the solar wind, J. Geophys. Res., 76, 7479-7490, 1971a.

LEMAIRE, J. and SCHERER, M., Simple model for an ion-exosphere in an open magnetic field, Phys. Fluids, 14, 1683-1694, 1971b.

LEMAIRE, J. and SCHERER, M., Ion-exosphere with asymmetric velocity distribution, Phys. Fluids, 15, 760-766, 1972.

LEMAIRE, J. and SCHERER, M., Kinetic models of the solar and polar winds, Rev. Geophys. Space Phys., 11, 427-468, 1973.

LEMAIRE, J. and SCHERER, M., Exospheric models of the topside ionosphere, Space Sci. Rev., 15, 591-640, 1974a.

LEMAIRE, J. and SCHERER, M., Ionosphere-plasmasheet field-aligned currents and parallel electric fields, Planet. Space Sci., 22, 1485-1490, 1974b.

LEMAIRE, J. and SCHERER, M., Field aligned distribution of plasma mantle and ionospheric plasmas, J.Atmos. Terr. Phys., 40, 337-343, 1978.

LEMAIRE, J. and SCHERER, M., Field-aligned current density versus electric potential characteristics for magnetospheric flux tubes, Annales Geophysicae, 1, 91-96, 1983.

LI, W., SOJKA, J.J. and RAITT, W.J., A study of plasmaspheric density distributions for diffusive equilibrium conditions, Planet. Space Sci., 31, 1315-1327, 1983.

LINSCOTT, G.R. and SCOURFIELD, M.W.J., Observations of the plasmapause and diffusive aurora, Planet. Space Sci., 24, 299-300, 1976.

LONGMIRE, C.L., Elementary Plasma Physics, Interscience, New York, 1963.

MAUK, B.H. and McILWAIN, C.E., Correlation of K_p with the substorm-injected plasma boundary, J. Geophys. Res., 79, 3193-3196, 1974.

MAUK, B.H. and MENG, C.-I., Characterization of geostationary particle signature based on the "injection boundary" model, J. Geophys. Res., 88, 3055-3071, 1983.

MAYNARD, N.C. and GREBOWSKY, J.M., The plasmapause revisited, J. Geophys. Res., 82, 1591-1600, 1977.

MAYNARD, N.C., GREBOWSKY, J.M. and HOFFMAN, J.H., Equatorial and ionospheric H^+ plasmapause, EOS, Trans. AGU, 58, 482, 1977.

MAYR, H.G., FONTHEIM, E.G., BRACE, L.H., BRINTON, H.C. and TAYLOR, H.A., Jr., A theoretical model of the ionosphere dynamics with interhemispheric coupling, J. Atmos. Terr. Phys., 34, 1659-1680, 1972.

MAYR, H.G., GREBOWSKY, J.M. and TAYLOR, H.A., Jr., Study of the thermal plasma on closed field lines outside the plasmasphere, Planet. Space Sci., 18, 1123-1135, 1970.

McDONALD, B.E., OSSAKOW, S.L., ZALESAK, S.T. and ZABUSKY, N.J., Scale sizes and lifetimes of F region plasma cloud striations as determined by the condition of marginal stability, J. Geophys. Res., 86, 5775-5784, 1981.

McILWAIN, C.E., Coordinates for mapping the distribution of magnetically trapped particles, J. Geophys. Res., 66, 3681-3691, 1961.

McILWAIN, C.E., Plasma convection in the vicinity of the geosynchronous orbit, in "Earth Magnetospheric Processes", ed. B.M. McCormac, D. Reidel Publ. Co., Dordrecht-Holland, pp. 268-279, 1972.

McILWAIN, C.E., Substorm injection boundaries, in "Magnetospheric Physics", ed. B.M. McCormac, D. Reidel Publ. Co., Dordrecht-Holland, pp. 143-154, 1974.

MEAD, G.D. and FAIRFIELD, D.H., A quantitative magnetospheric model derived from spacecraft magnetometer data, J. Geophys. Res., 80, 523-534, 1975.

MENDILLO, M. and CHACKO, C.G., The base level of ionospheric trough, J. Geophys. Res., 82, 5129-5137, 1977.

MISHIN, V.M. and NEMTZOVA, E.I., Investigation on Geomagn. Aeron. and Phys. of Sun, Irkutsk, 11, 221, 1970.

MOFFETT, R.J. and HANSON, W.B., Calculated distributions of hydrogen and helium ions in the low latitude ionosphere, J. Atmos. Terr. Phys., 35, 207-222, 1973.

MORGAN, M.G., Simultaneous observations of whistlers at two L ≅ 4 Alaskan stations, J. Geophys. Res., 81, 3977-3991, 1976.

MORGAN, M.G., BROWN, P.E., JOHNSON, W.C. and TAYLOR, H.A., Jr., Light ion and electron troughs observed in the mid-latitude topside ionosphere on two passes of OGO 6 compared to coincident equatorial electron density deduced from whistlers, J. Geophys. Res., 82, 2797-2800, 1970.

MORGAN, M.G. and MAYNARD, M.C., Evidence of dayside plasmaspheric structure through comparisons of ground-based whistler data and Explorer 45 plasmapause data, J. Geophys. Res., 81, 3992-3998, 1976.

MOSHUPI, M.C., ANGER, C.D., MURPHREE, J.S., WALLIS, D.D., WHITTEKER, J.H. and BRACE, L.H., Characteristics of trough region auroral patches and detached arcs observed by ISIS 2, J. Geophys. Res., 84, 1333-1346, 1979.

MOSHUPI, M.C., COGGER, L.L., WALLIS, D.D., MURPHEE, I.S. and ANGER, C.D., Auroral patches in the vicinity of the plasmapause, Geophys. Res. Letters, 4, 37-40, 1977.

MROZ, G.J., OLSON, W.P. and PFITZER, K.A., Induced magnetospheric electric fields, in "Quantitative Modeling of Magnetospheric Processes", ed. W.P. Olson, Geophys. Monograph 21, AGU, pp. 316-325, 1979.

MULDREW, D.B., F- layer ionization troughs deduced from Alouette data, J. Geophys. Res., 70, 2635-2650, 1965.

MULDREW, D.B., The formation of ducts and spread F and the initiation of bubbles by field-aligned currents, J. Geophys. Res., 85, 613-625, 1980.

MURDIN, J., SOJKA, J.J. and SCHUNK, R.W., Diurnal transport effects on the F-region plasma at Chatanika under quiet and disturbed conditions, Planet. Space Sci., 32, 47-61, 1984.

NESS, N.F., SCEARCE, C.S. and SEEK, J.B., Initial result of the IMP 1 magnetic field experiment, J. Geophys. Res., 69, 3531-3569, 1964.

NISHIDA, A., Formation of plasmapause, or magnetospheric plasma knee, by the combined action of magnetospheric convection and plasma escape from the tail, J. Geophys. Res., 71, 5669-5679, 1966.

NORTHRUP, T.G., Adiabatic Motion of Charged Particles, Wiley (Interscience), New York, 109 pp., 1963.

NORTHRUP, T.G. and TELLER, E., Stability of the adiabatic motion of charged particles in the Earth's field, Phys. Rev., 117, 215-225, 1960.

OLSEN, R.C., Equatorially trapped plasma populations, J. Geophys. Res., 13, 11235-11245, 1981.

OLSEN, R.C., The hidden ion population of the magnetosphere, J. Geophys. Res., 87, 3481-3488, 1982.

OLSEN, R.C., SHAWHAN, S.D., GALLAGHER, D.L., GREEN, J.L. and CHAPPELL, C.R., Observation of plasma heating at the Earth's magnetic equator, submitted to J. Geophys. Res., 1985.

OLSON, W.P. and PFITZER, K.A., A quantitative model of the magnetospheric magnetic field, J. Geophys. Res., 79, 3739-3748, 1974.

ORR, D., Probing the plasmapause by geomagnetic pulsations, Ann. Géophys., 31, 77-91, 1975.

ORR, D. and WEBB, D.C., Statistical studies of geomagnetic pulsations with periods between 10 and 70 sec and their relationship to the plasmapause region, Planet. Space Sci., 23, 1169-1178, 1978.

PANNEKOEK, A., Ionization in stellar atmosphere, Bull. Astron. Inst. Neth., 1, 107-118, 1922.

PARK, C.G., Whistler observations of the interchange of ionization between the ionosphere and the protonosphere, J. Geophys. Res., 75, 4249-4260, 1970.

PARK, C.G., Westward electric fields as the cause of nighttime enhancements in electron concentrations in midlatitude F region, J. Geophys. Res., 76, 4560-4568, 1971.

PARK, C.G., Some features of plasma distribution in the plasmasphere deduced from Antarctic whistlers, J. Geophys. Res., 79, 169-173, 1974.

PARK, C.G., CARPENTER, D.L. and WIGGIN, D.B., Electron density in the plasmasphere : whistler data on solar cycle, annual and diurnal variations, J. Geophys. Res., 83, 3137-3144, 1978.

PARK, C.G. and MENG, C.-I., Vertical motions of the midlatitude F2 layer during magnetospheric substorms, J. Geophys. Res., 76, 8326-8332, 1971.

PEDERSEN, A., CATTELL, C.A., FÄLTHAMMAR, C.-G., FORMISANO, V., LINDQVIST, P.-A., MOZER, F. and TORBERT, R., Quasi-static electric field measurements with spherical double probes on the GEOS and ISEE satellites, Space Sci. Rev., 37, 269-312, 1984.

QUEGAN, S., BAILEY, G.J., MOFFETT, R.J., HEELIS, R.A., FULLER-ROWELL, T.J., REES, D. and SPIRO, R.W., A theoretical study of the distribution of ionization in the high-latitude ionosphere and the plasmasphere : first results on the mid-latitude trough and the light-ion trough, J. Atmos. Terr. Phys., 44, 619-640, 1982.

RAITT, W.J., SCHUNK, R.W. and BANKS, P.M., Quantitative calculations of helium ion escape fluxes from the polar ionospheres, J. Geophys. Res., 83, 5617-5623, 1978.

RASPOPOV, O.M., Sur le diagnostic des champs électriques dans la magnétosphère de la Terre, Ann. Geophys., 26, 751-759, 1970.

RICH, F.J., SAGALYN, R.C. and WILDMAN, P.J.L., Electron temperature profiles measured up to 8000 km by S3-3 in the late afternoon sector, J. Geophys. Res., 84, 1328-1332, 1979.

RICHARDS, P.G., SCHUNK, R.W. and SOJKA, J.J., Large-scale counterstreaming of H^+ and He^+ along plasmaspheric flux tubes, J. Geophys. Res., 88, 7879-7886, 1983.

RICHMOND, A.D., Self-induced motions of thermal plasma in the magnetosphere and the stability of the plasmapause, Radio Science, 8, 1019-1027, 1973.

RICHMOND, A.D., Electric field in the ionosphere and plasmasphere on quiet days, J. Geophys. Res., 81, 1447-1450, 1976.

RIJNBEEK, R.P., COWLEY, S.W.H., SOUTHWOOD, D.J. and RUSSELL, C.T., A survey of dayside flux transfer events observed by ISEE 1 and 2 magnetometers, J. Geophys. Res., 89, 786-800, 1984.

ROEDERER, J.G. and HONES, E.W., Jr., Motion of magnetospheric particle clouds in a time-dependent electric field model, J. Geophys. Res., 79, 1432-1438, 1974.

ROSSELAND, S., Electrical state of a star, Month. Notices Roy. Astron. Soc., 84, 720-728, 1924.

RYCROFT, M.J., Magnetospheric plasma flow and electric field derived from whistler observations, in "Correlated Interplanetary and Magnetospheric Observations, ed. D.E. Page, D. Reidel Publ. Co., Dordrecht-Holland, pp. 317-335, 1974.

RYCROFT, M.J. and BURNELL, S.J., Statistical analysis of movements of the ionospheric trough and the plasmapause, J. Geophys. Res., 75, 5600-5604, 1970.

RYCROFT, M.J. and THOMAS, J.O., The magnetospheric plasmapause and the electron density trough at the Alouette I orbit, Planet. Space Sci., 18, 65-80, 1970.

SAGREDO, J.L., SMITH, I.D. and BULLOUGH, K., The determination of whistler nose-frequency and minimum group delay and its implication for the measurement of the east-west electric field and tube content in the magnetosphere, J. Atmos. Terr. Phys., 35, 2035-2046, 1973.

SAMIR, U., WRIGHT, K.H., Jr., and STONE, N.H., The expansion of a plasma into a vacuum : basic phenomena and processes and applications to space plasma physics, Rev. Geophys. Space Phys., 21, 1631-1646, 1983.

SAUNDERS, M.A., Recent ISEE observations of the magnetopause and low latitude boundary layer : a review, J. Geophys. Res., 52, 190-198, 1983.

SCHUNK, R.W. and WATKINS, D.S., Comparison of solutions to the thirteen-moment and standard transport equations for low speed thermal protons flows, Planet. Space Sci., 27, 433-444, 1979.

SHARP, G.W., Midlatitude trough in the night ionosphere, J. Geophys. Res., 71, 1345-1356, 1966.

SINGH, N. and SCHUNK, R.W., Numerical calculations relevant to the initial expansion of the polar wind, J. Geophys. Res., 87, 9154-9170, 1982.

SISCOE, G.L. and SUMMERS, D., Centrifugally driven diffusion of iogenic plasma, J. Geophys. Res., 86, 8471-8479, 1981.

SMITH, A.J., CARPENTER, D.L. and LESTER, M., Longitudinal variations of plasmapause radius and the propagation of VLF noise within small ($\Delta L \sim 0.5$) extensions of the plasmasphere, Geophys. Res. Letters, 8, 980-983, 1981.

SOBOLEVA, T.N., Global model of integral transversal electric conductivity of the ionosphere, Deponent VIMITIN 3504-71, Moscow, 1971.

SOJKA, J.J., RAITT, W.J. and SCHUNK, R.W., A theoretical study of the high-latitude winter F region at solar minimum for low magnetic activity, J. Geophys. Res., 86, 609-621 and 2491, 1981.

SONNERUP, B.U.Ö and LAIRD, M.J., On magnetospheric interchange instability, J. Geophys. Res., 68, 131-139, 1963.

SOUTHWOOD, D.J. and KAYE, S.M., Drift boundary approximations in simple magnetospheric convection models, J. Geophys. Res., 84, 5773, 1979.

SPIRO, R.W., HAREL, M., WOLF, R.A. and REIFF, P.H., Quantitative simulation of a magnetospheric substorm. 3. Plasmaspheric electric fields and evolution of the plasmapause, J. Geophys. Res., 86, 2261-2272, 1981.

SPITZER, L., Jr., Physics of Fully Ionized Gases, 105 pp., Interscience Publ., New York, 1956.

STERN, D.P., The motion of a proton in the equatorial magnetosphere, J. Geophys. Res., 80, 595-599, 1975.

STERN, D.P., Representation of magnetic fields in space, Rev. Geophys. Space Phys., 14, 199-214, 1976.

STERN, D.P., Large-scale electric fields in the earth's magnetosphere, Rev. Geophys. Space Phys., 15, 156-194, 1977.

STOREY, L.R.O., An investigation of whistling atmospherics, Phil. Trans. Roy. Soc. London, 246A, 113-141, 1953.

STÖRMER, C., Sur les trajectoires des corpuscules électrisées dans l'espace sous l'action du magnétisme terrestre, Arch. Sci. Phys., 24, 113, 221, 317, 1907.

SUGIURA, M. and POROS, D.J., A magnetospheric field model incorporating the OGOG 3 and 5 magnetic field observations, Planet. Space Sci., 21, 1763-1773, 1973.

TAYLOR, H.A., Jr., Evidence of solar geomagnetic seasonal control of the topside ionosphere, Planet. Space Sci., 19, 77-93, 1971.

TAYLOR, H.A., Jr., The light ion trough, Planet. Space Sci., 20, 1593-1605, 1972.

TAYLOR, H.A., Jr., BRINTON, H.C., CARPENTER, D.L., BONNER, F.M. and HEYBORNE, R.L., Ion depletion in the high-latitude exosphere; simulations OGO 2 observations of the light ion trough and the VLF cutoff, J. Geophys. Res., 74, 3517-3528, 1969.

TAYLOR, H.A., Jr., BRINTON, H.C. and DESHMUKH, A.R., Observations of irregular structure in thermal ion distributions in the duskside magnetosphere, J. Geophys. Res., 75, 2481-2489, 1970.

TAYLOR, H.A., Jr., BRINTON, H.C. and PHARO, M.W., III., Contraction of the plasmasphere during geomagnetically disturbed periods, J. Geophys. Res., 73, 961-968, 1968.

TAYLOR, H.A., Jr., BRINTON, H.C., PHARO, M.W. III. and RAHMAN, N.K., Thermal ions in the exosphere; evidence of solar and geomagnetic control, J. Geophys. Res., 73, 5521-5533, 1968.

TAYLOR, H.A., Jr. and CORDIER, G.R., In-situ observations of irregular ionospheric structure associated with the plasmapause, Planet. Space Sci., 22, 1289-1296, 1974.

TAYLOR, H.A., Jr. and GREBOWSKY, J.M., Structured variations of the plasmapause : evidence of a corotating plasma tail, J. Geophys. Res., 76, 6806-6814, 1971.

TAYLOR, H.A., Jr., GREBOWSKY, J.M. and CHEN, A.J., Ion composition irregularities and ionosphere-plasmasphere coupling : observations of a high latitude ion trough, J. Atmos. Terr. Phys., 37, 613-623, 1975.

TAYLOR, H.A. Jr., GREBOWSKY, J.M. and WALSH, W.J., Structured variations of the plasmapause : evidence of a corotating plasma tail, J. Geophys. Res., 76, 6806-6814, 1971.

TAYLOR, H.A., Jr., and WALSH, W.J., The light-ion trough, the main trough and the plasmapause, J. Geophys. Res., 77, 6716-6723, 1972.

TAYLOR, W.W.L., PARADY, B.K. and CAHILL, L.J., Jr., Explorer 45 observations of 1- to 30-Hz magnetic fields near the plasmapause during magnetic storms, J. Geophys. Res., 80, 1271-1286, 1975.

THOMAS, J.O. and RYCROFT, M.J., The exospheric plasma during the International Years of the Quiet Sun, Planet. Space Sci., 18, 41-63, 1970.

THOMAS, J.O. and SADER, A.Y., Electron density at the Alouette orbit, J. Geophys. Res., 69, 4561-4581, 1964.

TITHERIDGE, J.E., Plasmapause effects in the topside ionosphere, J. Geophys. Res., 81, 3227-3233, 1976.

TULUNAY, Y.K. and SAYERS, J., Characteristics of the mid-latitude trough as determined by the electron experiment on Ariel III, J. Atmos. Terr. Pys., 33, 1737-1761, 1971.

VOLLAND, H., A semiempirical model of large-scale magnetospheric electric fields, J. Geophys. Res., 78, 171-180, 1973.

VOLLAND, H., Models of global electric fields within the magnetosphere, Ann. Géophys., 31, 159-173, 1975.

VOLLAND, H., A model of the magnetospheric electric convection field, J. Geophys. Res., 83, 2695-2699, 1978.

WALKER, R.J., An evaluation of recent quantitative magnetospheric magnetic field models, Rev. Geophys. Space Phys., 14, 411-427, 1976.

WALKER, R.J., Quantitative modeling of planetary magnetospheric magnetic field, in "Quantitative Modeling of Magnetospheric Processes", ed. W.P. Olson, Geophysical Monograph 21, AGU, Washington D.C., pp. 9-34, 1979.

WOLF, R.A., Effects of ionospheric conductivity on convective flow of plasma in the magnetosphere, J. Geophys. Res., 75, 4677-4698, 1970.

WOLF, R.A., Calculations of magnetospheric electric fields, in "Magnetospheric Physics", ed. by B.M. McCormac, D. Reidel, Publ. Co., Dordrecht-Holland, pp. 167-177, 1974.

WOLF, R.A., HAREL, M., SPIRO, R.W., VOIGT, G.-H., REIFF, P.H. and CHEN, C.-K., Computer simulation of inner magnetospheric dynamics for the magnetic storm of July 29, 1977, J. Geophys. Res., 87, 5949-5962, 1982.

WRENN, G.L. and RAITT, W.J., In situ observations of mid-latitude ionospheric phenomena associated with the plasmapause, Ann. Géophys., 30, 17-28, 1975.

WRENN, G.L., SOJKA, J.J. and JOHNSON, J.F.E., Thermal protons in the morning magnetosphere : filling and heating near the equatorial plasmapause, Planet. Space Sci., 32, 351-363, 1984.

YOUNG, D.T., GEISS, J., BALSIGER, H., EVERHARDT, P., GHIELMETTI, A. and ROSENBAUER, H., Discovery of He^{2+} and O^{2+} ions of terrestrial origin in the outer magnetosphere, Geophys. Res. Letters, 4, 561-564, 1977.

YOUNG, D.T., PERRAUT, S., ROUX, A., DE VILLEDARY, C., GENDRIN, R., KORTH, A., KREMSER, G. and JONES, D., Wave-particle interactions near ΩHe^+ observed on GEOS 1 and 2. 1. Propagation of ion cyclotron waves in the He^+- rich plasma, J. Geophys. Res., 86, 6755-6772, 1981.

YOUNG, E.R., TORR, D.G., RICHARDS, P. and NAGY, A.F., A computer simulation of the midlatitude plasmasphere and ionosphere, Planet. Space Sci., 28, 881-893, 1980.

LIST OF SYMBOLS

$\underline{B}$	Magnetic induction (in nT)
B_{eq}	Equatorial value of magnetic induction (nT)
c	Velocity of light
C_{th}	Ion thermal velocity (eq. 3.21)
$\underline{E}$	Electric field intensity
E_I	Ionospheric electric field intensity
E_p	Polarization electric field (eq. 4.11)
erf(x)	Error function (eq. 2.22)
f	Scale factor of the E3H(f) electric field model
$f(\underline{v})$	Velocity distribution of particles
F	Flux of particles
$F_{\parallel}$	Field-aligned ion flux
$(F_{\parallel})_{PW}$	Polar Wind ion flux
$\underline{g}$	Gravitational acceleration
g_o	Gravitational acceleration at Earth's surface
G	Gravitational constant
h_o	Altitude of reference level (1000 km)
$\underline{i}_P$	Pedersen current density
J_p	Height integrated Pedersen current
k	Boltzman constant
$K_m(x)$	Integral function defined by eq. (2.22)
K_p	Three-hourly planetary geomagnetic index
L	Equatorial distance of a geomagnetic field line in Earth Radii (McIlwain, 1961)
L_c	Equatorial distance of the Zero Parallel Force surface
L_m	Equatorial distance of the Zero Radial Force surface
L_{pp}	Equatorial plasmapause position in the post-midnight sector
m_i, m_e	Ion and electron mass
M_E	Earth mass
n	Particle number density
n_{eq}	Equatorial plasma density

n_{eq}^{BG} Background equatorial plasma density

n_i, n_e Ion and electron density

n_s Critical threshold (eq. 5.1)

N_o Number density at the reference level

N_T Total number of particles in a 1 Weber magnetic flux tube

p Kinetic pressure

$\underset{-}{P}$ Polarization (eq. 4.4)

q_1 Expected number of Coulomb collisions along a field line in an ion-exosphere in Diffusive Equilibrium

q_2 Expected number of Coulomb collisions along a field line in an Exospheric Equilbrium

r, R Radial distance (in km)

r_o Radial distance of reference level

r_m Radial distance of the maximum of the field aligned potential, ψ

R_E Earth radius (6371 km)

$S(\lambda)$ Cross-section of magnetic flux tube

S_{eq} Equatorial section of a 1 Weber magnetic flux tube (eq. 3.1)

S_o Cross-section of a 1 Weber magnetic flux tube at the reference level

S_I Cross-section of magnetic flux tube at ionospheric level

t Universal Time (in hours)

t_B Characteristic broadening time

t_F Free flight time along a magnetic field line

t_S Coulomb collision time (eq. 4.20)

$T_\parallel$, $T_\perp$ Parallel and Perpendicular temperatures

T_i, T_e Ion and Electron temperatures

T_o Temperature at the reference level

$\underset{-}{u}$ Maximum plasma interchange velocity

U Thermal energy in a plasma element

V Volume of a 1 Weber magnetic flux tube above an altitude of 1000 km

$v_\parallel$, $v_\perp$ Particle velocity components parallel and perpendicular to the magnetic field direction

$\underset{-}{V}_B$ Gradient-B velocity (eq. 4.17)

$\underset{-}{V}_E$ Electric drift velocity (eq. 3.30)

$\underset{-}{V}_F$	Drift velocity due to external force (eq. 4.2)
$\underset{-}{V}_g$	Drift velocity due to gravitational force (eq. 4.3)
$\underset{-}{V}_G$	Curvature drift velocity (eq. 4.17)
$\underset{-}{V}_p$	Drift resulting from polarization E-field (eq. 4.14)
$\underset{-}{V}_{p,max}$	Maximum polarization drift velocity
$\underset{-}{V}'$	Total velocity of a plasma element : $\underset{-}{V}_E + \underset{-}{u}$
Z_i, Z_e	Ion and electron electric charges
γ	Fraction of a magnetic flux tube occupied by the plasma element
Δn_{eq}	Excess number density in equatorial plasma element
ε_o	Permittivity of free space
θ	Pitch angle
κ	Dielectric constant in a direction perpendicular to the magnetic field (eq. 4.7)
λ	Latitude
λ_o	Latitude of geomagnetic field line at reference level
Λ	Invariant latitude
Λ'_{pp}	Invariant latitude of plasmapause (eq. 4.54)
λ_m	Latitude at the maximum in the field aligned potential, $\psi(\lambda)$
μ_o	Permeability of free space
$\nu_{c,i}$	Ion collision frequency
$\nu_{L,i}$	Ion Larmor frequancy
ρ	Mass density per unit volume
ρ_c	Electric charge density per unit volume
σ_0, σ_1, σ_2	Parallel, Pedersen and Hall electric conductivity
$\sigma_p \equiv \sigma_1$	Pedersen electric conductivity
Σ_p	Height integrated Pedersen conductivity (eq. 4.21)
Σ_P^S, Σ_P^D	Components of height integrated Pedersen conductivity resulting from Solar photoionization and corpuscular bombardment
ϕ, ϕ_E	Electric potential
ϕ_g	Gravitational plus centrifugal potential (eq. 2.1)
ψ_i, $\psi_e(\lambda)$	Total gravitational and electric potential of an ion and an electron (eq. 2.4)
ψ_m	Maximum value of $\psi(\lambda)$
Ω	Angular velocity of an ion-exosphere
Ω_E	Angular velocity of the Earth

LIST OF ACRONYMS

(b)	Class of ballistic particles
Dawn	0600 hour Local Time
DE	Diffusive Equilibrium
Dusk	1800 hour Local Time
(e)	Class of escaping particles
EE	Exospheric Equilibrium
LCE	Last Closed Equipotential
LIT	Light Ion Trough
LT	Local Time
PP	Plasmapause
SP	Stagnation Point
SSC	Sudden Storm Commencement
(t_1, t_2, t_3, t_4)	Classes of trapped particles
ZPF	Zero Parallel Force
ZRF	Zero Radial Force

LIST OF FIGURES AND TABLES